IMPACT-INDUCED LARGE ELASTOPLASTIC DAMAGE IN FIBER-METAL LAMINATED PANELS

by

YANXIONG LIU

A dissertation submitted to the Graduate Faculty in Engineering in partial fulfillment of the requirements for the degree of Doctor of Philosophy, The City University of New York

2005

UMI Number: 3187451

ProQuest Information and Learning Company
300 North Zeeb Road
P.O. Box 1346
Ann Arbor, MI 48106-1346

This manuscript has been read and accepted for the Graduate Faculty in Engineering in satisfaction of the dissertation requirement for the degree of Doctor of Philosophy.

Sep. 14, 2005 Benjamin Liaw

Date Chair of Examining Committee

Sep. 14, 2005 Mumtaz K. Kassir

Date Executive Officer

Prof. Benjamin Liaw, Dept. of Mechanical Engineering, City College

Prof. Feridun Delale, Dept. of Mechanical Engineering, City College

Prof. Honghui Yu, Dept. of Mechanical Engineering, City College

Prof. Kolluru V. Subramaniam, Dept. of Civil Engineering, City College

Dr. Suresh Goyal, Bell Laboratories

Supervisory Committee

THE CITY UNIVERSITY OF NEW YORK

ABSTRACT

IMPACT-INDUCED LARGE ELASTOPLASTIC DAMAGE IN FIBER-METAL LAMINATED PANELS

by

Yanxiong Liu

Advisor: Professor Benjamin Liaw

In this study large elastoplastic damage induced by impact onto fiber-metal laminates (FMLs) were investigated through drop-weight testing and finite element simulations. Two forms of FMLs (GLARE and ARALL) were studied. The main goal of this investigation is to study impact-damage resistance of these novel composites so that they can be designed optimally for engineering applications.

Both destructive cross-sectional microphotography and nondestructive ultrasonic techniques were used to evaluate the damage inflicted by impact. The results indicate that the destructive cross-sectional micrographs give more detailed damage information whereas the nondestructive ultrasonic C-scans can only show the contour of the delamination. For thinner FMLs under lower energy impact, delamination occurs first between the nonimpact-side aluminum-alloy sheet and its adjacent fiber-reinforced epoxy layer; it is followed by visible cracks in the nonimpact-side aluminum layer and, finally, further delamination between the inner aluminum sheets and fiber-reinforced epoxy layers. More severe damages, such as through-thickness fractures, matrix cracking and fiber breakage, occur under higher energy impact. For thicker FMLs, delaminations appeared near the impact-side at relatively lower impact energy. Further damages, including cracks in the outer aluminum sheet and fiber breakage, were induced on the nonimpact-side when higher impact energy was introduced. Many parameters, such as the type of fibers and aluminum, fiber orientations, specimen thickness, impact energy, the size and shape of the impactor and the temperature, had significant effects on the damage patterns.

The finite element code, LS-DYNA3D, was used to perform numerical simulations of low-velocity impact on aluminum/acrylic sandwich panels and GLARE. With the incorporation of proper failure criteria, crack propagation characteristics, nonlinear constitutive laws, and boundary conditions, the computed impact force histories, the post-impact deformed shapes, and damage patterns were found to be fairly close to experimental results.

In this research, the complicated impact damage phenomenon in FMLs and the associated damage tolerance and strength reduction were understood in details. The conclusions obtained by this study should pave way for devising better methodology for optimal design and further development of FMLs.

ACKNOWLEDGEMENTS

The author wishes to acknowledge my academic advisor, Professor Benjamin Liaw, for his very valuable guidance throughout this study. I also want to thank Professors Feridun Delale and Honghui Yu from the Department of Mechanical Engineering, Professor Kolluru V. Subramaniam from the Department of Civil Engineering as well as Dr. Suresh Goyal from Bell Laboratories for the great advice during my research.

I would like to thank my research colleagues, Messrs. Thomas Cheung, Jianjun Liu, and all my friends who have been working in the Materials Processing and Solid Mechanics Lab in City College of New York. I am also thankful to Messrs. Glenn Zeichner and Alexis Pierides for the preliminary work of impact tests and ultrasonic technique, respectively, and to Mr. Waleed R. Gobran for his sectioning pictures.

I am grateful to NASA Faculty Award for Research (FAR) for supporting this project under Grant No. NAG3-2259 and PSC-CUNY under Grants 61429-00 30 and 62466-00 31. Dr. Kenneth J. Bowles and Dr. John P. Gyekenyesi were the technical monitors of the NASA grant. Part of the equipment used in this investigation was acquired through Army Research Office Grant No. DAAD19-99-1-0366.

Finally I will give my appreciation to my wife, Jun Lu, and my family for their supporting and patience, allowing me to spend such a long time to work on my research. Their encouragement and suggestion always helped me overcome any difficulty I have met during the course of my study.

Yanxiong Liu

August 2005 in New York

TABLE OF CONTENTS

LIST OF TABLES

LIST OF FIGURES

CHAPTER 1: INTRODUCTION

1.1 Impact on Composite Structures

Composite structures have been used widely for engineering applications since 1970s. Compared to metals, composite materials offer a number of distinct advantages, which include, but not limited to, higher strength-to-weight and stiffness-to-weight ratios, superior corrosion resistance, as well as improved fatigue properties [2-4, 36]. In spite of these advantages, composite materials suffer some crucial limitations for engineering applications. One of the major limitations is their relatively low impact resistance [2-4, 97]. It has been well known that impacts by foreign objects can occur during manufacturing, maintenance and service procedures through the entire life of structures. In many cases, serious damage can be induced even when a composite structure is impacted at very low energy and the damage is invisible to naked eyes. Impact-induced damage can cause significant reduction in compressive strength [48, 85, 174, 223, 314], which could be potentially dangerous for structures.

This study is focused on the responses and damage patterns due to low-velocity impact onto fiber-metal laminates (FMLs), which are a form of novel hybrid composites made of interleaving metallic (usually aluminum) and fiber-reinforced plastic layers. The main goal of this investigation is to acquire the information on impact-damage resistance of this class of novel composites needed for better design in engineering applications.

Through the years, extensive studies of impact on composite structures have been conducted worldwide [2, 36, 49, 97, 229, 250]. A review of these studies is discussed in the sequel.

1.1.1 Impact testing systems

Different types of impact can be classified based on impact energies, impact velocities, failure modes, etc. In a simple manner, impact problems can be divided into two separate cases, i.e. low-velocity impact and high-velocity impact. In real life, the tool dropping onto composite structures during manufacturing and service corresponds to the former case while the impingement of runway debris to airplanes is considered the latter. Usually, impact with a velocity below 10 m/s can be treated as a low velocity impact for which stress-wave propagation doesn't play a significant role. For high-velocity impact, the effects of stress-wave propagation must be considered. Various testing systems can be chosen depending on applications and requirements [2, 36, 229]. Some widely used impact testing systems are stated below.

a. Low-velocity impact:

(1) *Charpy and Izod pendulums* - The Charpy and Izod tests were originally developed to assess the impact strengths of metals. Both Charpy and Izod tests are easy to perform and can obtain the information of energy absorption and dissipation in composites. The disadvantages of these pendulum-type testing methods include high frequency harmonic oscillation and specimen geometric dependence. Therefore, they are only suitable for ranking the impact performance of composite structures with same geometry of bar- or beam-like shapes [49].

(2) *Drop-weight impact testers* - Many researchers adopt the drop-weight impact tester [2, 5, 36], which allows a weight to fall from a pre-determined height and strike the specimen. In general, different impact velocities can be obtained by varying the dropping height. A wide range of test geometries can be used with various impactors in different shapes or sizes. With certain design, impact tests can be conducted under various environments and temperatures. It is easy to obtain the contact-force histories and impact velocity with a data acquisition system attached to the tester. In this study, all impact tests were performed using an Instron-Dynatup 8250 pneumatically assisted drop-weight impact tester.

b. High-velocity impact:

(1) *Gas gun impact tester* - Impact testing at ballistic rates of strain can be achieved using a gas gun with high-pressure gas (e.g., helium or nitrogen), to drive the projectile. The impact velocity can reach 1,000 m/s or even higher and penetration usually occurs during impact.

(2) *Hopkinson-bar technique* - For very high strain rates, Hopkinson-bar systems are generally used, where the indirect measurement method is adopted. Impact signals can be obtained using strain gages mounted on the input and output bars. The desired impact responses and material properties can be obtained by applying stress-wave propagation theory.

1.1.2 Low-velocity impact tests on composite structures

The impact responses of composite structures are dominated by the constituent materials, fiber orientations and lay-up configurations, impact energies, geometry of structures, types of impactors, etc. Various factors, which can affect the impact responses, have been studied extensively [2, 36, 229, 250]. A brief literature review is given below.

Yang and Sun [304] obtained an indentation law for composite laminates modified from the Hertzian law of contact based on the static indentation tests. In their study, the contact forces corresponding to loading and unloading, F, can be related to the indentation, α, by the following equations:

$$\text{Loading:} \quad F = k\alpha^{n} \tag{1.1}$$

$$\text{Unloading:} \; F = F_m\left(\frac{\alpha - \alpha_0}{\alpha_m - \alpha_0}\right)^{q} \tag{1.2}$$

where k is the contact coefficient which depends on the material properties and the radii of curvature at the contact point of the target and the impactor; F_m is the contact force at which unloading begins; α_m is the indentation corresponding to F_m whereas α_0 denotes the permanent indentation in an unloading cycle; n and q are power indices (For example, the material system studied by Yang and Sun [304], $n = 1.5$ and $q = 2.5$). Several other researchers [50, 62, 79, 170, 176, 265] used the above indentation laws to analyze the impact on laminated composites. For elastoplastic contact, Cairns [30] pointed out that the contact exponent is expected to be from 1.0 to 1.5.

The damage sequence is important for understanding the impact mechanism. Sun, et al. [76, 139, 169] and Chang, et al. [52, 59, 60, 154] and Collombet, et al. [71] studied impact damage in various composites. From their results, two key conclusions can be drawn: (1) matrix cracks are the initial impact damage mode and (2) delamination is induced by matrix cracks. Liu [179] further pointed out that delamination mainly results from bending stiffness mismatches among laminae. The bigger the difference of fiber angles between two adjacent laminae, the smaller the initiation energy for delamination [124]. The low-velocity impact responses of composites were found to be very similar to those observed in static tests except that vibration was observed through impact tests [130, 258, 265, 293]. However, some researchers did find the rate dependence of some material properties. Liu [182] showed that the interaction between the delamination and matrix cracks exists only in the impact case. Wu, et al. [299] presented different damage patterns of composites subject to impacts of various velocities. The fracture toughness is also rate dependent [15, 159].

Mechanical properties of composites can vary by changing the constituents of composites, i.e. different types of fibers and matrices. Williams and Rhodes [286] evaluated 24 different resin systems and indicated that ductile resin can improve the impact resistance of composites. Griffin [111] found out tougher resins increase the strength and residue compressive strength of composites. Some researchers showed that impact resistance of composites could be significantly improved by using thermoplastic matrix instead of thermoset resin [19, 54, 73, 165, 200, 253]. Pintado, et al. [219] showed that the interleaved system offered superior impact resistance than the tough and brittle systems. Other material systems were also studied [227]. Another way to improve impact resistance of composites is to use hybrid composites, as demonstrated by several researchers [49, 91, 170, 213, 216, 264]. Wang, et al. [280] suggested that the addition of glass fibers into graphite fiber reinforced laminates could effectively improve the impact resistance of the materials. Cheon, et al. [58] showed that adding Kevlar fibers into the glass epoxy composites could improve the capability of impact energy absorption of structures.

The stacking sequence of composites can also affect impact resistance. Hitchen and Kemp [122] showed that the initiation energy of delamination was significantly increased by placing 45° fibers in the surface plies and slightly increased by increasing the number of dissimilar interface with the maximum absorbed energy being about the same. Strait, et al. [254] indicated that the quasi-isotropic lay-ups possess better overall impact resistance than cross-ply or [0/±45] lay-ups. Some researchers studied the woven or braided composites and found that the impact resistance of such materials was even higher than quasi-isotropic lay-ups [74, 109, 110]. Sankar and Zhu [238] showed that stitching could effectively prevent the extension of delamination in composite beams.

Damage patterns in composites could be different due to various impactors. Most of researchers conducted impact tests using hemispherical impactors. Choi, Chang and their associates [52, 59, 60] adopted a line-nose impactor to study the impact damage mechanisms of composites, which can be substantially simplified from a three-dimensional to a two-dimensional event. They also found that the impact responses of composites could be affected by the mass of impactor. Zhao, et al. [309] used a conical-tip indenter for the force-indentation study of composites. Their results indicated that the contact force was proportional to the square of the indentation when a conical indenter was used, instead of the conventional 1.5 power of the indentation for a hemispherical indenter. Zhou [312] performed a study of impact damage mechanisms in composite laminates by a flat-ended impactor. Kim and Goo [149] showed that a higher impact force and longer impact duration were obtained when the shape of impactor was blunter through a dynamic contact analysis. Caprino and Lopresto [43] pointed out that the penetration energy for composites was related to the total fiber thickness and the impactor diameter in a power law.

Some other parameters, such as temperature effect [121], multiple impacts [98, 113], effect of damage on impact responses [156], and specimen size [145, 224, 262], have also been studied. Cantwell and Morton [35] showed that long thin structures failed in a flexural mode whereas short thick targets failed by interlaminar shear directly under the point of impact. The influence of materials thickness on the response of composites to low-velocity impact studied by Caprino, et al. [44, 241] indicated that the force at the point of delamination initiation, the maximum force and related energy, and penetration energy followed the same trend and increased to the power of approximately 1.5 with increasing plate thickness.

Composite sandwich panels present many advantages and have been used extensively [2, 3, 206, 244, 283, 288]. These sandwich panels comprise a lightweight foam, honeycomb or corrugated core with two composite panels as facesheets. The investigation methods used for sandwich panels are similar to those for regular composites. Some early work of impact on composite sandwich panels conducted by Oplinger [97] and Shih [244], et al. presented basic damage patterns of facesheets and core materials. Kim, et al. [146] showed that the face lay-up with small relative orientation between adjacent plies and higher density core are desirable in sandwich plates to reduce the impact delamination. Caprino and Teti [45] indicated that the contact force history essentially depends on the local rigidity of the panel and the residual tensile strength after impact is correlated to fiber failure rather than to the extent of delamination. Mines, et al. [198, 199] and Herup and Palazotto [120] pointed out the limitation of the applicability of common assumption that low-velocity impact is a quasi-static process since the impact behavior of a composite sandwich, in general, is rate dependent. Torre and Kenny [267] found out that corrugate sandwich panels show a better performance in terms of impact energy absorbing properties and better strength in comparison to traditional sandwich structures. Anderson and Madenci [7] observed the types and extent of the impact damage in a variety of sandwich configurations. A qualitative and quantitative study of the effect of low-velocity impacts on foam and honeycomb structures was performed as well. Cantwell, et al. [39] studied the interfacial fracture between the composite skin and the lightweight core in a sandwich structure through a three-point-bending test on a specimen with specific geometry.

Based on extensive impact studies, some researchers tried to give a scale parameter for impact damage. However, their conclusions sometimes are in conflict with each other. Basically, two major approaches are available so far, i.e. the force-based approach and the energy-based approach. Some researchers analyzed the impact force history curves and identified two thresholds: the first damage force and the maximum force [13, 80, 132, 241, 315]. They pointed out that the sudden drop in force curve is attributed to the propagation of damage, so they chose the impact force as the scale parameter of damage. Wiggenraad, Zhang and Davies [284] asserted that the force map was rather more revealing and showed that all impact sites had a sudden increase in damage at a critical load. On the other hand, the indentation depth, the residual tensile strength and the delamination area were measured as a function of impact energy [42, 78, 124, 208, 230, 268]. Delfosse and Poursartip [82] indicated that a force-based approach only worked well up to the onset of damage while an energy-based approach could be more helpful in examining the extent of damage beyond the onset. Sometimes, these two approaches should be combined to identify the damage initiation and extension [60, 65, 79, 311, 313, 314]. There are other parameters used for a damage resistance parameter; for example, Fuoss, et al. [101] adopted a parameter based on bending strain as a measure for predicting the impact damage resistance.

1.2 Low-Velocity Impact Damage Assessment of Composites

All the studies reviewed above are mainly experimental investigations. However, a lot of researchers performed studies of impact on composites based on impact tests combined with impact models and damage analysis. In the following section, work on analysis of impact, such as impact models and damage prediction, will be reviewed.

1.2.1 Damage modes of composite under low-velocity impact

Because composite materials are the combination of two or more constituents, the damage modes are much more complicated when compared with monolithic materials. The damage modes induced by low-velocity impact on composites include [2, 68, 71, 75, 229, 232]:

- Matrix crack caused by tension or shear
- Debonding between the fiber and matrix
- Delamination at the interface of adjacent plies with different fiber directions
- Fiber breakage and pull out from the matrix

1.2.2 Damage detection techniques

In general, the damage patterns are different in size, shape, and orientation, and vary through the thickness in composites. To fully understand the damage characteristics, not only the surface damage but also the internal damage must be assessed. Damage detection techniques applied to composite structures are classified into two categories: nondestructive and destructive techniques. Abrate [2] and Kim, et al. [103, 229] gave comprehensive reviews of both nondestructive and destructive assessments in details. Here, only major methods are stated briefly.

a. Nondestructive techniques:

(1) *Visual inspection and optical microscopy* - they are applied to obtain useful information from surface damage or for transparent materials.

(2) *X-rays detection* - this is one of very powerful NDE techniques [9, 34, 229]. The profile of the delamination as well as major cracks can be detected. It is still difficult to use the technique to find the variation of damage through the thickness.

(3) *Ultrasonic technique* - this technique is used very widely, maybe the most used in NDE. Doyle and Scala [316] gave a review on some early work. In 1980s, more researchers made significant contributions to ultrasonic technique for use in NDE. Time-of-flight C-scans, B-scans and modified C-scans were conducted (Clark, Moran, Daniel and their associates) [27, 28, 69, 72, 77, 99, 152, 222]. A three-dimensional ultrasonic imaging has become possible (Wooh and Daniel [76, 291], Potel, et al. [221]). Recently Aymerich and Meili [9] used ultrasonic evaluation to detect matrix damage. Other researchers made a ply-by-ply damage detection using ultrasonic technique [103, 239]. Mouritz, et al. [201] applied the pulse-echo ultrasonic to thick glass-fiber reinforced plastic (GRP) composites while Dong, et al. [90] adopted an ultrasonic inspection system to explore on-line damage detection. However, the technique encounters difficulty to locate the damage through the thickness when composite specimens are suffered large deformation.

(4) *Acoustic emission* (*AE*) - the advantage of AE is to monitor the damage initiation and progress in real-time [22, 89, 104, 138, 177, 245, 320] even though it cannot locate the damage. Benmedakhene, et al. [15] showed that it could determine different damage mechanisms based on acoustic-emission analysis and microscopic observations.

(5) *Dynamic photoelasticity* - the optical coherent gradient sensing (CGS) technique combined with high-speed photography can obtain qualitative information regarding the stress field and observe the progression of damage (see Walter, Xu, Rosakis and their associates [159, 178, 279, 302]). The particular geometry of specimens and test set-up used here limit the spread application of this technique.

(6) *Others* - including optical-fiber communication technologies [229, 235], electronic speckle pattern interferometry (ESPI) [233] and some other techniques based on new theories [282].

b. Destructive techniques:

De-ply technique and cross-sectional micrograph are two available destructive techniques [2, 229]. In the de-ply technique [214], the damaged composite specimen is soaked in a solution to allow the solution to penetrate into the internal cracks. Then the specimen is treated under high temperature for certain time, resulting in partial pyrolysis of the polymer matrix. The individual plies are then separated. Under an optical microscope, delamination, matrix cracking and fiber breakage can be detected. The results from de-ply are very accurate and reliable. However, this method is time-consuming and not suitable for thermoplastic matrix. In cross-sectional technique [23, 181, 234], the damaged specimen is sectioned into a sufficient number of thin strips at different locations and orientations over the whole damage zone. A series of microscopic images can be taken and a 3D map be constructed. The damage distribution through the whole damaged zone can then be established. Using cross-sectional micrographs, more detailed damage information can be obtained than any other nondestructive assessment. Like de-ply technique, cross-sectional micrograph is also time-consuming and destructive. Extreme precautions should be taken to avoid causing new damage during sectioning.

It is worth noting that the combination of the above damage assessment techniques is needed for adopting full damage evaluation in most cases. The principle of choosing suitable techniques depends on the damage patterns and objective [34, 37, 38, 76]. In this study, nondestructive ultrasonic scans combined with destructive cross-sectional micrographs were adopted in order to fully investigate the complex damage patterns of hybrid composites.

1.2.3 Damage prediction

a. Impact models:

To fully understand the impact procedure, an impact model must be developed. Many models proposed in the literature can be classified into three categories: energy-balance models, spring-mass models, and complete models [2,4].

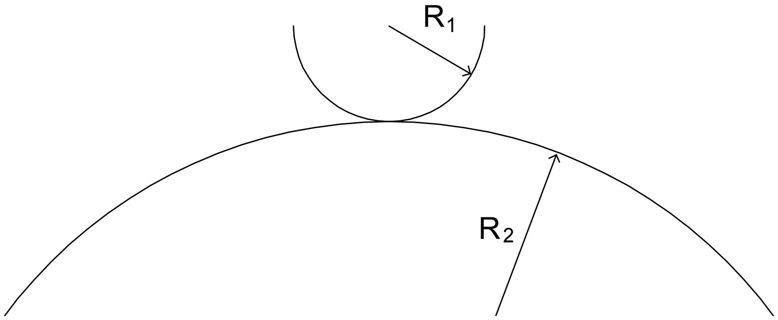

Figure 1.1 Contact of an indenter and a target.

First of all, a contact law is needed to describe the contact between the indenter and the target since it is the foundation for all the models. The most extensively used contact law is the Hertzian law of contact, which is validated for composites through the indentation test studied by Yang and Sun [304]. During the loading phase, the contact force, F, is related to the indentation, α, by

$$F = k\alpha^{1.5} \tag{1.3}$$

here the contact stiffness, k, is

$$k = \tfrac{4}{3} E R^{1/2} \tag{1.4}$$

where

$$\frac{1}{R} = \frac{1}{R_1} + \frac{1}{R_2} \text{ and } \frac{1}{E} = \frac{1-\nu_1^2}{E_1} + \frac{1-\nu_2^2}{E_2} \tag{1.5}$$

here R_1, R_2, E_1, E_2, ν_1 and ν_2 are the radii of curvature, the Young's moduli, and the Poisson's ratios of the indenter and the target, respectively (see Fig. 1.1). During the unloading phase the contact law follows Eq. (1.2).

Cairns [30], Christoforou, et al. [64, 306] derived the elasto-plastic contact law for composites, which indicated that the power of 1.5 is only for perfectly elastic contact while the contact exponent is between 1.0 and 1.5 for elasto-plastic contact. Wu, et al. [1, 144, 292, 294] studied the contact pressure distribution between the indenter and the target. Suemasu, et al. [255] studied the thickness effect on indentation through theoretical and numerical analyses.

1) Energy-balance models

Shivakumar, et al. [248] developed this simple energy-balance model, which is based on the principle of conservation of total energy of the plate-impactor system. Assuming the whole system behaves quasi-statically. All the initial kinetic energy of the impactor is used to deform the plate when the plate reaches its maximum deflection. The energy-balance equation of this whole system is

$$\tfrac{1}{2}MV_0^2 = E_c + E_b + E_s + E_m \tag{1.6}$$

where the subscripts c, b, s and m refer to contact, bending, shear and membrane, respectively. Using the above contact law and plate theory, the maximum impact force can be derived from equation (1.6). This simple model gives the maximum impact force and impact duration, but cannot predict the impact force history, which can be obtained from the following spring-mass models.

2) Spring-mass models

In this spring-mass model, the impactor and plate are represented by two masses M_1 and M_2 connected through a Hertzian spring k that represents the force-indentation relationship of contact (Figure 1.2(a)). M_2 represents the effective mass of plate. K_b, K_s and K_m correspond to the bending stiffness, shear stiffness, and membrane stiffness of plate, respectively [2, 4, 248].

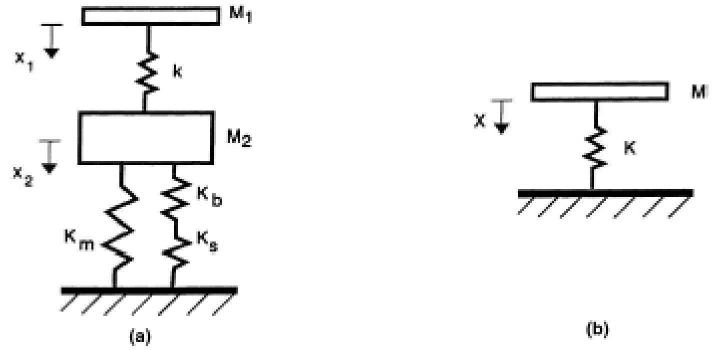

Figure 1.2 Two degree-of-freedom and one degree-of freedom spring-mass models

The dynamic equation of this system can be written as

$$M_1\ddot{x}_1 + F = 0 \tag{1.7a}$$

$$M_2\ddot{x}_2 + K_{bs}x_2 + K_m x_2^3 - F = 0 \tag{1.7b}$$

where F represents the contact force that is a nonlinear function of the indentation $|x_1 - x_2|$. From equations (1.7) with the initial conditions

$$\dot{x}_1(0) = V_0,\ \dot{x}_2(0) = 0,\ x_1(0) = x_2(0) = 0 \tag{1.8}$$

the impact response can be solved numerically. For small deflection problem, the membrane effect is negligible. If the impactor is much heavier than the plate, the inertial effect of the plate is negligible as well. Hence, the impact system can further be simplified to a one degree-of-freedom system shown in Figure 1.2(b), where K should be treated as the combination of contact spring k, K_b, K_s and K_m.

Some other investigators [41, 157, 197] also adopted the spring-mass model to study the impact behavior of composites. The agreement between test data and prediction is fairly well for lower energy impact. However, structures yield to significant damage under higher energy impact and the force curve is not smooth. This simple model cannot predict such kind of force history. Rydin and Karbhari [236] modified the above spring-mass model into a visco-plastic model, which can predict the energy partitioning during impact.

3) Complete models

The impact information predicted from simple models was limited and not accurate enough. Hence, complete models, in which the whole impact system was fully modeled, were developed and accurate solutions could be obtained [2, 4]. The appropriate structural theories were used in complete models. These theories included the three-dimensional dynamic theory of elasticity [303], classical lamination theory [295] and higher order plate or shell theories [67, 140, 141, 153, 158, 242, 249, 266]. To get the solution of complete models, series expansions combined with other techniques were involved [16, 31, 46, 63, 66, 87, 88, 118, 147, 209, 210, 225, 261]. Some numerical methods were used during analysis [21, 94, 106, 151, 263, 285]. Usually, the derivation was very lengthy and complicated. Three-dimensional analyses were needed sometimes [53, 194, 269] and damage could be predicted if damage criteria were adopted in analysis [32, 217, 220, 242].

The above models are based on impact on composite structures. However, they can be easily applied to impact on sandwich structures if corresponding modifications are taken into account [3, 125, 126, 168].

b. Finite element simulation

Theoretical models can only give limited information of the complete impact responses for particular geometry or material systems. To get the impact information in details, such as the stress and strain fields, the damage size and location, etc., finite element approach is a powerful tool for solving such a problem. Many investigators used finite element programs to study the impact on composites. The following is a brief review.

In order to predict the damage in composites, proper failure criteria must be chosen. Many failure criteria presented by various researchers are available in the literature [51, 70, 71, 133, 137, 195, 226, 228, 251, 260, 290, 307, 308]. There are many similarities between the predictions of various theories; however, some striking differences exist as reported by Soden, et al. [251]. For instance, differences as great as 570% had been recorded when various strength predictions were used. Hence it is still a challenge to apply suitable failure criteria for composite structures. Among the damage modes mentioned above, interlaminar delamination is of major importance. Garg [105] reviewed some studies about prediction of delamination and concluded that there are two approaches for the onset of delamination: one based on fracture mechanics and the other on strength. In the fracture-mechanics-based approach, the prediction of delamination onset is made on the basis of either the stress intensity factor, K or the strain energy release rate, G. The strength-based approach to predict the delamination onset involves the detailed stress analysis in conjunction with proper failure criteria. Delamination growth depends upon the stress state of the crack tip, which is governed by the mixed-mode stress intensity factors K_I, K_{II} and K_{III} or the corresponding strain energy release rates G_I, G_{II} and G_{III}. Only one or two modes may dominate the fracture propagation. The most extensively adopted delamination propagation law is in the following form

$$(\frac{G_I}{G_{IC}})^m + (\frac{G_{II}}{G_{IIC}})^n = 1 \tag{1.9}$$

where G_I and G_{II} are the mode I and II strain energy release rates, respectively. G_{IC} and G_{IIC} represent the critical mode I and II strain energy release rates and are materials properties. Parameters m and n are constants. In addition, other empirical delamination onset criteria have been developed through other researchers' studies [215, 325].

Tan and Sun [265] adopted a nine-node isoparametric plate finite element associated with an empirical contact law to predict the impact responses of composite plates. Then numerical results were in good agreement with experimental data. Chen and Sun [55, 56, 256] studied the impact responses of composite plates under various loading conditions using finite element method based on the Mindlin plate theory and large deflection assumption. Byun and Kapania [29] presented a study of nonlinear impact responses of laminated plates using finite element method based on the modified Hertzian contact law. Sekine et al. [243] studied the impact response of composite laminates with a delamination based on the indentation law proposed by Tan and Sun [265] combined with the Lagrange multiplier technique. Gu and Sun [112] made the prediction of impact damage in SMC composites with the damage region being determined using a critical strain energy density criterion. Sun and Liou [176, 259] investigated the stress and deflection of composite plates during impact using a three-dimensional hybrid stress finite element method. Jih and Sun [136] predicted the low-velocity impact delamination by using a statically interlaminar fracture toughness in association with the static linear beam model. Zheng and Sun [310] proposed a double-plate finite element model to simulate the impact-induced delamination dominated by strain energy release rate. Wu and Chang [298] conducted a finite element analysis of composite plates subjected to impact. In their study global responses (velocity, impact force and deflection histories) were predicted. Their model also presented the stress and strain histories throughout the whole plate (but no damages were considered). Kutlu and Chang [155] constructed a finite element model that can predict the through-the-width delamination propagation based on a delamination growth law similar to Equation (1.9). Based on a strength failure criterion, Choi, Chang, et al. [61, 62] used finite element method to predict the onset of matrix cracks and delaminations as well as the delamination growth. By adopting the strength criterion for the onset of matrix cracks and delamination combined with a fracture criterion for delamination growth, Liu, Chang, et al. [183-185] simulated the damage development procedure of composite plates under impact.

Shivakumar, et al. [247] analyzed clamped circular composite plates under static equivalent loads based on the minimum total potential energy method and Tsai-Wu criterion as well as the maximum stress criterion; global responses and damage patterns were obtained from this finite element analysis. Lin and Lee [175] investigated the impact response of composite shell structure with linear shell element, in which the deflection, stresses as well as the effects of curvature were presented. Meimaris and Day [196] presented an investigation of transient responses on laminated plates with a 20-node solid element model. Sridhar and Rao [252] performed a large deformation finite element analysis. Their results indicate that the quasi-isotropic lay-up provides the maximum stiffness for uniformly distributed loading. Liao and Tsai [172] used a partial mixed 3-D finite element model to analyze dynamic responses of composites subjected to impact. Pai and Palazotto [211] developed a nonlinear finite element model, which can analyze the composite shell with large deformation. Kim and Voyiadjis [148] presented shell element formulation based on the first order transverse shear deformation to estimate the imperfection sensitivity of composite panels. Using finite element model Leylek et al. [171] studied the impact response as a function of panel curvature, mesh density, weight of impactor, velocity and impactor size on curved composite panels, etc. De Freitas, Silva and Reis [81] performed a linear static analysis to evaluate the impact failure mechanisms on composites using the maximum load obtained from the experimental impact test. Salpekar [237] conducted analysis of delamination at the tip of impact induced matrix cracks and suggested that the interlaminar stress singularities caused delaminations between 0°/90° and 90°/0° interfaces. Wu and Springer [300] presented a finite element model, which could predict the damage size and location with an error less than 20%. In Wang and Yew's model [281], a ply-by-ply impact damage distribution was predicted by using a three-dimensional analysis together with Hashin's failure criterion. Naik, Sekher and Meduri [203] conducted a 3D transient finite element analysis on woven-fabric composites subjected to low-velocity impact, where contact force was studied using a modified Hertz law and the in-plane failure evaluated by means of Tsai-Hill failure criterion. Armanios, et al. [8] studied the damage patterns in a quasi-isotropic double cracked-lap-shear specimen made of composites in which matrix cracking controlled by the resin strain to failure; delamination controlled by the fracture toughness; and fiber breakage controlled by the fiber strength. Ambur, et al. [6] conducted a transient analysis to study the impact damage initiation where no delamination was accounted for. Ganapathy, et al. [102] used a nonlinear finite element static analysis to simulate low-velocity impact on composites. Reddy, et al. [228] developed a non-linear progressive failure analysis of composites using a generalized laminate plate theory. Naganarayana and Atluri [202] proposed an accurate prediction of delamination growth in a plate model based on the energy release rate distribution. Fuoss, et al. [100, 101] studied the effects of stacking sequence on the impact resistance in composite. Collombet, et al. [70, 71] studied matrix cracking and delamination using the explicit 3D finite element code combined with an experimental approach. Kim, et al. [150] investigated the dynamic response and impact-induced damage in composite shells with various curvatures, which indicated that shells were more susceptible to foreign-object impact than plates. Several researchers introduced an interface element to model the delamination in composite materials [83, 108, 289] while Hitchings et al. [123] modeled the delamination by inserting some spring interface element at the interface.

Luo, et al. [188] showed that the impact damage initiation and propagation in composite plates could be evaluated through an approach based on strength criterion only. Feng, et al. [95] presented an implicit method to analyze the impact of deformable body instead of the more popular explicit model. Hu, et al. [130] presented the effect of delaminations on impact responses of composites by employing a modified Lagrange multiplier technique [129]. Espinosa et al. [93] conducted a 3-D finite element study for composites with a mesh adaptive technique. Varadi and co-workers [271] studied the ball indentation on composites with the finite element contact analysis involving both macro and micro models, which indicated that the micro-model provided more realistic displacement, strain and stress results.

Besides studies based on self-designed finite element programs, many investigators used commercial finite element packages to analyze the damage in composites. Martin and Jackson [193] made a damage prediction of curved composite laminates subjected to static and fatigue loading using the finite element package MSC/NASTRAN. Lammerant and Verpoest [160] adopted ANSYS to model the interaction between matrix cracks and delaminations during impact. The mesh was built with prisms elements and spring element at the interfaces where crack growth controlled by fracture toughness could occur. Xia, Chen and Ellyin [301] developed a meso/micro-mechanical model for damage progression in glass-fiber/epoxy cross-ply laminates through ADINA.

Mahajan [189] investigated the indentation behavior of an orthotropic laminated beam using ABAQUS. Luo, et al. [186, 187] also used ABAQUS with solid elements based on a strength failure criterion to simulate the impact damage of composite plates.

De Moura and Marques [84] predicted the matrix failure and delamination areas based on a special shell element included in the ABAQUS software along with a specific failure criterion. Oguibe and Webb [207] investigated the impact response of a laminated composite plate with a failure mode incorporated in ABAQUS. The resultant impact force, displacement, stress, as well as the contact pressure were plotted in their paper. Ireman, et al. [131] performed damage propagation analyses in composite structural elements with ABAQUS for static responses and LS-DYNA3D for dynamic cases. Lee and co-workers [167] investigated the influence of the mass and shape of impactor, initial velocity, and specimen thickness on the impact behavior in sheet molding compounds (SMC), in which both experimental approach and numerical predictions using LS-DYNA3D were adopted. Belingardi, et al. [12] presented a numerical simulation of fragmentation of composite plates due to impact using DYNA3D and the force history and absorbed energy history were predicted in good agreement with experiments. Hou, et al. [127,128] implemented a modified Chang-Chang failure criterion [51] in DYNA3D to predict the impact damage of composite plate. Their results agree fairly well with test data. Borg, et al. [24] also used LS-DYNA to simulate the delamination in composites with a discrete cohesive crack model.

In recent years, some researchers applied damage mechanics to composites [278]. Guinard, et al. [114] adopted a damage meso-modeling based on damage mechanics to analyze the impact damage of laminated composites. Nguyen [205] achieved damage distributions of laminated composites by the use of multiplayer finite elements based on continuum damage mechanics. Williams and Vaziri [287] developed a plane-stress, continuum damage mechanics-based model for composite materials and implemented in the non-linear finite element code, LS-DYNA3D, to simulate the impact response of composite materials. Borg, et al. [25] implemented a delamination model based on a damage formulation in LS-DYNA and the results were shown to be in agreement with experimental results.

Several investigators performed damage analyses of impact on composite sandwich structures. Nemes and Simmonds [204] presented a methodology for predicting the response of foam-core sandwich composites subject to low velocity impact. Noor, et al. [206] presented a review of computational models for sandwich panels and shells. Lee and co-workers [166] studied the impact responses of composite sandwich plate using finite element method, where the faces of sandwich were modeled as two separate Mindlin plates whereas the core was considered to have both transverse shear and normal stiffness. Manet [191] analyzed the behavior of sandwich structures using ANSYS and compared the results based on various types of elements available in ANSYS. It should be pointed out that damage was not considered in Manet's study. Lee and Tsotsis [168] investigated the indentation failure behavior of honeycomb sandwich panels based on experimental and analytical approaches together with finite element analysis. They concluded that core shear failure dominates the onset of indentation failure. Besant, et al. [17] studied the impact response of composite sandwich panels with models consisting of shell elements for the skins and brick elements for the core. Failure was considered while the skins were assumed remaining attached to the core during the impact. El-Sayed, et al. [92] modeled a cohesive layer along a pre-existing delamination or a pre-identified plane of crack propagation to simulate the crack growth in sandwich composite beams by using ABAQUS software package. Vaidya and co-workers [270] investigated low velocity impact response of sandwich composites using an ABAQUS-based finite element model with experimental data. Palazotto, et al. [212] predicted the core failure load and the load displacement curve on composite sandwich plates using finite element method. Meo et al. [323] studied the low-velocity impact on an aircraft sandwich panel using LS-DYNA3D and obtained the depth of indentation as well as the delamination based on several strength failure criteria.

1.3 Fiber Metal Laminates

In the aerospace industry, it's important to choose suitable materials that offer high specific strength and stiffness and better damage resistance for easy maintenance, which implies lower cost since besides safety, maintenance cost is the major element for cost. It constitutes a high percentage (approximately 20%) of the direct operating costs [277]. There was an investigation on repairs of 71 fuselages of Boeing 747 with an average life of 29,500 flying hours and the results showed that the damages were mainly involved in three categories; namely, fatigue cracks (57.6%), corrosion (29.4%) and impact damage (13.0%). Aluminum alloys have been the predominant choice of materials used in aircrafts. Its poor fatigue strength becomes a limitation for applications of aluminum. Fiber reinforced composite materials are chosen for their competing strength, stiffness and good fatigue resistance. However, composites are usually sensitive to impact and need skilled technicians to make repairs under particular environment once damage occurs [33, 48, 180]. Is it possible to make a new material that can overcome most of the disadvantages and take advantage of both aluminum and fiber reinforced composites? As an answer to the above question, fiber-metal laminates (FMLs) were born in Netherlands about 20 years ago (around 1980) [161, 277]. The so-called FMLs are hybrid materials built up from alternating thin metal sheets and fiber-reinforced adhesives (Figure 1.3). The aim of engineering design for these materials is to combine the best properties of metals and fiber-reinforced composites [161].

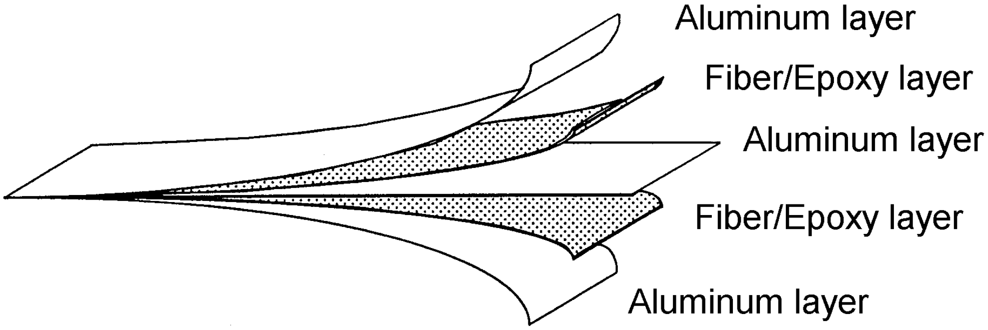

Figure 1.3 Schematic of fiber-metal laminates

The first generation of fiber-metal laminates is called ARALL, which are aramid-fiber reinforced FMLs and were developed by Vogelesang and his coworkers at the Delft University of Technology in the Netherlands [161, 277]. Following ARALL, various aluminum sheets and fiber-reinforced prepreg were used to build fiber-metal laminates. Up to now, two types of laminates have been fully developed and are commercially available in various configurations. They are ARALL and GLARE. ARALL consists of thin aluminum sheets and aramid fiber prepregs while GLARE is made of aluminum sheets with glass fiber prepregs. The primary objective to develop FMLs is for their excellent fatigue strength over monolithic materials adopted in modern civilian aircrafts. However, several types of FMLs offer additional advantages, such as higher impact resistance and damage tolerance, fire resistance, corrosion resistance, and so on. Furthermore, FMLs can be handled and fabricated just like conventional aluminum sheets and be repaired easily if needed. From the thesis work done by Bianchi [18], a special type of GLARE, called GLARE 5, could withstand a level of impact energy

20~30% higher than a 2024-T3 aluminum sheet with the same thickness. Figure 1.4 shows the comparison of impact properties for different materials given by Structural Laminates Company [318]. The density of FMLs is lower than that of monolithic aluminum but greater than fiber reinforced composites. With the saving in density, plus the added strength of FMLs over monolithic metals, a structure made of FMLs can save up to 30 percent of its self-weight [161].

As mentioned above, the primary aim of developing FMLs was to achieve higher fatigue strength. Early study conducted by Schijve, et al. [240] indicated that fatigue crack growth in thin sheet was somewhat slower than in thick sheets. This could be explained by the higher fracture stiffness for a thin sheet (plane stress) than for a thick plate (plane strain). Moreover, crack growth in laminated aluminum was much slower than monolithic aluminum plate with the same total thickness. After this earlier development, the aramid-based ARALL, which possess even superior fatigue properties, were developed [192]. The improved fatigue resistance is due to fiber bridging across fatigue cracks in the aluminum layer by the fiber composite layer [273, 274]. Other researchers made contributions to the studies on fatigue properties of FMLs. Through optical and scanning electron microscopes, Vasek et al. [272] observed that fatigue crack initiation mechanism in notched laminates was different from monolithic materials. They gave a brief explanation using finite element program to calculate the residual stress and equivalent plastic strain at the notch contour. Kawai, et al. [142] investigated the off-axis fatigue behavior of a unidirectional fiber-metal laminate, called GLARE 2. Their results showed that the fatigue strength of GLARE 2 changed gradually from about two times as high as that of aluminum alloys in the longitudinal direction to almost one-half in the transverse direction.

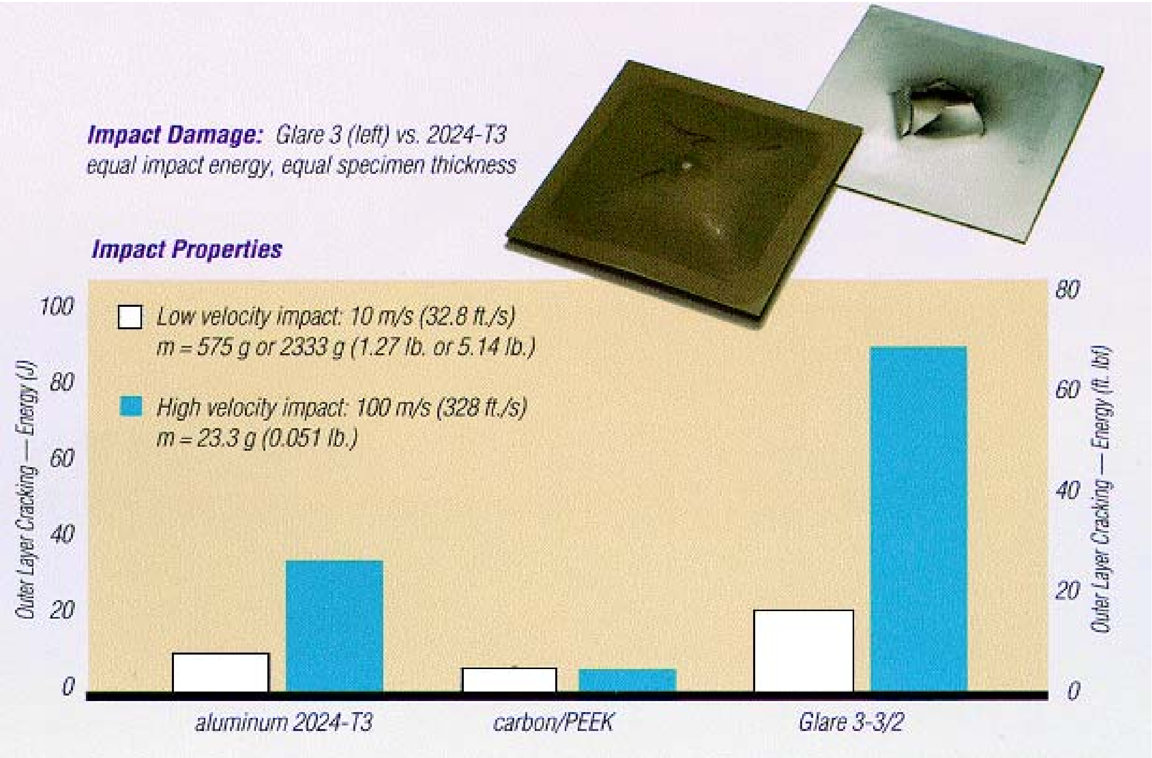

Figure 1.4 Impact properties of various materials

Other mechanical properties of FMLs have also been studied. Wu [296] performed a statistical analysis of tensile strength of ARALL laminates and the data indicated that the strength of laminates could be fitted to a two-parameter Weibull distribution. Wu [297] also studied the temperature dependence of the tensile properties of a special type of ARALL, called ARALL 4, and showed that there was no significant degradation of tensile strength and modulus at temperatures up to 177°C (350°F). Chen and Sun [57] modeled the orthotropic elastic-plastic properties of ARALL by a macromechanical orthotropic plasticity theory in conjunction with the classical laminated plate theory. Kawai, et al. [143] studied the off-axis inelastic and fracture behavior of GLARE 2 by static tensile tests and the classical laminated plate theory. A bilinear stress-strain curve can be found from both tests and analyses. Recently, Castrodeza, et al. [47] investigated the fracture micromechanism of ARALL using a small single edge bend specimens inside a scanning electron microscope. Castrodeza, Bastian and Perez-Ipina studied the critical fracture toughness of unidirectional fiber-metal laminates and showed that all fiber-metal laminates presented higher fracture toughness and crack tolerance than their constituent alloys [321].

Recently, there are other kinds of fiber-metal laminates being studied. For example, Lawcock, et al. [162-164] studied carbon-fiber-reinforced metal laminates and Cantwell, et al. [40, 231] worked on the mechanical properties of FMLs based on thermoplastic matrix.

The impact properties of fiber-metal laminates have been studied extensively (Vlot, et al. [18, 273-276]). The materials studied including various ARALL and GLARE under low and high velocity impact conditions. Comparison was made between different materials. GLARE (especially with cross-ply fiber-epoxy) shows higher impact resistance than other materials and a higher tensile strength at high strain rate due to the rate dependence of glass fibers. Reyes and Cantwell [231] investigated the mechanical properties of thermoplastic-based fiber-metal laminates, where drop-weight low velocity impact tests were conducted and the incident energy was absorbed through plastic deformation in the aluminum layers and localized micro-cracking within the composite plies. Cantwell, et al. [40, 322] also conducted high-velocity impact study on fiber-metal laminates. Other researchers (Sun, et al. [257] on ARALL; Liaw, et al. [173, 218] on various FMLs) also conducted impact effects on fiber-metal laminates.

From literature, some simplified impact models are available for analyzing the impact response of fiber-metal laminates. The first model is the mass-spring model. Helms, et al. [119] and Vlot [273, 276] applied this model for low velocity impact on FMLs to predict the impact responses. Vlot [274, 276] used elasto-plastic impact model based on simplified Von Karman equations to solve the impact problem. It should be noted that the above models could only analyze the impact responses under lower impact energies without significant damage occurring in specimens. When significant damage is induced, finite element analysis may need to be adopted.

So far only a few finite element analyses have been conducted for fiber-metal laminates. Hashagen, et al. [117] proposed a nonlinear solid-like shell element to model the fiber-metal laminates. In their models, the whole stacking sequence of the layered composite is represented by one element, which cannot simulate the interlaminar effects. To overcome this deficiency, every layer may be modeled individually by an element with interfaces represented by special interface element. The latter model has been incorporated to simulate the delamination behavior of FMLs (see Reference [116]) where the growth of delamination is controlled by the fracture toughness of the interface calculated via the virtual crack closure technique [319]. Finally, Yeh [305] developed a finite element model employing special interface elements to simulate the fatigue crack growth in fiber-metal laminates. To the author’s knowledge, there are no finite element analyses of low-velocity impact on FMLs. In this study, finite element simulations were adopted to analyze the impact responses of fiber-metal laminates.

1.4 The Purpose of This Study

If the new fiber-metal laminates could be applied to primary structures, significant weight and cost savings could be realized for the aerospace industry. However, certification of these materials is still a major issue. More work has to be performed on the optimal design of FMLs under various loading conditions.

One main purpose of this study is to understand how to enhance damage tolerance and hence to increase life expectation of such relatively new engineering materials through strengthening mechanisms during design and manufacturing processes. Based on the experimental results, some suggestions can be recommended for better design and manufacturing processes of FMLs. In particular, this study may provide necessary information for improving their impact damage tolerance. In this study finite element models were developed to simulate experimental results with very good accuracy and the proposed model may be used to predict other impact damage events of FMLs; thus, indicating a reliable finite element model may be used in lieu of costly tests for further development and verification of design methodology.

CHAPTER 2: METHODS OF APPROACH

This study is focused on the responses and damage patterns of fiber-metal laminates (FMLs) under low-velocity impact conditions. The main goal of this investigation is to obtain the information on impact-damage resistance needed for better design of fiber-metal laminates for engineering application.

Mechanical properties of fiber-metal laminates can vary drastically due to different constituents. Therefore two kinds of fiber-metal laminated panels: ARALL and GLARE were studied. The major part of this study was concentrated on GLARE in which the effects of constituents, fiber orientations and lay-up configurations, thickness were considered. As hybrid composites, both metal layers and composite layers can affect the impact responses and damage patterns. Two types of aluminum alloys were chosen as constituents with one of them (2024-T3) being tougher and more ductile than the other (7475-T76). Four different lay-up sequences of glass-fiber prepregs: unidirectional, [0°/90°] cross-ply, [45°/–45°/–45°/45°] angle-ply and [0°/45°/–45°/90°] quasi-isotropic were used to study the effect of fiber orientation. The thickness effect on the impact behavior of GLARE 5, which is made of aluminum 2024-T3 sheets interleaved with [0°/90°/90°/0°] glass fiber reinforced composite layers, was investigated. Since fiber-metal laminates are used outdoors for many applications, some panels were tested under various temperatures in order to learn the reliability under different environmental conditions. The effect of shapes and masses of impactors were also studied.

The methods of approach in this study include both experiments and finite element simulations. Low velocity impact tests on fiber-metal laminates were conducted and damage evaluation was performed by both nondestructive (ultrasonic scanning) and destructive (mechanical sectioning) techniques. The resultant impact responses were simulated through an explicit 3-D dynamic nonlinear finite element package – LS-DYNA3D.

All impact tests with various impact energies were performed using an Instron-Dynatup 8250 drop-weight impact tester equipped with an environmental chamber. During impact tests, the histories of impact velocity, force, energy and deflection were recorded. After visual observation, ultrasonic B- and C-scan nondestructive techniques were applied to evaluate the damage patters of the impacted FML specimens. Some of the impacted specimens were machined into two halves through the impact center by a diamond saw. Post-mortem micro-fractographs were then taken so that detailed damage patterns due to impact can be recorded.

In order to understand fully the whole impact event and details of damage, the LS-DYNA finite element code, incorporated with proper failure criteria, nonlinear constitutive laws and realistic boundary conditions, was used to perform the simulation of impact responses. Due to the complexity of hybrid composites, some preliminary examples were studied on relative simple materials before simulations on FMLs were conducted. Aluminum/acrylic sandwich panels were studied first by using a simplified finite element model. Both the impact force histories and delamination were simulated. Further finite element simulations were conducted on GLARE 5(3/2) with [0°/90°/90°/0°] cross-ply glass-epoxy, which is a type of GLARE FML with unidirectional glass-epoxy layers, as well as other kinds of GLARE subjected to various types of impactors. Beside the impact force histories, velocity, deflection, and various forms of energies were also calculated. The damage patterns, including delamination, failure in fiber-epoxy layers, and cracks in aluminum layers, had also been investigated through the finite element model developed in this study.

In the sequel, Chapter 3 briefly describes fiber-metal laminates panels, impact tester and the ultrasonic nondestructive detection system used in this study. Impact experiments and damage assessment are discussed in Chapter 4. Finite element simulations are presented in Chapter 5 where numerical results are compared with experimental results. Conclusions are drawn in Chapter 6, and several recommendations for future studies are also discussed in Chapter 6. A brief theory of explicit 3-D nonlinear dynamic finite element method is described in Appendix. All references are listed at the end of this study.

CHAPTER 3: MATERIALS AND TEST SET-UP

3.1 Specimens

Materials investigated in this study were fiber-metal laminated panels provided by Aviation Equipment Structures, Inc. These FML panels, most of which are commercially-available advanced structural materials widely used in aerospace industry, are listed in Table 3-1. Table 3-2 shows the typical mechanical properties of FMLs.

Table 3-1 Fiber-metal laminate panels

Panel	Type	Configuration	Metal Alloy	Metal Thickness	Prepreg Constituents	Prepreg Plies & Orientation	Prepreg Thickness	Total Thickness
1	GLARE 1	3/2	7475-T76	0.012”	Glass-Epoxy	$[0^\circ_2]$ Unidirectional	0.010”	0.056”
2	GLARE 2	3/2	2024-T3	0.012”	Glass-Epoxy	$[0^\circ_2]$ Unidirectional	0.010”	0.056”
3	GLARE 3	3/2	2024-T3	0.012”	Glass-Epoxy	[0°/90°] Angle-Ply	0.010”	0.056”
4	GLARE 5	2/1	2024-T3	0.012”	Glass-Epoxy	[0°/90°/90°/0°] Angle-Ply	0.020”	0.044”
5	GLARE 5	3/2	2024-T3	0.012”	Glass-Epoxy	[0°/90°/90°/0°] Angle-Ply	0.020”	0.076”
6	GLARE 5	4/3	2024-T3	0.012”	Glass-Epoxy	[0°/90°/90°/0°] Angle-Ply	0.020”	0.108”
7	GLARE 5	5/4	2024-T3	0.012”	Glass-Epoxy	[0°/90°/90°/0°] Angle-Ply	0.020”	0.140”
8	GLARE 5	6/5	2024-T3	0.012”	Glass-Epoxy	[0°/90°/90°/0°] Angle-Ply	0.020”	0.172”
10	ARALL 3	3/2	7475-T76	0.012”	Aramid-Epoxy	[0°] Unidirectional	0.0085”	0.053”
11	CCNY A	3/2	2024-T3	0.012”	Glass-Epoxy	$[0^\circ_4]$ Unidirectional	0.020”	0.076”
12	CCNY B	3/2	2024-T3	0.012”	Glass-Epoxy	$[90^\circ_4]$ Unidirectional	0.020”	0.076”
13	CCNY C	3/2	2024-T3	0.012”	Glass-Epoxy	[45°/-45°/-45°/45°] Angle-Ply	0.020”	0.076”
14	CCNY D	3/2	2024-T3	0.012”	Glass-Epoxy	[0°/45°/-45°/90°] Quasi-Isotropic	0.020”	0.076”

The configuration notation *m*/*n* used in Table 3-1 means the panel is composed of *m* aluminum-alloy layers interlaced with *n* fiber-reinforced epoxy laminae. For example, Figure 3.1 shows the unfold view of GLARE 5 (2/1) laminates which consist of two layers of 2024-T3 aluminum layers and one composite lamina made of four layers of glass-fiber reinforced epoxy in a lay-up configuration of [0°/90°/90°/0°] (see Reference [18]). In this study, the afore-mentioned various types of FML panels were cut into square specimens of 100mm × 100mm (or 4" × 4") for impact tests.

Table 3-2 Typical values of mechanical properties [318]

		GLARE 1 (3/2)	GLARE 2 (3/2)	GLARE 3 (3/2)	ARALL 3 (3/2)	2024-T3 (2/1)
Tensile Ultimate Strength (MPa)	L	1282	1214	717	821	455
	LT	352	317	716	379	448
Tensile Yield Strength (MPa)	L	545	360	305	607	359
	LT	333	228	283	324	324
Tensile Modulus (GPa)	L	65	65	58	68	72
	LT	50	50	58	49	72
Ultimate Strain (%)	L	4.2	4.7	4.7	2.2	19
	LT	7.7	10.8	4.7	8.8	19
Compressive Yield Strength (MPa)	L	424	414	309	345	303
	LT	403	236	306	365	345
Compressive Modulus (GPa)	L	67	67	60	66	74
	LT	51	52	60	50	74

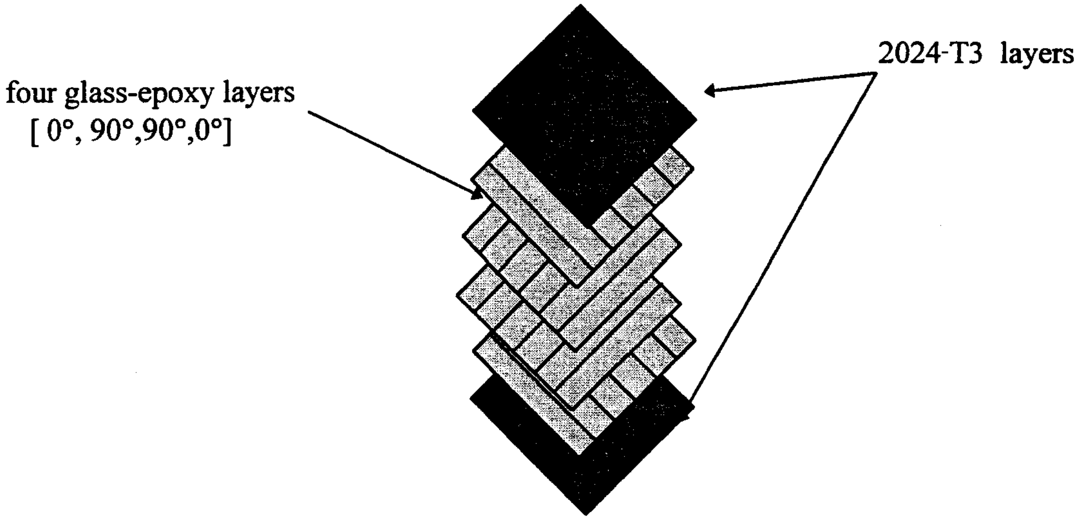

Figure 3.1 Scheme of GLARE 5 (2/1) laminates

3.2 The Drop-weight Impact Tester

In this study, all impact tests were performed using an Instron-Dynatup 8250 impact testing machine, which is a PC-driven, pneumatically assisted drop-weight impact tester equipped with an environmental chamber (Figure 3.2) [324]. By changing the drop height or using the attached pneumatic assist system, the impact velocity can be varied in the range of 0.61 m/sec up to 13.41 m/sec. With the drop weight varying from 2.5 kg up to more than 45 kg, the impact energy can be from 0.67 joules up to around 440 joules. Impactors with various shapes were used; nevertheless, most impact tests in this study were conducted using a diameter of 16 mm hemispherical steel impactor with a weight of 6.1 kg.

Figure 3.2 Drop-weight tester

Before impact

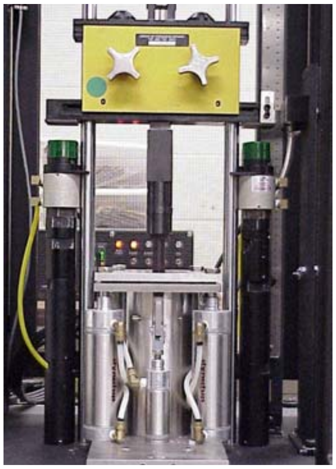

During impact

Figure 3.3 The specimen fixture

With the accompanied environmental chamber, the impact properties of materials can be investigated under high or low environmental temperatures. The temperature range is −50°C (−60°F) to 175°C (350°F). A 1.3-kW open coil heater provides high temperatures whereas low temperatures are achieved through the use of either liquid nitrogen or liquid carbon dioxide. Specimens are clamped circumferentially along a diameter of 76 mm (or 3 inches) in the specimen fixture (Figure 3.3). There is a pneumatic break to ensure no multiple strikes during each test. With the Dynatup 930-I data acquisition system, we can record time history of impact load, which are measured using a load cell located just above the impact nose, as well as the impact velocity history, which is measured by a pair of photoelectric-diodes attached to the base of the test machine.

It should be noted that with the Dynatup 930-I data acquisition system, only the load (i.e., the resistive force of the specimen) vs. time and the initial impact velocity (just prior to impact) could be measured directly. Using equations of motion, energy absorbed by the specimen, velocity of impactor and deflection at the impact center can be derived and recorded into files. The procedures are as following (assuming data starts at t=0):

$$f(t) = mg - p(t) \tag{3-1}$$

$$a(t) = \tfrac{f(t)}{m} = g - \tfrac{p(t)}{m} \tag{3-2}$$

$$v(t) = v_i + \int a(t)dt = v_i + gt - \tfrac{1}{m}\int p(t)dt \tag{3-3}$$

$$x(t) = \int v(t)dt = v_i t + \tfrac{1}{2}gt^2 - \tfrac{1}{m}\int(\int p(t)dt)dt \tag{3-4}$$

$$E(t) = K(t) + V(t) + E_a(t) = K(0) \tag{3-5}$$

$$K(0) = \tfrac{1}{2}mv_i^2 \tag{3-6}$$

Since the displacement is really small, the potential energy can be neglected. The energy absorbed by specimen can be computed as following:

$$E_a(t) = K(0) - K(t) = \tfrac{1}{2} m \{ v_i^2 - [v(t)]^2 \} \tag{3-7}$$

Notation	
v_i	Impact velocity measured by photodiodes.
$p(t)$	Load value measured by 930-I at time t.
m	Total mass of impactor (impact tower and nose
g	Acceleration of gravity
$f(t)$	Total force acting on the impactor at time t.
$a(t)$	Resultant acceleration of the impactor at time t.
$v(t)$	Velocity of the impactor at time t.
$x(t)$	Deflection (position) of the impactor at time t.
$K(t)$	Kinetic energy of the impactor at time t.
$V(t)$	Potential energy of the impactor at time t.
$E_a(t)$	Energy absorbed by the specimen at time t.
$E(t)$	Total energy of the impactor /specimen system at time t.

3.3 The Ultrasonic Damage Evaluation System

In this study, UltraPAC, an advanced, modular and expandable ultrasonic system offered by Physical Acoustics Corporation (Figures 3.4 and 3.5), was used to conduct post-mortem damage evaluation of the impacted specimens. Both pulse-echo (Figure 3.6) and through-transmission (Figure 3.16) techniques were used in this study. Flat and focused transducers (0.25 inch-diameter) with various frequencies (5 to 25 MHz) were chosen in this study. Figure 3.7 shows the ultrasonic pulse-echo C-scan using a 5 MHz flat transducer as compared with the optical image for a cracked cast acrylic panel. It is obvious that flat transducers cannot detect flaws accurately. More accurate C-scan images can be produced by using focused transducers (Figure 3.8). In general, the higher frequency of a transducer, the higher resolution it provides. More details of damage can be detected using a higher frequency transducer.

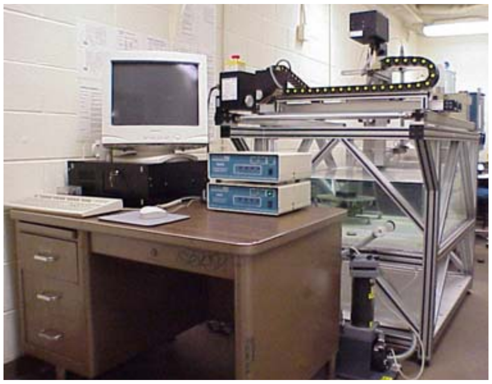

Figure 3.4 The UltraPAC system

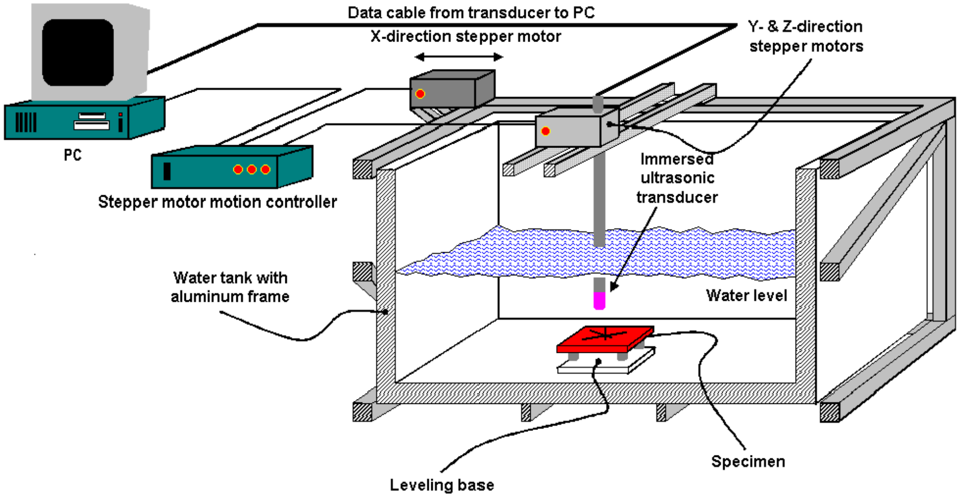

Figure 3.5 Schematic of a typical immersion ultrasound system

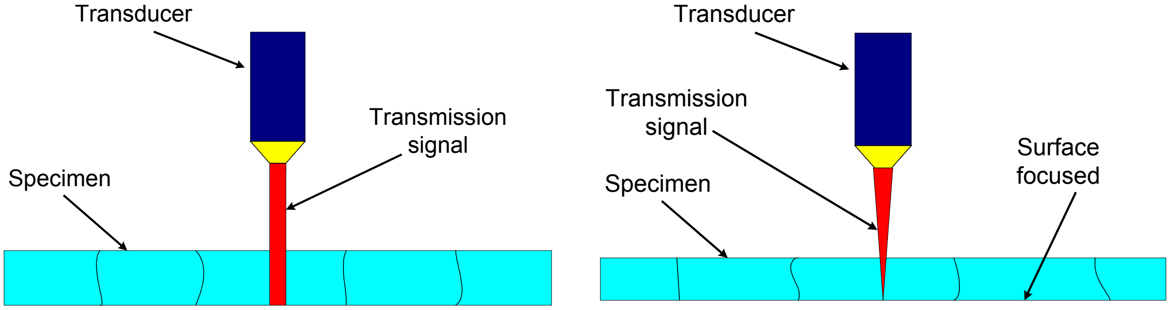

Figure 3.6 Pulse-echo techniques (Left: flat transducer; Right: focused transducer)

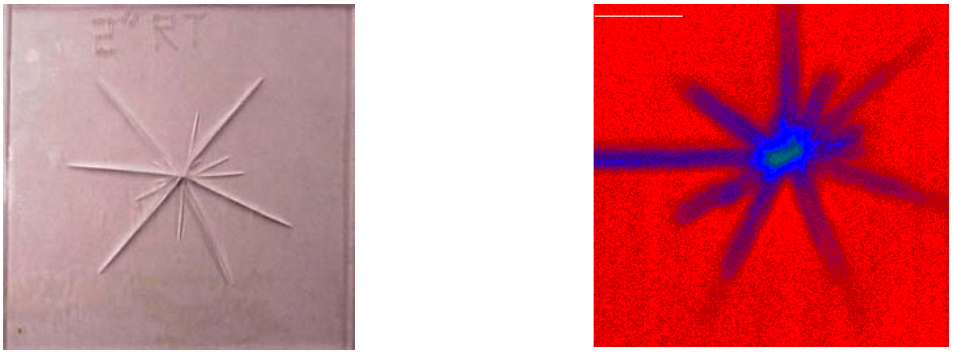

Optical image Flat transducer

Figure 3.7 Optical and ultrasonic pulse-echo C-scan (5 MHz flat transducer) image for a cast acrylic panel with cracks

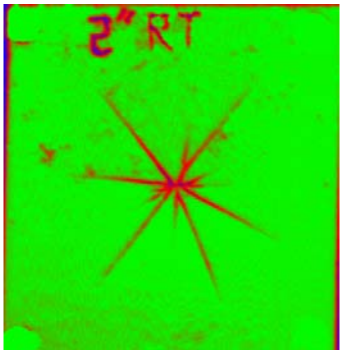

(5 MHz transducer)

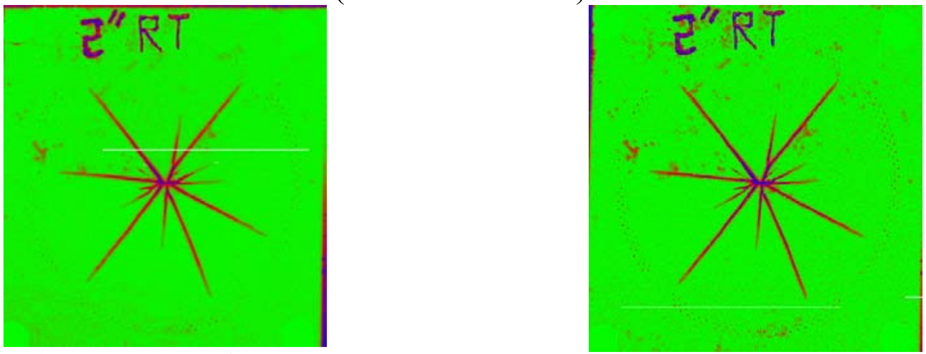

(15 MHz transducer) (25 MHz transducer)

Figure 3.8 Ultrasonic pulse-echo C-scans of a cast acrylic plate with cracks using focused transducers

The above-mentioned ultrasonic pulse-echo technique was applied to aluminum/cast acrylic sandwich plates with impact damages (Figure 3.9). Both optical image and ultrasonic C-scan from the cast acrylic side are shown in Figure 3.10. Again, the higher frequency of a transducer, which has a better resolution, produces more details of damage information.

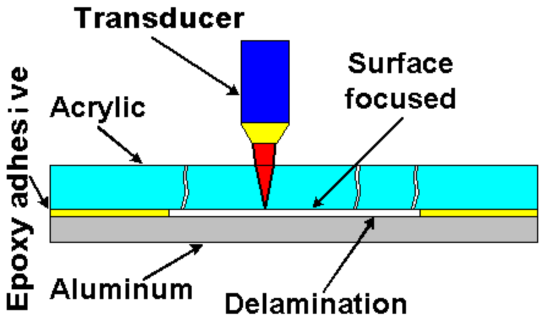

Figure 3.9 Pulse-echo scan on a damaged aluminum/cast acrylic plate scanning from cast acrylic side

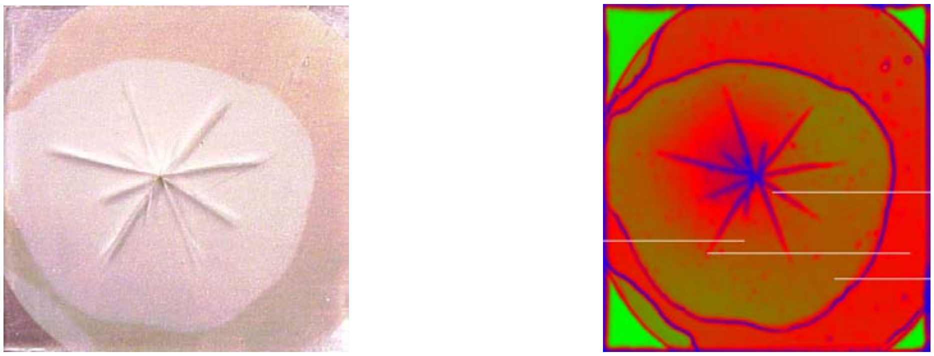

Optical image

C-scan (5 MHz)

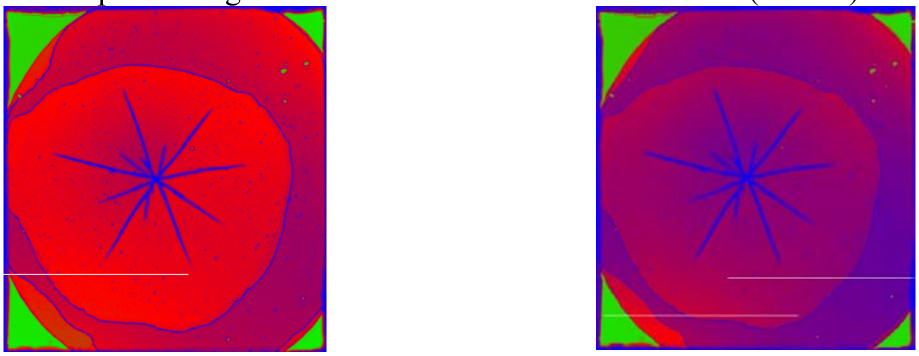

C-scan (15 MHz)

C-scan (25 MHz)

Figure 3.10 Optical and ultrasonic C-scan images of sandwich plate with cracks and delamination scanned from cast acrylic side

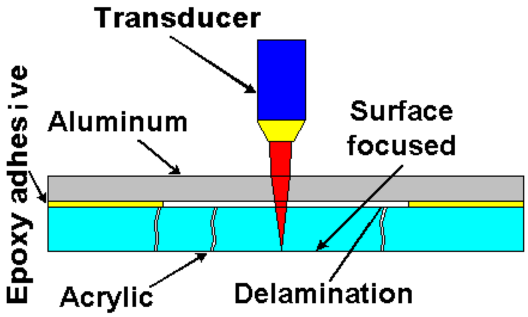

Figure 3.11 Pulse-echo scanning on a damaged aluminum/cast acrylic plate from aluminum side

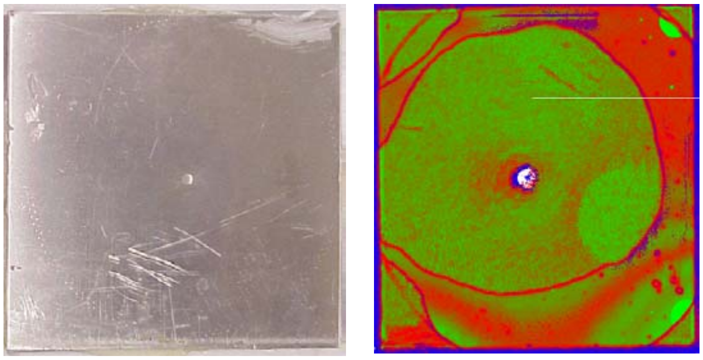

Optical image C-scan (25 MHz)

Figure 3.12 Optical and ultrasonic C-scan images of sandwich plate with cracks and delamination scanned from aluminum side (25 MHz transducer)

The advantage of ultrasonic technique is for flaw detection in an opaque material. The same technique was used to scan the aforementioned damaged specimens from the aluminum side. Figure 3.11 shows the technique and Figure 3.12 presents the optical as well as the C-scan images. Only the indentation and delamination were detected by the ultrasonic technique. Because of the presence of delamination, the back-echo signals from the cracked cast acrylic plate were “overshadowed” by the strong echoes from the debonded interface. In other words, the “air gap” within the delamination area attenuated most of the energy from the back-echo signals. The experimental evidence was illustrated by a typical A-scan signal, which is shown in Figure 3.13.

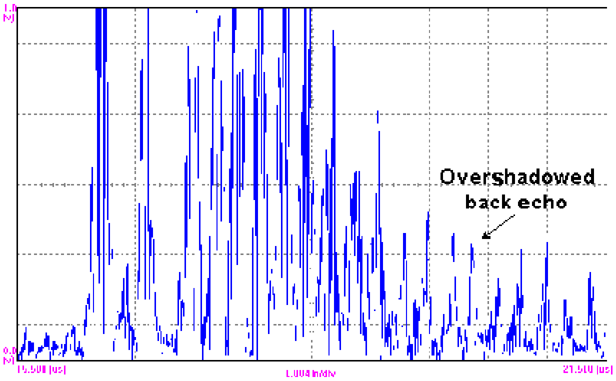

Figure 3.13 Ultrasonic A-scan signal showing overshadowed back echoes

To further verify the filtering effect of delamination on the ultrasonic signals, a pre-cracked cast acrylic plate was adhered to an aluminum sheet, in which the delamination was artificially removed. In this case, without the blocking from delamination, the cracking pattern can be detected clearly if the specimen is scanned from the aluminum side. Detailed results are shown in Figure 3.14 and the corresponding A-scan is illustrated in Figure 3.15, which shows identifiable back echoes.

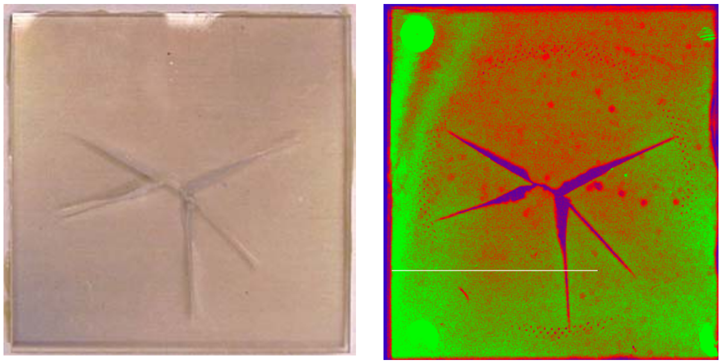

Optical image C-scan (25 MHz)

Figure 3.14 Optical and ultrasonic C-scan images of a pre-cracked cast acrylic plate shielded by an aluminum panel

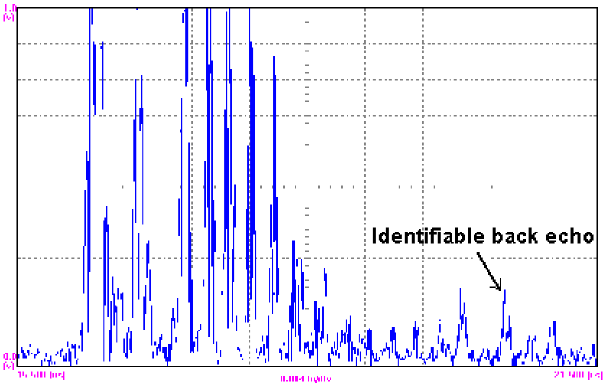

Figure 3.15 Ultrasonic A-scan signal showing an identifiable back echo

Finally, pulse-echo technique is very sensitive and accurate for flat specimens. However, it is not valid for specimens with large curvature induced by large deformation. For specimens with large deformation, a through-transmission technique, which is shown in Figure 3.16, should be chosen in order to evaluate the damage. A standard through-transmission technique employs two flat transducers, which usually generates relatively blur ultrasonic images. To tackle this issue, a modified through-transmission technique, which incorporates a flat and a focused transducer, was used in this study. As shown in Chapter 4, this simple modification improves the quality of ultrasonic-scanned images drastically.

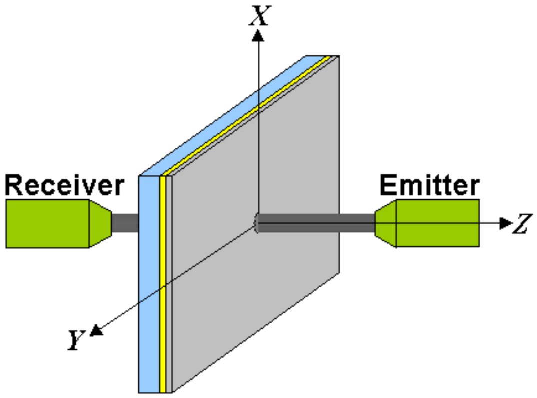

Figure 3.16 Through-transmission techniques

CHAPTER 4: TEST RESULTS AND DISCUSSION

4.1 Low-Velocity Impact Tests

The impact properties of fiber-metal laminates vary with their constituents (i.e. fibers, resin and alloy types), fiber orientation, stacking sequence, thickness, operating temperature, geometry and material type of the impactor, and surface preparation technique, etc. In this section, the effects of constituents, fiber orientation and stacking sequence, thickness, operating temperatures, and geometry of the impactor will be discussed. Unless specified otherwise, all impact experiments were performed using a steel impactor with a hemispherical tip diameter of 16 mm and a weight of 6.1 kg.

Table 4-1 Mechanical properties of constituents [318]

PROPERTY	2024-T3	7475-T76	Glass Fiber	Aramid Fiber
Tensile Ultimate Strength (MPa)	455	545	4600	2800
Tensile Yield Strength (MPa)	359	476	--	--
Compressive Yield Strength (MPa)	304	442	--	--
Tensile Modulus (GPa)	72	69	86	125
Ultimate Strain (%)	19	13	5.3	2.3
Density (g/cm^3)	2.79	2.79	2.54	1.45

Table 4-1 lists typical mechanical properties of aluminums and fibers used in fiber-metal laminates. Table 4-2 shows the experimental results for different kinds of materials tested at room temperature, where the permanent deflection is measured from the nonimpact side of specimens to the clamped boundary (Figure 4.1). Please refer to Tables 3-1 and 3-2 for the detailed configuration of materials and typical properties. The thickness of aluminum 2024-T3 panels is 0.0625 (1/16) inch. Increasing the impact energy can increase deflection (details are depicted in Figure 4.2) of specimens except for ARALL 3, which only shows local dent or penetration at the impact center.

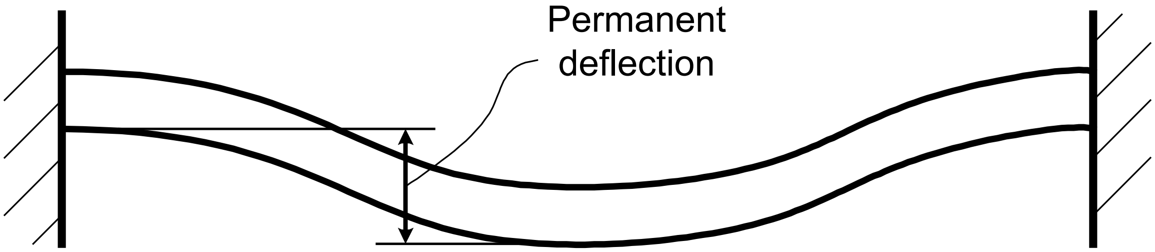

Figure 4.1 Measurement of permanent deflection

Table 4-2 Impact properties of various materials tested at room temperature (25°C)

Material	Impact Energy (Joule)	Crack length in outer layer (mm)		Permanent Deflection (mm)
		Impacted side	Nonimpact side	
2024-T3	10	0	0	3.2
2024-T3	15	0	0	4.0
2024-T3	20	20	20	5.0
2024-T3	25	35	35	7.6
2024-T3	30	40	40	8.8
ARALL3	10	27	40	3.8 (local dent)
ARALL3	20	Penetration	Penetration	--
ARALL3	30	Penetration	Penetration	--
GLARE 1	10	0	18	3.1
GLARE 1	20	80	80	4.8
GLARE 1	30	90	90	5.3
GLARE 2	10	0	0	3.8
GLARE 2	15	0	15	5.5
GLARE 2	20	26	32	7.3
GLARE 2	25	40	40	7.8
GLARE 2	30	58	60	8.9
GLARE 3	10	0	0	3.6
GLARE 3	20	0	10	5.4
GLARE 3	25	0	22	6.3
GLARE 3	30	22	35	7.4

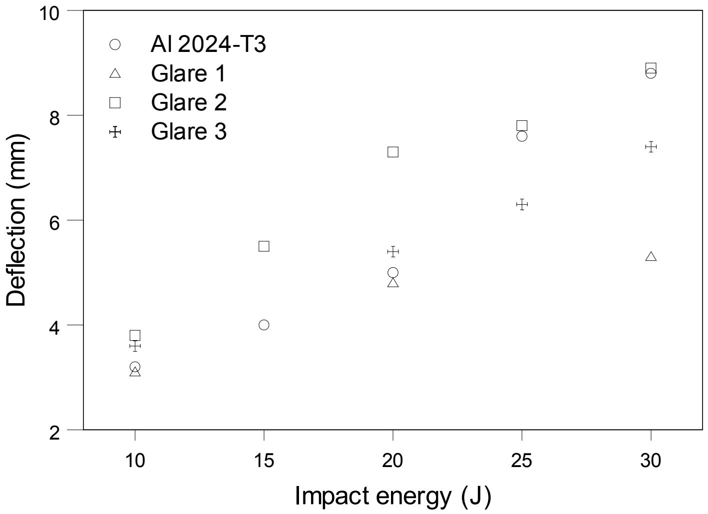

Figure 4.2 Deflection versus impact energy

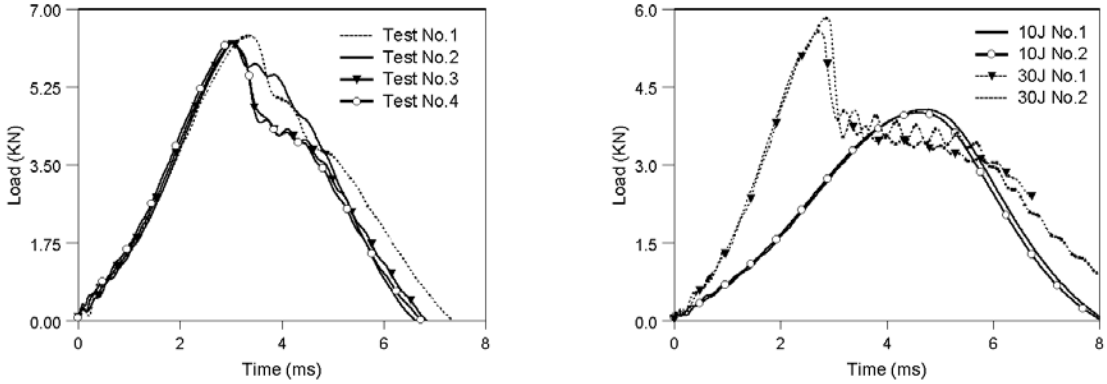

(a) Aluminum 2024-T3 subject to 20-joule impacts

(b) GLARE 2 due to different impact energies

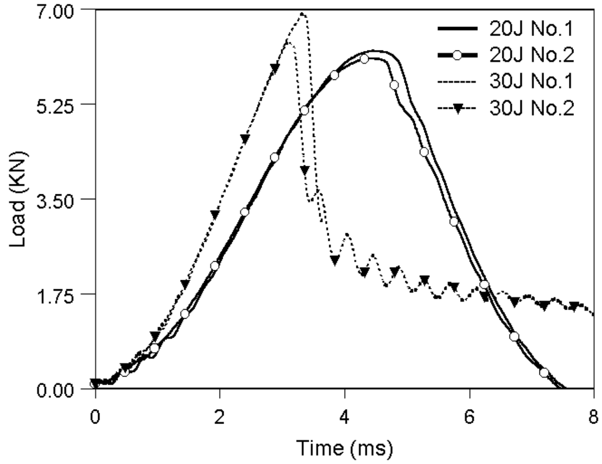

(c) GLARE 5 (2/1) at different impact energy

Figure 4.3 Impact load-time histories of various materials tested at room temperature

Typical impact load-time history curves as shown in Figure 4.3 indicate that test results are quite repeatable under the same experimental condition (i.e. same material, same temperature, same weight set and same impact velocity) using the Instron-Dynatup 8250 drop-weight impact tester.

4.1.1 Effects of different fibers

As mentioned in earlier, there are two types of commercially available fiber-metal laminates: GLARE and ARALL with different fiber-epoxy layers as their constituents, i.e. glass-epoxy and aramid-epoxy respectively. In this study (Table 3-1), two types of FMLs were chosen: GLARE 1, which consists of 3 layers of 7475-T76 aluminum sheets (0.012” per layer) with two layers of unidirectional glass-epoxy prepreg and ARALL 3, which is made of the same aluminum sheets but with unidirectional aramid-epoxy prepreg instead.

The thickness of ARALL 3 (0.053”) is just slightly thinner than that of GLARE 1 (0.056”). Comparing with glass-fiber (Table 4-1), aramid is stiffer but more brittle. Both GLARE 1 and ARALL 3 were subjected to impact tests of 10-joule, 20-joule and 30-joule. All tests were performed at room temperature (25°C). Results indicate that GLARE 1 possesses higher impact damage tolerance than ARALL 3. Figures 4.4 and 4.5 show damage patterns and global impact responses of corresponding panels, respectively. As shown in Table 4-2 and Figure 4.4(a), only small crack occurred on the nonimpact side of GLARE 1 under a 10-joule impact while ARALL 3 showed remarkable local indentation with the same test condition. The corresponding force histories and absorbed energies curves are shown in Figures 4.5(a) and 4.5(b).

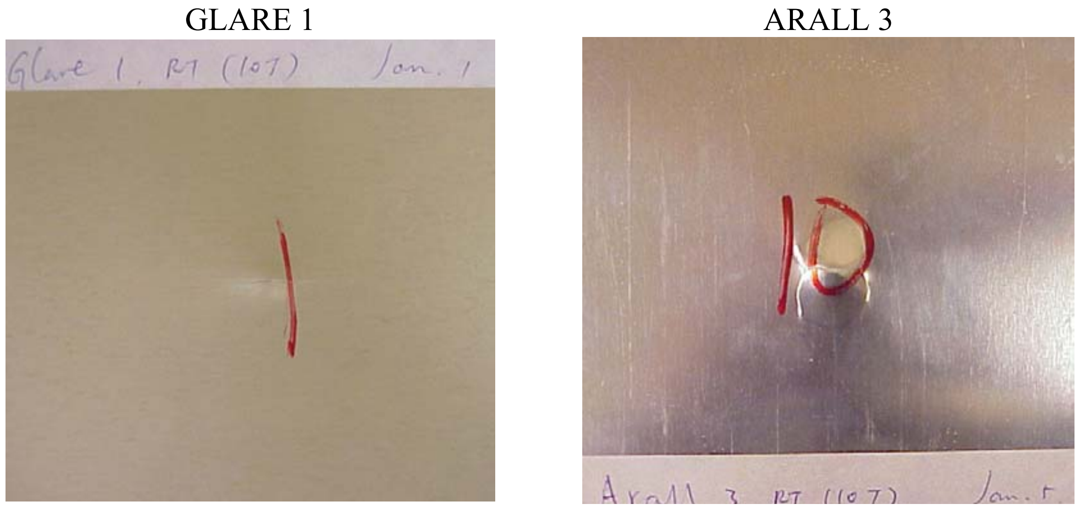

(a) 10 J

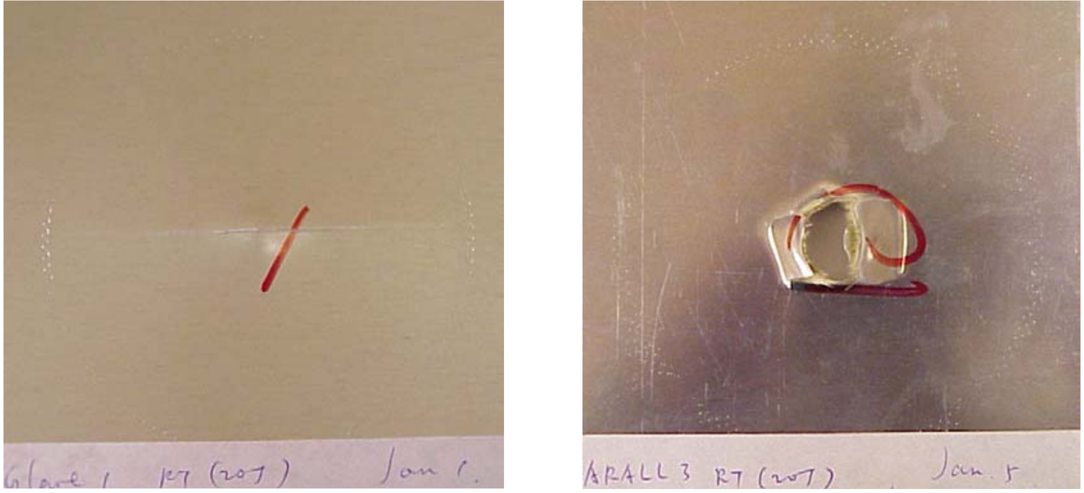

(b) 20 J

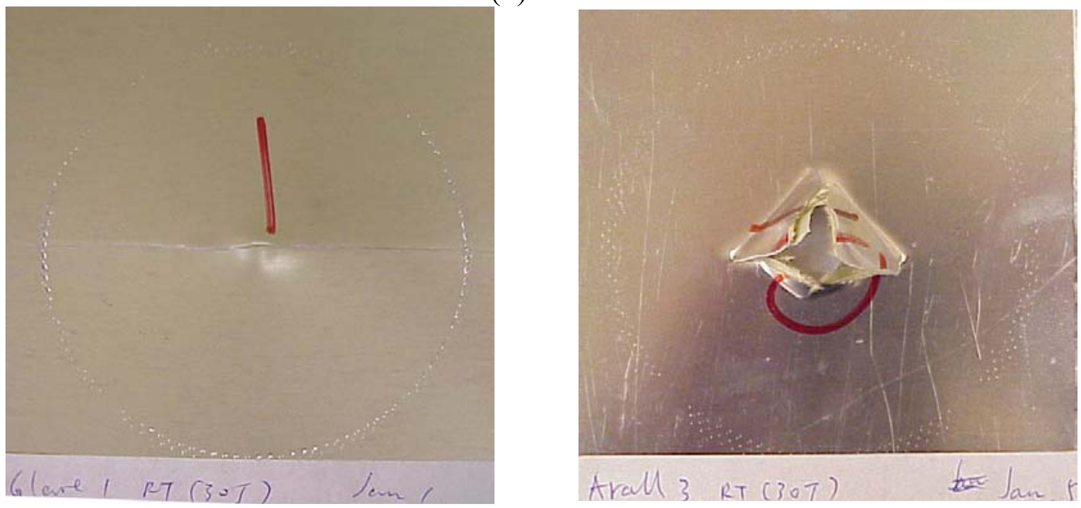

(c) 30 J

Figure 4.4 Damage patterns of GLARE 1 and ARALL 3 panels subjected to impact with different energies at room temperature

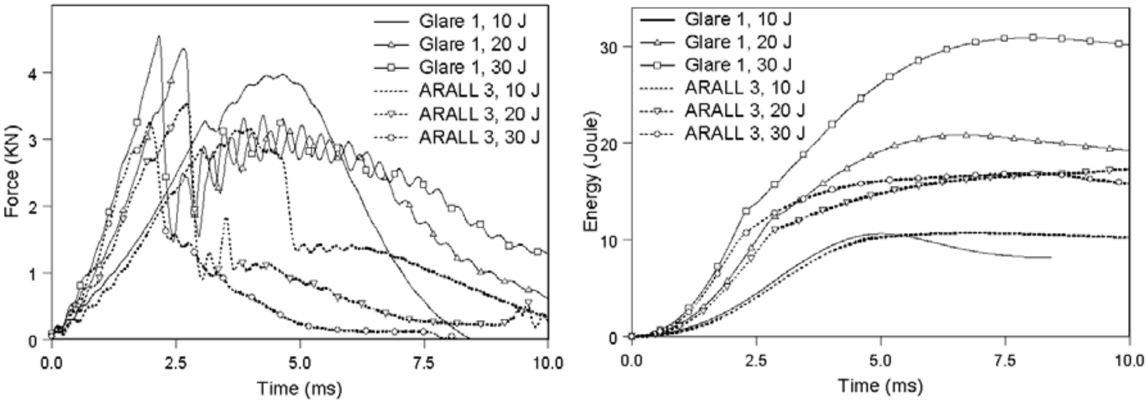

(a) Force vs. time (b) Absorbed energy vs. time

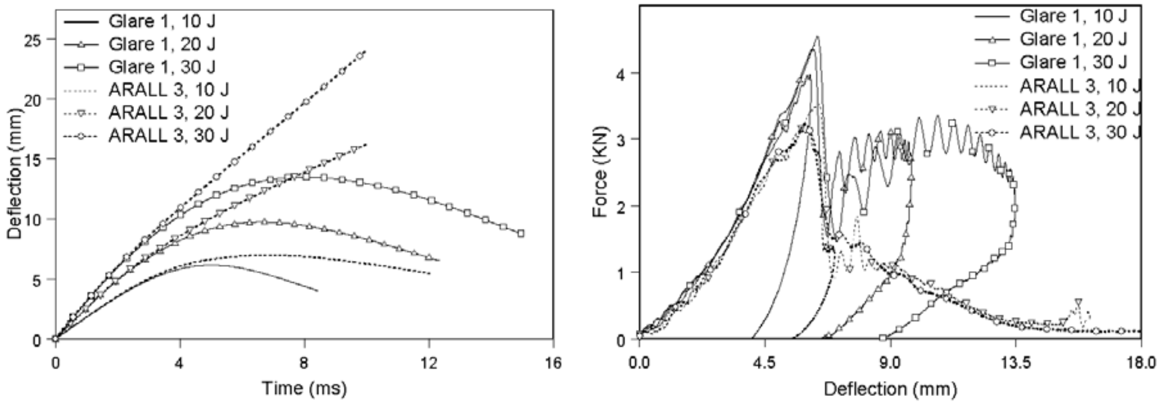

(c) Impact center deflection vs. time (d) Force vs. impact center deflection

Figure 4.5 Impact responses of GLARE 1 and ARALL 3 panels subjected to different energies at room temperature

Other than a small drop at about 3 ms in the force versus time curve of GLARE 1, the whole curve is fairly smooth, indicating that the energy was mainly attenuated out through damping and plastic work. For ARALL 3, there was a large drop after 4.5 ms in the force history curve; implying significant damage might have occurred in the specimen. The corresponding curves in Figures 4.5(b), 4.5(c) and 4.5(d) indicate bigger "springback" in GLARE 1 than in ARALL 3 under the 10-joule impact. Under 20- and 30-joule impacts, the impactor penetrated ARALL 3 panels while rebounded from GLARE 1. The force history curves from ARALL 3 show that only very small force remained after a drastically reduction. The remaining force mainly came from friction between impactor and specimen. From the absorbed energy curves of ARALL 3, a maximum 15-joule of energy could be attenuated through penetration. Deflection history and force versus deflection also show the occurrence of penetration (i.e. no “springback”). For GLARE 1 under 20- and 30-joule impacts, notable damage occurred although it still could “hold” the impactor without penetration. Cracks from both sides propagated to the clamped boundary. In short, GLARE 1 is better than ARALL 3 if impact resistance shall be considered.

4.1.2 Effects of different aluminum alloys

Instead of more brittle 7475-T76 aluminum alloys used in GLARE 1, GLARE 2 uses aluminum 2024-T3, which is more ductile, as its constituent material. Because of different mechanical properties from various materials, the impact resistance can be different between GLARE 1 and GLARE 2 even though they have the same thickness. For comparison, GLARE 2 was subjected to the same impact condition as GLARE 1, i.e., 10-, 20- and 30-joule impact energies at room temperature, respectively. The impact responses of these two materials are shown in Figure 4.6. The damage patterns for GLARE 2 are shown in Figure 4.7 together with GLARE 3, which will be discussed more detailed in the next section. In order to evaluate the damage, more tests were conducted for GLARE 2 (15- and 25-joule impacts). Both nondestructive and destructive evaluation techniques were used to assess the impact damages in impacted panels. After impact, the impacted specimens were first examined by ultrasonic C-scan technique, then were cut by a diamond saw through the impact center and were polished for micrographing. Only global delamination could be detected by ultrasonic C-scan. On the other hand, the cross-sectional technique gave more detailed damage assessment. All ultrasonic C-scan results and cross-sectional micrographs are listed in Figures 4.8 to 4.11. Here 25 MHz ultrasonic transducers were used to scan damages inside specimen and through-transmission technique was adopted because of large deformation.

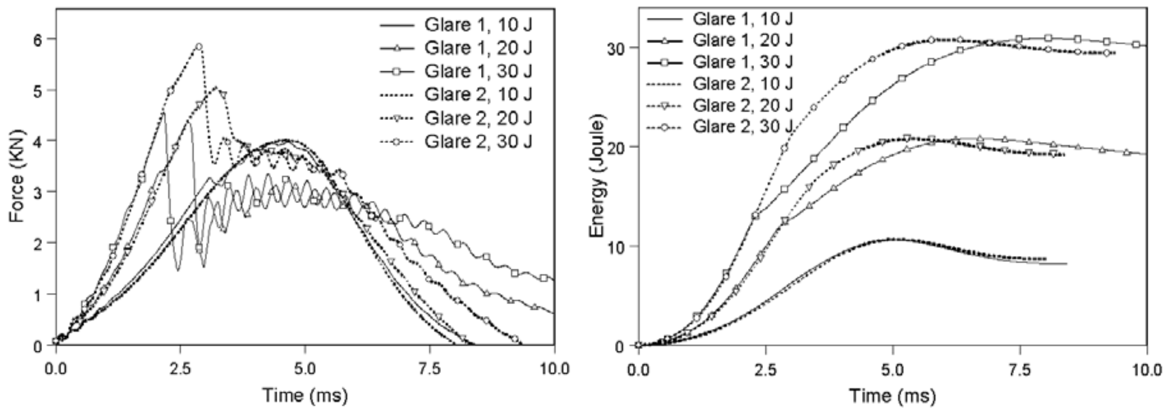

(a) Force vs. time

(b) Absorbed energy vs. time

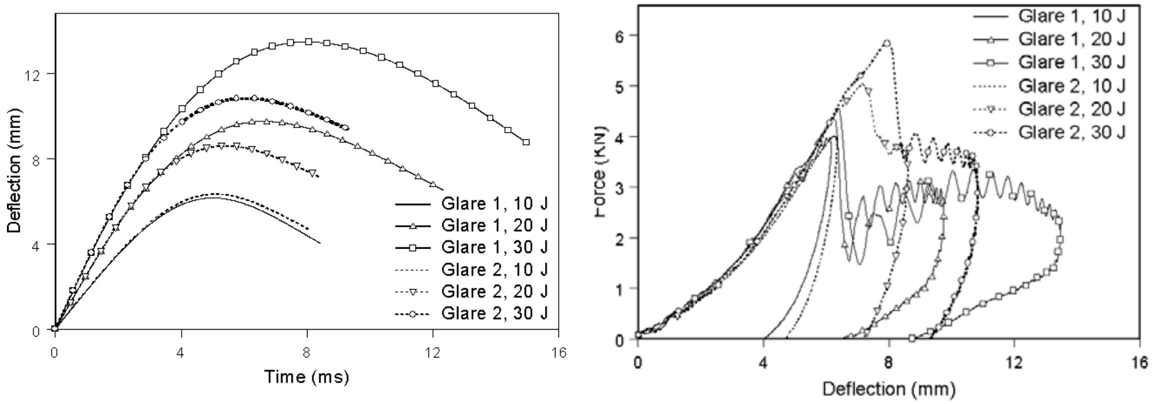

(c) Impact center deflection vs. time

(d) Force vs. impact center deflection

Figure 4.6 Impact responses of GLARE 1 and GLARE 2 panels subjected to different energies at room temperature

Both impact responses and results of damage assessment show that GLARE 2 offers better impact resistance over GLARE 1. Figure 4.6 indicates GLARE 1, as expected, appears stiffer (smaller permanent deflection) than GLARE 2 under various impact energies. When subjected to a 10-joule impact, GLARE 1 resulted an 18 mm crack visible in the nonimpact side and local dent while GLARE 2 showed only a local dent (no visible crack). As shown in Figure 4.6, the force, absorbed energy and deflection histories are nearly identical for GLARE 1 and GLARE 2 subjected to 10-joule impacts. Ultrasonic C-scans depicted a small damage zone in GLARE 2 than in GLARE 1. Fracture in outer layer aluminum, severe damage in outer layer glass fiber-epoxy, as well as delamination between outer layer glass fiber-epoxy and middle layer aluminum just under the impact center could also be found from cross-sectional micrograph in GLARE 1. There is no manifest damage shown in GLARE 2 (Figure 4.8). Up to 15-joule impact, GLARE 2 depicted similar damage except a deeper dent as compared with GLARE 1 under 10-joule impact (Figure 4.9).

More severe damages appeared for tests of 20-joule impact onto GLARE 1 and GLARE 2. Visible cracks were observed in both sides (impacted and nonimpact) for two specimens. This conclusion can also be drawn from the apparent dropping in the force history curves. For GLARE 1, the cracks propagated to the clamp edge of specimen in both sides and created cracks of about 80 mm long. Cracks extended to a shorter length (26 mm on impacted side and 32 mm on the other side) in GLARE 2. Back to Figure 4.6, even though GLARE 2 yields a higher impact force than GLARE 1, the maximum absorbed energies are almost the same for these two materials under the same test condition. However, as shown in Figure 4.6(c), GLARE 1 experienced larger deflection than GLARE 2 during the impact events. In addition, GLARE 2 reached maximum energy earlier than GLARE 1, as depicted in Figure 4.6(b). Further observation shows that a much significant local dent was induced in GLARE 2 while GLARE 1 appeared to be more like a global deformation. This phenomena results from the fact that GLARE 2 consists of more ductile aluminum 2024-T3 while GLARE 1 uses brittle aluminum 7475-T76.

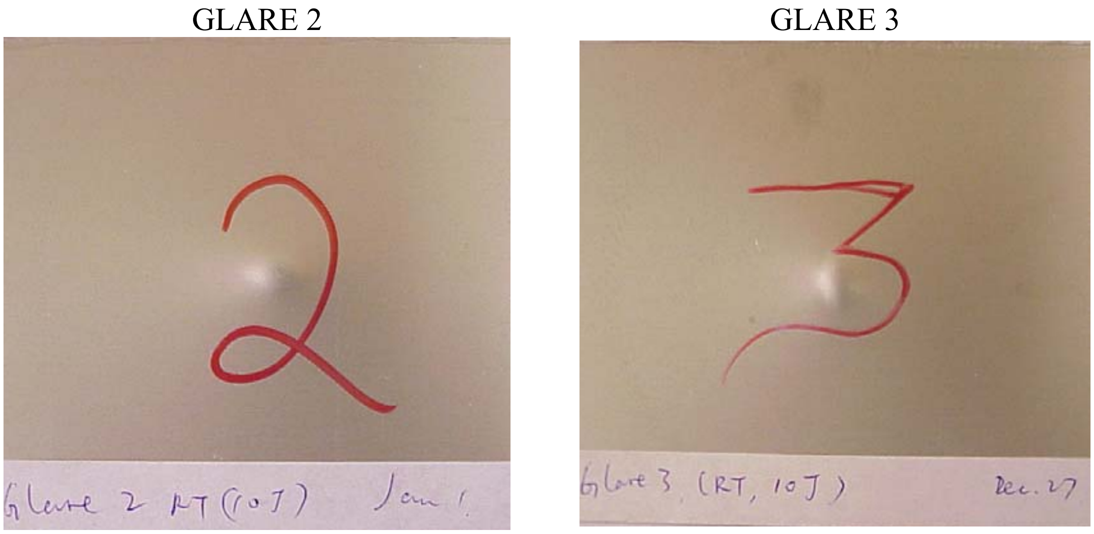

(a) 10 J

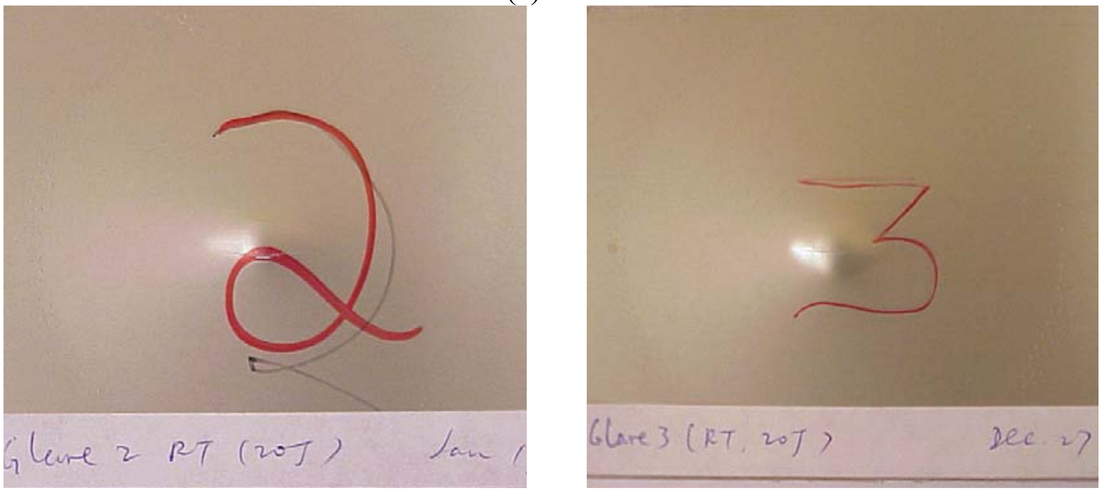

(b) 20 J

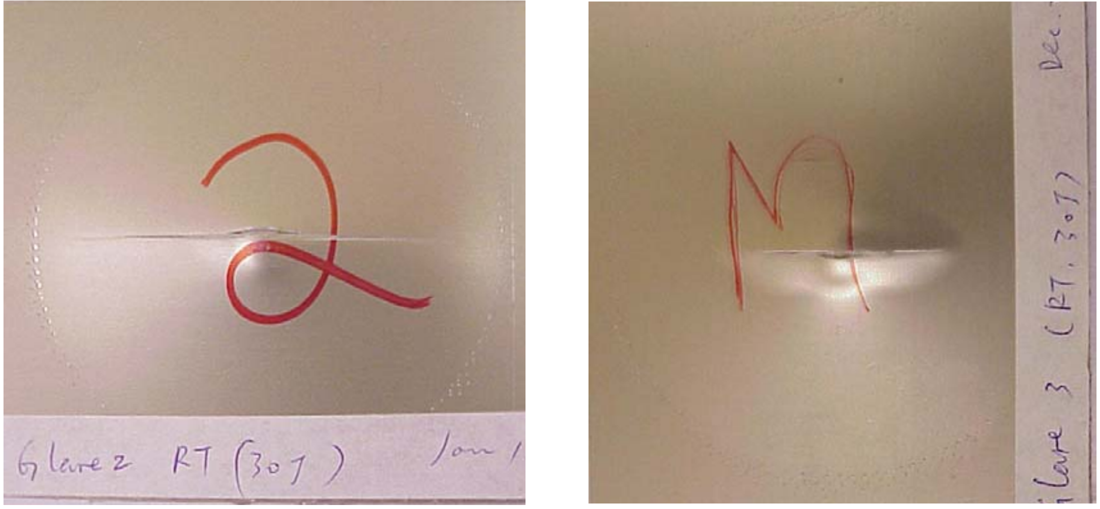

(c) 30 J

Figure 4.7 Damage patterns of GLARE 2 and GLARE 3 panels subjected to impact with different energies at room temperature

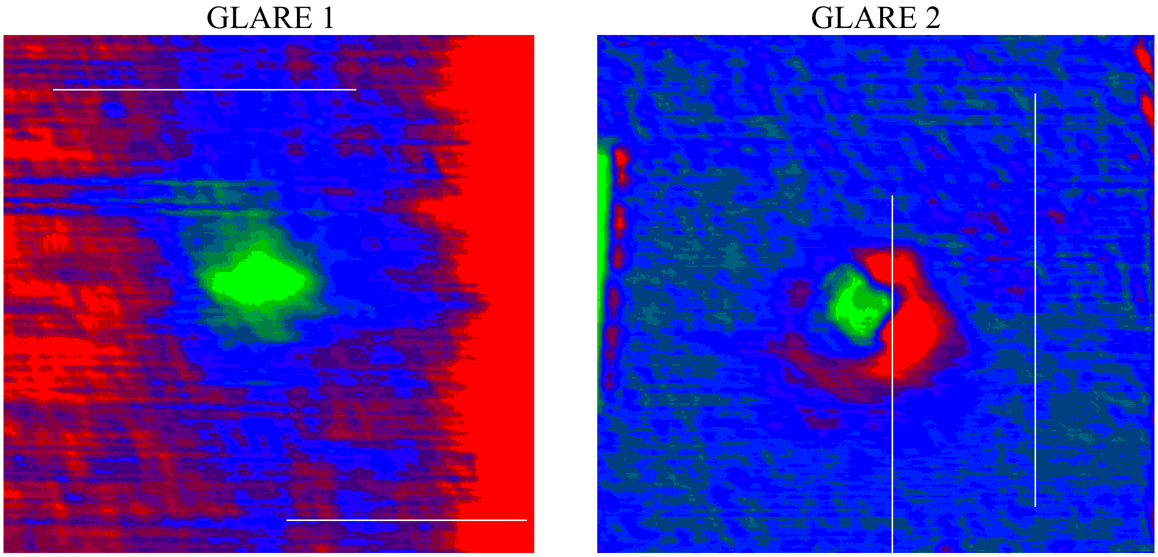

(a) Ultrasonic C-scan (through transmission, 25 MHz transducer)

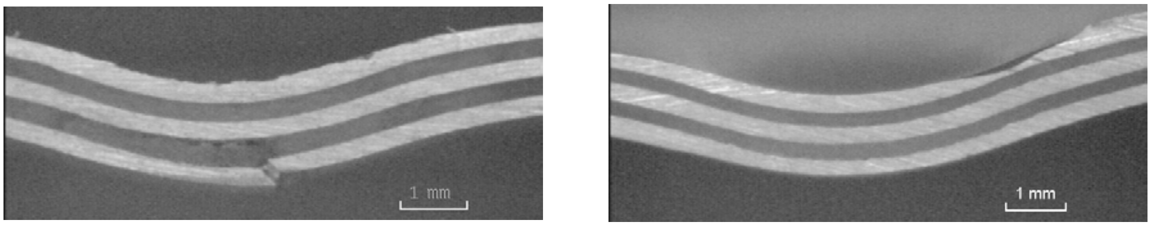

(b) Cross-sectional micrograph

Figure 4.8 C-scan and cross-sectional micrograph of GLARE 1 and GLARE 2 subjected to 10-joule impacts

Figure 4.10 indicates that there is a bigger damage zone around impact center in GLARE 2 from C-scan and the cross-sectional micrographs show the difference of local deflection between the two panels. It can also be found that GLARE 1 suffered more severe damage, including fractures of aluminum layers, fiber breakage, delamination and matrix crack under the impact zone. So more energy was attenuated by locally substantial plastic deformation in GLARE 2 whereas dissipation from fracture was needed for GLARE 1. Similar observation can be made for 30-joule impact case when even more significant damages were induced. Figure 4.11 depicts the severe damage in GLARE 2 subjected to a 30-joule impact. Under microscopic observation, all cracks occurring in aluminum layers are along the fiber direction due to lower stiffness and weaker strength in transverse direction.

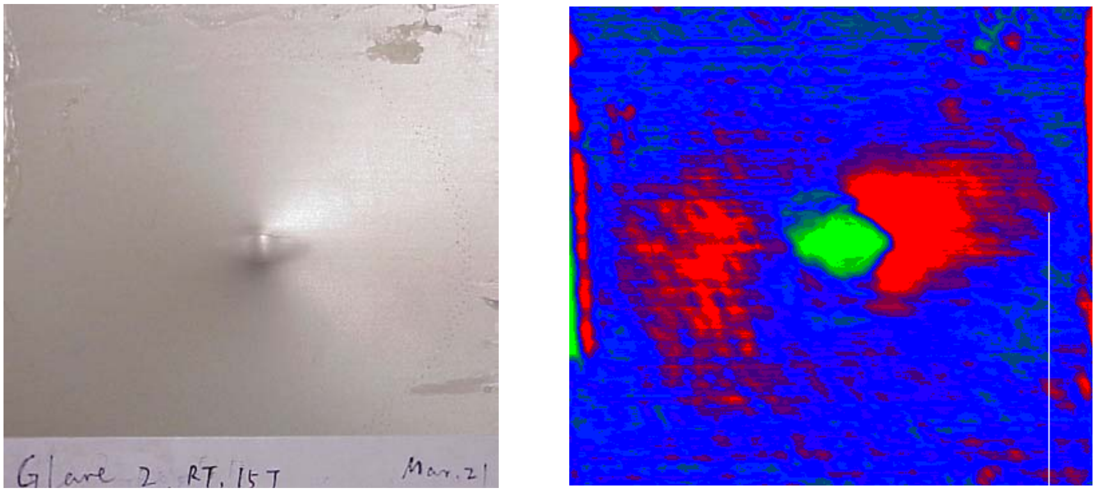

(a) Optical picture (b) C-scan

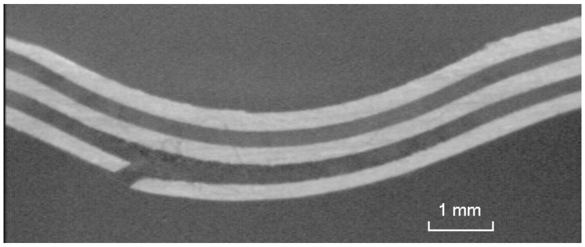

(c) Cross-sectional micrograph

Figure 4.9 Damage pattern of GLARE 2 subjected to a 15-joule impact

The fractures on aluminum layers are very interesting. For thin laminated penal subjected to transverse loading, the outer layer can be broken by bending. In Figures 4.8(b) and 4.9(c), the outer aluminum layers for both GLARE 1 and GLARE 2 fractured at about a 45° angle relative to the tensile direction. This indicates ductile fracture by shear stress for both specimens. For higher impact energy, all aluminum layers fracture in the same mode as observed in Figures 4.10(b) and 4.11(b). However, the fracture in outer layer was induced by global bending whereas the local stress concentration enabled the shear failure in inner aluminum layer. The middle layer fracture looks more like an outcome of the combination of global bending and local stress concentration.

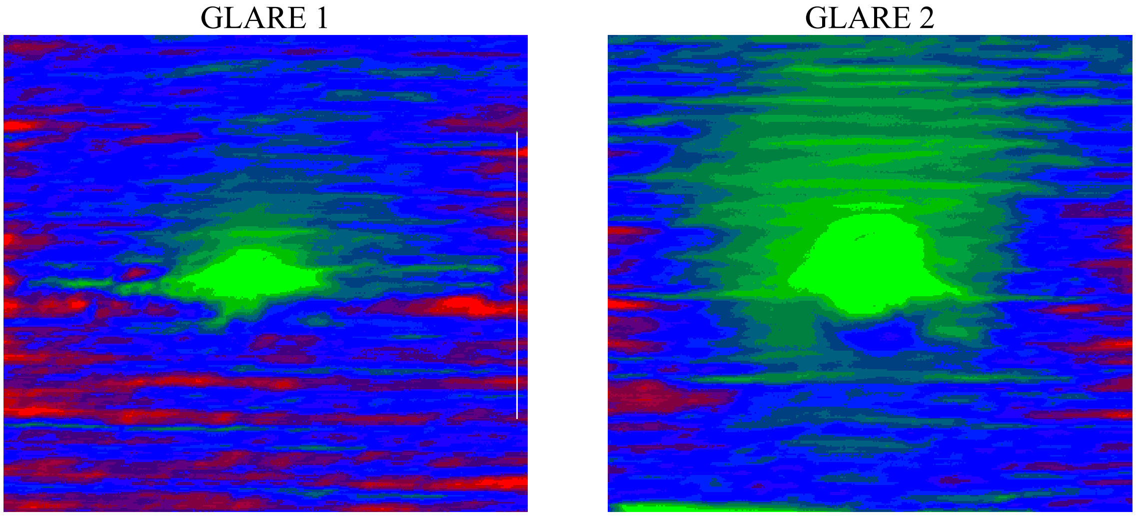

(a) Ultrasonic C-scan (through transmission, 25 MHz transducer)

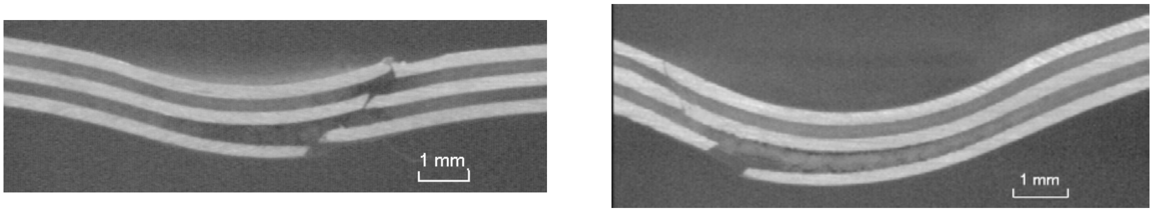

(b) Cross-sectional micrograph

Figure 4.10 C-scan and cross-sectional micrograph of GLARE 1 and GLARE 2 subjected to 20-joule impacts

Similar results had been obtained by Sun, et al. [257] for ARALL laminates under low velocity impact. It can therefore be concluded that shear dominates the failure of aluminum layers in both GLARE 1 and GLARE 2.

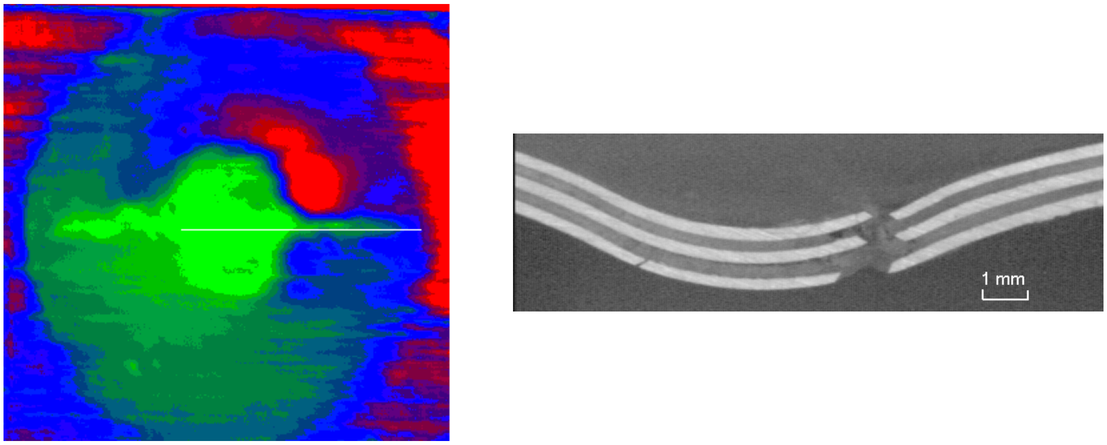

(a) C-scan
(b) Cross-sectional micrograph

Figure 4.11 C-scan and cross-sectional micrograph of GLARE 2 subjected to 30-joule impact

The damage area can be obtained from the above-mentioned ultrasonic C-scans shown in Figures 4.8 to 4.11. Choosing the impact energy as a scale parameter to measure the impact damage, the relationships between square-root of damage area and impact energy are plotted in Figure 4.12 for GLARE 1 and GLARE 2, respectively. The square root of damage area can fairly be fitted into a straight line along with the impact energy.

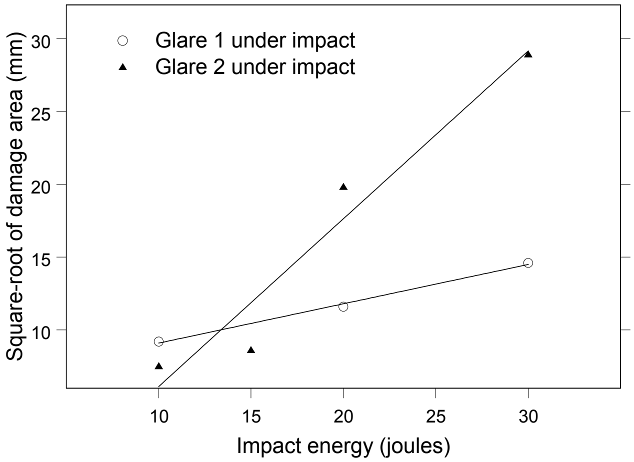

Figure 4.12 Relationship of damage area versus impact energy on GLARE 1 and 2

4.1.3 Effects of fiber orientations

The previous discussion only considered the effect of constituent materials. As well known, the fiber orientation in composite materials is important for properties of materials. In this section, two sets of GLARE panels were tested to evaluate the effects of fiber orientations.

4.1.3.1: GLARE 2 and GLARE 3. Instead of unidirectional glass-epoxy in GLARE 2 (3/2), [0°/90°] angle-ply glass-epoxy are adopted in GLARE 3 (3/2). Both laminates have the same thickness of 0.056” (1.42 mm). Figure 4.13 gives the ply sequences of GLARE 2 and 3.

2024-T3 Aluminum	2024-T3 Aluminum
0° Glass-Epoxy	0° Glass-Epoxy
0° Glass-Epoxy	90° Glass-Epoxy
2024-T3 Aluminum	2024-T3 Aluminum
0° Glass-Epoxy	0° Glass-Epoxy
0° Glass-Epoxy	90° Glass-Epoxy
2024-T3 Aluminum	2024-T3 Aluminum

Figure 4.13 Ply sequences of GLARE 2 (left) and GLARE 3 (right)

From the relationship between permanent deflection and impact energy (Figure 4.2), under the same test condition GLARE 3 yields smaller deflection than GLARE 2 which can be expected for the lower stiffness in transverse direction (i.e. perpendicular to the fiber direction) of GLARE 2. Damage patterns of GLARE 2 and GLARE 3 are compared in Figure 4.7. Combining Table 4-2 and Figure 4.7, one can conclude that GLARE 3 offers higher impact resistance than GLARE 2. In other words, cross-ply laminates are better than unidirectional laminates when subjected to transverse impact. The comparison of global impact responses between GLARE 2 and GLARE 3 is shown in Figure 4.14. Ultrasonic C-scan and cross-sectional micrographs were also performed for damage assessment. Corresponding results are given in Figure 4.15. For lower level energy impact (10-joule), the impact responses of GLARE 2 and GLARE 3 are nearly identical. There are no visible cracks for both panels. The force, absorbed energy as well as deflection histories are close to each other between GLARE 2 and GLARE 3 (Figure 4.14). As depicted in Figure 4.15(a), there is evident delamination between the outer aluminum layer (nonimpact side) and the outer glass-epoxy layer in GLARE 3. On the other hand, GLARE 2 shows almost invisible damage.

When impact energy was increased to 20-joule, more severe damages were induced in GLARE 2 than in GLARE 3. First of all, GLARE 2 yielded through-thickness crack while just a short crack (10 mm long) in the nonimpact side was observed for GLARE 3 (Table 4-2). For the force history curves, there was a slightly drop near the maximum point in the curve for GLARE 3 whereas a drastically reduction for the GLARE 2 case occurred (Figure 4.14). GLARE 3 experienced smaller deflection, but absorbed almost the same amount of maximum energy comparing to GLARE 2. After impact, GLARE 3 released more energy through the so-called "springback".

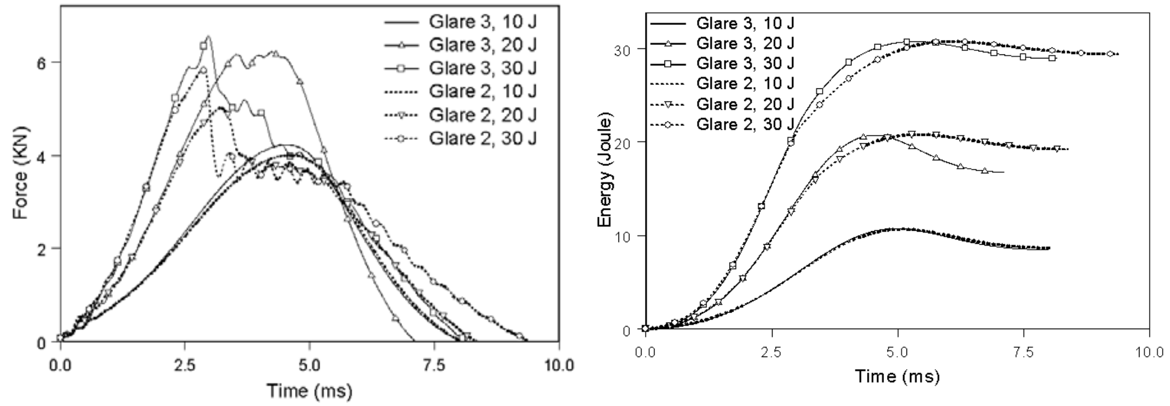

(a) Force vs. time (b) Absorbed energy vs. time

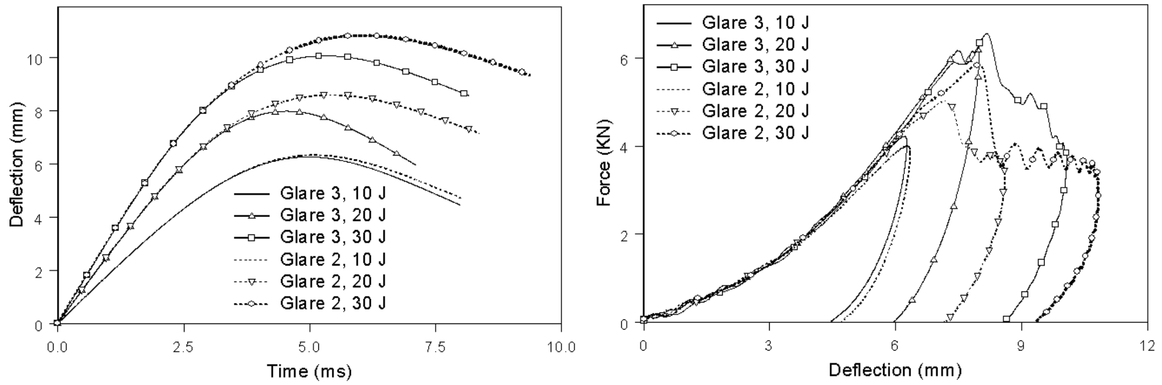

(c) Impact center deflection vs. time (d) Force vs. impact center deflection

Figure 4.14 Impact responses of GLARE 2 and GLARE 3 panels subjected to different energies at room temperature

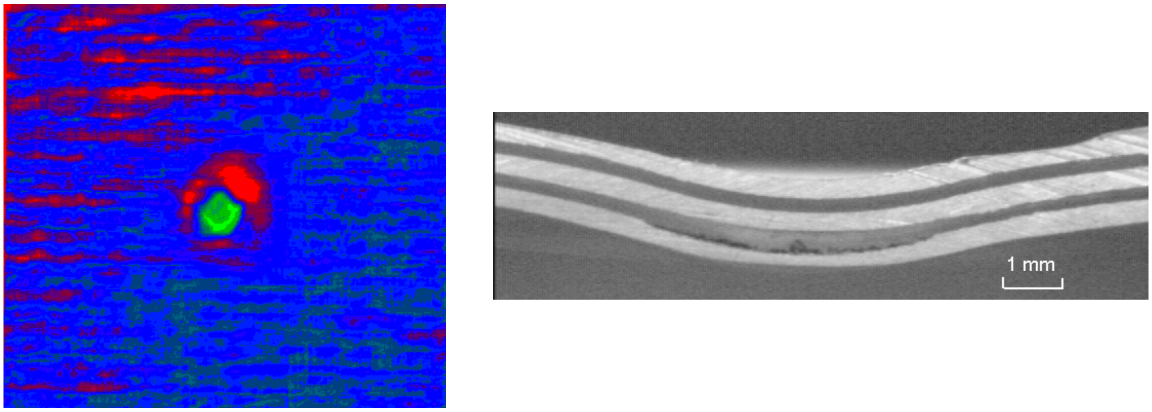

(a) 10-joule impact

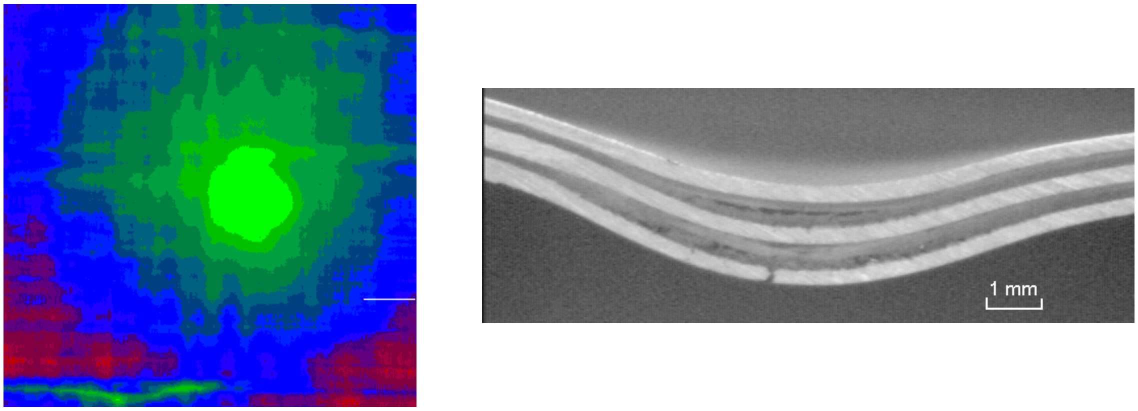

(b) 20-joule impact

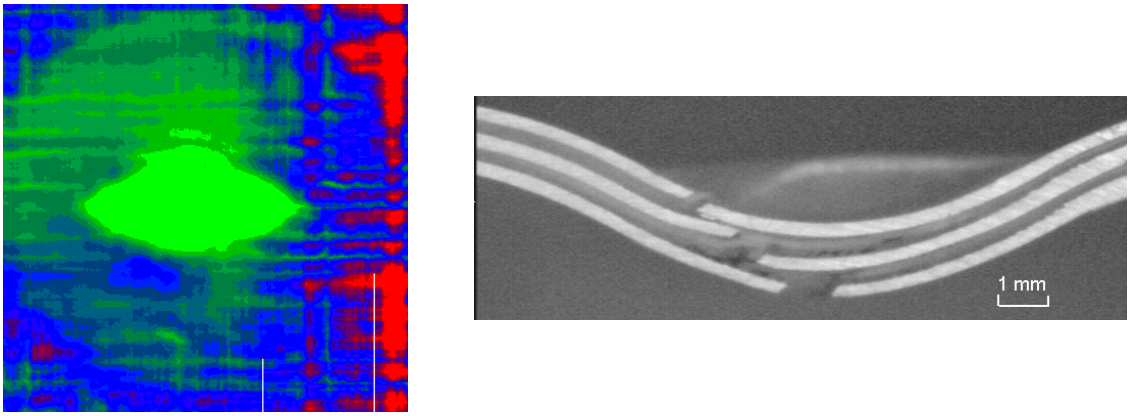

(c) 30-joule impact

Figure 4.15 C-scan and cross-sectional micrographs of GLARE 3 subjected to 10-, 20- and 30-joule impacts, respectively

Ultrasonic C-scan shown a slightly smaller damage zone in GLARE 3 than in GLARE 2 (Figures 4.10 and 4.15). From the cross-sectional micrograph, it is obvious that only an outer-layer crack in the aluminum layer occurred in GLARE 3 while a through-thickness crack appeared in GLARE 2. It is interesting to note that there was a delamination inside the inner glass-epoxy layer under impact zone. At the same time, delaminations appeared between outer glass-epoxy layer and adjacent aluminum layers in GLARE 3 when subjected to 20-joule impact as observed in Figure 4.15(b).Up to 30-joule impact, both panels suffered significant damages. There was a shorter through-thickness crack in GLARE 3 than in GLARE 2 (refer to Table 4-2 and Figure 4.7).

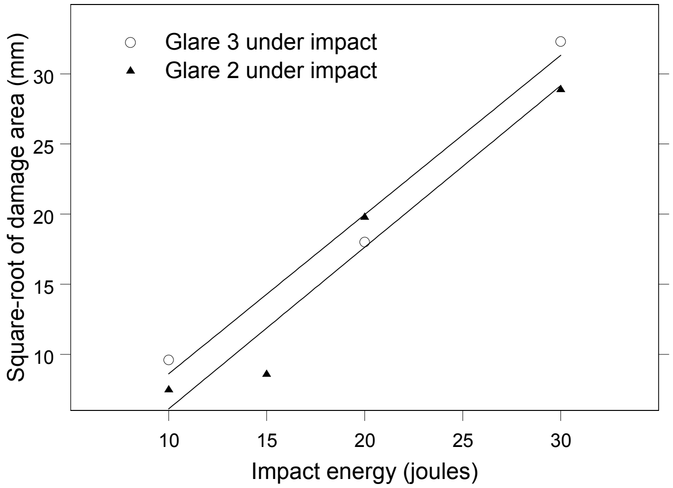

Figure 4.16 Relationship of damage area versus impact energy on GLARE 2 and 3

Figure 4.15 also describes the damage developing procedures in GLARE 3: At 10-joule impact, only a delamination was induced between the outer layer aluminum and the outer glass-epoxy layer; When impact energy was increased to 20 joules, crack initiated in the nonimpact side along with delaminations between glass-epoxy and aluminum layers around the impact center. At this time, the fracture of aluminum is dominated by bending. For even higher impact energy (30 joules), through-thickness crack and significant delamination occurred inside the whole panel. Bending dominated the outer (nonimpact) layer crack while local stress concentration induced the inner layer (impact side) fracture. Again, the aluminum layers fractured at a 45° angle relative to the tensile direction in GLARE 3 similar to GLARE 1 and GLARE 2. So the fracture was still ductile. The crack propagation direction was parallel to the 90° glass-fibers as observed under a microscope. Finally the relationships between square-root of damage area and impact energy for GLARE 3 is plotted in Figure 4.16, where square-root of damage area increases linearly along with the impact energy.

4.1.3.2: GLARE 5 (3/2), CCNY A, CCNY B, CCNY C and CCNY D.

Materials investigated here are GLARE 5 (3/2) and CCNY A, B, C and D. Table 3-1 lists the detail description for all the materials. For convenience they are briefly represented again: These five panels have the same thickness of 0.076"(1.93 mm). All these panels are made of three 2024-T3 aluminum layers and two glass-epoxy layers. The difference comes from the fiber orientation in the glass-epoxy layers: [0°/90°/90°/0°] cross-ply for GLARE 5, [$0°_4$] unidirectional for CCNY A, [$90°_4$] unidirectional for CCNY B, [45°/-45°/-45°/45°] angle-ply for CCNY C and [0°/45°/-45°/90°] quasi-isotropic for CCNY D. Based on Table 4-2, some impact properties of the above panels are listed in Table 4-3. The permanent deflection versus impact energy is shown in Figure 4.17. It can be concluded that unidirectional panels deformed easier than other panels while the quasi-isotropic panels yielded the smallest deflection under the same impact condition. Since there is a negligible difference of mechanical properties between rolling direction and transverse direction for aluminum, under the same test condition nearly identical test results were obtained from [$0°_4$] unidirectional and [$90°_4$] unidirectional panels, i.e. CCNY A and CCNY B (Figure 4.18). Figures 4.19, 4.20(a-d) and 4.21 depict the impact responses and damage evaluation of above panels. In a nutshell, unidirectional panels offer the lowest impact resistance while quasi-isotropic panels seem to be the best when subjected to impact.

Table 4-3 Impact properties of GLARE with various fiber orientations (25°C)

Material	Impact Energy (Joule)	Crack length in outer layer (mm)		Permanent Deflection (mm)
		Impacted side	Nonimpact side	
GLARE 5(3/2)	20	0	0	3.9
GLARE 5(3/2)	30	0	10	6.0
GLARE 5(3/2)	40	7	19	7.3
CCNY A	10	0	22	3.4
CCNY A	20	0	35	6.1
CCNY A	30	50	60	8.0
CCNY B	10	0	22	3.2
CCNY B	20	15	35	5.8
CCNY B	30	65	70	6.7
CCNY C	20	0	0	4.7
CCNY C	30	0	0	6.0
CCNY C	40	0	14 (curve)	7.3
CCNY D	20	0	0	3.9
CCNY D	30	0	0	4.3
CCNY D	40	0	8 (curve)	6.5

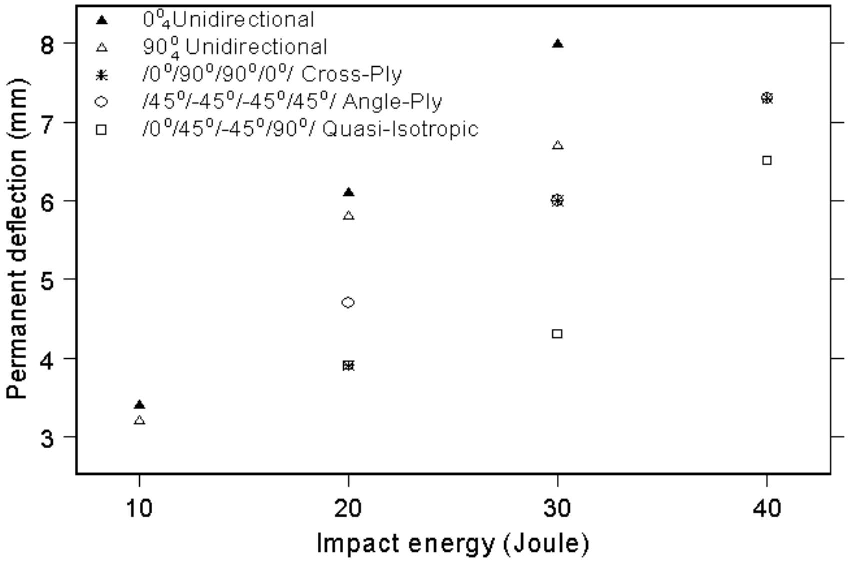

Figure 4.17 Permanent deflection versus impact energy corresponding to various fiber orientations

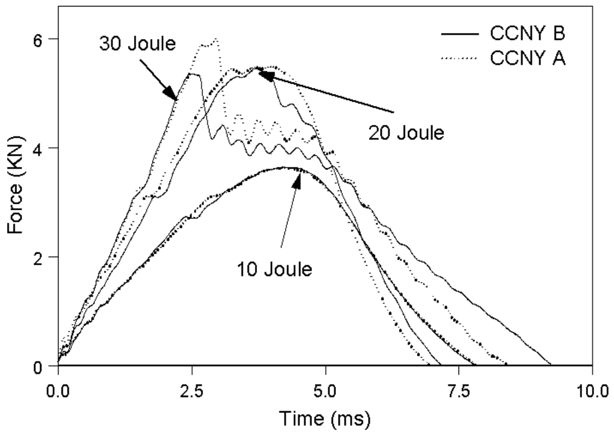

Figure 4.18 Impact force histories of CCNY A and CCNY B

Even when subjected to lower energy impact, such as 10-joule impact, significant damage could be induced in unidirectionally plied panels (CCNY A and CCNY B). A visible crack could be found in the nonimpact side. When subjected to a 30-joule impact, through-thickness cracks occurred in CCNY A and CCNY B with cracks extended to the clamped edge. For panels with other fiber orientations, there was no visible crack in those panels under 10- or 20-joule impact. Under a 30-joule impact, a crack initiated from the nonimpact side in GLARE 5 while there was still no visible crack in CCNY C and CCNY D. When impact energy was increased to 40 joules, cracks occurred from nonimpact sides of CCNY C and CCNY D. It is worth noting that cracks in CCNY C and CCNY D were not straight lines whereas straight cracks were induced in unidirectional and cross-ply panels (Figure 4.21). Another interesting phenomenon is that the maximum absorbed energies for different panels were about the same although damage patterns were significantly different. The unidirectional panels can release less energy after impact event than others. Under 30 or 40-joule impact, panels including 45° plies glass-epoxy offered slightly higher resistant force and released more energy than cross-ply panels while the quasi-isotropic panels offered even higher resistant force and released even more energy. Some researchers [36] have found the similar phenomenon for regular composite materials because of the relatively lower mismatch of bending stiffness between two adjacent plies. Further damage assessment were conducted through ultrasonic C-scan and cross-sectional micrograph on specimens suffered to 30-joule impact (Figure 4.20).

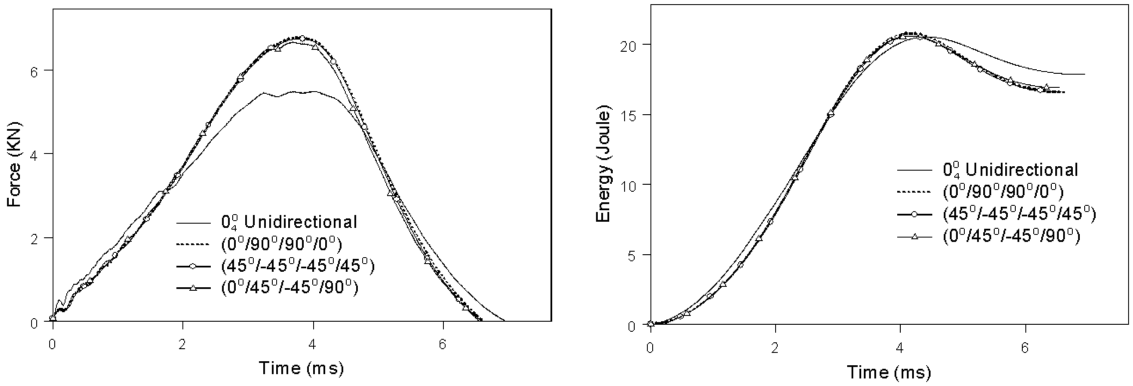

(a) 20-joule impact

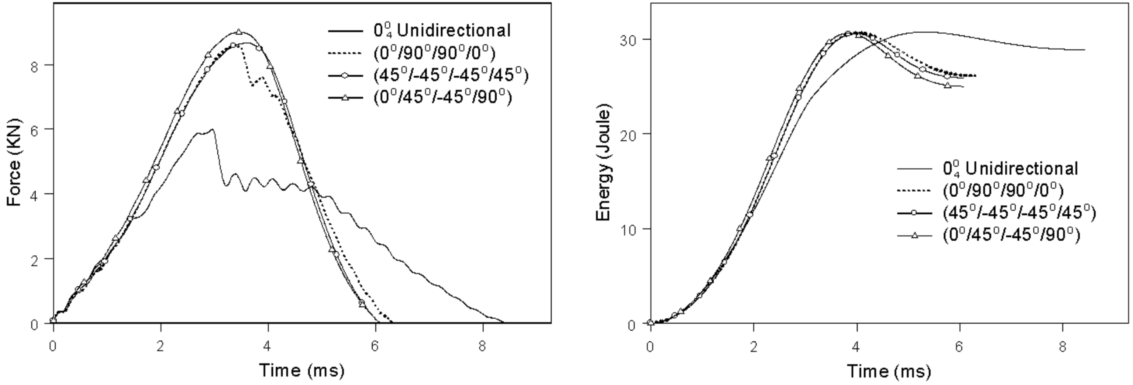

(b) 30-joule impact

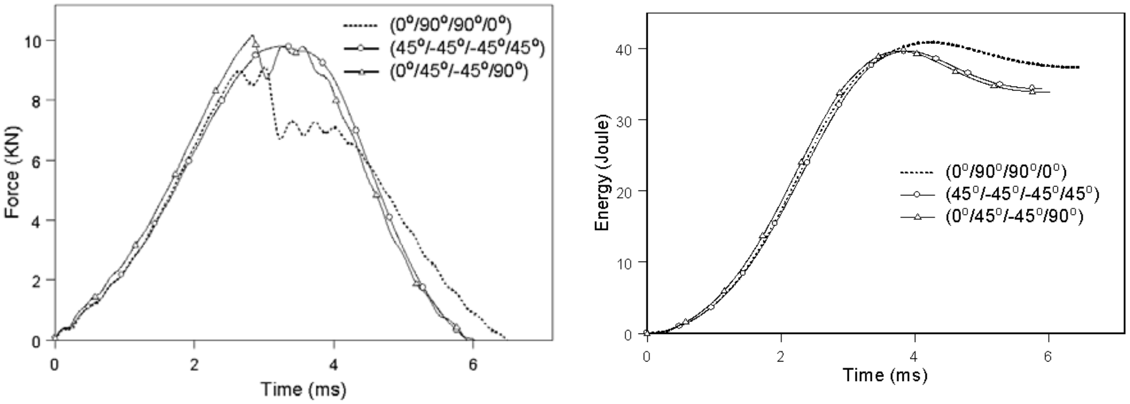

(c) 40-joule impact

Figure 4.19 Global impact responses of GLARE 5, CCNY A, CCNY C and CCNY D

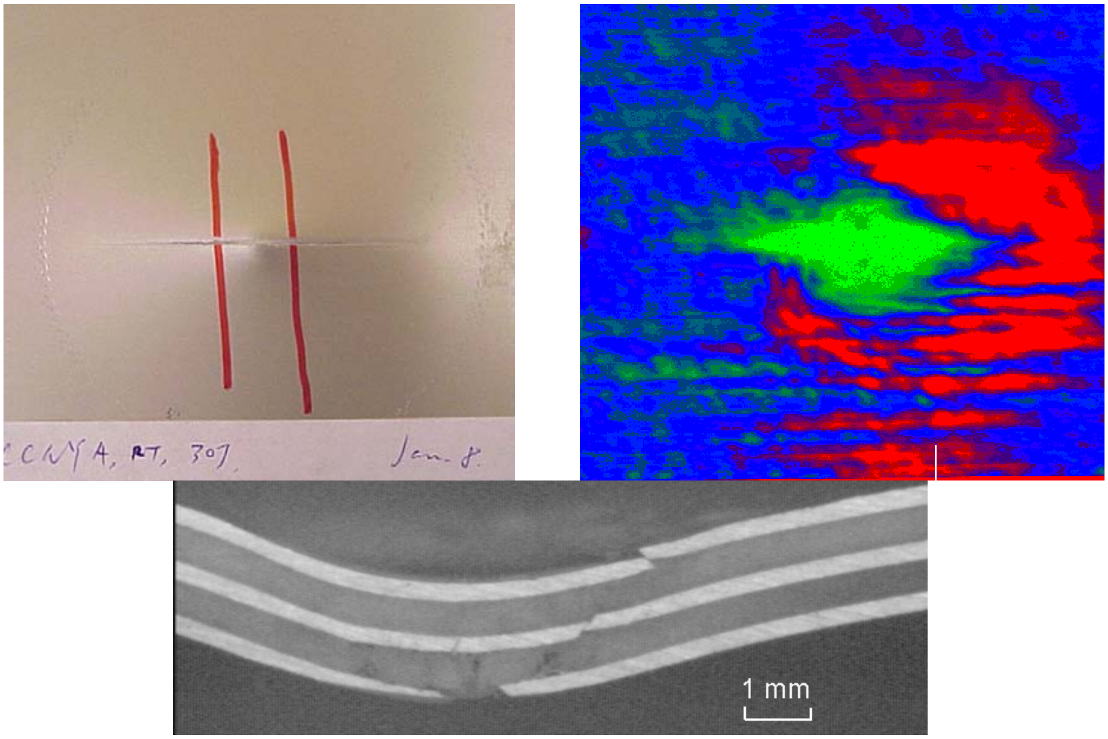

Figure 4.20(a) Damage assessment of CCNY A subjected to 30-joule impact

Based on Figures 4.19 and 4.20, more detailed discussion can be made. For GLARE with unidirectional fiber-epoxy (CCNY A), Figure 4.20(a) shows the damage patterns with 30-joule impact. A long visible through-thickness crack occurred and the damage zone observed from C-scan looks like a spindle with the major axis aligned along the fiber direction. The cross-sectional micrograph gives more detailed information. Surprisingly, there is not much delamination besides fracture of aluminum layers and split of glass-epoxy layers. The fracture of aluminum in nonimpact side was resulted from bending while the stress concentration induced the crack in the impact side aluminum layer. Under the same test condition, GLARE 5 (3/2) just displays a short crack in the nonimpact side with certain amount of delamination. Higher impact force with a smaller sharp reduction in force-time history in comparison with unidirectional glass-epoxy panel indicates that GLARE 5 offers a higher impact resistance than CCNY

A. A diamond-shaped damage zone was induced with diagonals along 0° and 90°, respectively. Significant delamination can be found from the cross-sectional micrograph. The major delamination locates between the nonimpact side aluminum layer and the adjacent glass-epoxy layer. Some small region of delamination around the middle layer aluminum can also be found. Fiber breakage in 0° glass-epoxy layer and matrix cracks in 90° layers took place for [0°/90°/90°/0°] plies near the nonimpact side. Different from CCNY A and GLARE 5, the force-time histories of CCNY C and CCNY D are fairly smooth which indicate no significant damage induced during impact. Discontinuous delamination in CCNY C and a continuous region delamination between nonimpact aluminum layer and the adjacent glass-epoxy layer in CCNY D can be located through cross-sectional micrographs. Comparing to the diamond-shaped damage zone in GLARE 5, an approximately circular damage zone can be found by ultrasonic C-scan for CCNY D panel.

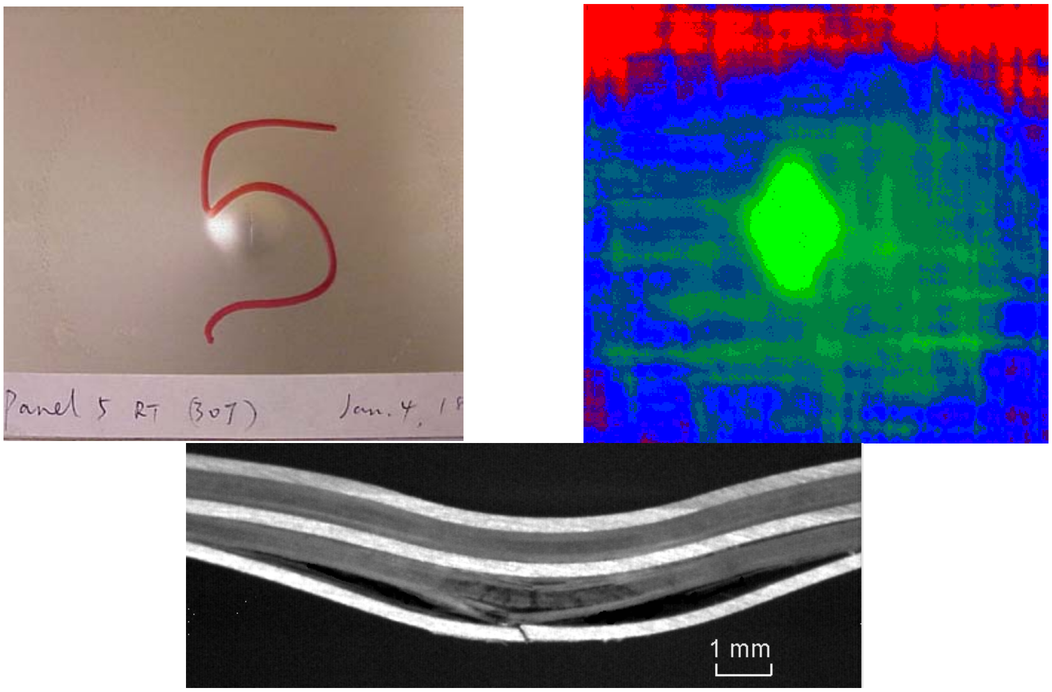

Figure 4.20(b) Damage assessment of GLARE 5 (3/2) subjected to 30-joule impact

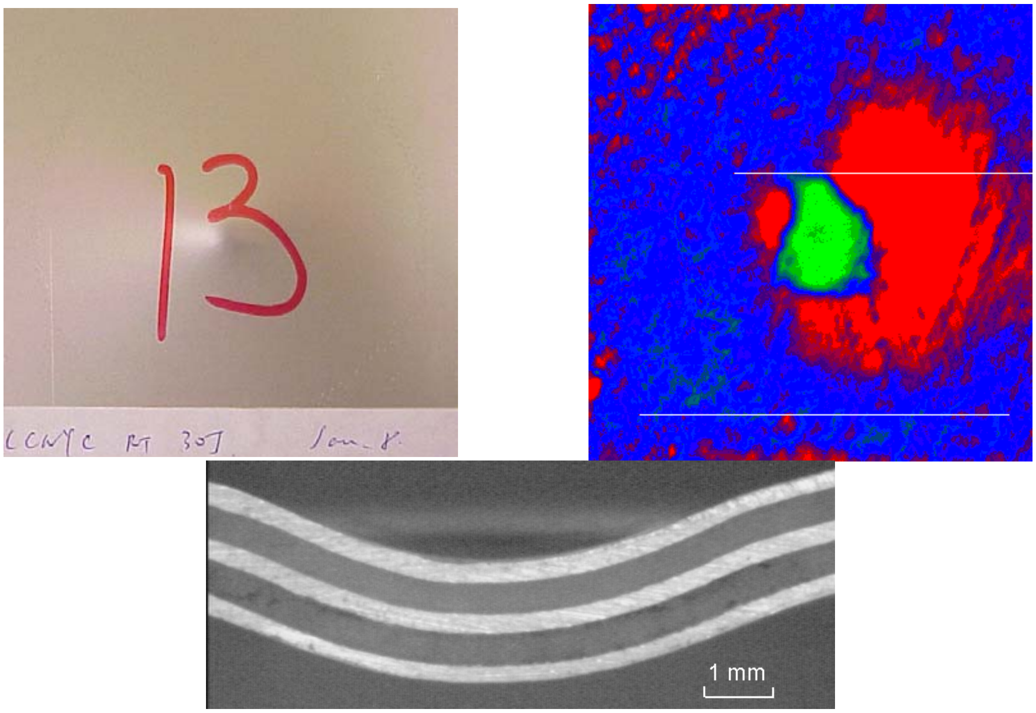

Figure 4.20(c) Damage assessment of CCNY C subjected to 30-joule impact

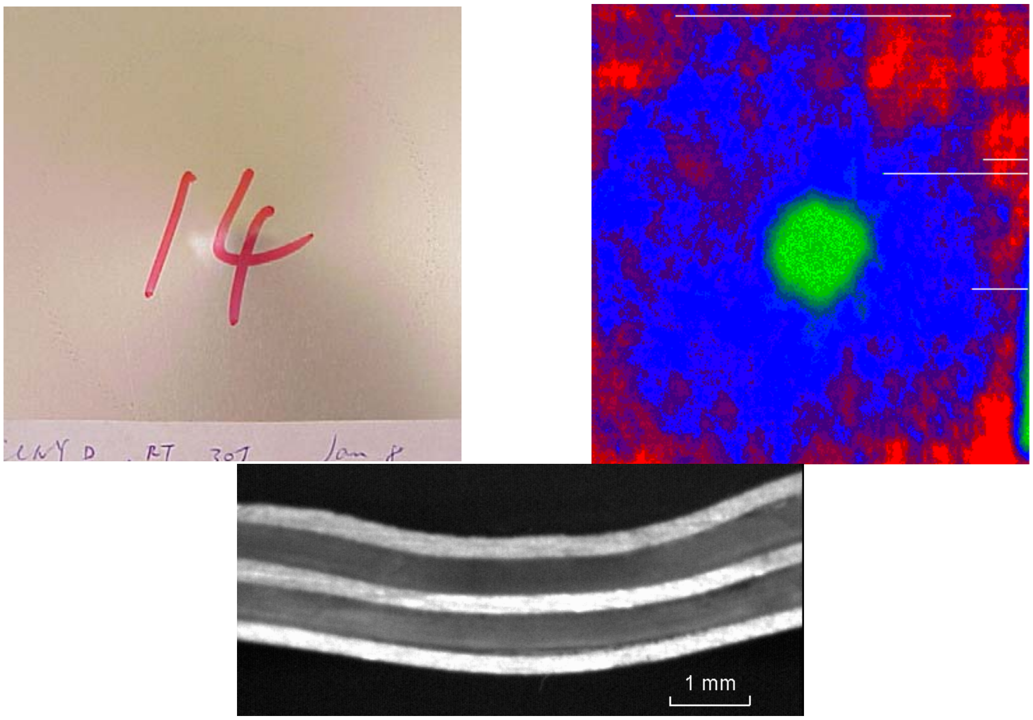

Figure 4.20(d) Damage assessment of CCNY D subjected to 30-joule impact

Figure 4.21 depicts damage patterns of different panels when subjected to impact with 40-joule energy. Visible crack occurred in all specimens with more severe damage in GLARE 5.

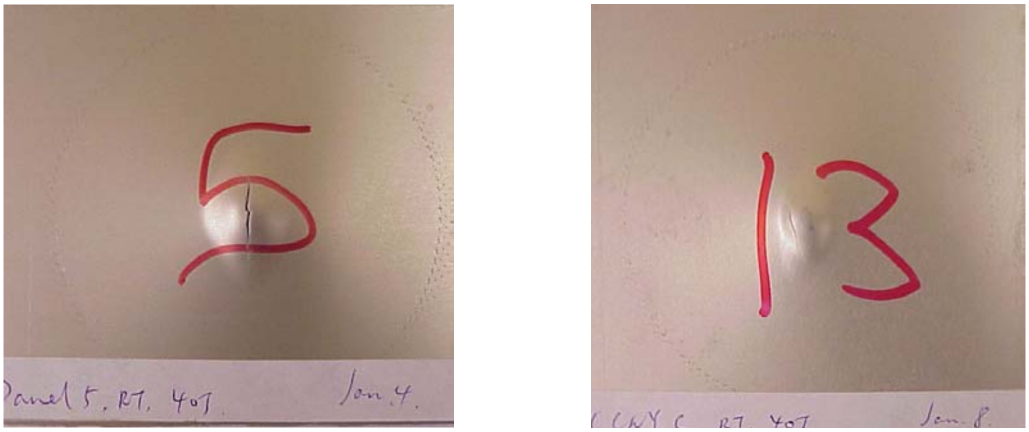

GLARE 5 (3/2) ([0°/90°/90°/0°] Cross-ply)   CCNY C ([45°/-45°/-45°/45°] Angle-ply)

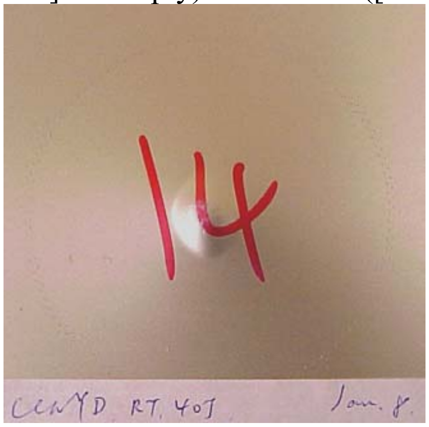

CCNY D ([0°/45°/-45°/90°] Quasi-Isotropic)

Figure 4.21 Damage patterns of GLARE 5 (3/2), CCNY C and CCNY D subjected to 40-joule impact

4.1.4 Effects of specimen thickness

In this study, GLARE 5 panels with different thickness were chosen to assess the thickness effect. The range of thickness is from 0.044" (1.12 mm) of GLARE 5(2/1) up to 0.172" (4.37 mm) of GLARE 5(6/5). Table 4-4 lists impact responses of GLARE 5 with different thickness. As expected, the thicker the panel, the more energy needed to induce comparable damage. In other words, thicker panels offer higher impact resistance than thinner panels. Figure 4.22 shows the deflection-impact energy relationship for GLARE 5 panels with different thickness. Obviously, increasing thickness can significantly reduce the permanent deflection under the same impact conditions.

It's worth noting that there is a sharp drop in force-time historic curves for those tests with a visible crack on the nonimpact side. So the threshold impact energy to induce visible crack is interesting. Figure 4.23 depicts the relationship between threshold cracking energy and thickness of specimens. The result indicates that this threshold energy versus thickness can be fitted using a parabolic plot by least square method. The fitting plot is also shown in Figure 4.23. Similar to discussions made in previous section, impact responses of GLARE 5 panels are listed in Figure 4.24 corresponding to the threshold cracking energies. Thicker specimens offer higher impact resistance over thinner panels. Except GLARE 5(2/1), all GLARE 5 panels experienced about the same amount of maximum deflection (around 8 mm) during impact event as shown in Figures 4.24 (c) and (d) even though the impact forces and absorbed energies were different for various panels.

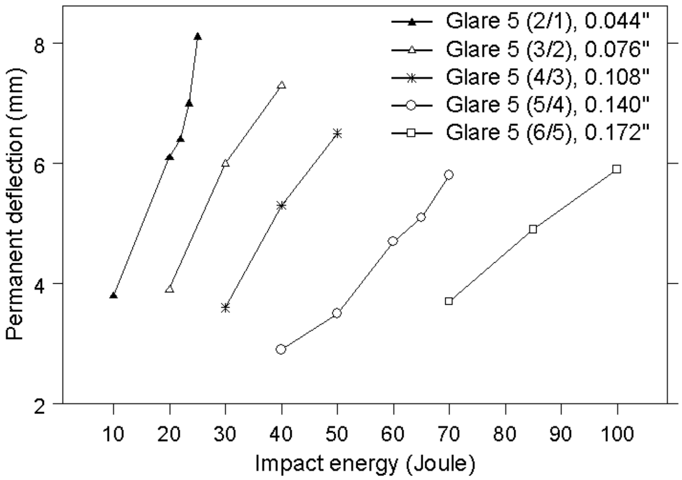

Figure 4.22 Deflection-impact energy relationship for different GLARE 5 panels

Table 4-4 Impact properties of GLARE 5 with different thickness (25°C)

Material & Thickness (in)	Impact Energy (Joule)	Crack length in outer layer (mm)		Permanent Deflection (mm)
		Impacted side	Nonimpact side	
GLARE 5(2/1), 0.044	10	0	0	3.8
GLARE 5(2/1), 0.044	20	0	0	6.1
GLARE 5(2/1), 0.044	22	0	0	6.4
GLARE 5(2/1), 0.044	23.5	8	10	7.0
GLARE 5(2/1), 0.044	25	Through curved crack		8.1
GLARE 5(2/1), 0.044	30	Penetration		
GLARE 5(3/2), 0.076	20	0	0	3.9
GLARE 5(3/2), 0.076	30	0	10	6.0
GLARE 5(3/2), 0.076	40	7	19	7.3
GLARE 5(4/3), 0.108	30	0	0	3.6
GLARE 5(4/3), 0.108	40	0	7	5.3
GLARE 5(4/3), 0.108	50	0	18	6.5
GLARE 5(5/4), 0.140	40	0	0	2.9
GLARE 5(5/4), 0.140	50	0	0	3.5
GLARE 5(5/4), 0.140	60	0	0	4.7
GLARE 5(5/4), 0.140	65	0	12	5.1
GLARE 5(5/4), 0.140	70	5	20	5.8
GLARE 5(6/5), 0.172	70	0	0	3.7
GLARE 5(6/5), 0.172	85	0	10	4.9
GLARE 5(6/5), 0.172	100	6	20	5.9

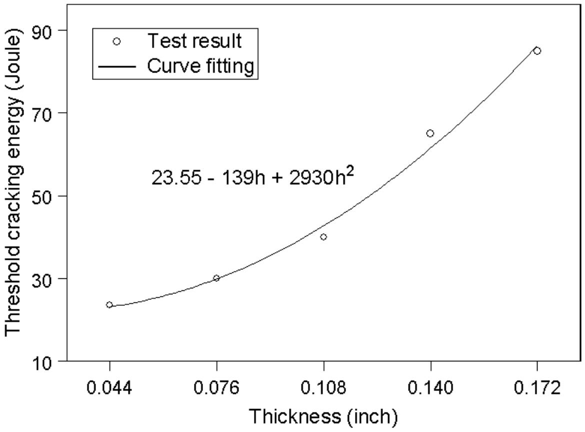

Figure 4.23 Threshold cracking energy versus thickness of specimens

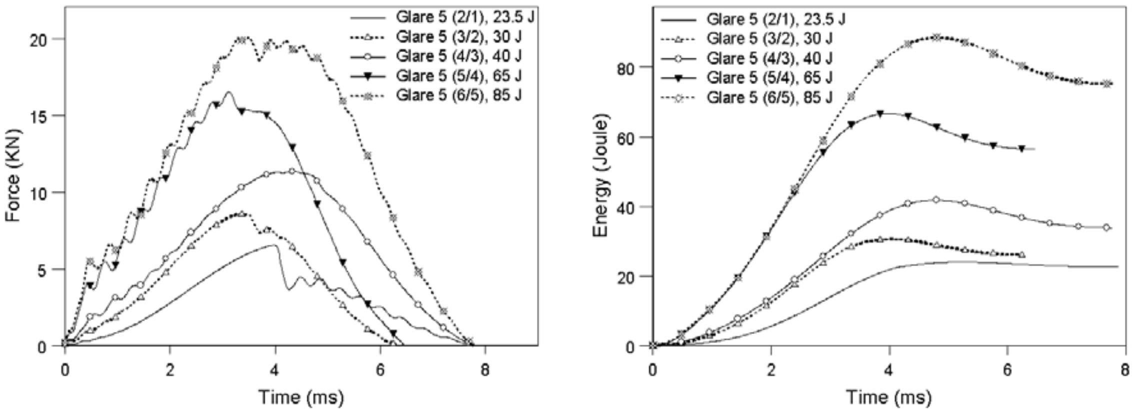

(a) Force vs. time (b) Absorbed energy vs. time

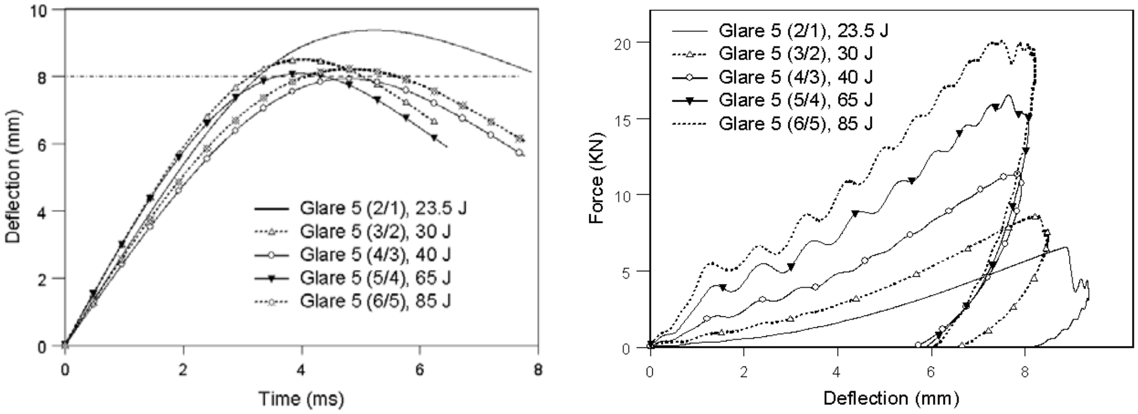

(c) Impact center deflection vs. time (d) Force vs. impact center deflection

Figure 4.24 Impact responses of GLARE 5 with different thickness

Now it's time to discuss the damage evaluation for GLARE 5 at various impact energy levels using optical pictures, ultrasonic C-scans and cross-sectional micrographs. The material discussed here is GLARE 5 (3/2) with 0.076" thickness subjected to 20-, 30- and 40-joule impact, respectively. Figures 4.20(b), 4.25 and 4.26 were taken into consideration for different impact energies. It can be found that the damage area and local indentation increase with the increasing of impact energies. At 20-joule impact, there was no visible damage except local indentation with delamination between glass-epoxy layer and aluminum sheet at the nonimpact side. At 30-joule impact, visible crack was observed in aluminum sheet at the nonimpact side and fiber breakage also occurred in glass-epoxy layer near nonimpact side. Cracks in all aluminum layers and more severe damage in glass-epoxy layers could be observed when impact energy increases to 40 joules. Another interesting phenomenon is that cracks in aluminum layers are in 90° direction and perpendicular to adjacent glass fibers as observed under microscope. This is different from GLARE 3 where cracks are parallel to the adjacent 90° glass fibers.

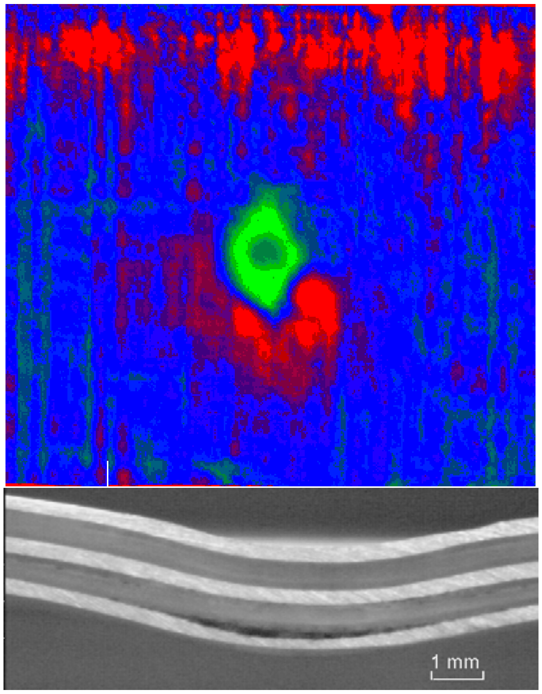

Figure 4.25 C-scan and Cross-sectional micrograph of GLARE 5(3/2) subjected to 20-joule impact

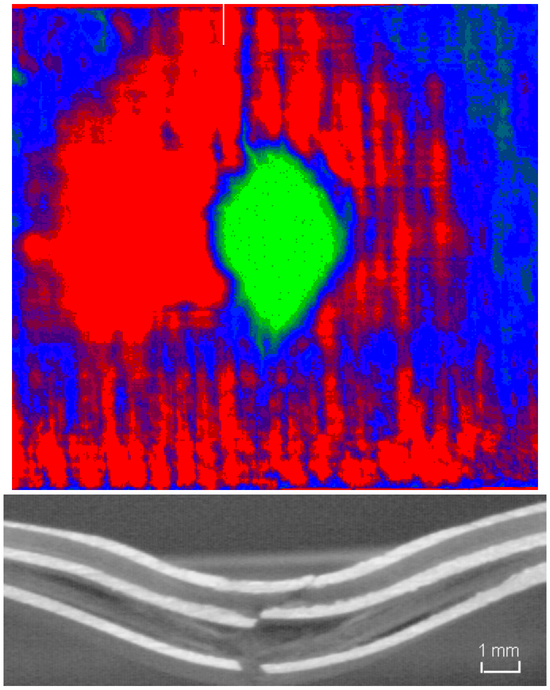

Figure 4.26 C-scan and Cross-sectional micrograph of GLARE 5(3/2) subjected to 40-joule impact

It must be noted that damage patterns in thicker panels, like GLARE 5(6/5), maybe different from those in thinner panels since the stress concentration induced from higher impact force can dominate the cracks around the impact site. More ultrasonic inspection and cross-sectional micrographs were taken for damage evaluation of GLARE 5(4/3) and GLARE 5(6/5) subjected to impact. Figure 4.27 shows the impact force histories of GLARE 5(4/3). Fairly smooth curve for 30-joule impact indicates there was no severe damage induced. The slightly dropping around 5 millisecond point on the curve of 40-joule impact corresponds to the short crack on the nonimpact side, whereas the sudden dropping at the point of maximum impact force is due to the severe damages (delamination and cracks) in GLARE 5 (4/3) when subjected to 50-joule impact.

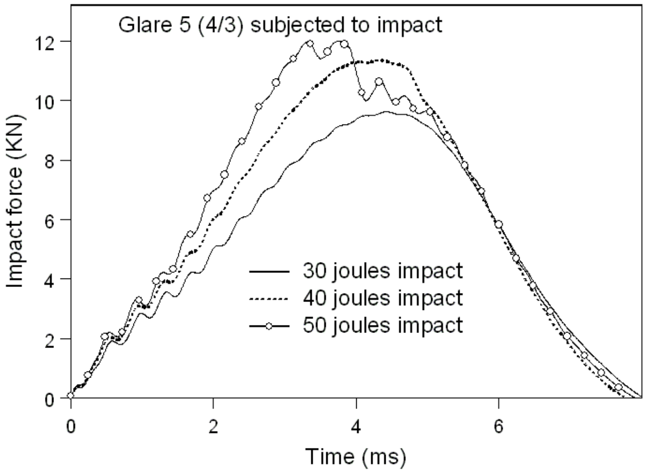

Figure 4.27 Impact force histories of GLARE 5 (4/3)

Damage inspections are shown in Figures 4.28 (a ~ c) for GLARE 5 (4/3) impacted under 30, 40 and 50-joule. In general, higher impact energy can induce bigger impact force, more severe damage and larger damage area. At 30-joule impact, no visible crack occurred with delamination between the first layer of composite and the second layer of aluminum from the impact side. This is due to the higher impact force, which caused large local indentation. Up to 40-joule impact, more delaminations were induced in all three layers of glass-epoxy with adjacent aluminum sheets. The largest gap occurred between the aluminum and composite on the nonimpact side because there is no constraint on the outer aluminum sheet after crack. There was also fiber breakage in the composite layer on the nonimpact side. Under 50-joule impact, cracks were induced in all three layers of aluminum and severe damage in glass-epoxy layers. In summary, the first delamination occurred near the impact side whereas the more severe damages were induced on the nonimpact side for the thicker fiber-metal laminates — GLARE 5 (4/3).

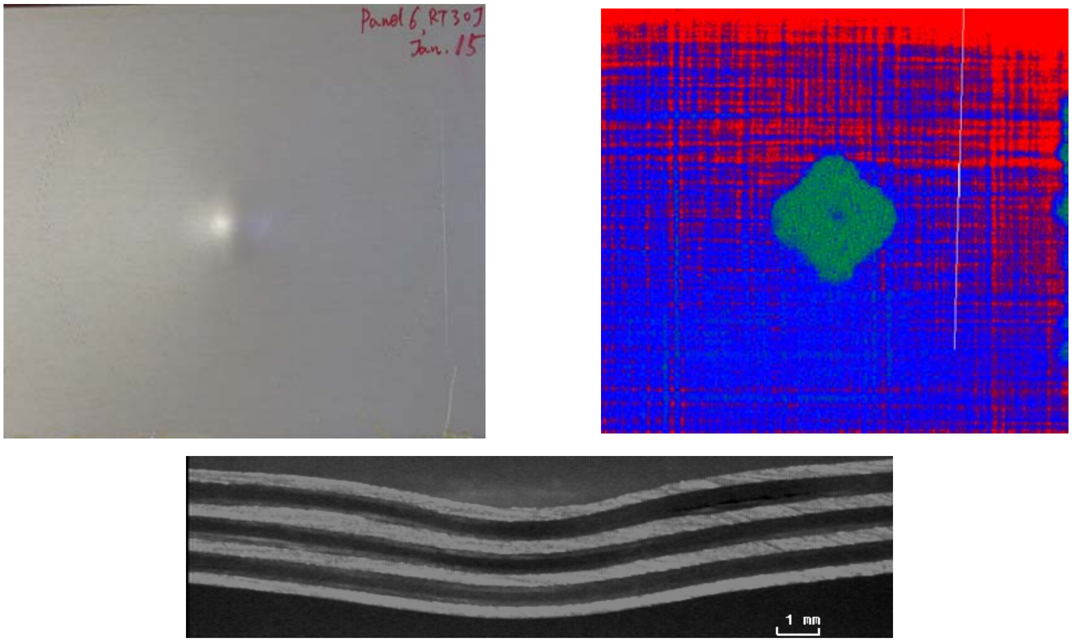

Figure 4.28 (a) Damage patterns of GLARE 5 (4/3) subjected to 30-joule impact

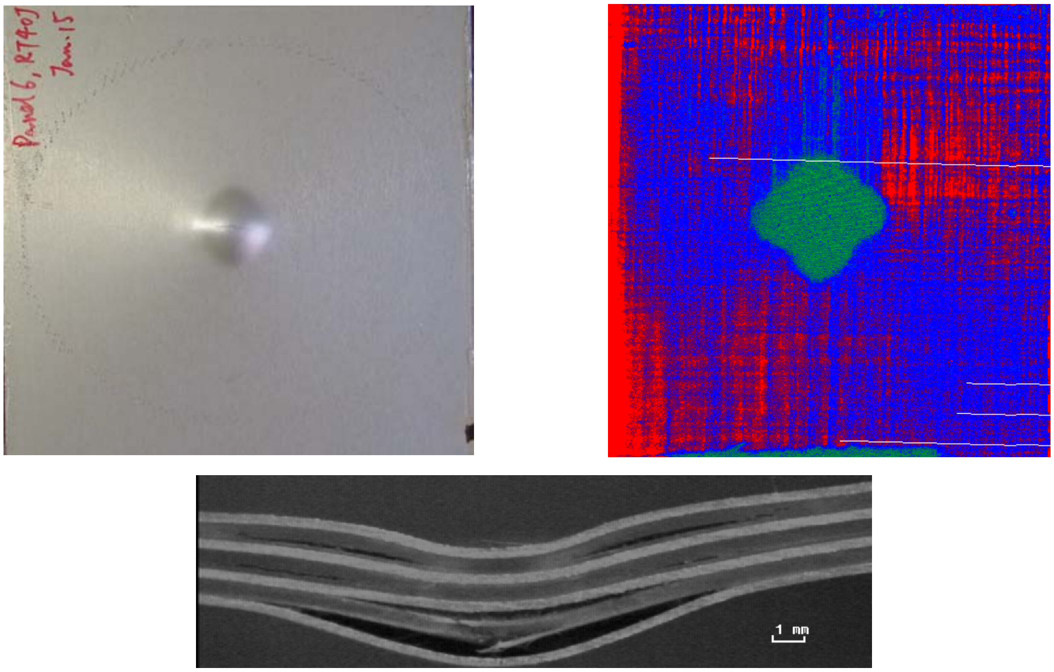

Figure 4.28 (b) Damage patterns of GLARE 5 (4/3) subjected to 40-joule impact

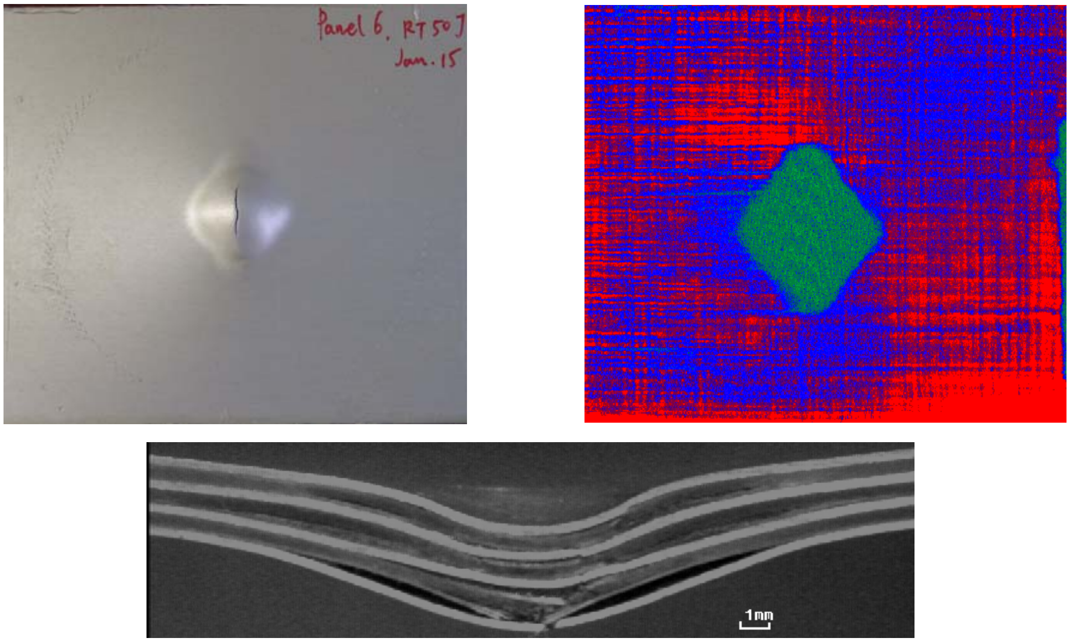

Figure 4.28 (c) Damage patterns of GLARE 5 (4/3) subjected to 50-joule impact

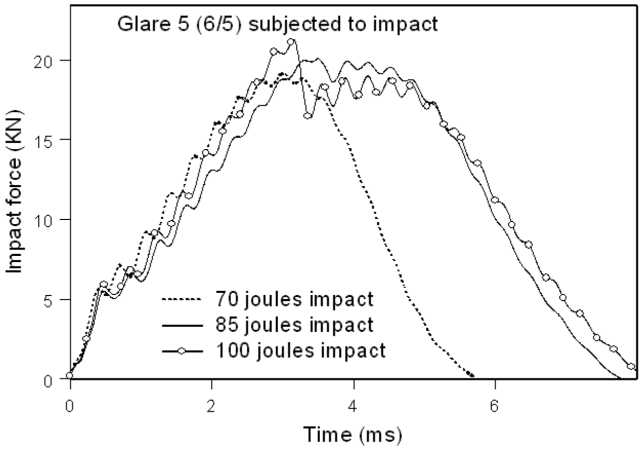

Figure 4.29 Impact force histories of GLARE 5 (6/5)

For even thicker GLARE 5 (6/5), results of impact forces and damage evaluation are shown in Figure 4.29 and Figure 4.30 with 70 joules, 85 joules and 100 joules as impact energy. The ultrasonic C-scans were taken by using 15 MHz transducers instead of 25 MHz transducers because the specimens are too thick for 25 MHz transducers. Again, the higher the impact energy, the bigger impact force and more severe damage induced. Delaminations occurred near the impact side at relatively lower impact energy.

More severe damage including the crack in the outer aluminum sheet and fiber breakage in composite layer was induced on the nonimpact side when impact energy was higher.

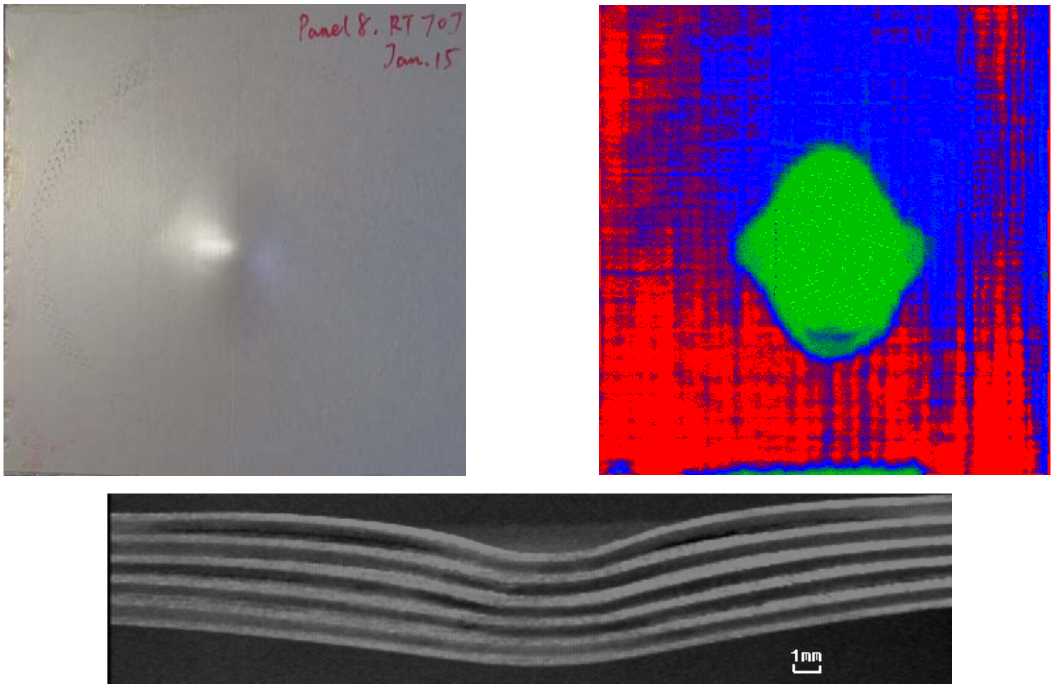

Figure 4.30 (a) Damage patterns of GLARE 5 (6/5) subjected to 70-joule impact

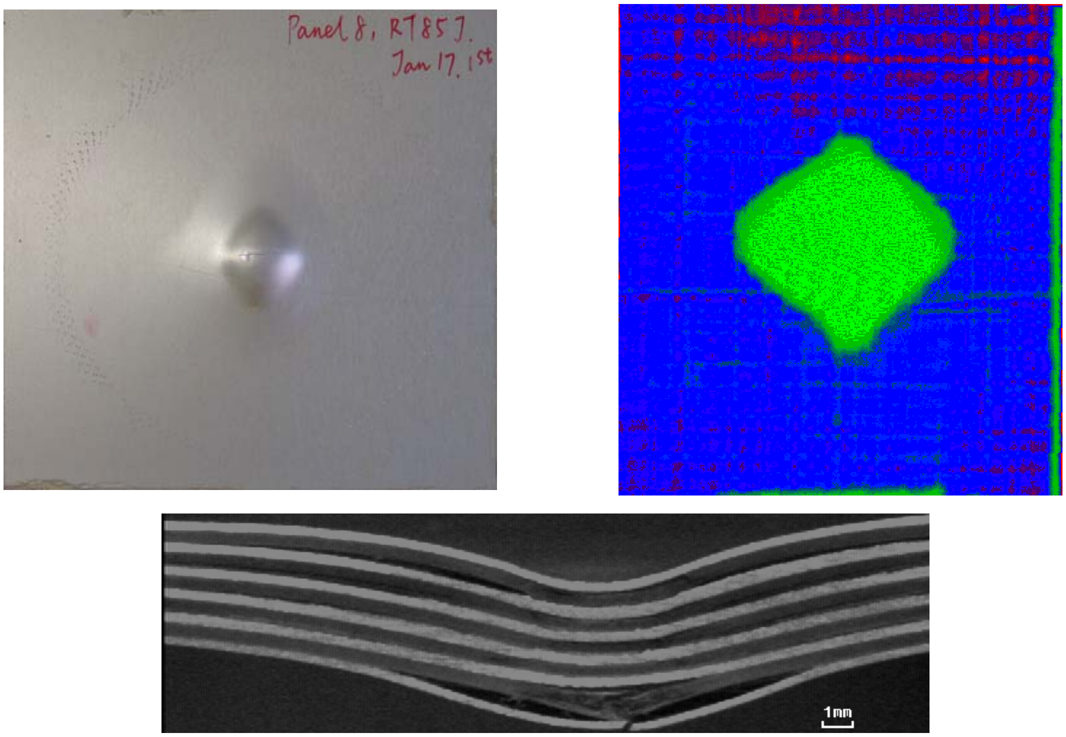

Figure 4.30 (b) Damage patterns of GLARE 5 (6/5) subjected to 85-joule impact

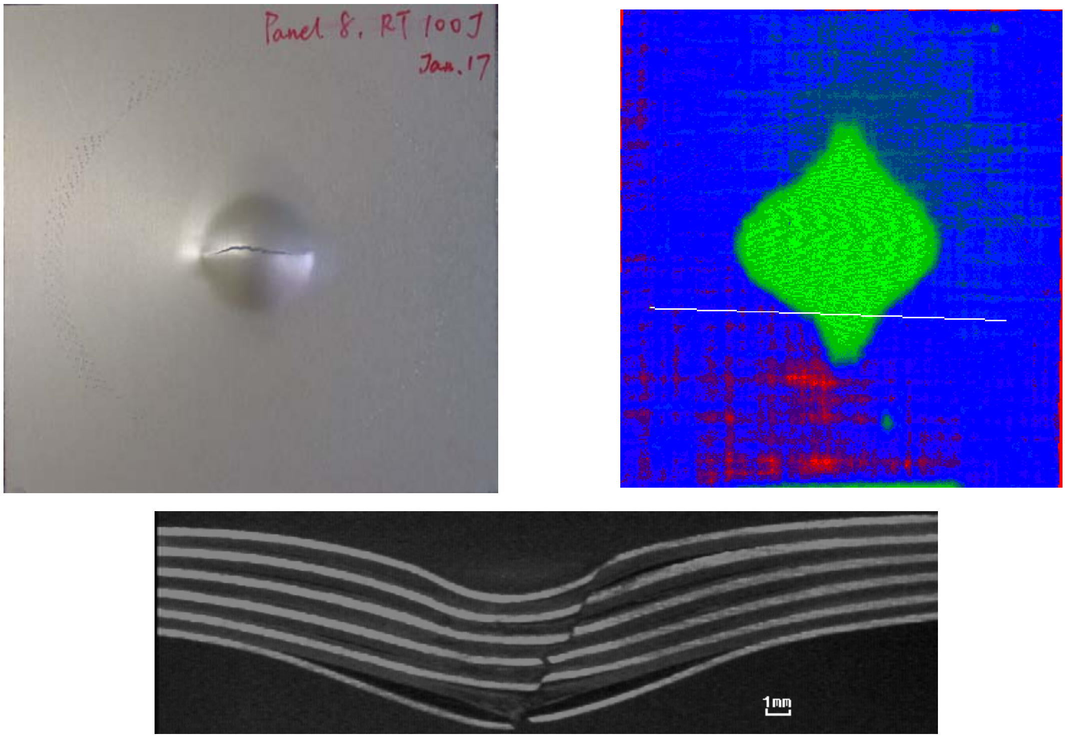

Figure 4.30 (c) Damage patterns of GLARE 5 (6/5) subjected to 100-joule impact

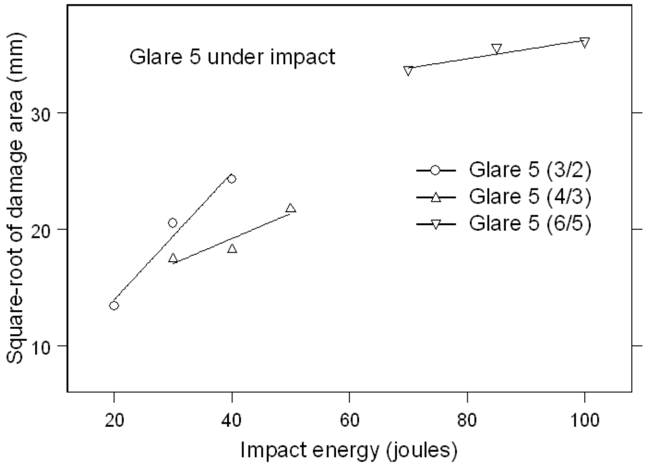

Figure 4.31 Damage size of GLARE 5 in terms of impact energy

The impact energy can be used as the scale parameter for impact damage. Figure 4.31 provides the damage size in terms of impact energy. A linear relationship between the square root of damage area and impact energy is shown for GLARE 5. The damage area increases slower in thicker GLARE 5 than in thinner GLARE 5 along with the increasing of the impact energies.

4.1.5 Effects of temperatures

Mechanical properties of materials usually change with the environmental temperatures, so the impact responses may vary with temperatures. In this section, GLAREs are investigated under different temperature using the environmental chamber equipped in the impact tester. All specimens were kept in the chamber for about 30 minutes after the desired temperature had reached so that there was no temperature gradient effect during the test. Only GLARE 5(3/2) were tested in the full temperature range (-51°C and up). The results show that GLARE 5 was significant soft once the temperature increases to 150°C and lost the ability for bearing weight. Table 4-5 gives the impact properties of GLARE 5 (3/2) when subjected to 30-joule impact within a temperature range from -51°C up to 120°C. There was no manifest change of impact responses within the above temperature range. The force-time history curves are depicted in Figure 4.32 and damage patterns are shown in Figure 4.33 for GLARE 5(3/2) subjected to 30-joule impact under different temperatures. From Table 4-5, there is no visible crack observed when temperature is lower than -40°C or higher than 85°C. Further cross-sectional micrographs (Figures 4.20(b), 4.34 and 4.35) indicate that GLARE 5 provides higher impact resistance under lower temperatures (-40°C and lower) while 88°C impact test gives almost identical cross-sectional micrograph with room temperature test (25°C). More tests were conducted for GLARE 5(3/2) with different impact energies (Figures 4.36, 4.37) and other kinds of GLARE were also investigated under lower temperatures (Figures 4.38-4.40). All impact test results imply that temperature effect, if any, is not significant to impact responses of fiber-metal laminates.

Table 4-5 Impact properties of GLARE 5 (3/2) under various temperatures (30-joule)

Temperature	Crack length in outer layer (mm)		Permanent Deflection (mm)
	Impacted side	Nonimpact side	
-60°F (-51°C)	0	0	5.1
-40°F (-40°C)	0	0	5.2
-4°F (-20°C)	0	7	5.4
77°F (25°C)	0	10	6.0
140°F (60°C)	0	8	5.9
180°F (82°C)	0	7	5.7
185°F (85°C)	0	0	5.4
190°F (88°C)	0	0	5.7
203°F (95°C)	0	0	6.0
248°F (120°C)	0	0	5.8

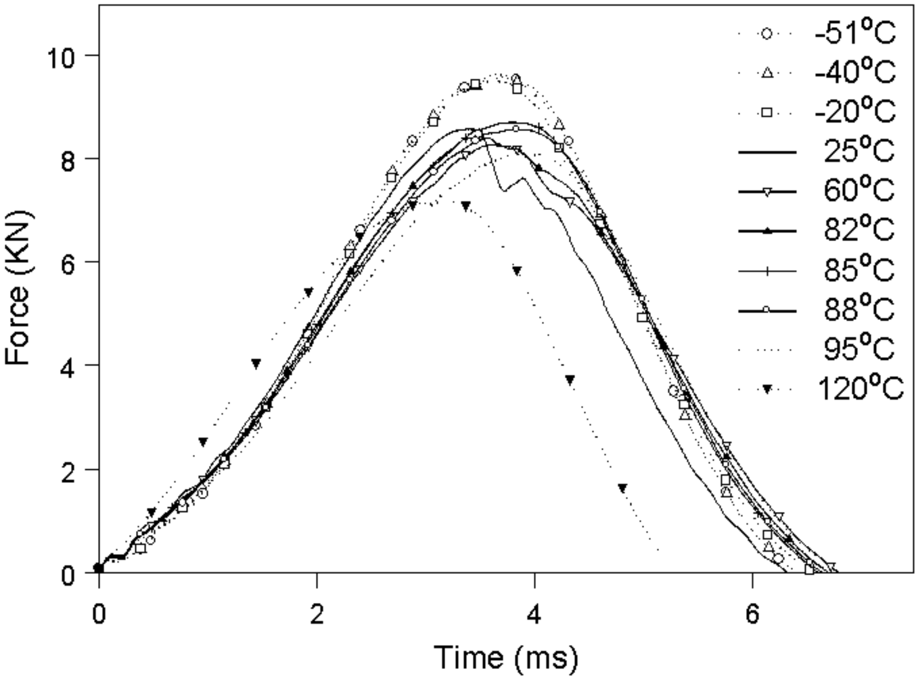

Figure 4.32 Force-time historic curves of GLARE 5(3/2) subjected to 30-joule impact

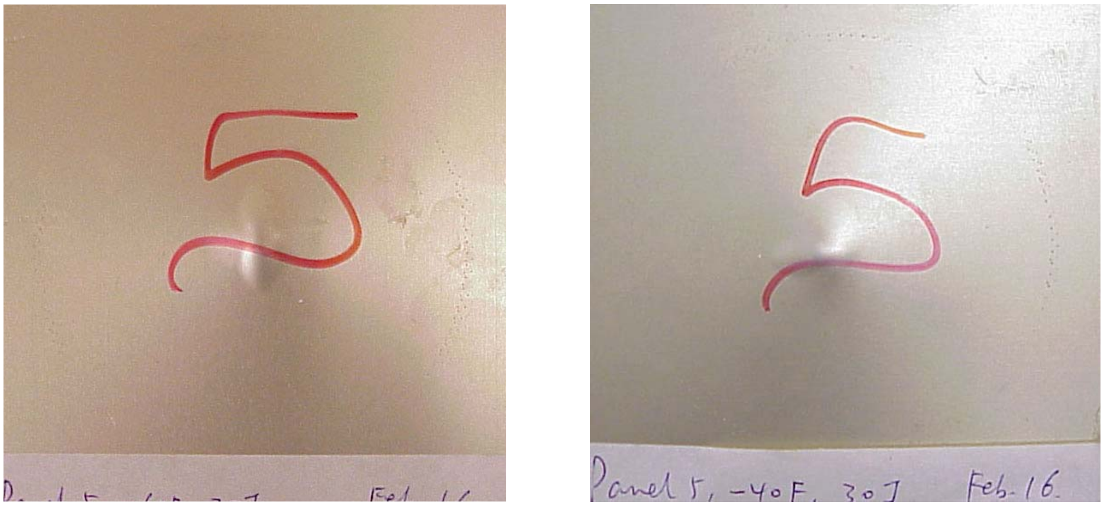

-51°C -40°C

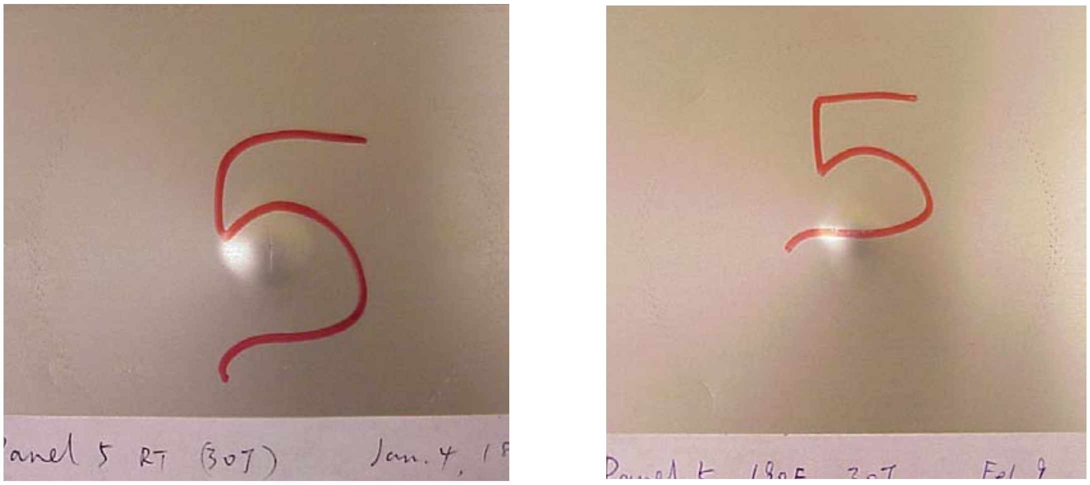

25°C 88°C

Figure 4.33 Damage patterns of GLARE 5(3/2) subjected to 30-joule impact

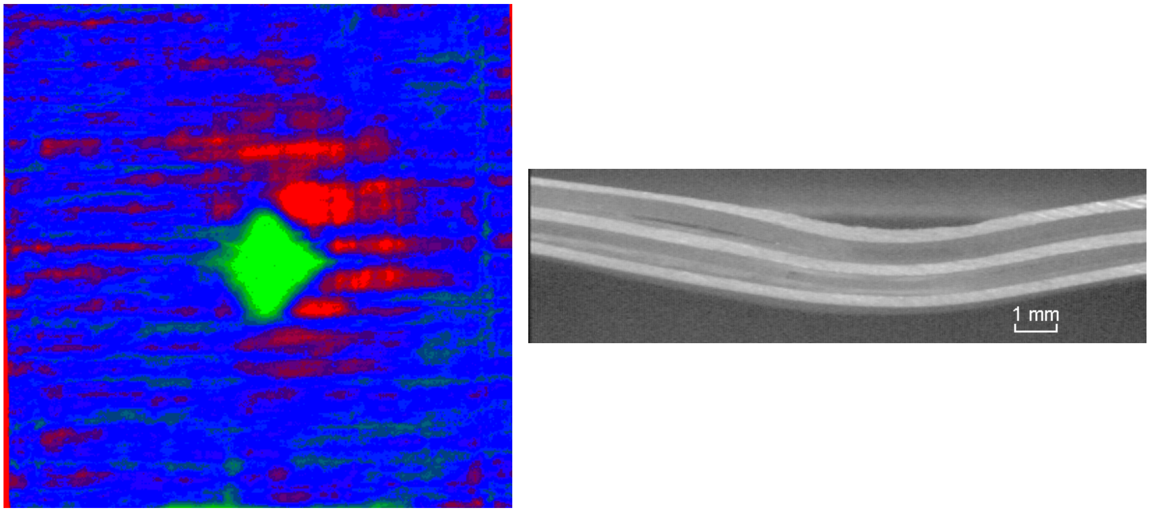

Figure 4.34 C-scan and cross-sectional micrograph of GLARE 5(3/2) subjected to 30-joule impact under -40°C (-40°F)

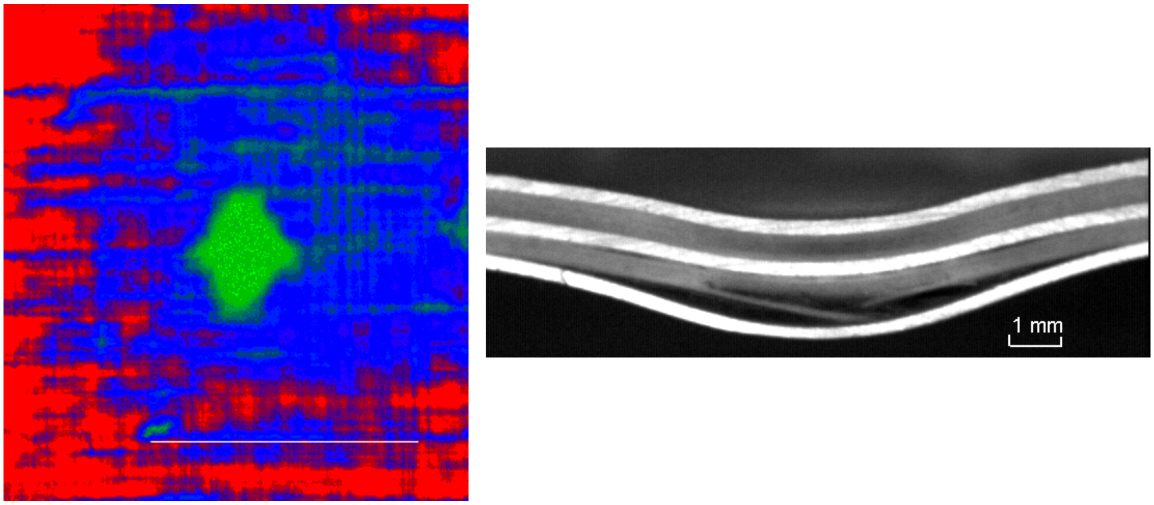

Figure 4.35 C-scan and cross-sectional micrograph of GLARE 5(3/2) subjected to 30-joule impact under 88°C (190°F)

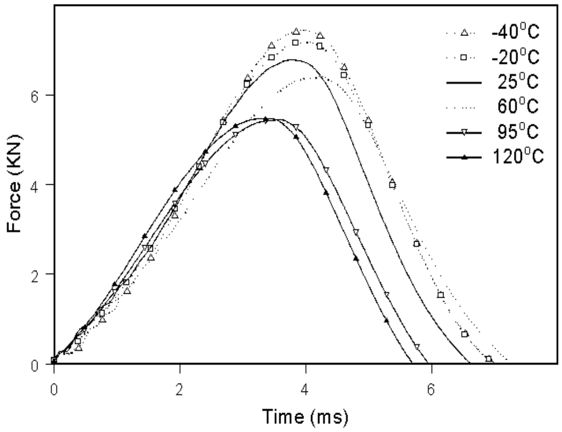

Figure 4.36 Force-time curves of GLARE 5(3/2) subjected to 20-joule impact

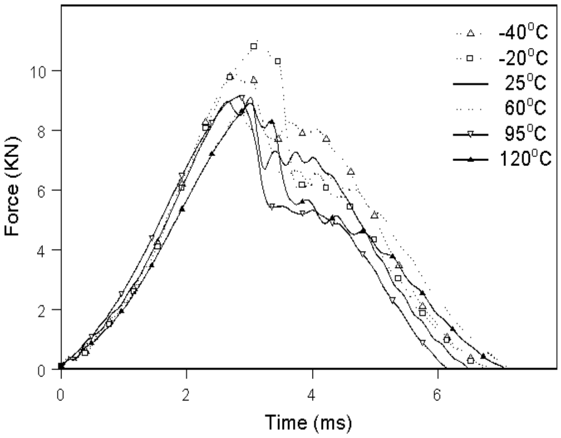

Figure 4.37 Force-time curves of GLARE 5(3/2) subjected to 40-joule impact

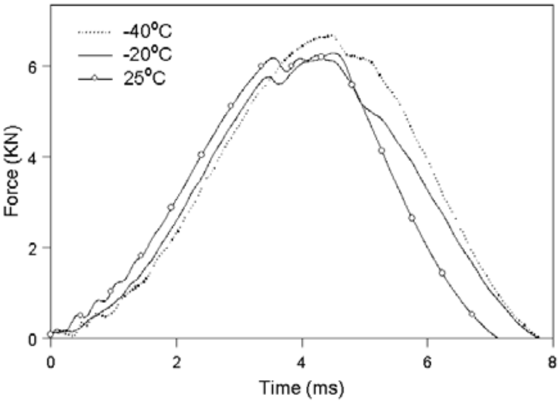

Figure 4.38 Force histories of GLARE 3 (20-joule impact)

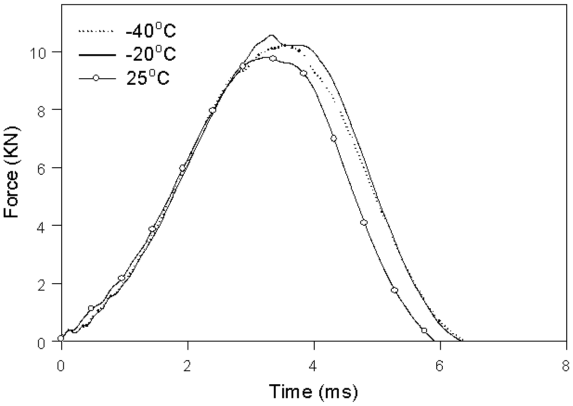

Figure 4.39 Force histories of CCNY C (40-joule impact)

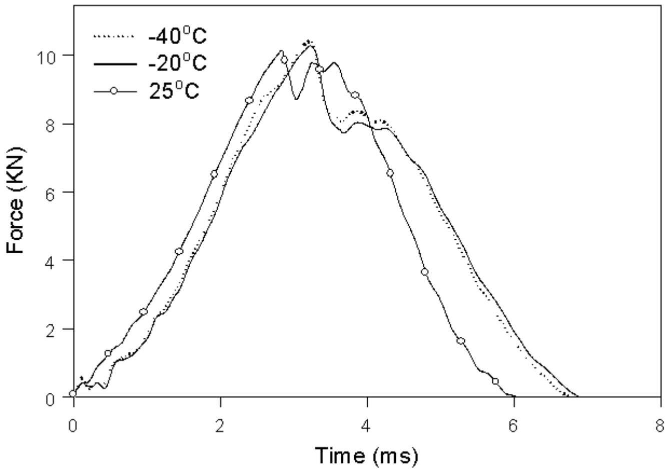

Figure 4.40 Force histories of CCNY D (40-joule impact)

4.1.6 Effects of geometry of impactor

Besides material properties of target and temperatures, characteristics of impactor, such as materials, mass and geometry of impactor, can also affect the impact responses. In this study, different impact tup inserts were used to investigate the impact responses. Table 4-6 lists all the impact tup inserts used.

Table 4-6 Impact Tup inserts

IMPACTOR NO.	SHAPE	MASS (g)
1	0.625 inch (16 mm) Diameter Hemispherical	130
2	1” (25.4 mm) Diameter Hemispherical	250
3	2” (50.8 mm) Diameter Hemispherical	825
4	2” Spherical Radius Tup Insert (4” spherical diameter on 2” diameter body)	850
5	0.5 inch Spherical Diameter Insert on 5/8 inch diameter body	140
6	1.5 inch Diameter Hemispherical	485
7	1 inch Conical Diameter Tup Insert	445
8	2” Spherical Radius Insert (4” spherical diameter on a 1.5” diameter shank)	850
9	10 mm Diameter Flat Face (Cylindrical) Tup Insert	80
10	Charpy Tup Insert ($\frac{7}{8} \times \frac{3}{16}$ inch)	150
11	Charpy Tup Insert ($\frac{3}{4} \times \frac{1}{8}$ inch)	130
12	0.5” Radius Tup Insert ($\frac{9}{8} \times \frac{1}{2}$ inch)	200

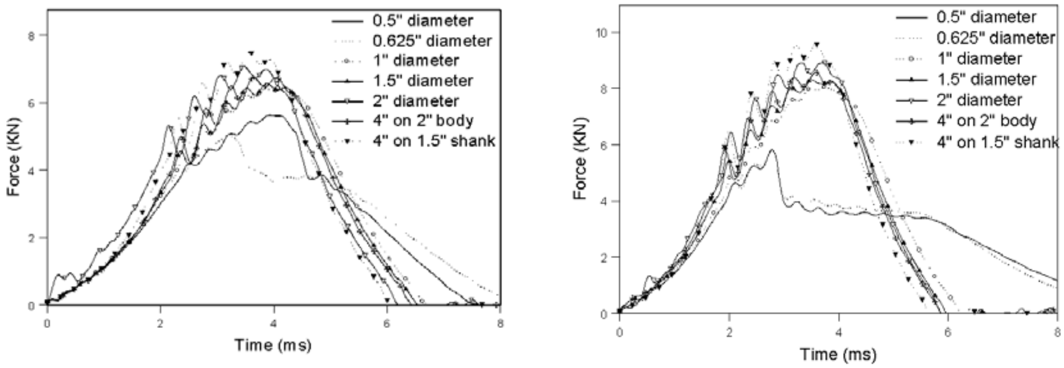

(a) GLARE 2 under 20-joule impact (b) GLARE 2 under 30-joule impact

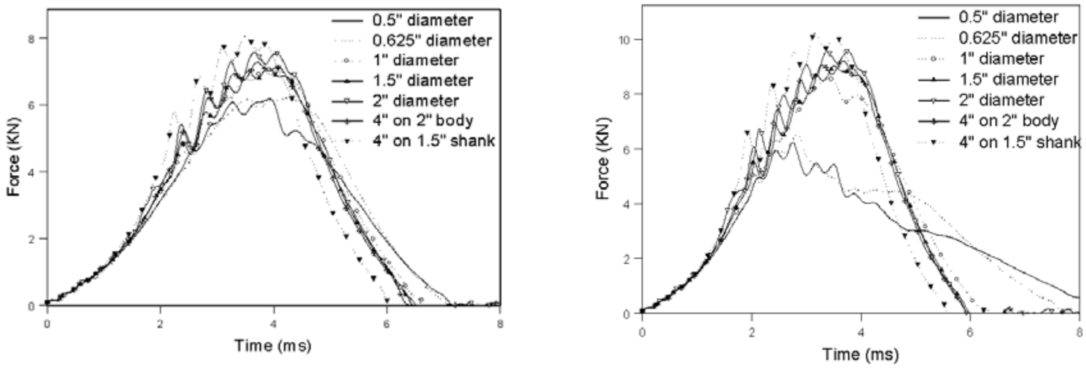

(c) GLARE 3 under 20-joule impact (d) GLARE 3 under 30-joule impact

Figure 4.41 Impact force histories of GLARE 2 and GLARE 3

First, hemispherical indenters with different diameters (from 0.5 inch up to 4 inches) were adopted to conduct impact tests on GLARE 2 and GLARE 3. Figure 4.41 shows the impact force histories of GLARE 2 and GLARE 3 corresponding to various sizes of indenters under 20 and 30-joule impact, respectively. Optical pictures were taken from impacted specimens and shown in Figures 4.42 and 4.43 for 30-joule impact. Severe localized damages around impact center were induced through small indenters (0.5” and 0.625” in diameter) whereas no significant local damages were found once the diameter of indenters went beyond 1 inch. For larger indenters, the impact forces were likely increasing slightly along with the increasing of the diameter of indenter. This is probably because of the larger contact area when larger indenter was used. GLARE 3 provides higher maximum impact force than GLARE 2 under the same test condition because of the higher stiffness of GLARE 3. The energy was dissipated through severe local damage (fracture, delamination and plastic dent) for impact with small indenters, while more energy was absorbed through global deformation when larger indenters were used. Further investigation through ultrasonic C-scan and cross-sectional micrographs can provide more details of impact damages. The results from C-scan and cross-sectional micrographs are also depicted in Figures 4.42 and 4.43 for GLARE 2 and GLARE 3 subjected to 30-joule impact, respectively. Through-transmission techniques were adopted using 25 MHz transducers and the through-thickness damage zones were detected successfully.

In general, the damage zone in GLARE 3 is smaller than in GLARE 2 under the same impact condition. More damage information can be found from the cross-sectional micrographs cutting through the impact center. For GLARE 2, there was no severe damage induced when the indenter was larger (1.5” diameter or larger); a visible crack only in the nonimpact outer aluminum layer is observed with 1” indenter; while severe through-thickness cracks occur when 0.625” diameter indenter was used. There was no obvious delamination observed in GLARE 2. On the contrary, for GLARE 3, only delamination between the nonimpact outer aluminum layer and adjacent glass-epoxy layer was induced from 1.5” diameter indenter; delamination and crack in the nonimpact outer aluminum layer happened when 1” diameter indenter was adopted; significant cracks through the whole thickness and delamination could be induced while the diameter of indenter was reduced to 0.625”. For both GLARE 2 and GLARE 3, all the cracks in aluminum layers showed a 45° angle relative to the tensile direction, indicating the fracture was ductile.

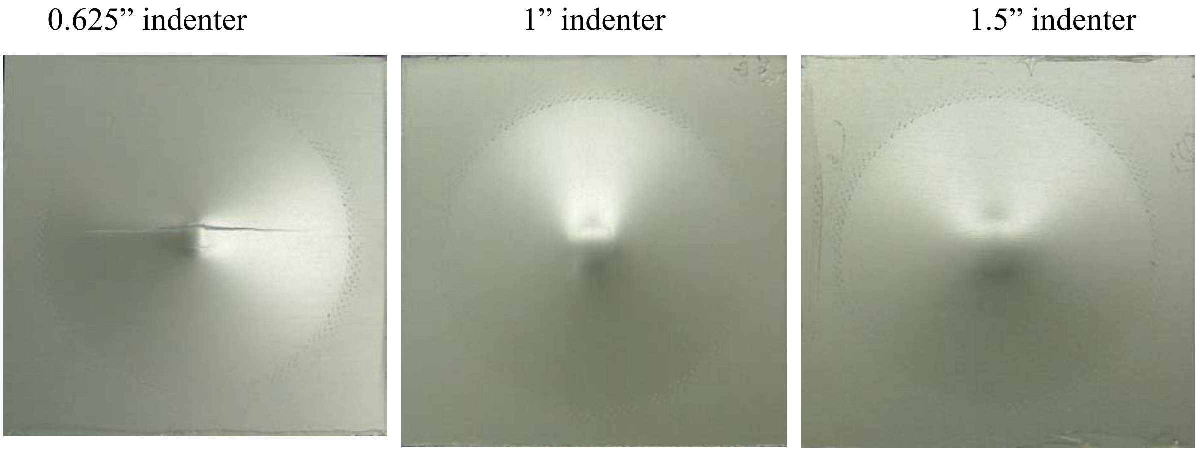

Optical pictures

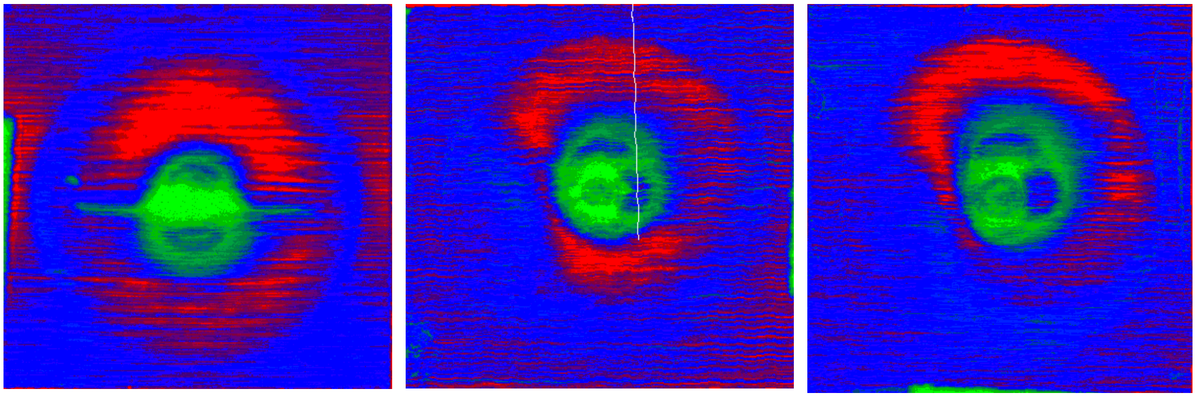

Ultrasonic C-scans

Cross-sectional micrographs

Figure 4.42 Damage patterns of GLARE 2 under 30-joule impact

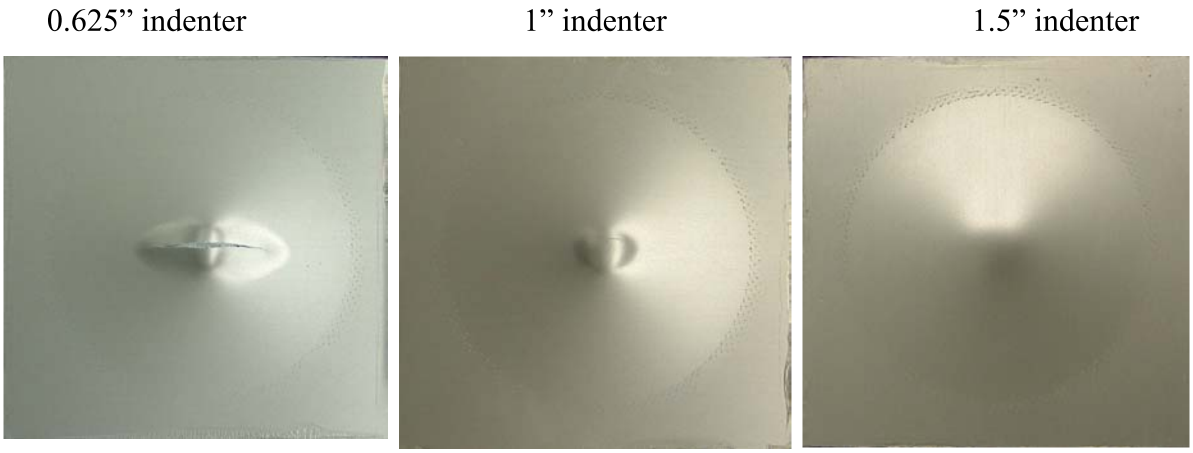

(a) Optical pictures

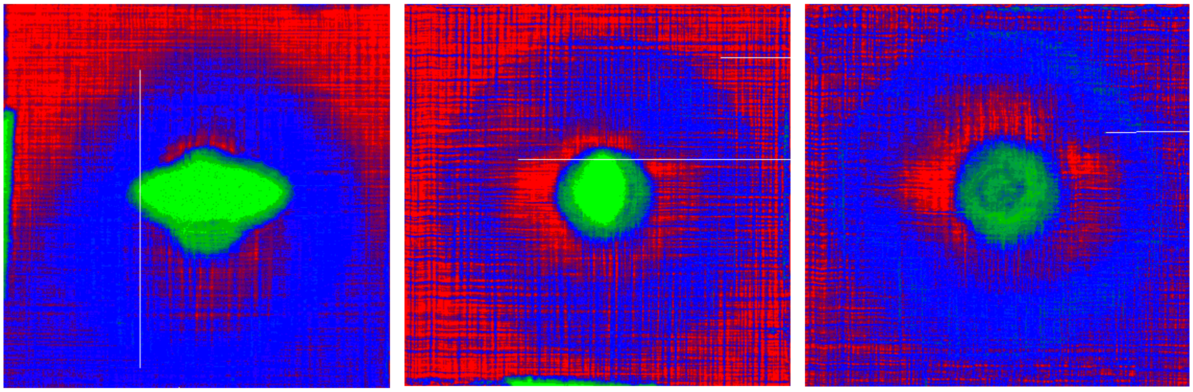

(b) Ultrasonic C-scans

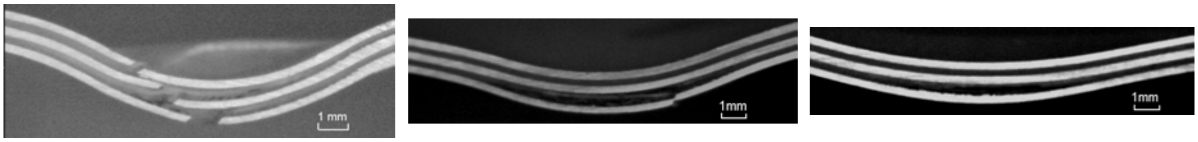

(c) Cross-sectional micrographs

Figure 4.43 Damage patterns of GLARE 3 under 30-joule impact

It is worth noting that the conventional through-transmission technique, which uses two flat transducers (unfocused), could not provide a clear C-scan image because of the larger diameter of ultrasonic signal beam. Hence, a modified through-transmission technique using a flat transmitter and a focused receiver was adopted in this study [77].

Figure 4.44 shows the comparison of C-scans from conventional through-transmission and above modified through-transmission for the same damaged specimen. The modified through-transmission C-scan picks up more details of damage and material configurations. Hence all C-scan images were conducted by the modified through-transmission in current study except special stated.

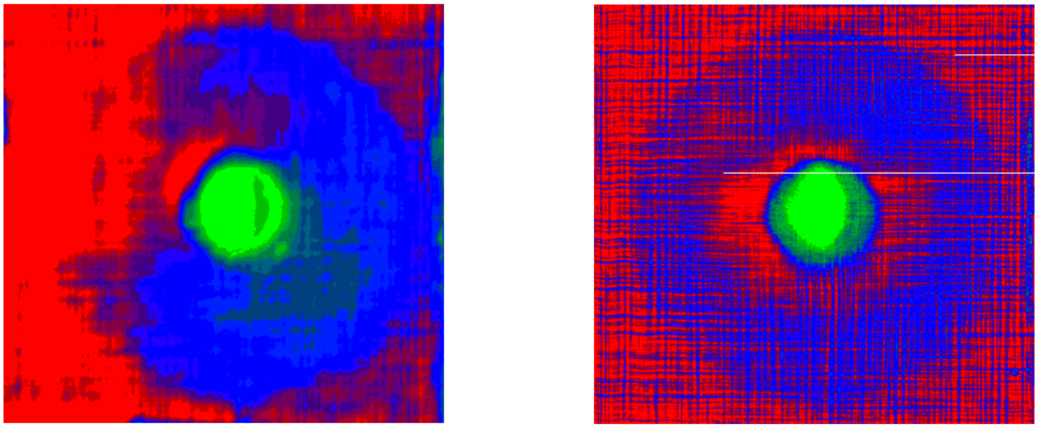

Figure 4.44 Comparison of C-scans (Left: Flat transmitter and receiver; Right: Flat transmitter with focused receiver)

In this study, three different line-like Charpy indenters were chosen to conduct impact tests on fiber-metal laminates (Table 4-6). Figure 4.45 shows the impact force histories of GLARE 2 subjected to 30-joule impact with indenters paralleled to the fiber direction (0°). The corresponding optical photographs are shown in Figure 4.46. Again, more severe local damages occurred with smaller indenter whereas larger global deformation induced when larger indenter was used. In details, a 0.75” by 0.125” indenter caused completely penetration; through-thickness cracks were induced from a 0.875” by 0.1875” indenter; and no visible cracks were observed when impacted by a 1.125” by 0.5” indenter.

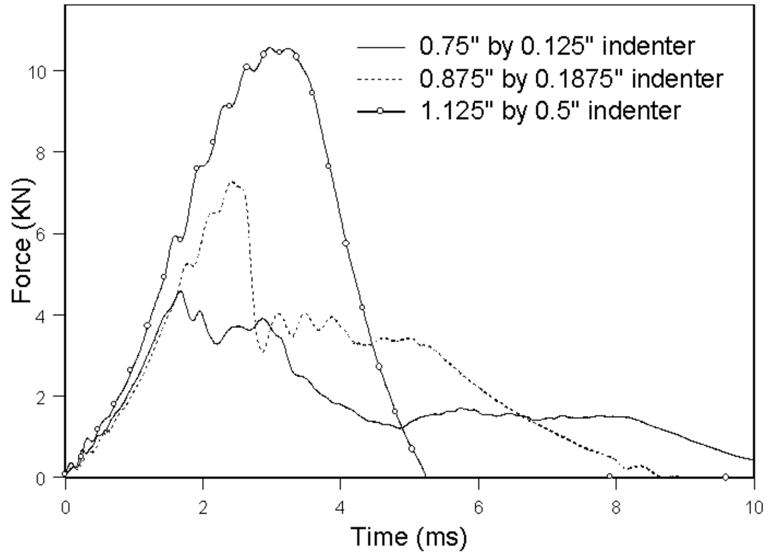

Figure 4.45 Impact force histories of GLARE 2 subjected to 30-joule impact (Charpy indenters, 0°)

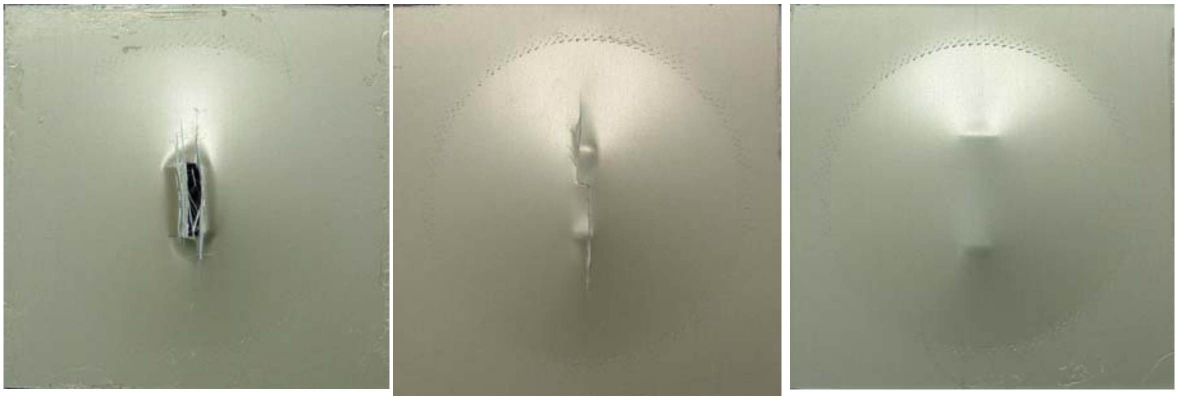

0.75” by 0.125” indenter 0.875” by 0.1875” indenter 1.125” by 0.5” indenter

Figure 4.46 Optical photographs of GLARE 2 subjected to 30-joule impact (Charpy indenters, 0°)

When a line-like indenter was adopted, damage patterns might vary with the relative angle between the indenter and fibers. A 0.875” by 0.1875” Charpy indenter was used to investigate the effect of above relative angles on GLARE 2 and GLARE 3. Only 30-joule impact results are presented. For GLARE 2 (aluminum with unidirectional glass-epoxy), three different relative angles were chosen, i.e. 0°, 45° and 90°. Only two different relative angles (0° and 45°) were adopted for GLARE 3 (aluminum with 0°/90° angle-ply glass-epoxy).

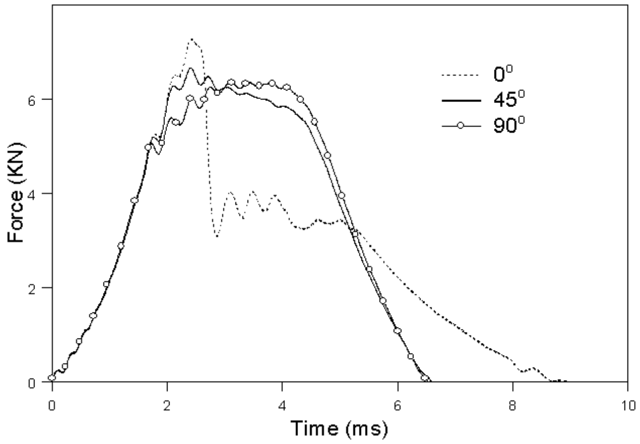

(a) Impact force histories

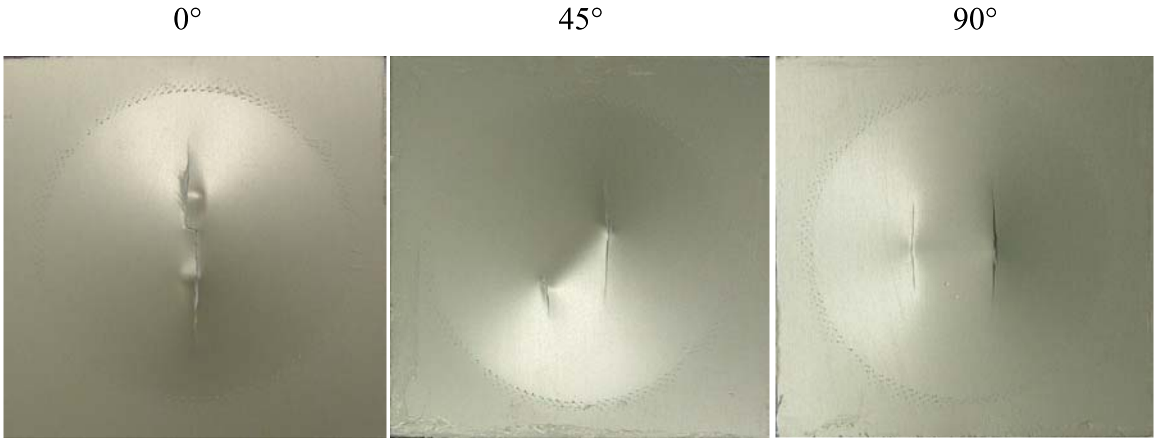

(b) Optical photographs

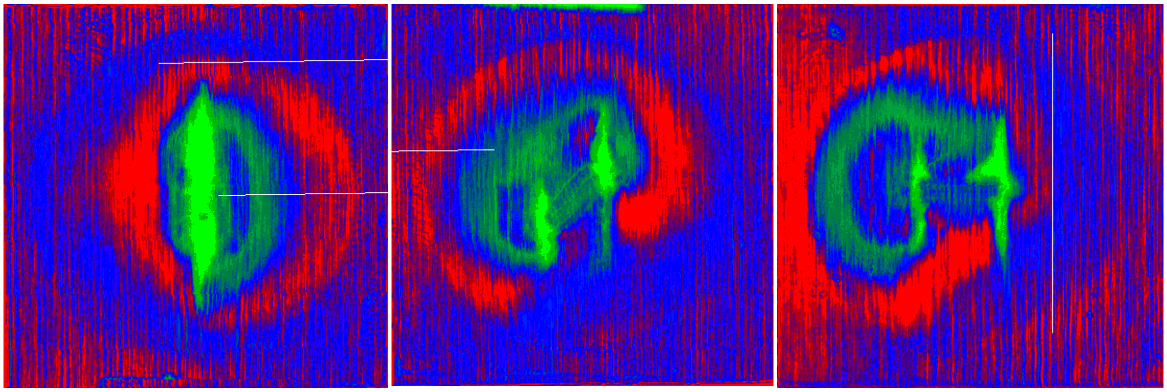

(c) Ultrasonic C-scans

Figure 4.47 The effect of relative angles between the indenter (0.875” by 0.1875”) and fibers on GLARE 2

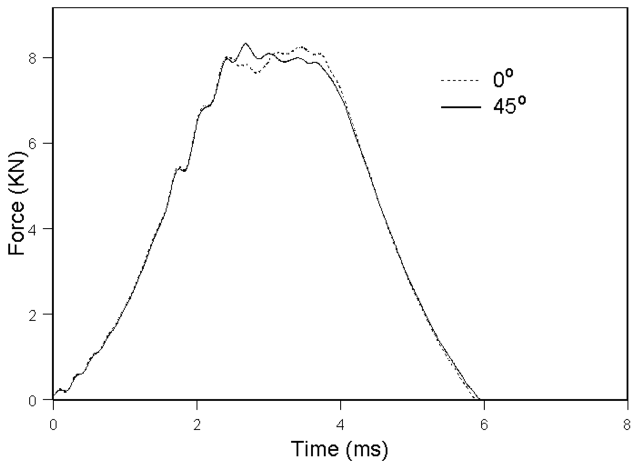

(a) Impact force histories

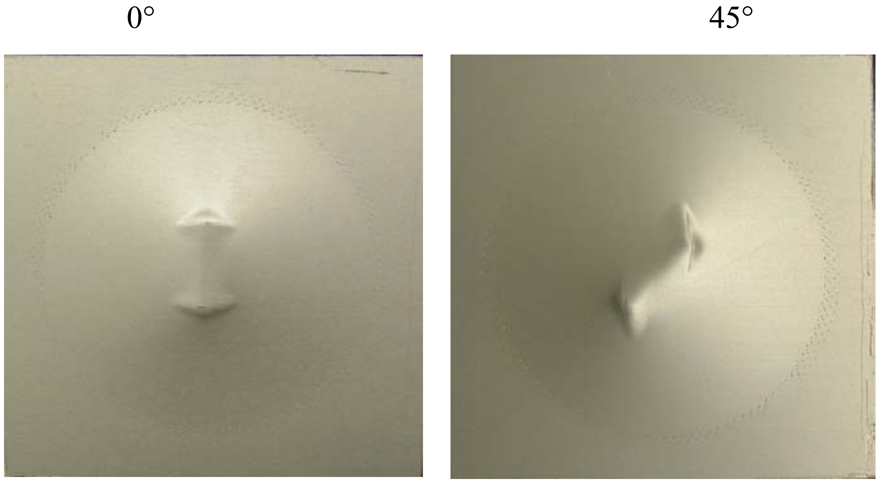

(b) Optical photographs

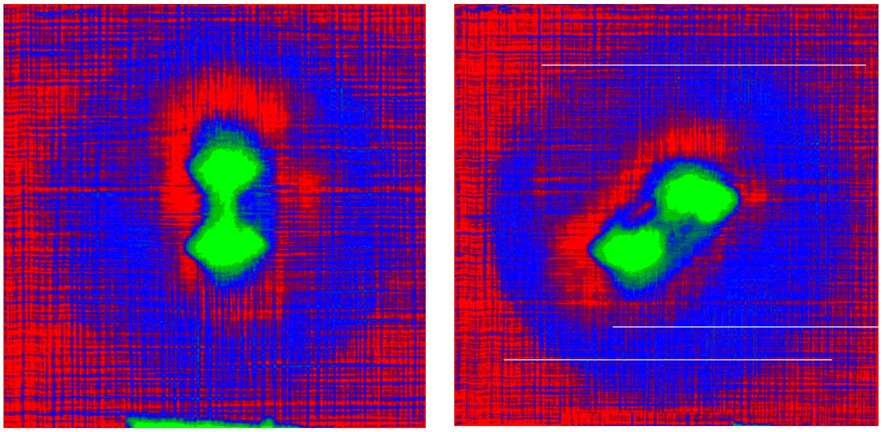

(c) Ultrasonic C-scans

Figure 4.48 The effect of relative angles between the indenter (0.875” by 0.1875”) and fibers on GLARE 3

The impact force histories, optical photographs and ultrasonic C-scans are presented in Figure 4.47 and Figure 4.48 for GLARE 2 and GLARE 3, respectively. As seen in Figure 4.47, there were two through-thickness cracks starting from the two tips of indenter and propagating along the direction of fibers in GLARE 2 when subjected to line-like impact no matter what the relative angles were. From Figure 4.48, two small visible cracks appeared at the two tips of indenter for both of 0° and 45° impact in GLARE 3 with two impact force histories were almost identical. Both optical and C-scan images manifest that there is no significant effect by changing the relative angle of indenter and fibers for GLARE 3. On the other hand, GLARE 3 provides a higher impact resistance than GLARE 2 subjected to line-like impact.

4.2 Summary

From above discussion, some conclusions can be drawn for fiber-metal laminates subjected to low velocity impact.

1. GLARE 1 (consists of glass-fiber) possesses higher impact damage tolerance than ARALL 3 (consists of aramid-fiber).
2. The impact resistance of GLARE can be improved by using more ductile aluminum alloy as constituent materials.
3. GLARE made of unidirectional fibers offers the worst impact damage resistance; followed by 0°/90° cross-ply, while GLARE consist of 45° plies shows the best resistance to impact.
4. Increasing the thickness can increase the impact resistance of GLARE 5. The threshold impact energy causing visible crack is parabolic proportional to the thickness.

5. Only the contour of entire damage area can be obtained using ultrasonic C-scan whereas more details of damage are provided through cross-sectioning techniques.
6. The damage stages along with the increasing of impact energies are as following: For thinner fiber-metal laminates, only delamination can be induced between the aluminum layer and the adjacent fiber-epoxy layer near the nonimpact side when subjected to lower energy impact; then, the nonimpact side aluminum fractures in accompany with delamination inside; through the thickness cracks occur under higher energy impact. For thicker FMLs, delaminations occur near the impact side at relatively lower impact energy. More severe damage including the crack in the outer aluminum sheet and fiber breakage in composite layer is induced on the nonimpact side when higher impact energy is introduced.
7. The impact energy can be used as a scale parameter of damage size.
8. Temperature does not significantly affect the impact responses of GLARE.
9. More severe local damages appear with smaller indenters whereas larger global deflection occurs if larger size indenters are used, which indicate the energy is dissipated mainly through delamination and cracks for impact with smaller size indenters while more energy may be absorbed due to large global deformation of fiber-metal laminates for impact with larger size indenters.

CHAPTER 5: FINITE ELEMENT SIMULATIONS

In recent years, finite element programs become so powerful that some complicated problems, such as contact, penetration, fracture and nonlinear problems, can be solved with high accuracy. In this study, low-velocity impact problems were analyzed using LS-DYNA program, which is a commercially available general-purpose finite element code for analysis of 3-D large deformation dynamic response of structures based on explicit-time integration scheme [107, 317]. Since fiber-metal laminates are hybrid composites, hence the numerical models required for analyzing such structures are usually very complex. For this reason, some preliminary studies were performed first on aluminum plates, cast acrylic (PMMA) plates and aluminum/acrylic sandwich panels. Finite element simulations on fiber-metal laminates were conducted thereafter.

5.1 Impact on Aluminum Plates

Figure 5.1 shows the schematic diagram of the low-velocity impact test set-up of pure aluminum 2024-T3 plates with a dimension of 101.6 mm×101.6 mm×1.6 mm (4”×4”×1/16”). The plate was clamped around a circle of 76.2 mm (3”) centered at the midpoint of the plate. The impactor is a 16 mm-diameter spherical impact tup with a weight of 6.1 kg. The finite element mesh of aluminum plate is given in Figure 5.2, which is consisting of Belytschko-Tsay shell elements. Since the elastic modulus of impactor is much higher than the target plate, the impactor is assumed to be made of rigid material. Because of symmetry only one quarter of the whole specimen is modeled. To simulate the impact event, proper boundary condition must be adopted. Four different of boundary conditions are chosen for this study, i.e. fixed, pinned, sliding and rollered (Figure 5.3).

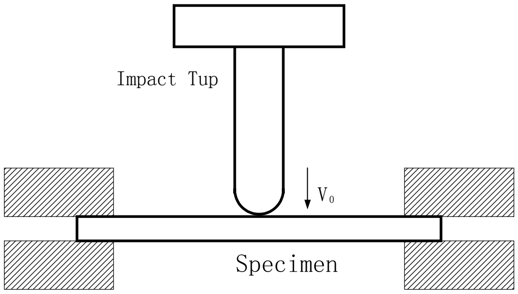

Figure 5.1 Schematic diagram of the low-velocity impact test set-up.

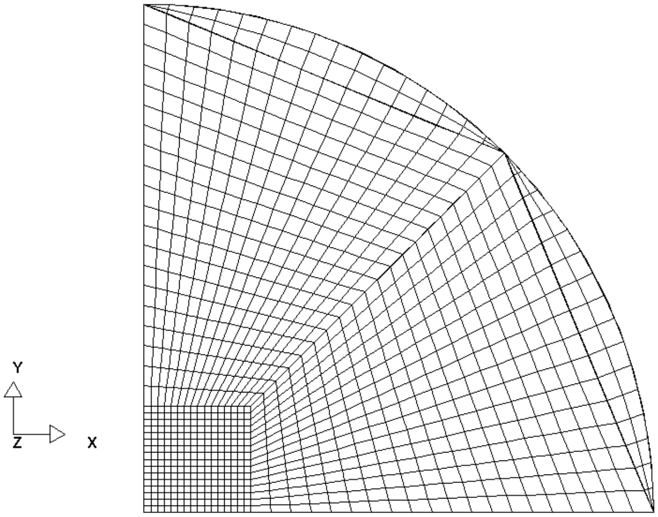

Figure 5.2 A typical finite element mesh

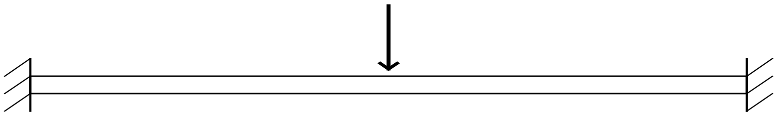

(a) Fixed

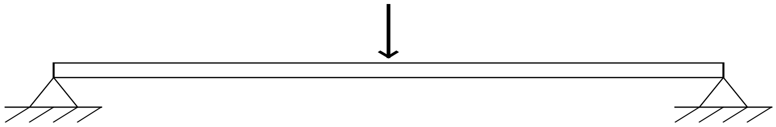

(b) Pinned

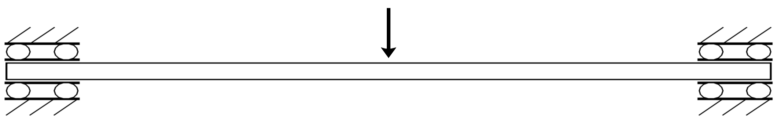

(c) Sliding

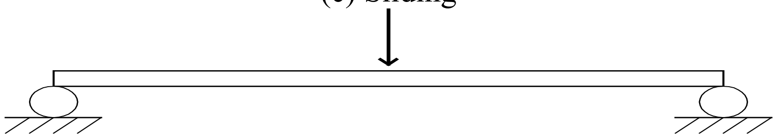

(d) Rollered

Figure 5.3 The boundary conditions.

Another important factor, which can affect the numerical results, is the mechanical properties of material. In this simulation, the aluminum 2024-T3 panel was assumed elastic first and then considered as bilinear. The mechanical properties of aluminum are listed in Table 5-1.

Table 5-1 Mechanical properties of aluminum 2024-T3

Density	Young's modulus	Yield strength	Tangent modulus for bilinear model
2790 kg/m^3	72 GPa	359 MPa	520 MPa

Only the 10-joule impact case is simulated using the above model. Both results from LSDYNA calculations and the experimental test are plotted in Figure 5.4. As observed from the experimental, there are no cracks but plastic deformation in the aluminum specimen under such this testing condition. As shown in Figure 5.4, a huge error exists if the elastic material model is adopted. On the other hand, the bilinear material model, regardless which boundary condition is assumed, always gives better simulation result. Among the four boundary-condition cases, it seems that the sliding boundary condition fits the test result best.

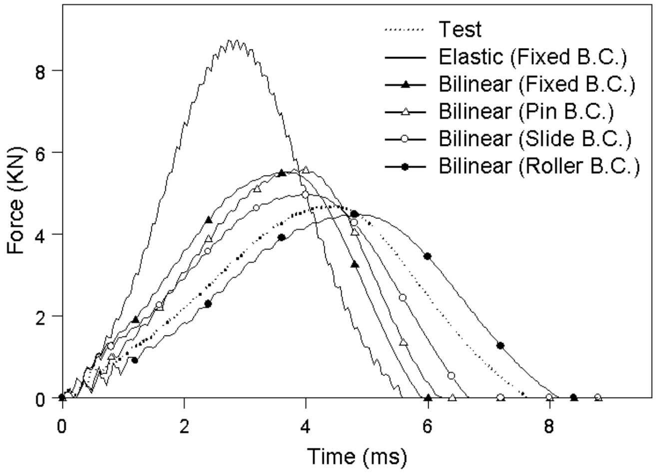

Figure 5.4 Impact force histories of various material models and boundary conditions.

The time histories of impact force and absorbed energy from sliding boundary condition case are shown in Figure 5.5. The energy partition (Figure 5.6) indicates that the kinetic energy of the aluminum specimen can be neglected, which means quasi-static analysis may be enough for low velocity impact. That is, the portion of kinetic energy of the impactor is mainly consumed as the strain (internal) energy and plastic work in aluminum as well as the sliding friction at the impactor/aluminum contact surface. It must be noted that none of above boundary conditions can simulate exactly the real-life boundary condition in experiment. More accurate results may be obtained by using more precise material model and improved conditions at the clamped boundary and the contact surface.

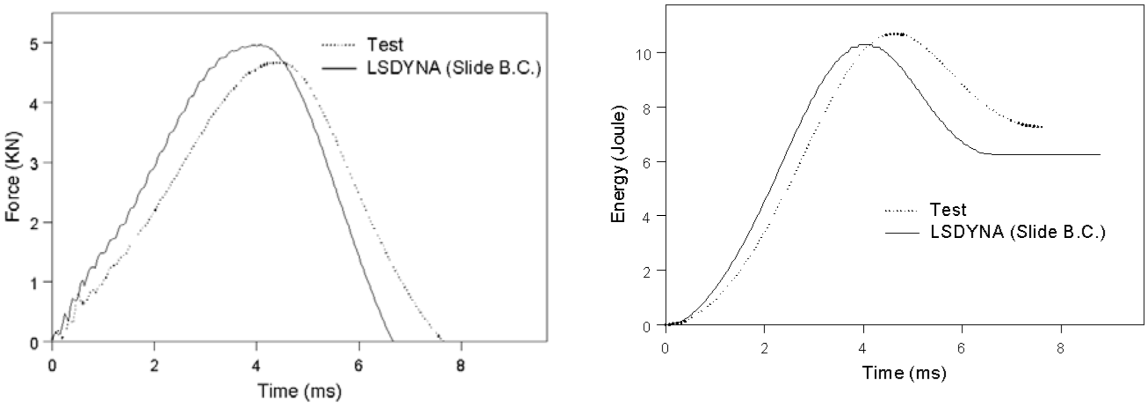

(a) Impact force histories (b) Absorbed energy histories

Figure 5.5 Simulation results using the sliding boundary condition.

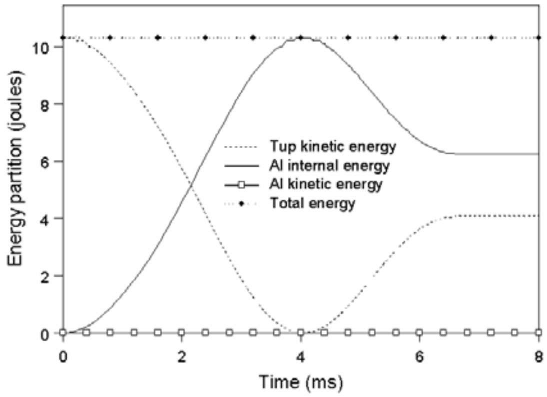

Figure 5.6 Energy partition from LS-DYNA simulation under 10-joule impact.

5.2 Impact on Cast Acrylic (PMMA) Panels

5.2.1 Introduction

Brittle materials, including glass, ceramics, rock and concrete, are widely used in many structures. It is needed to concern about the impact effect of foreign objects since such impact can occur during the service life of structures and may cause severe damage. The impact responses of brittle materials and structures have been studied extensively. In their earlier work, Tsai and Kolsky [326] studied the impact fractures in glass block in 1967. Knight, et al. [327] conducted the impact of steel ball on glass surfaces in 1977. Even up to recent years, because of its importance in engineering applications, many researchers still investigated the impact behaviors of brittle materials, e.g., Bouzid, et al. in 2001 [26], Han and Sun in 2000 [115], Gorham, Salman and Pitt in 2003 [343]. All these investigations showed similar cracks patterns in various impact speed ranges. Segreti, et al. [341] studied the impact effect on puncture of PMMA, where a direct impact technique of a projectile on specimen was applied and all tests indicated a strong influence of the puncture velocity on the mechanical response of PMMA. Chaudhri [342] conducted the impact breakage study on semi-brittle sphere using high-speed photography and showed that the cracks propagated in velocities up to 80% of the Rayleigh surface wave velocity of the sphere material.

For brittle materials, the major damage pattern is fracture. Hence fracture mechanics plays an important role for investigating the mechanical behavior under various loading conditions (Lawn, 1993 [328]; Fineberg and Marder, 1999 [329]). One of the main objectives in fracture mechanics is to predict the crack initiation and propagation in brittle materials. However, only a few simple cases can be solved analytically and most fracture problems require numerical approximations based on certain assumptions and criteria developed through fracture mechanics. The most powerful and most used numerical tool is finite element method [14]. The first step to study the fracture behavior is to establish a fracture criterion. There are two categories of fracture criterion, i.e. stress based [336] and energy based [246]. Vaughan [330] studied the crack propagation under mixed-mode loading condition by using the maximum-tensile-stress failure criterion. Andrews and Kim [332] pointed out that the threshold condition for fragmentation of the glass particles was governed by a critical Mises stress condition. For brittle materials, the predictions of crack initiation based on the maximum tensile stress criterion have been generally accepted [96]. To model the fracture propagation, the node-splitting technique has been predominant adopted in which the adjacent elements along a crack path are separated by splitting the duplicated nodes. The node-splitting technique reduces to a ‘node-release’ technique when a plane of symmetry is assumed and the crack propagates along the line of symmetry. Repetto, et al. [331] adopted a tension-shear cohesive-law model to separate element nodes along the crack trajectory in order to simulate the formation and propagation of cracks on fragmentation of glass rod. Because of the singularity of the crack tip, ‘infinite’ elements were used to cover the model boundary used by Jayaraman, et al. [134], which means a very fine mesh has to be applied and the computing cost is significantly high. A remeshing technique was developed with the node-splitting technique to decrease the number of element needed and to save the numerical calculation time. Tradegard, Nillson and Ostlund [335] studied the crack growth with a combination of remeshing and nodal relaxation using the commercial finite element code ABAQUS. Koenke, et al. [334] performed crack simulation on adaptive remeshing techniques. Cao and Zhang [333] provided an element-failure approach to simulate the crack growth in which cracked elements based on the average maximum principal stress criterion are removed from the whole element mesh as the element stiffness diminishes to zero. Beissel and co-workers [11] presented an element-failure algorithm to study the dynamic crack propagation, where the crack path was predicted through the energy release criterion.

The impact force was considered in many investigations. Basically the contact force was suggested in the classical Hertz's theory [340]. Yang and Sun [304] indicated that the Hertz's law was valid for quasi-static impact condition. Using a finite element code, Mahajan and Dutta [190] calculated the impact force under low velocity impact based on Hertz's contact law. Bittencourt and Creus [20] conducted finite element analysis of three-dimensional contact, in which the contact force was provided through the penalty method. The Lagrange multiplier technique can also give the contact force if the zero-penetration condition is adopted [14].

In this section, low-velocity impact tests on cast acrylic plates were carried out using the Instron-Dynatup drop-weight tester. The temperature effect was also investigated by changing the experimental temperature. A finite element model through LS-DYNA was developed to simulate the damage patterns of impact on cast acrylic based on the experimental results, where the maximum tensile stress criterion was adopted to capture the onset of crack initiation and the node-splitting technique was used to simulate the crack growth.

5.2.2 Experimental procedures and results

In this study, square cast acrylic (PMMA) specimens with a dimension of of 101.6 mm×101.6 mm×5.1 mm (4”×4”×0.2”) were used. Again, the plate was clamped around a 76.2 mm (3”) circle. Typical mechanical properties of the cast acrylic were listed in Table 5.2.

Table 5.2 Mechanical properties of acrylic

Density (kg/m^3)	Tensile Modulus (GPa)	Tensile Strength (MPa)	Fracture Toughness ($MPa\sqrt{m}$)	Glass Transition Temperature (°F)
1,190	2.24 ~ 3.24	55 ~ 76	0.7 ~ 1.6	195 ~ 220

Figure 5.7 shows some typical impact damage patterns of cast acrylic subject to the impact of a drop weight of 4.018 kg with impact velocities from 1.15 m/s up to 2.05 m/s. Only radial cracks occurred for low velocity impact whereas Hertzian cone crack were reported for static indentation [115, 328]. In general, five or six cracks were induced and propagated from the impact center to the clamp boundary under the above impact conditions. Bouzid, et al. [26] provided similar results for float glass plates subjected to low rate of loading. The corresponding time histories of impact force were plotted in Figure 5.8 for cast acrylic subjected to various impact velocities, i.e. 1.15 m/s, 1.68 m/s and 2.05 m/s, respectively. All force history curves showed a sudden drop at one particular point, which may indicate the onset of fracture. It was worth noting that the fracture occurred very suddenly during impact and may be explained through unstable dynamic fracture [14]. Such a crack can propagate at a velocity on the same order of elastic stress wave in the sample [14, 342]. For a thin plate, the propagation velocity of such a wave, called the plate wave speed c_p, is given by [337]:

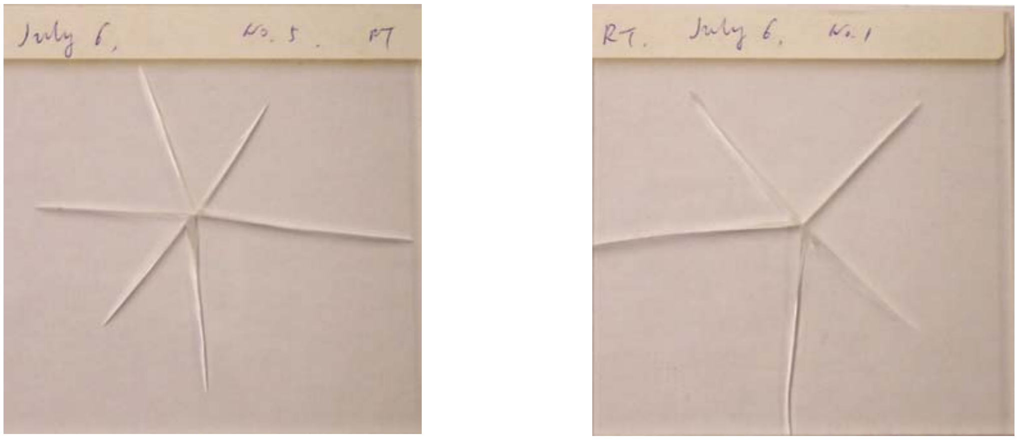

(a) 1.15 m/s impact (b) 2.05 m/s impact

Figure 5.7 Damage patterns of cast acrylics subjected to different impact velocities.

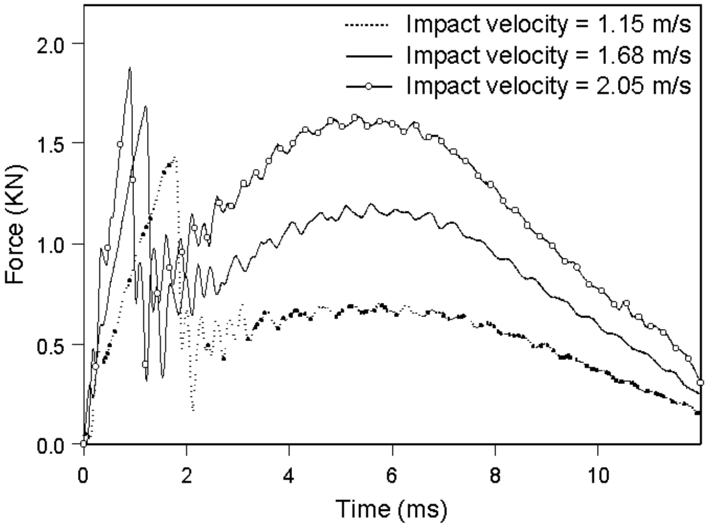

Figure 5.8 Force histories of impact with different velocities on cast acrylics.

$$c_p = \sqrt{\frac{E}{\rho(1-\nu^2)}} \tag{5-1}$$

For cast acrylic, this crack propagation velocity is about 1,680 m/s if Young's modulus is chosen to be 3 GPa, density 1,190 kg/m^3, and Poisson's ratio 0.33. In this study, it took about 23 μs for such a crack to traverse a length of 3.8 cm (1.5").

It's well known that there is a so-called glass transition temperature for glasses and polymers. This temperature indicates the transition from brittle to ductile [338]. As shown in Table, the glass transition temperature for cast acrylic is within the range of 195 to 220°F. To study the effect of temperature, a weight set of 6.75 kg was dropped from a 5” height (about 1.58 m/s) onto the afore-mentioned acrylic plate under different temperatures. Figure 5.9 showed the total crack length versus temperature. The sudden decrease in total crack length lay between 185°F and 205°F indicated that the occurrence of nil-ductile transition (i.e., the existence of the glass transition temperature). The force histories (the left side of Figure 5.10) manifested that cracks were induced at 185°F (the right side of Figure 5.10) whereas no crack occurred at 205°F.

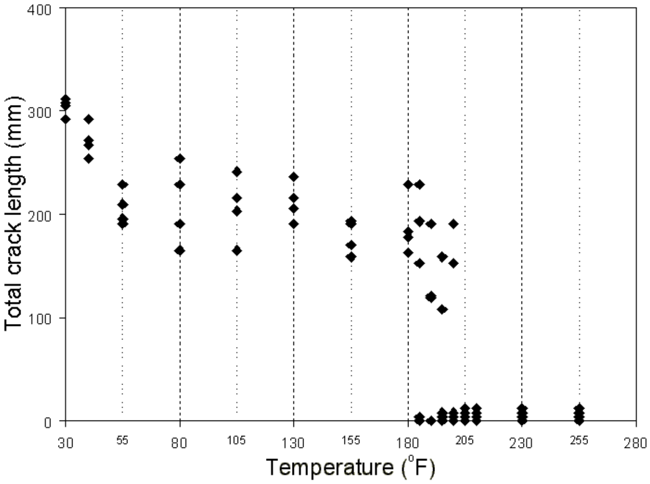

Figure 5.9 Temperature effect on total crack length in cast acrylic.

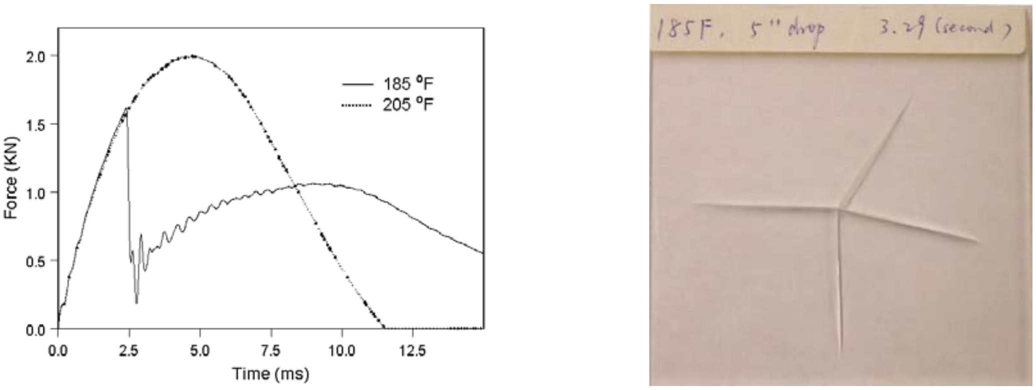

(a) Force histories

(b) Crack pattern for the 185°F case

Figure 5.10 Cast acrylics impacted at different temperatures with a 6.75 kg weight dropped from 127 mm (5”).

5.2.3 Theoretical models

The basic theory and assumption are stated as following.

5.2.3.1 Governing equations. The equilibrium equation of the impact problem usinf finite element method (see Figures 5.1 and 5.2) can be written as:

$$[M]\{\ddot{u}\}+[C]\{\dot{u}\}+[K]\{u\}=\{F\} \tag{5-2}$$

where $[M]$ is global mass matrix, $[C]$ is the damping coefficient matrix, $[K]$ is the stiffness matrix, $\{F\}$ is the external force vector, $\{\ddot{u}\}$, $\{\dot{u}\}$ and $\{u\}$ are the acceleration, velocity and displacement vectors, respectively. By neglecting the damping, the above equation can be rewritten as:

$$[M]\{\ddot{u}\}+[K]\{u\}=\{F\} \tag{5-3}$$

It should also be noted that in this study, the penalty method, which is available in LS-DYNA, is used to calculate the contact force.

5.2.3.2 Failure criterion. The damage pattern for cast acrylic due to low velocity impact is radial cracks. In this study, it is assumed that cracks occur when the following condition is met:

$$\sigma_t \geq S_t \tag{5-4}$$

where σ_t is the principal tensile stress and S_t is the maximum tensile strength.

5.2.3.3 Crack propagation. Once a crack is initiated, it usually propagates at a very high velocity. The assumed crack propagation speed was set to be $0.15c_p$, where the plate wave speed c_p is defined in Equation (5-1). In finite element method, the crack extension is shown schematically in Figure 5.11 using the so-called the virtual crack closure technique [319]. Here the nodal forces are decreased linearly with respect to the crack opening displacement during the virtual crack propagation period (see Figure 5.12).

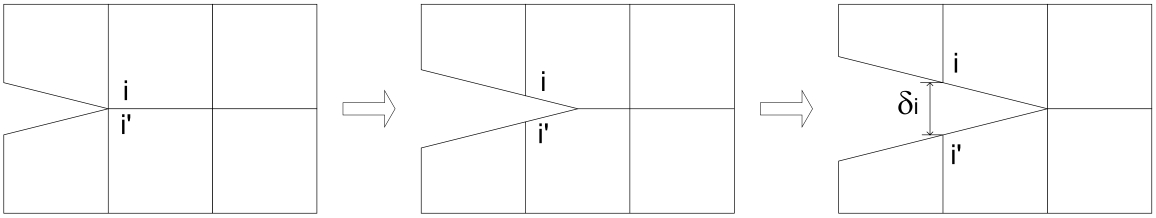

Figure 5.11 The dynamic crack extension procedure.

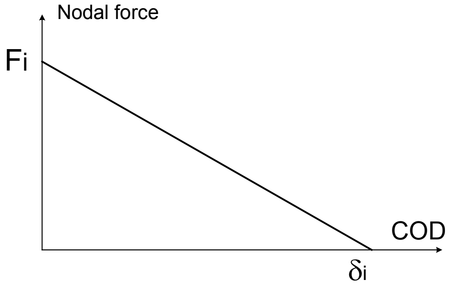

Figure 5.12 Nodal force releasing

The strain energy release rate of fracture via this virtual crack closure technique [319] is calculated in this study. Assuming that the energy absorbed in the process of a crack extension was equal to the work required to close the crack. Hence, the absorbed energy for crack opening between node *i* and *i′* can be described as:

$$W_i = \tfrac{1}{2} F_i \delta_i \tag{5-5}$$

The total absorbed energy for each step was equal to:

$$W = \sum W_i = \sum F_i \delta_i \tag{5-6}$$

If the new created crack surface area was *A*, the strain energy release rate can be calculated as:

$$G = {}^{W}\!\big/_{A} \tag{5-7}$$

5.2.4 Finite element simulations

In this research, both the steel impactor and the cast acrylic plate are modeled with 8-node solid elements. Because of the much higher elastic modulus of the steel impactor than that of the cast acrylic plate, the impactor is assumed to be rigid whereas the cast acrylic is elastic. First, the simulation was performed for the test of 2.05 m/s impact. Based on the experimental result, there were five cracks growing from the impact center to the clamped boundary. Thus, the whole cast acrylic plate was modeled by five equal pie-shaped portions linked together through tied “interfaces”. The boundary conditions of the above model are as following: fixed for the bottom clamped edge of cast acrylic and slide for the top clamped edge. To simulate the onset of fracture, the maximum tensile stress criterion was adopted with a tensile strength of 75 MPa for cast acrylic. The finite element meshes were drawn in Figure 5.13.

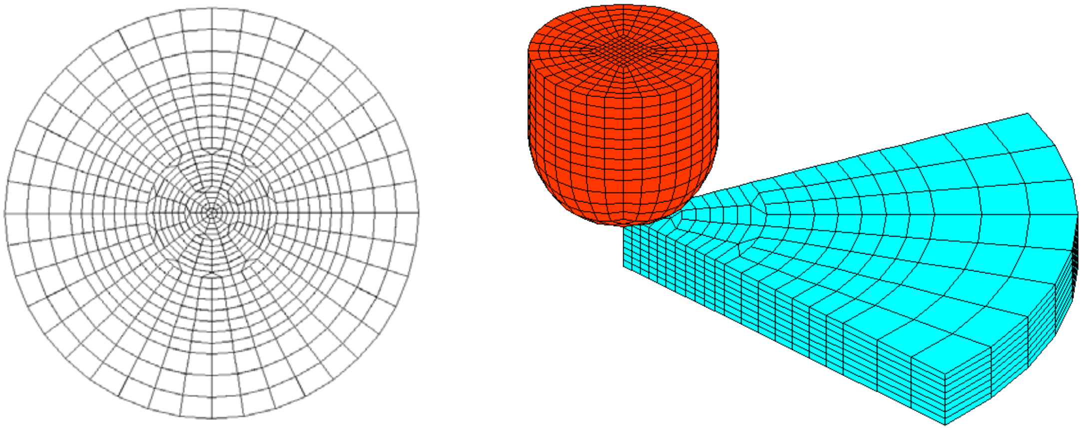

Top view of the cast acrylic plate

The 3-D view
(Note: only 1/5 of the cast acrylic is shown)

Figure 5.13 The finite element mesh.

Typical material properties in this simulation were listed in Table 5.3. From Equation (5-1), the crack propagation time is about 23 μs, which accounts for only around 0.15% of the total impact duration (about 15 ms). Due to such a short crack propagation time, the tied “interfaces” along the experimentally-determined crack propagation paths were released suddenly once cracks were initiated.

Table 5.3 Mechanical properties

Material	Density (kg/m^3)	Tensile Modulus (GPa)	Tensile Strength (MPa)	Poisson's ratio
Cast acrylic	1,190	3	75	0.33
Steel impactor	--------	200	---------	0.33

The number of layers of elements used to represent cast acrylic can affect the accuracy of the simulation result as well as the required computational power. In general, a minimum number of layers are required to reflect the bending-mode of deformation of a plate subject to drop-weight impact at center. In this study, cast acrylic plates were modeled with four, eight and sixteen layers of solid elements, respectively. Figure 5.14 showed force history plots for finite element simulations with an impact velocity of 2.05 m/s. The result indicates that eight-layer model is good enough for this low-velocity impact simulation. Thereafter all other simulations were made with eight layers of elements.

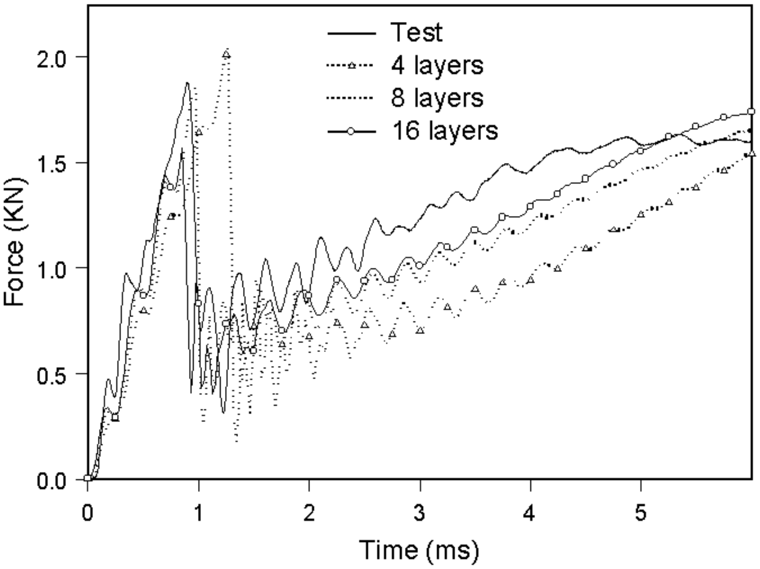

Figure 5.14 Effect of different layers of elements used in finite element simulations.

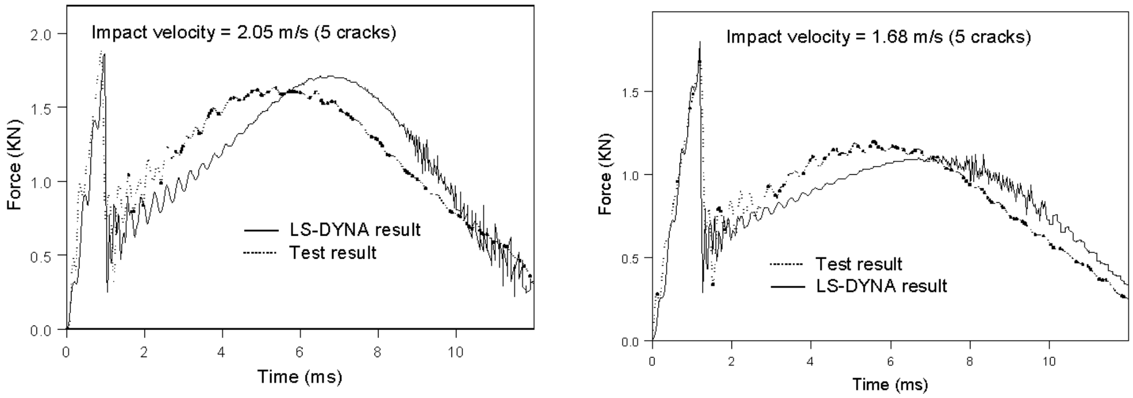

(a) v = 2.05 m/s, T = room temperature (b) v = 1.68 m/s, T = room temperature

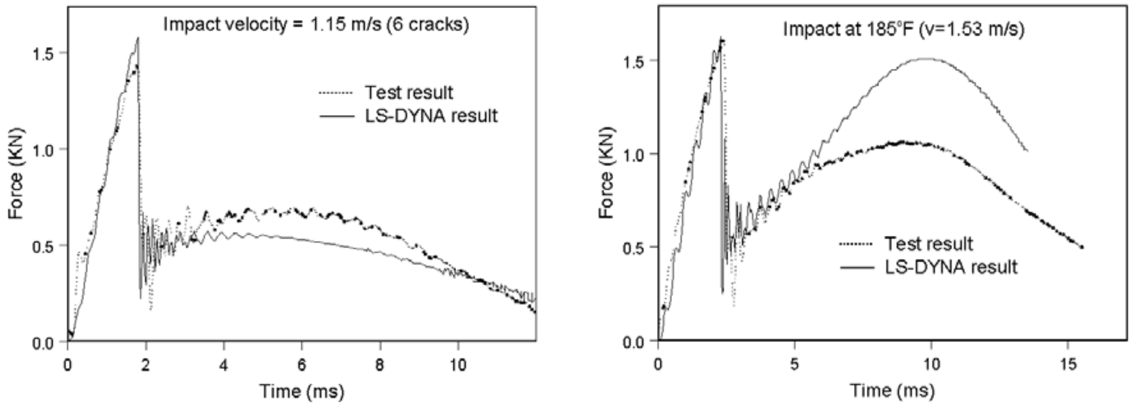

(c) v = 1.15 m/s, T = room temperature (d) v = 1.53 m/s, T = 185°F

Figure 5.15 Impact force histories of finite element simulation and experiment subject to different impact velocities at room and high temperatures.

The comparison of contact force histories for an acrylic plate subject to different impact velocities at room and high temperatures using finite element simulations with eight layers of elements and the corresponding experiment results are given in Figure 5.15. Some characteristic parameters were listed in Table 5.4. In order to obtain a better simulation for the 185°F test, as the one shown in Figure 5.15(d), a much lower Young's modulus of 1.7 GPa (*vs* 3 GPa for room-temperature tests) and a slightly lower tensile strength of 70 MPa (*vs* 75 MPa for room-temperature tests) were used for cast acrylic. This may be due to the "softening" effect of mechanical properties near the glass-transition temperature, which lies within the range of 195-220°F.

Table 5.4 Comparison between experiments and simulations

Impact velocity (m/s)	Testing temperature (°F)	Maximum force (kN)		Time to maximum force (ms)	
		Test	FE Simulation	Test	FE Simulation
2.05	room	1.88	1.86	0.90	0.98
1.68	room	1.69	1.80	1.20	1.20
1.15	room	1.44	1.58	1.70	1.80
1.53	185	1.61	1.63	2.40	2.27

To account for the finite (even though fact) crack propagation speed, an improved algorithm was carried out by releasing the crack interface stepwise to simulate the real crack propagation. The improved algorithm, called the stepwise releasing technique, is as following: At first the crack plane as observed from experiment was modeled by a group of node pairs. Each pair of the adjacent nodes were joined together using the option:

TIED_SURFACE_TO_SURFACE_FAILURE

which is available in LS-DYNA. The event of the acrylic plate impacted by a drop weight was then simulated by LS-DYNA with the nodal forces at each node pairs being recorded. The time and location of first crack initiation was identified by a strength-based failure criterion with an assumed failure strength of 75 MPa. Once the failure condition was reached, the corresponding node pairs at the failure location was released following the release rule illustrated in Figure 5.12, where crack propagation speed was set to $0.15c_p$ (see Equation (5-1)). This impact-fracture process was continued and the nodal forces of adjacent node pairs of the released node pair were monitored carefully. A node pair remained tied if their nodal forces were compression and released if in tension with the same releasing rule. The process was repeated until the crack arrested, i.e., no further node pairs were found in tension. Using this stepwise crack releasing procedure, the more realistic crack front contours were simulated.

It should be reported that the stepwise releasing technique is very cumbersome and time-consuming. Only one experiment ($v = 2.05$ m/s at room temperature) was simulated with this procedure. The experimental crack surface is photographed in Figure 5.16(a) whereas the propagating crack front obtained by the finite element simulation is drawn in Figure 5.16(b), which indicates the two results are in good agreement. Note that there is no any crack opening at upper portion of crack surface in the experimental result, Figure 5.16(a), which was also predicted by the finite element simulation using the stepwise releasing technique, Figure 5.16(b).

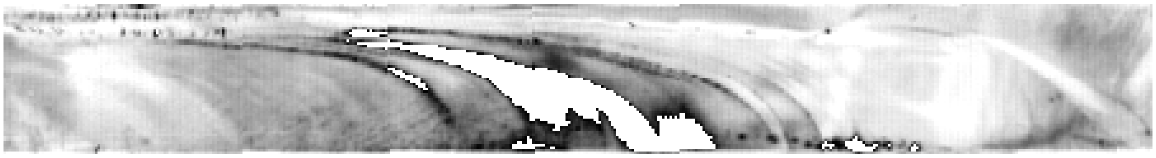

(a) Photograph of the experimental crack surface

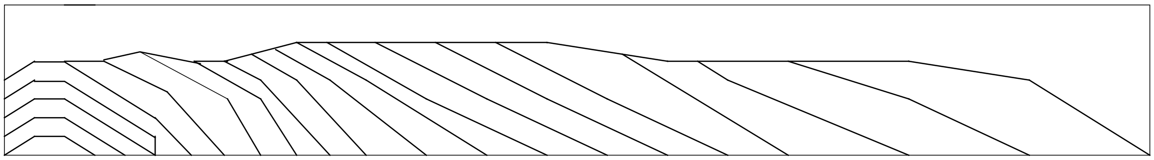

(b) Finite-element simulated contours of the propagating crack front

Figure 5.16 The experimental and finite element simulated propagating crack fronts.

Impact force histories calculated using the sudden releasing and the stepwise releasing technique were given in Figure 5.17, which shows that the stepwise releasing technique provides slightly better results in comparison with the experimental data throughout the entire crack propagation period.

It is worth noting that the above stepwise releasing technique may be further modified to achieve closer simulation results. Nevertheless, the procedure could be really tedious numerically. The main purpose of this part of study was just intended to show that such kind of techniques could be adopted to solve the very complicated 3-D dynamic fracture problems of brittle materials.

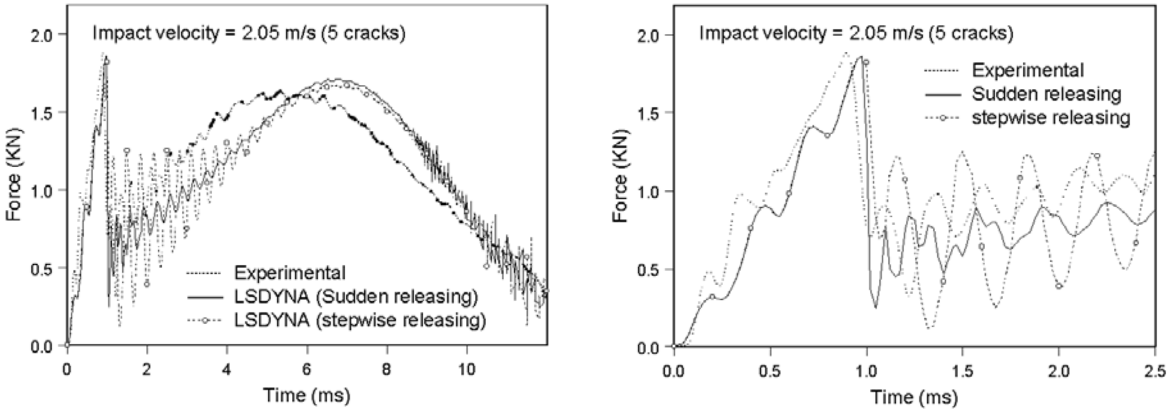

(a) The whole impact period (b) The partial impact period

Figure 5.17 Impact force histories of simulation and experiment (v = 2.05 m/s, 5 cracks).

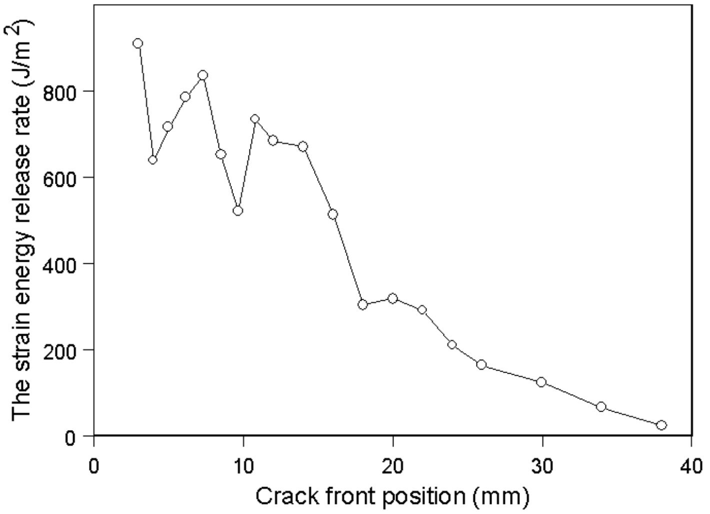

Figure 5.18 The strain energy release rate versus crack front position.

The simulation also shows that mode I fracture dominated the impact damage of the acrylic plate. Figure 5.18 gives the mode I strain energy release rate (G_I) versus crack front position. A large value of G_I corresponded to the initiation of crack. During the crack propagation phase, G_I was decreasing until it was reduced to a small value of G_I

until the crack arrested. Since the relation between the plane-strain fracture toughness and the strain energy release rate can be described as:

$$G = \frac{(1-\nu^2)K_I^2}{E} \tag{5-8}$$

Take the typical value of the static fracture toughness $K_{I,\mathrm{stat}}$ in Table 5.2 and assume $E = 3$ GPa, Poisson's ratio $\nu = 0.33$, the corresponding strain energy release rate $G_{I,\mathrm{stat}}$ will be in the range of 146 to 760 J/m^2. The dynamic strain energy release rate $G_{I,\mathrm{dyn}}$ calculated in this study (Figure 5.18) is in the range of 20 to 900 J/m^2. The upper bound (900 J/m^2) is due to the bursting effect at crack initiation whereas the lower bound (20 J/m^2) represents the dynamic crack-arrest strain energy release rate, $G_{I,\mathrm{arrest}}$ which can be substantially lower than $G_{I,\mathrm{stat}}$ due to inertial effect as been reported for ceramics and glass [352,353].

5.2.5 Conclusions of this section

Some conclusions can be drawn based on the above studies:

- Radial cracks in cast acrylic can be induced through low velocity impact below the glass transition temperature.
- The glass transition temperature lies in the range of 185 to 205°F.
- The global impact responses of cast acrylic can be simulated accurately using finite element methods with proper failure criteria and node-splitting techniques.

5.3 Impact on Aluminum/Acrylic Sandwich Panels

5.3.1 Introduction

Sandwich plates are multi-layered structures consisting of different materials and have been adopted widely in engineering design and applications. Damage mechanisms due to low-energy foreign-object impact on sandwich panels have been studied extensively [2]. In general, low-velocity impact damage patterns are characterized by incomplete penetration with damage consisting of delamination, cracking, and fiber failure if the sandwich plate is reinforced by fibers.

To simplify the analysis of composites or composite sandwiches, many researchers investigated sandwich specimens made of ductile metal sheets and brittle polymer layers different loading conditions. Walter and Ravichandran [279] performed an experimental simulation of matrix cracking and debonding in an Aluminum/Homalite 100 epoxy resin specimen through the optical method of coherent gradient sensing (CGS). It was showed that the sequence of damage was highly dependent on the strain rate under quasi-static loading. Han and Sun [115] studied layered plates consisting of brittle glass and ductile aluminum layers under static indentation and dynamic impact tests. A 2D finite element model was adopted to simulate the Mode I dominated connoid cracking under static indentation. Behr, Ji, et al. [10, 135] studied low velocity impacts on laminated glass, where dynamic strains and damage probability were investigated using the finite element code, DYNA2D. Xu and Rosakis [302] presented the generation and subsequent evolution of dynamic failure modes in metal/polymer sandwich plates subjected to low-velocity impact based on high-speed photography and dynamic photoelasticity. Their results indicated that the shear-dominated interfacial delamination always appeared first, followed by the intra-layer cracking in polymer layers. Anderson and Madenci [7] observed the types and extent of the impact damage in a variety of sandwich configurations. Akil, Hazizan and Cantwell [350] studied the low velocity impact response of an aluminum honeycomb sandwich structure, in which a drop-weight impact test combined with the simple energy-balance model was adopted, They showed that the partition of the incident energy depended strongly on the geometry of the impacting projectile.

Besides experimental study, computational models especially finite element methods were used to investigate damages in sandwich structures. Noor, Burton and Bert [206] presented a review on the computational models for sandwich panels and shells. Kwon and Wojcik [347] studied the impact responses of sandwich beam and plate using the finite element code VEC/DYNA3D, in which the deflection, strain histories and failure location were investigated. Park, et al. [348] performed an impact study on composite sandwich by using a finite element code with an 18-node solid element and a proposed modified Hertzian contact law to simulate the impact forces and contact time. Besant, et al. [17] studied the impact responses of composite sandwich panels with models consisting of shell elements for the skins and brick elements for the core. Failure was considered while the skins were assumed remaining attached to the core during the impact. El-Sayed and Sridharan [92] modeled a cohesive layer along a pre-existing delamination or an identified plane of crack propagation to simulate the crack growth in sandwich composite beams by using the ABAQUS software package. Meo, et al. [349] studied the low-velocity impact on an aircraft sandwich panel using LS-DYNA3D and obtained the depth of indentation as well as the delamination in good agreement with experimental results. Icardi and Zardo [351] carried out a delamination damage analysis based on a zig-zag plate finite element model, where the impact force and delamination were simulated according to the Hertz's contact law and several strength-based failure criteria.

In this section, impact responses of aluminum/acrylic sandwich plates were studied experimentally and numerically. Impact force histories and delamination between aluminum sheet and cast acrylic layer were calculated and compared with experimental results.

5.3.2 Specimens and impact tests

Square sandwich specimens with dimensions of 101.6 mm×101.6 mm (4”×4”) were made of 1.6 mm (1/16”) thick 6061-T6 aluminum alloy adhered to 5.1 mm (0.2”*)* thick cast acrylic (PMMA) by epoxy. All materials properties were listed in Table 5.5.

Table 5.5 Constituent properties

Materials	6061-T6	Cast acrylic	Epoxy
Density (kg/m^3)	2,700	1,190	2,000
Tensile modulus (GPa)	69	2.24 ~ 3.24	3.45
Tensile strength (MPa)	310	55 ~ 76	31
Yielding strength (MPa)	276	60	--------
Elongation at break	12%	4.2% ~ 5.5%	--------
Poisson’s ratio	0.33	0.33	0.35
Fracture toughness (MPa $\sqrt{\text{m}}$)	29	0.7 ~ 1.6	--------
Thickness (mm)	1.6	5.0	--------

All impact tests were conducted using the above-mentioned Instron-Dynatup 8250 pneumatic-assisted, instrumented drop-weight impact tester, where the sandwich specimen was clamped circumferentially in a 76.2 mm (3”) diameter fixture and impacted by a 16 mm diameter spherical impactor with a weight of 6.1 kg. The following are experimental results and discussion.

Figures 5.19 and 5.20 present impact damage patterns and force-time histories for specimens impacted from different heights onto the aluminum side. Only a circular delamination approximately 25 mm in radius at the aluminum/acrylic interface was observed for the 1”-height impact case. Its associated force-time history is a rather smooth curve. When impacted from 1.5” height, the delamination extended to a circular shape of approximately 35 mm in radius along with a group of radial cracks formed into a “✳”-shaped with an average crack length of 25 mm in the cast acrylic layer. There is a sudden drop in its force-time history, indicating the occurrence of these radial cracks.

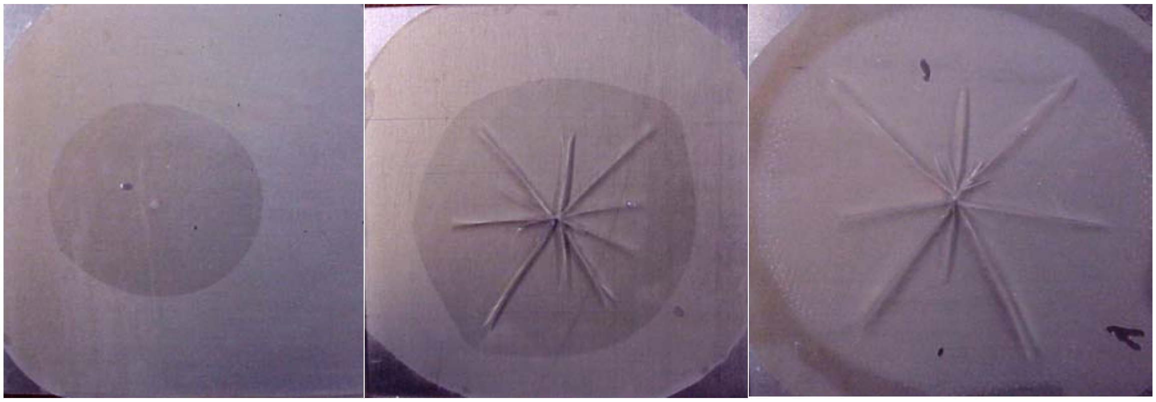

Impacted from 1” Impacted from 1.5” Impacted from 3”

Figure 5.19 Damage patterns of aluminum/acrylic sandwich panels impacted from different heights onto the aluminum side.

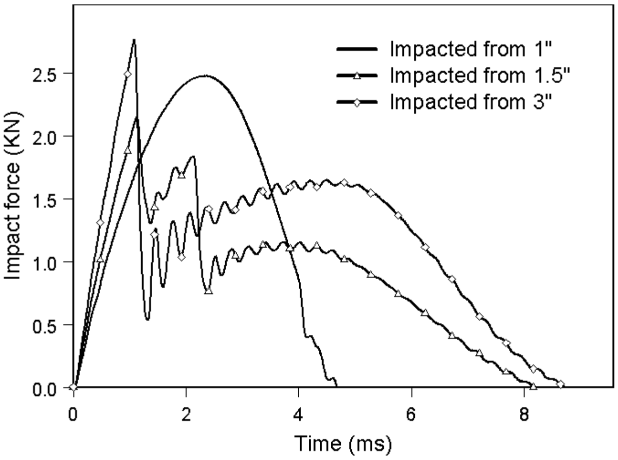

Figure 5.20 Force-time histories of aluminum/acrylic sandwich panels impacted from different heights onto the aluminum side.

Finally, under an impact from 3” height, full delamination reaching the clamped boundary (76.2 mm in diameter) was formed along with the radial “✳”-shaped cracks propagating almost to the clamped boundary. Two sudden drops were recorded in its impact force history. The first drop corresponded to the formation of radial cracks whereas the second indicated the moment when the delamination reached the clamped boundary. This is reasonable since the crack propagation speed in the relatively brittle cast acrylic is faster than the delamination speed in the epoxy adhesive, which is viscoelastic in nature and tends to retard the expansion of the delmination. It should also be noted that there was no conoid crack observed, which is different from the high-speed impact tests conducted by Han and Sun [115], where the conoid-shaped of damage was induced during impact penetration.

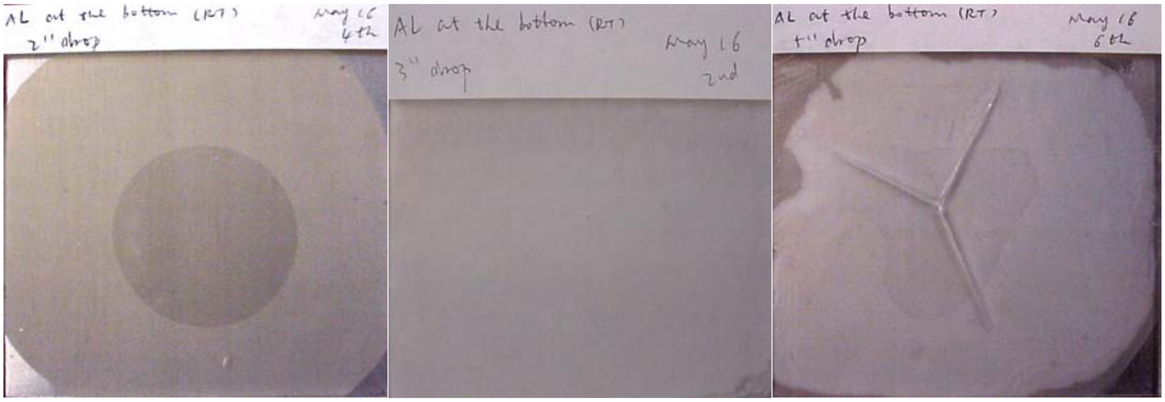

Impacted from 2”   Impacted from 3”   Impacted from 5”

Figure 5.21 Damage patterns of aluminum/acrylic sandwich panels impacted from different heights onto the acrylic side.

When the aluminum/acrylic sandwich panel was impacted from different heights onto the cast acrylic side, the results are shown in Figures 5.21 and 5.22. As shown in these figures, impact from 2” height induced only a partial delamination of 22 mm in radius and a smooth impact force time history. On the other hand, a 3” impact caused full delamination between the cast acrylic layer and the aluminum sheet, which was accompanied by a sudden drop in impact force history. Finally, full delamination with three radial cracks reaching the clamped boundary were formed if the sandwich specimen was impacted by a drop height of 5”. Again, its force-time curve contains two sudden drops, as depicted in Figure 5.22.

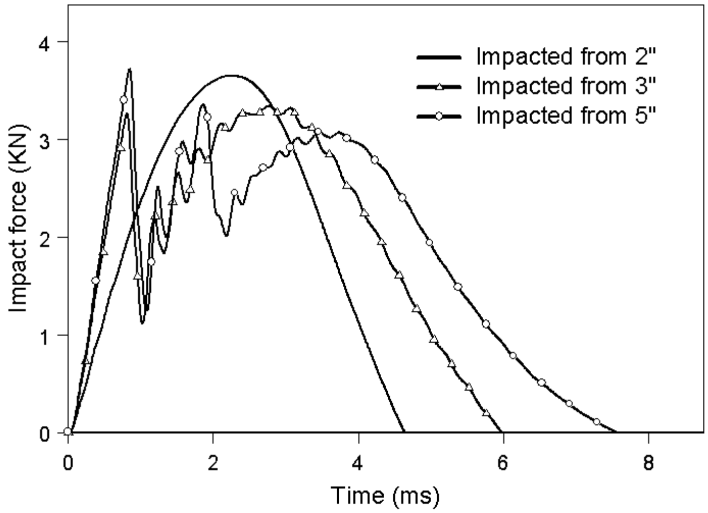

Figure 5.22 Force-time histories of aluminum/acrylic sandwich panels impacted from different heights onto the acrylic side.

The above results indicate that the impact resistance for aluminum/acrylic sandwiches is higher if impacted on the acrylic side than impacted on the aluminum side. Higher impact peak force and less severe damage occurred when impacted on the cast acrylic side. This can be explained through the maximum-tensile-stress fracture criterion, and the fact that mode I cracks dominate the crack propagation in brittle materials [115, 330]. When subjected to the same impact condition, smaller bending-caused maximum tensile stress will occur in the cast acrylic layer if it is supported by an aluminum sheet on the bottom. The viscous adhesive and the ductile aluminum sheet can also form a damping foundation,; thus reducing if not preventing completely, crack propagation in the acrylic layer.

5.3.3 Theoretical models

Several theories and models have been developed by many investigators (details in Abrate's book [2]). The basic theory and assumption for this study are stated as following.

5.3.3.1 Governing equations. The equilibrium equation of the whole impact system is the same as presented in Equations 5-2 and 5-3. The penalty method is used to calculate the contact force in this study.

The energy partition for the whole system is given through the following equation

$$K_0 = K + P + U_{al} + U_{ac} + E_{delamination} + E_{crack} + E_{contact} \tag{5-9}$$

where K_0 is the initial impact energy (i.e., kinetic energy of the impactor right before impact), K and P are the kinetic and potential energies of impact system during impact duration, U_{al} and U_{ac} are the strain energies stored in aluminum and in cast acrylic, respectively, $E_{delamination}$, E_{crack} and $E_{contact}$ are the energies dissipated by delamination, cracks, and the contact, respectively. In this study, the contact occurred during impact is assume frictional, hence its associated dissipated energy $E_{contact}$ is zero.

5.3.3.2 Failure criteria. The damage patterns for aluminum/cast acrylic sandwiches induced by low velocity impact are radial cracks in cast acrylic layer and delamination between aluminum and acrylic. A radical crack occurs when the following condition is met

$$\sigma_t \geq S_t \tag{5-10}$$

where σ_t is the principal tensile stress and S_t is the maximum tensile strength.

The delamination criterion is expressed as following.

$$\left(\frac{\max(0, \sigma_n)}{N_{\text{int}}} \right)^2 + \left(\frac{\sigma_s}{S_{\text{int}}} \right)^2 \geq 1 \tag{5-11}$$

where σ_n and σ_s are the normal and shear stresses acting on the interface, respectively, while N_{int} and S_{int} are the normal and shear strengths of the interface, respectively.

5.3.4 Finite Element Simulation

The finite element program LS-DYNA was used to analyze the response of aluminum/acrylic sandwich plates under low-velocity impact. Eight-node solid elements were adopted to build the model, in which the contact between the impactor and the sandwich plate was treated as type 3 (SURFACE_TO_SURFACE) [344]. Due to the various damage patterns, either one-quarter or the full model was created for simulation. Various boundary conditions were also taken into consideration, i.e. fixed, pinned, sliding and rollered (Figure 5.3). As proved previously, comparison between the experimental and numerical results indicates that the real boundary condition lies somewhere “between” the fixed and the sliding boundary cases. It also depends on which side of the sandwich plate is impacted (i.e., is the aluminum or the acrylic impacted first?). The treatment of contact between aluminum and acrylic was needed to modify for different impact conditions. All six experiments stated previously were simulated and results were given below.

5.3.4.1 Impact on aluminum side from 1” height. Only a circular delamination with a radius of 25 mm at the interface was observed from this impacted specimen. Due to symmetry, only one quarter of the whole impact system was modeled. Figure 5.23 shows the 3-D finite element mesh.

Table 5.6 Material type and mechanical properties

Part	Material type	Density (kg/m^3)	Young’s modulus (GPa)	Yield stress (MPa)	Tangent modulus (GPa)	Poisson’s ratio
Impactor	Rigid	------	200	------	------	0.33
Aluminum	Plastic_Kinematic	2700	69	276	1	0.33
Acrylic	Elastic	1190	2.5	------	------	0.33

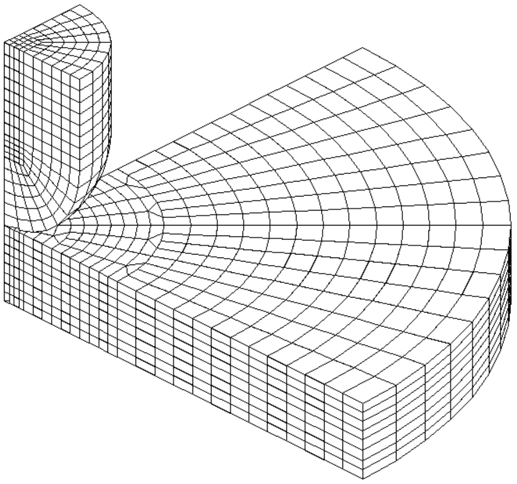

Figure 5.23 A 3-D finite element model.

The material types and properties are listed in Table 5.6. The lower half of the specimen was fixed by the specimen fixture, whereas the upper half was clamped through pneumatic pressure during impact. Hence, the boundary of the specimen (especially the upper surface) might slip. Thus, a so-called "mixed" boundary condition, in which the lower boundary was handled as fixed while the upper boundary was assumed to be sliding, was also investigated in this simulation. To simulate the adhesive bonding of the aluminum/acrylic sandwich plate, the tiebreak interface available in LS-DYNA was used [344, 345]. Choosing *NFLS* and *SFLS* to denote the normal and shear failure stresses, respectively, and noting that compressive stress makes no contribution to the failure equation, the failure criterion can be expressed as following:

$$\left(\frac{\max(0,\sigma_n)}{NFLS}\right)^2+\left(\frac{\sigma_s}{SFLS}\right)^2\geq 1 \qquad (5\text{-}12)$$

To implement the simulation, various *SFLS* values were tried to predict the delamination. The von Mises yielding criterion was applied to the adhesive [346], i.e. $SFLS = NFLS/\sqrt{3}$. The finite element results in this study showed that the delamination was dominated by the shear stress.

In order to obtain accurate and reliable numerical results, an effective and proper finite element mesh must be adopted [190]. The mesh effect was studied by using models with different layers of elements (Figure 5.24) and various coarseness levels of elements (Figure 5.25). Impact force histories from an 8-layers element model (2 layers for aluminum and 6 layers for acrylic) as well as a 16-layer element model (4 layers for aluminum and 12 layers for acrylic) are shown in Figures 5.26 and 5.27 for fixed and mixed boundaries, respectively. Here the sandwich specimen was modeled with the mesh shown in Figure 5.25(c) and the shear strength was assumed to be 18 MPa for the interface of aluminum/acrylic. The results indicated that there was nearly no difference between two models in terms of stiffness under the same boundary condition. That is, an 8-layer model was good enough for this simulation. Therefore, 8-layer models were chosen for all of the following simulations in the sequel.

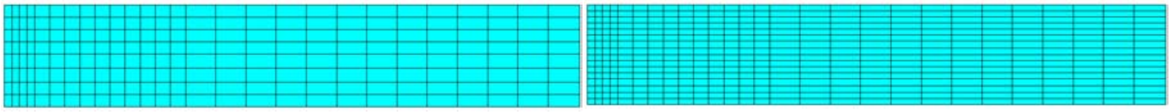
(a) (b)

Figure 5.24 The cross-sectional view of finite element meshes with different layers of elements (for the target only).

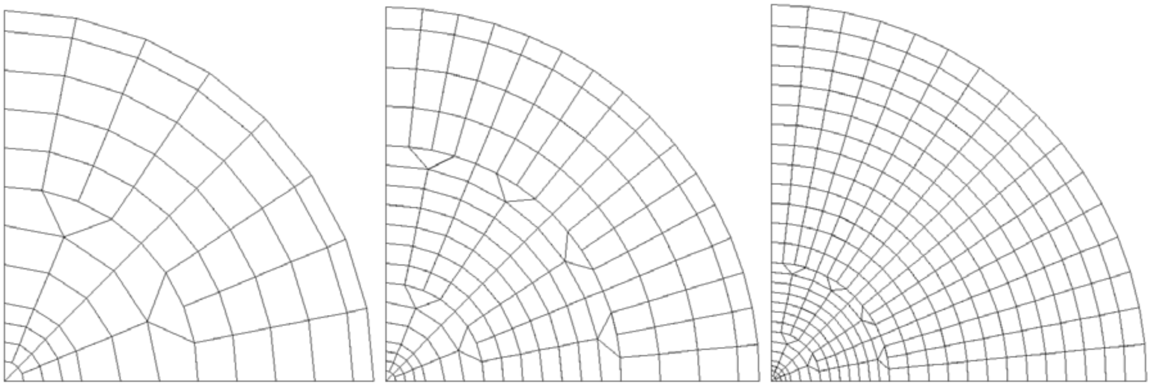
(a) (b) (c)

Figure 5.25 The top view of finite element meshes with various coarseness levels of elements (for the target only).

By choosing different meshes (Figure 5.25), two series of simulations were conducted for fixed and mixed boundary conditions with 18 MPa as the shear strength of the interface. Results were given in Figure 5.28 and Figure 5.29, respectively. More severe oscillation, which might caused by numerical instability, occurred in curves of impact force history with models built of coarse meshes, i.e. mesh (a) and (b) shown in Figure 5.25. The delamination sizes were different due to mesh density (Table 5.7). Compared with the experimental result, the finest mesh, which was shown in Figure 5.25 (c), provided a fairly smooth force history curve. Hence mesh (c) was chosen for all simulations in this study except otherwise stated.

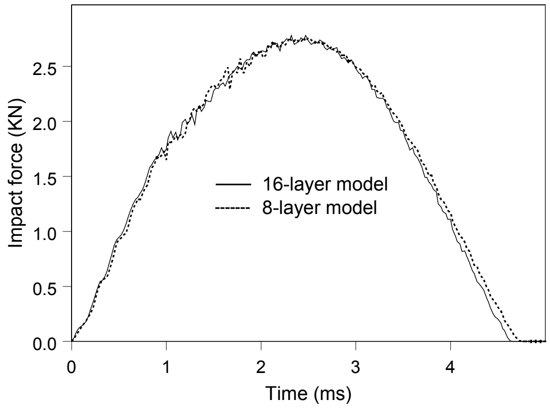

Figure 5.26 Comparison of 8-layer and 16-layer model (fixed boundary)

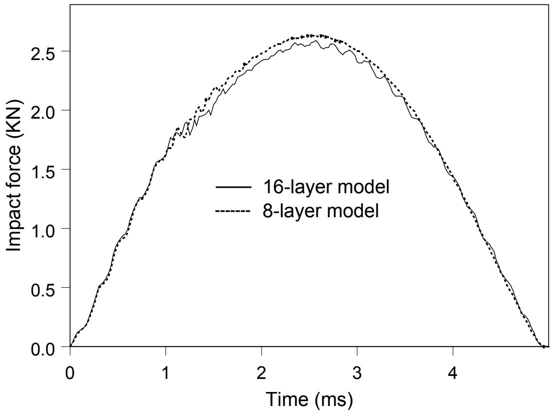

Figure 5.27 Comparison of 8-layer and 16-layer model (mixed boundary)

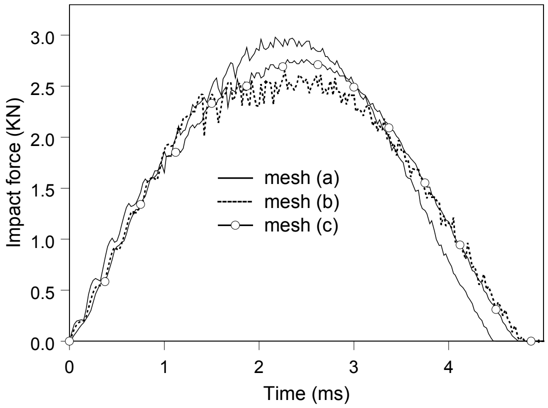

Figure 5.28 Mesh coarseness effect (fixed boundary)

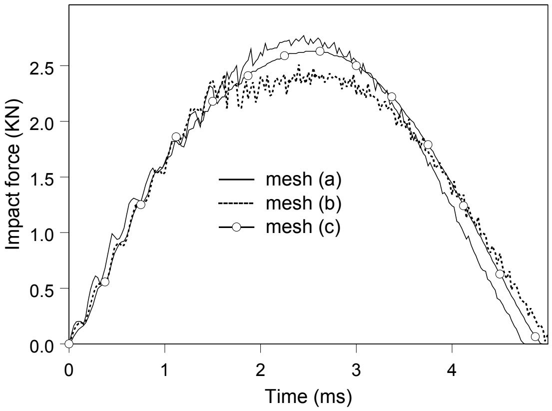

Figure 5.29 Mesh coarseness effect (mixed boundary)

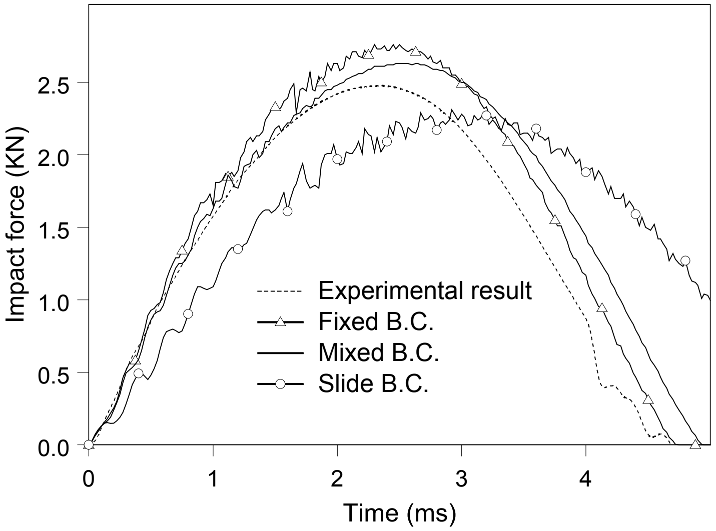

Figure 5.30 Impact force histories under various boundary conditions

The boundary conditions played an important role in the finite element simulations. Impact force histories under various boundary conditions were drawn in Figure 5.30 with the shear strength of interface assumed 18 MPa. As comparison, the experimental curve was also plotted in the same graph. The mixed boundary provided the closest result but without significant difference compared to the result from fixed boundary, whereas the result from slide boundary was way off from the experimental data.

The simulation results could be various when different interface strength was chosen. For the adhesive used in this study, 31 MPa was the shear strength provided by the manufacturer. The aluminum/acrylic sandwiches were artificially made and the interface strength was needed to find out through trial and error. Different values of shear strength were tried in the range from 31 MPa down to 12 MPa. For comparison, the interface without delamination was also considered. This could be implemented by choosing an extremely large value of strength. Both of fixed and mixed boundaries were chosen to perform the investigation. For both of fixed and mixed boundary conditions with the same mesh (c), the smaller interface shear strength adopted, the earlier delamination occurred. The delamination size increased when the interface strength reduced.

Compared to the experimental result, the finite element model with 15 MPa as the interface shear strength provided the closest delamination zone (24 mm). But the impact force history was significantly differed from experimental curve (Figure 5.30). A mixed boundary condition and 18 MPa shear strength resulted the closest impact force history. The larger experimental delamination size may be caused through propagating after impacted until measured from specimen and multiple strikes even though a pneumatic break was used. So the “real” delamination zone exactly after the first strike may smaller than the measured size. Another phenomenon obtained from finite element simulations was that the delamination didn’t start on the center of impact but on the position around 1 to 1.5 mm away from the center. The energy partition was shown in Figure 5.31 (with mixed B.C. and 18 MPa as the interface shear strength).

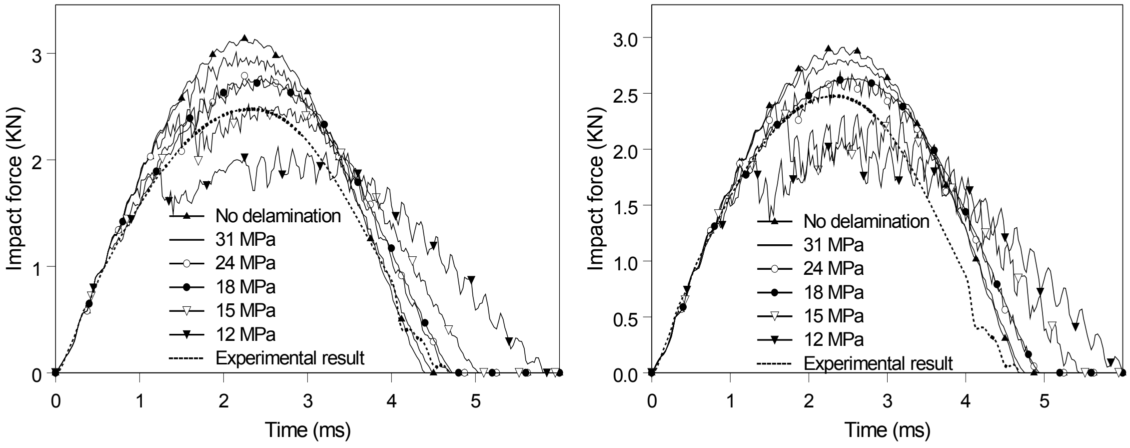

Fixed boundary condition Mixed boundary condition

Figure 5.31 Impact force histories with various shear strength of interface

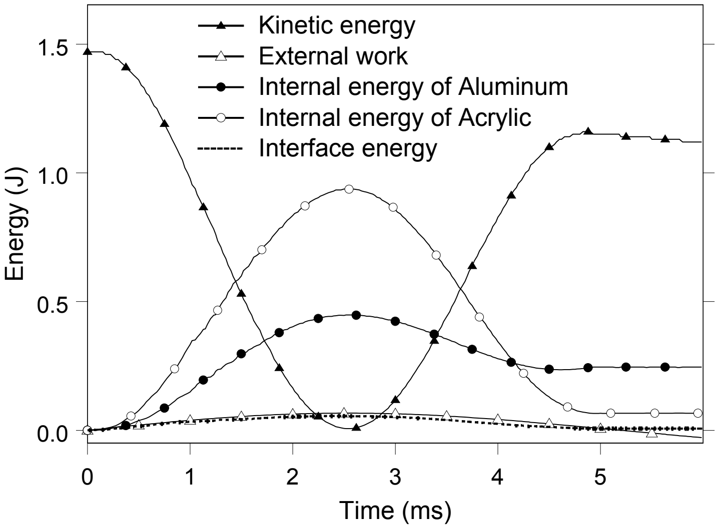

Figure 5.32 Energy partition

Table 5.7 Delamination calculated by finite element models

Boundary condition	Finite element mesh	Interface shear strength (MPa)	Delamination start		Delamination end	
			Time (ms)	Position* (mm)	Time (ms)	Position* (mm)
Fixed	Mesh (c)	31	0.973	1	2.15	7
		24	0.799	1	1.48	14
		18	0.641	1.5	1.62	14
		15	0.598	1.5	1.65	20
		12	0.491	1	2.21	30
	Mesh (a)	18	0.768	2	1.42	8
	Mesh (b)	18	0.719	1	1.82	16
Mixed	Mesh (c)	31	1.07	1	1.89	6
		24	0.846	1	1.69	12
		18	0.724	1	1.45	14
		15	0.641	1	1.77	24
		12	0.573	1.5	2.55	30
	Mesh (a)	18	0.85	2	1.59	8
	Mesh (b)	18	0.796	1	1.72	16
Slide	Mesh (c)	18	1.04	1	2.15	14
Experimental delamination size			25 mm in radius			

* Radius measured from impact center

Figure 5.32 indicated that only a small portion of energy (about 21%) was dissipated, where most was dissipated through plastic deformation of aluminum. However, more accurate energy partition could be obtained if the deformation of acrylic was considered and fracture criterion was adopted for the slide interface.

5.3.4.2 Impact on aluminum side from 1.5” height. As seen above from experiment, full delamination occurred and a “✳” shape cracks pattern was formed with average 25 mm for each cracks.

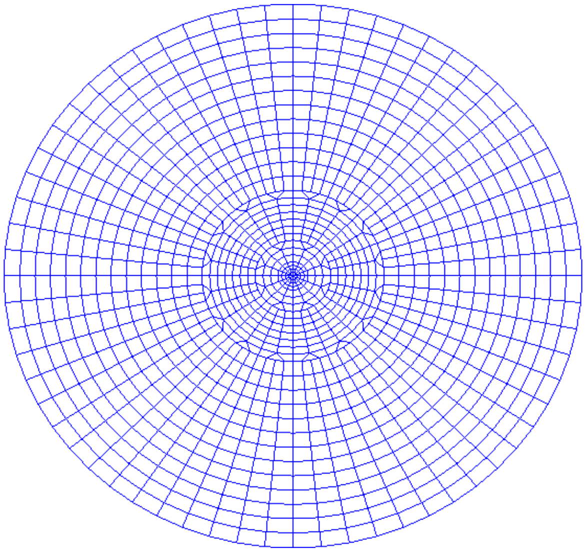

Figure 5.33 Finite element mesh of sandwich plate

A full finite element model, shown in Figure 5.33, was adopted. The mixed boundary condition was used and a tiebreak interface was chosen to simulate the delamination between aluminum and acrylic, in which the shear strength was assumed 18 MPa. In order to simulate the crack propergation, the whole plate model was “precracked” through eight radial cracks with a 26-mm radius from the center. Some researchers showed that cracks in glass surface tended to open and propagate at the location of maximum tensile stress [26, 96], therefore the maximum tensile stress criterion was adopted to simulate the onset of cracks. This can be accomplished by using tied interface between cracks surfaces with failure, where the tensile failure stress was chosen through trial and error. A close simulation result could be achieved when the tensile strength reached 75 MPa.

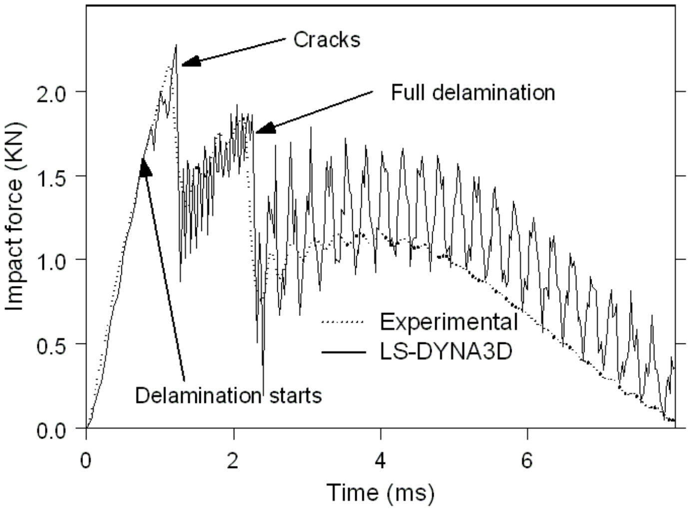

Figure 5.34 Impact force histories of sandwich impacted from 1.5” on aluminum side

Showed in simulation, the delamination between aluminum and acrylic started at 0.614 milliseconds after impact 1.5 millimeters away from the impact center. At 1.2 milliseconds, cracks initiated and the delamination propagated to 16 millimeters wide. The fractures in acrylic occurred very suddenly during impact and may be explained through unstable dynamic fracture [329]. Such a crack can propagate at a velocity on the same order of elastic stress wave in the sample. For a thin plate, the propagation velocity of such waves is given in equation 5-1 [337].

In cast acrylic, the propagation velocity is about 1680 m/s if Young’s modulus is chosen to be 2.5 GPa, density is 1190 kg/m^3, and Poisson’s ratio 0.33. It only takes about 17 microseconds for such a crack to traverse a length of 26 mm (1.5”). Tied crack interfaces were suddenly released once the fracture started. After 2.25 milliseconds, the tiebreak interface between aluminum and acrylic also released in order to simulate the full delamination. Figure 5.34 shows the impact force histories.

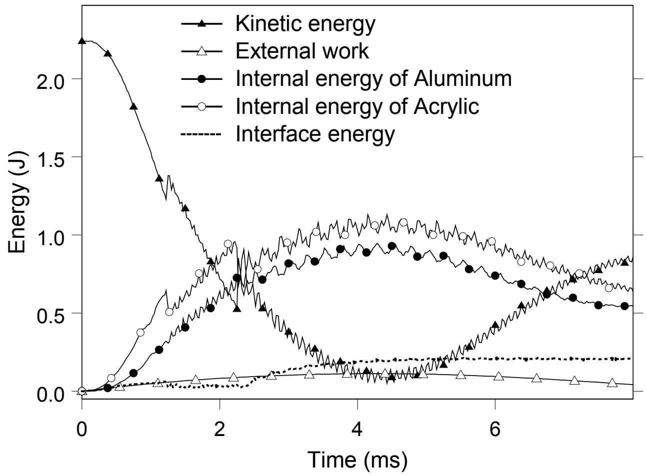

Figure 5.35 Energy partition of sandwich impacted from 1.5” on aluminum side

The energy partition is given in figure 5.35. This time, around 63 percent of total energy (2.24 joules) was attenuated, where 9.3 percent (0.208 joules) dissipated through interface, 24.9 percent (0.558 joules) dissipated by aluminum and 28.5 percent (0.639 joules) by acrylic due to deformation.

5.3.4.3 Impact on aluminum side from 3” height. Full delamination and a “✳” shape cracks pattern with cracks reaching the boundary were induced under 3” impact. The same finite element model as the one for 1.5” impact was used but “pre-cracked” from the impact center to the boundary.

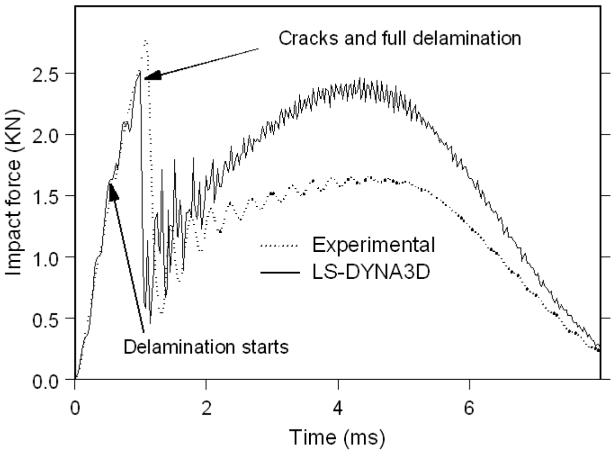

Figure 5.36 Impact force histories of sandwich impacted from 3” on aluminum side

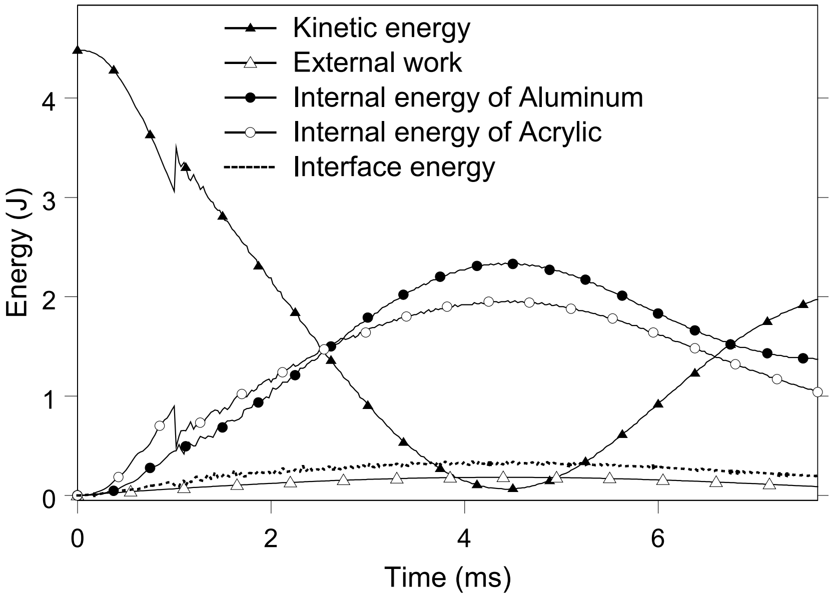

Figure 5.37 Energy partition of sandwich impacted from 3” on aluminum side

Similar to previous case (impacted from 1.5” height), The delamination started from 0.42 milliseconds after impact at the position of 1.5 millimeters away from the impact center. At 1.0 milliseconds, cracks started and tied cracks surfaces as well as the tiebreak interface between aluminum and acrylic were released suddenly to simulate the fast crack propagation and full delamination. Figures 5.36 and 5.37 give the plots of impact force and energy partition. 57 percent of total energy (4.48 joules) was attenuated, where 4.5 percent (0.2 joules) dissipated through interface, 30.8 percent (1.38 joules) dissipated by aluminum and 21.4 percent (0.96 joules) by acrylic.

5.3.4.4 Impact on acrylic side dropping from 2” height. Only partial delamination at the interface was observed from the impacted specimen. The delamination zone is circular with a radius of 22 mm. One quarter of impactor and sandwich plate was modeled (Figure 5.23). The interface shear strength assumed 18 MPa and various boundary conditions were investigated. All simulation results were shown in Table 5.8, Figure 5.38 and Figure 5.39, respectively. Impact force histories in Figure 5.38 and delamination size in Table 5.8 indicated that fixed boundary provided the closest result to the experimental data. With acrylic on top of aluminum, the pneumatic controlled fixture can grip the acrylic firmly since the thorn-like steel fixture surface could stick into acrylic layer. This could make the experimental boundary condition really close to fixed. Again, the delamination started at about 3.0 millimeters away from the impact center and the delamination zone calcuted was smaller than measured from specimen. Small portion of impact energy was dissipated, i.e. 0.2 of total 3 joules absorbed by aluminum, 0.11 joules attenuated by interface and 0.08 joules lost due to the deformation of acrylic.

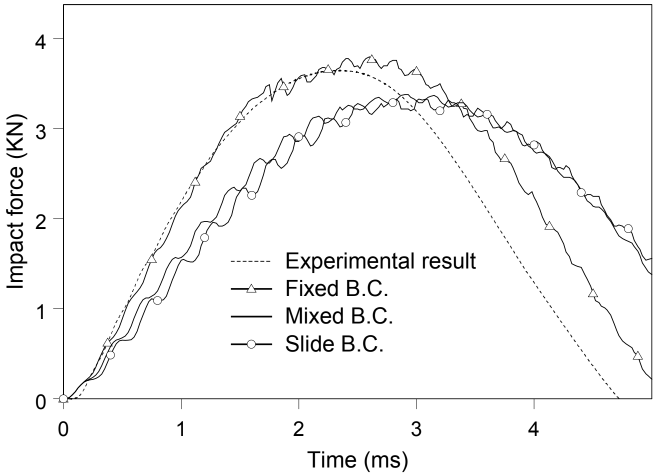

Figure 5.38 Impact force histories of sandwich impacted on acrylic side from 2” height

Table 5.8 Delamination simulated for sandwich impacted on acrylic side from 2”

Boundary condition	Finite element mesh	Interface shear strength (MPa)	Delamination start		Delamination end	
			Time (ms)	Position* (mm)	Time (ms)	Position* (mm)
Fixed	Mesh (c)	18	1.30	3.0	2.0	16
Mixed	Mesh (c)	18	1.80	3.0	2.35	12
Slide	Mesh (c)	18	1.92	4.0	2.72	12
Experimental delamination size			22 mm in radius			

* Radius measured from impact center

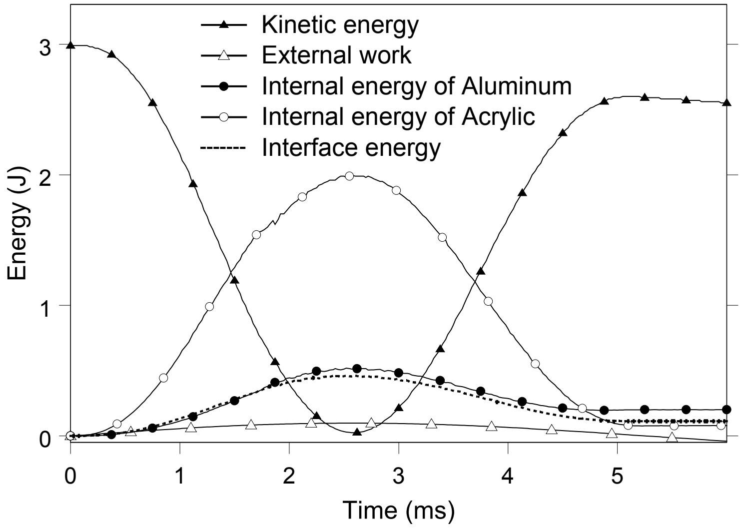

Figure 5.39 Energy partition of sandwich impacted on acrylic side from 2" (fixed B.C.)

5.3.4.5 Impact on acrylic side dropping from 3" height. The experiment showed that full delamination induced without any crack in acrylic layer. The same finite element model with the same materials and interface properties was used as impacted on acrylic side from 2" height. The only case with fixed boundary condition was simulated.

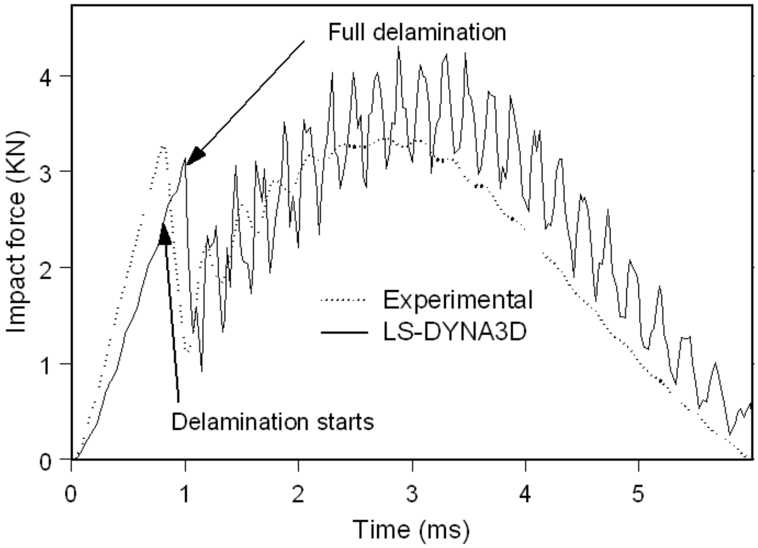

Figure 5.40 Impact force histories of sandwich impacted on acrylic side from 3" (fixed B.C.)

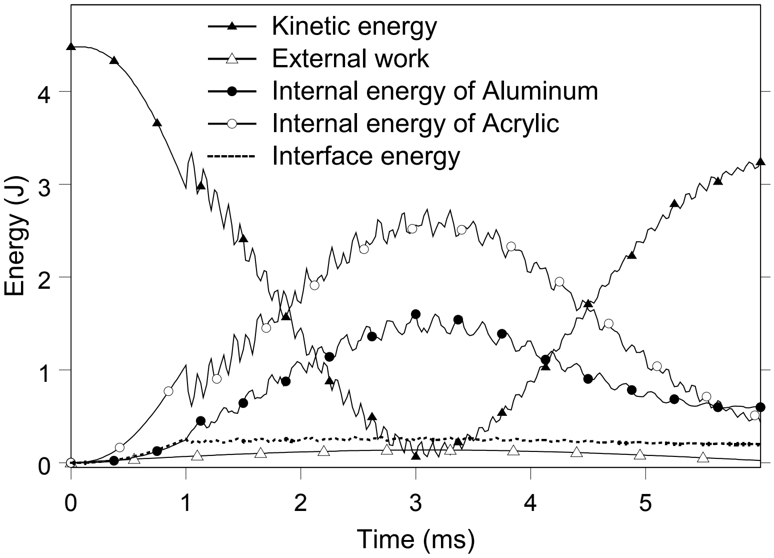

Figure 5.41 Energy partition of sandwich impacted on acrylic side from 3” (fixed B.C.)

The finite element calculation showed that the delamination started at 0.9 milliseconds after impact and 4 millimeters away from the impact center. The delamination propagated very fast and the tiebreak interface released at 1.0 millisecond to simulate the full delamination. Figures 5.40 and 5.41 provided the force histories and energy partition, respectively. Around 28% of total 4.48 joules impact energy was dissipated, in which 13.4% (0.60 J) attenuated by aluminum, 9.8% (0.44 J) by acrylic and 4.5% (0.20 J) through interface.

5.3.4.6 Impact on acrylic side dropping from 5” height. Under 5” impact, full delamination as well as three cracks in acrylic from the center to the boundary were induced. A full finite element model similar to the one used for 3” impact on aluminum side, where only three “pre-cracks” were modeled instead of eight, was adopted. The boundary condition was fixed, tiebreak interface with the shear strength of 18 MPa was chosen for the interface of acrylic and aluminum, while the maximum tensile strength criterion (75 MPa for the tensile strength of acrylic) was used to simulate the crack opening.

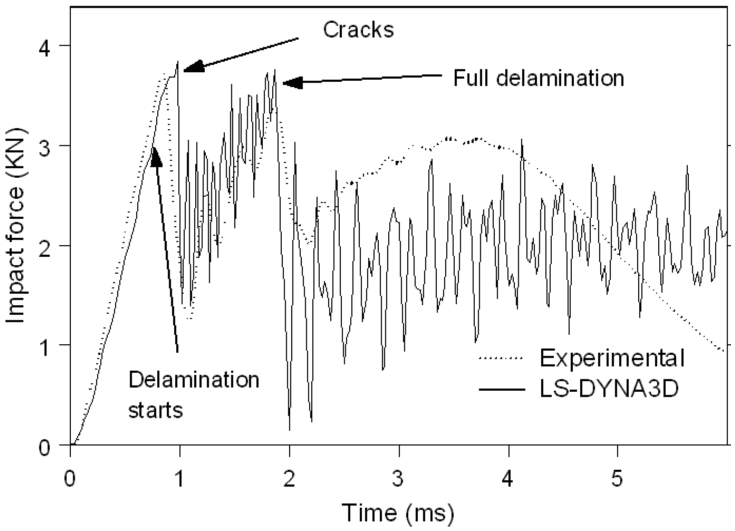

Figure 5.42 Impact force histories of sandwich impacted on acrylic side from 5" (fixed B.C.)

The delamination started at 0.794 milliseconds at the location of 5 millimeters away from the impact center. In order to simulate the two drastic dropping points found in the experimental impact force curve, the tied pre-cracks were suddenly released at 0.97 milliseconds and the tiebreak interface was also released to radius of 20 millimeters, then the tiebreak interface was fully released at 1.9 milliseconds for full delamination. Results were presented in Figures 5.42 and 5.43.

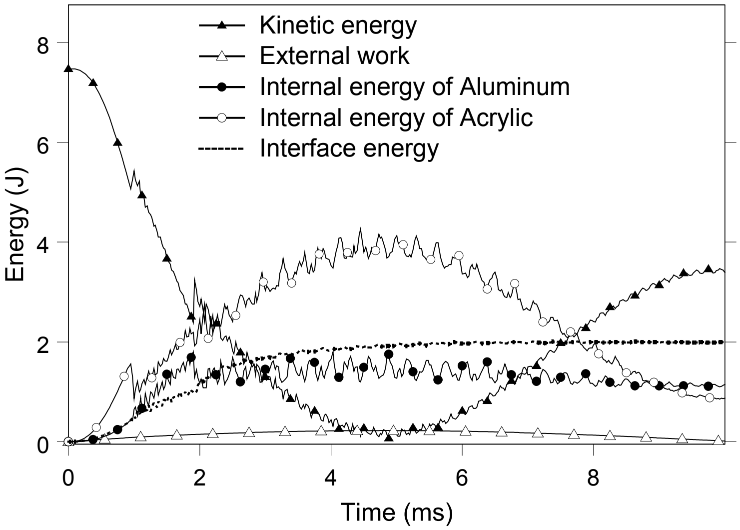

Figure 5.43 Energy partition of sandwich impacted on acrylic side from 5" (fixed B.C.)

5.3.5 Discussions

- Damage patterns include partial delamination, full delamination, cracks in the acrylic layer and permanent deformation in the aluminum sheet for aluminum/acrylic sandwich plates subject to low-velocity impact.
- Damage appears to be more severe if impacted on the aluminum side.
- The histories of impact force and delamination can be predicted by finite element program such as LS-DYNA.
- The delamination between aluminum and acrylic occurred first and took relatively longer time to propagate than cracks in acrylic layer.

5.4 Impact on Fiber-Metal Laminates

5.4.1 Failure criteria

Several theories and models for impact on composites have been developed from many investigators [2]. The basic failure criteria for this study are stated as following. The damage patterns for fiber-metal laminates induced by low velocity impact include delamination between aluminum sheets and fiber-reinforced composite layers, cracks in aluminum sheets and failure in composite layers. The criterion for delamination between aluminum and composites is:

$$\left(\frac{\max(0,\sigma_n)}{N_{\text{int}}}\right)^2 + \left(\frac{\sigma_s}{S_{\text{int}}}\right)^2 \geq 1 \qquad (5\text{-}13)$$

where σ_n and σ_s are normal and shear stresses acting on the interface, respectively, while N_{int} and S_{int} are normal and shear strengths of the interface, respectively. Cracks in aluminum occur when the following maximum tensile strain criterion is met:

$$\varepsilon \geq \varepsilon_{\max} \qquad (5\text{-}14)$$

where ε is the principal tensile strain and $\varepsilon_{\max}$ is the maximum tensile strain.

The Chang-Chang progressive damage model is chosen for the fiber-reinforced composites [51, 317]. Assuming the composites obey linear elastic behavior, the failure criterion can be stated as following:

(1) The matrix cracking failure is determined from:

$$\left(\frac{\sigma_2}{S_2}\right)^2 + \left(\frac{\tau_{12}}{S_{12}}\right)^2 \geq 1 \qquad (5\text{-}15)$$

where σ_2 and S_2 are the tensile stress and the associated tensile strength in the transverse direction, τ_{12} and S_{12} are the in-plane shear stress and the associated shear strength between fibers and the matrix. Once this type of failure occurs, the material constants E_2 (Young's modulus in the transverse direction), G_{12} (in-plane shear modulus), ν_1 and ν_2 (Poisson's ratio in 1 and 2 direction) are set to zero.

(2) The compression failure occurs when:

$$\left(\frac{\sigma_2}{2S_{12}}\right)^2+\left(\frac{\tau_{12}}{S_{12}}\right)^2+\left[\left(\frac{C_2}{2S_{12}}\right)^2-1\right]\frac{\sigma_2}{C_2}\geq 1 \qquad (5\text{-}16)$$

then material constants E_2, ν_1 and ν_2 are set to zero.

(3) The fiber breakage is given by:

$$\left(\frac{\sigma_1}{S_1}\right)^2+\left(\frac{\tau_{12}}{S_{12}}\right)^2\geq 1 \qquad (5\text{-}17)$$

after fiber breakage, E_1 (Young's modulus in the longitudinal direction), E_2, G_{12}, ν_1 and ν_2 are all set to zero.

where S_1, S_2, S_{12} and C_2 are the longitudinal tensile strength, transverse tensile strength, shear strength and transverse compressive strength, respectively.

5.4.2 Finite element simulations

The finite element code LS-DYNA3D was used in this study to simulate the low-velocity impact on fiber-metal laminates. 8-node solid elements were chosen to model the impact system and only one quarter of indenter and specimen was used because of symmetry. Figure 5.44 shows the finite element mesh of fiber-metal laminates. The indenter was modeled with rigid material and aluminum was assumed to follow the bilinear plasticity with 18% as the failure strain (Table 5.9). Once aluminum failed, the failed element will be removed from the model, so that the cracks in aluminum can be simulated. The composite model with Chang-Chang damage criteria was chosen for the glass-epoxy layers. The mechanical properties of unidirectional glass-epoxy composite were given in Table 5.10 (some data are provided by the Structural Laminates Company).

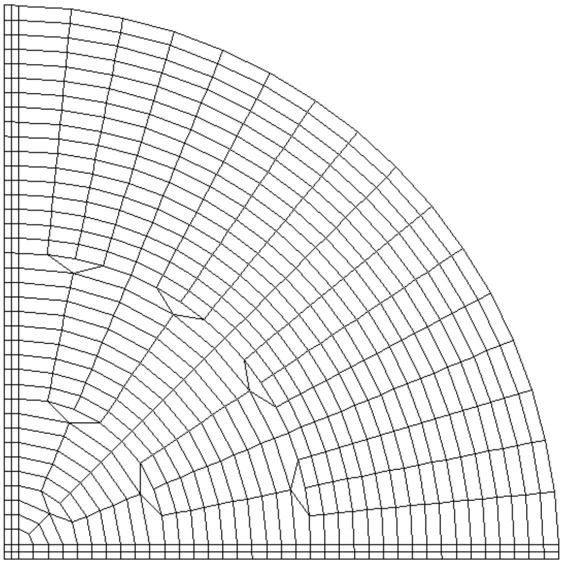

Figure 5.44 Finite element mesh of fiber-metal laminates

Table 5-9 Material types and mechanical properties

Part	Material type	Density (kg/m^3)	Young's modulus (GPa)	Yield stress (MPa)	Tangent modulus (GPa)	Poisson's ratio
indenter	Rigid	------	216	------	------	0.33
aluminum	Plastic_Kinematic	2790	72	360	0.5	0.33

Table 5-10 Material type and mechanical properties of unidirectional glass-epoxy

Material type	Density (kg/m^3)	Young's modulus (GPa)	Shear modulus (GPa)	Poisson's ratio	Strength (MPa)
composite	2000	E_1=54 E_2= E_3=9.4	G_{12}=G_{23}=G_{31}=5.6	ν_{21}=ν_{31}=0.0575 ν_{32}=0.33	S_1 =1900 S_2 =57 S_{12} =76 C_2=285

5.4.2.1 Numerical simulations on GLARE 5 (3/2) ([0°/90°/90°/0°] cross-ply).

For GLARE 5, every aluminum sheet was modeled with single layer of elements and angle-plied glass-epoxy was modeled with three layers of elements so that each unidirectional sub-layer was modeled with one layer of element. The interface between aluminum and glass-epoxy was modeled with tiebreak interface option in LS-DYNA3D in order to simulate the delamination. First, simulations with trial and error were conducted and indicated that the delamination was dominated by the shear strength of interface. In this study, the interface followed the von Mises yield criterion with 65 MPa as the shear strength. After separated, the interface acted as SURFACE_TO_SURFACE contact with zero penetration as the constraint condition.

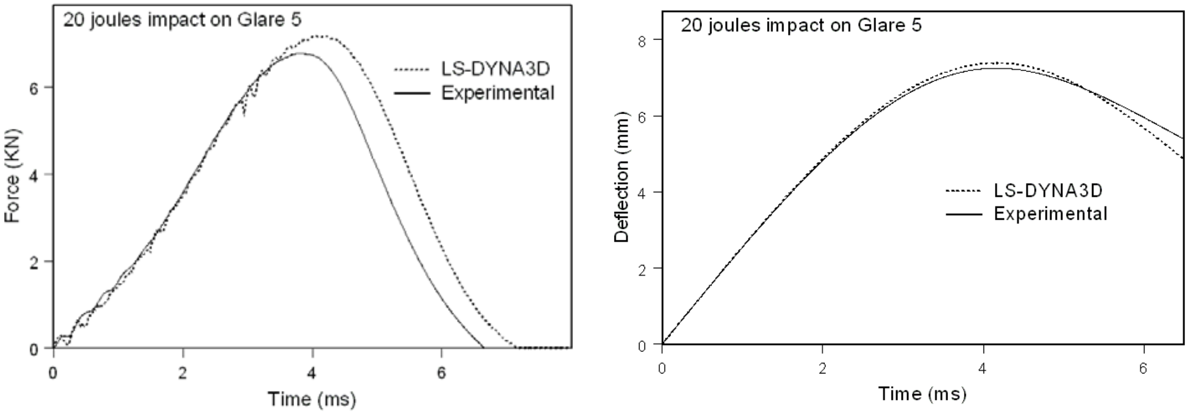

(a) Impact force histories

(b) Deflections of impactor

Figure 5.45 Impact responses of GLARE 5 under 20-joule impact

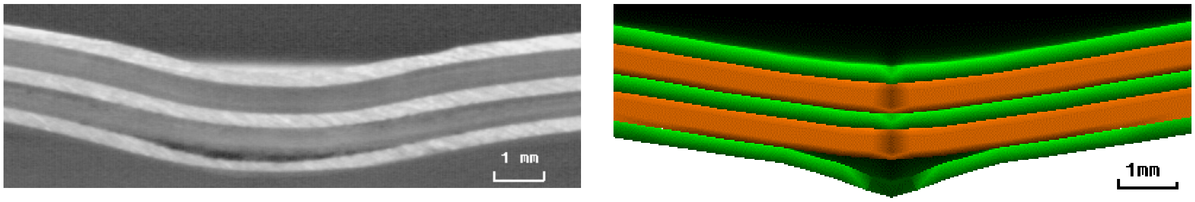

Figure 5.46 Cross-sections of GLARE 5 under 20-joule impact
(Left: experimental; Right: finite element simulation)

First, impact on GLARE 5 under 20-joule was studied. From experimental results, only delamination induced between aluminum and glass-epoxy composite on the non-impacted side. Figure 5.45 shows the impact force histories and deflections of impactor for both experiments and finite element simulation. Fairly close results obtained from simulation compared to experimental data. The smooth force history curves indicate that there is no severe damage induced in GLARE 5 under 20-joule impact. The comparison of cross-sections through the impact center is given in Figure 5.46. Totally around 55 percent of total impact energy was attenuated, where most was absorbed by the aluminum through the plastic deformation (47% of total energy), part of energy dissipated by glass-epoxy composite (6.5% of total energy), and very little portion of energy lost through interfaces from the energy partition calculated by finite element model (Figure 5.47). Above results indicate that the finite element model, which is used in this study, is valid for fiber-metal laminates GLARE 5 under impact condition.

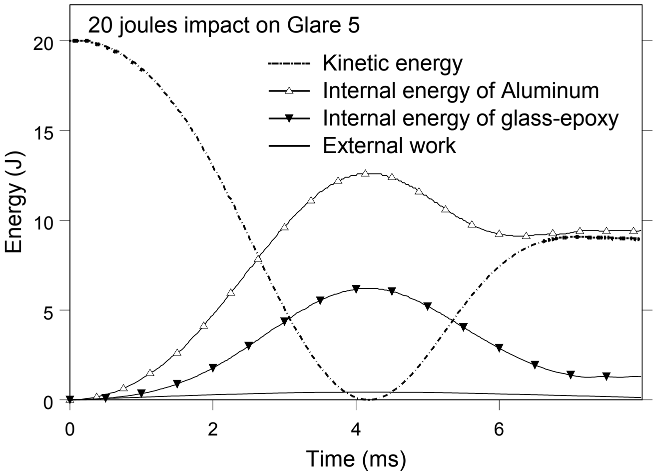

Figure 5.47 Energy partition of GLARE 5 under 20-joule impact

Finite element simulation was conducted on GLARE 5 (3/2) under 30-joule impact. The impact force histories and deflection of impactor were drawn in Figure 5.48. The sudden drop around 4-millisecond point in the force history indicated severe damage induced. Figure 5.49 and 5.50 provide the cross-section and the non-impacted side of the impacted GLARE 5 specimen, respectively. Only one 10mm long crack induced in the non-impacted side aluminum sheet from experimental result, but more severe damages, which include failure in all aluminum sheets, were predicted from simulation. This is due to the stress concentration just under the impact center. A “+” shape crack in the non-impacted side was predicted whereas only one single straight crack induced in experiment. This maybe improved by using the fracture based failure criterion in the materials model. Again, the energy partition from simulation is presented in Figure 5.51. About 59% of total energy was absorbed by aluminum and 19% of total energy was dissipated by glass-epoxy.

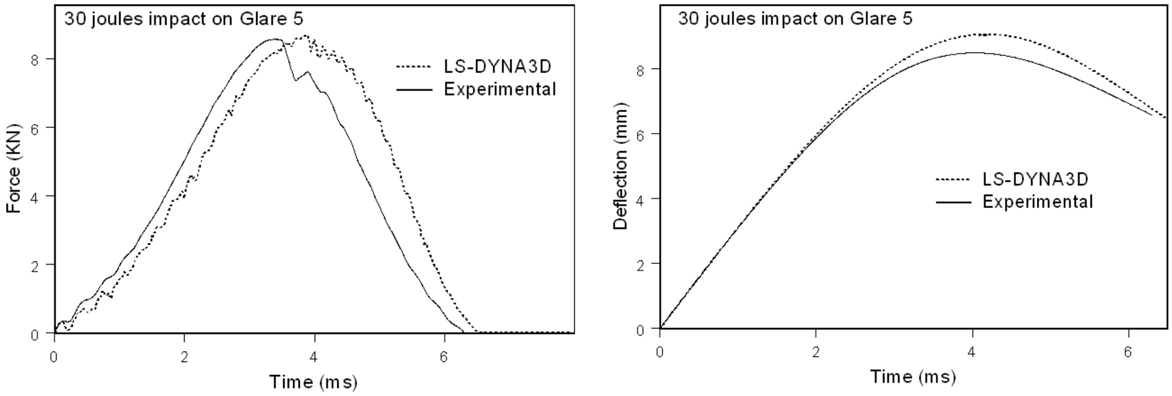

(a) Impact force histories (b) Deflections of impactor

Figure 5.48 Impact responses of GLARE 5 under 30-joule impact

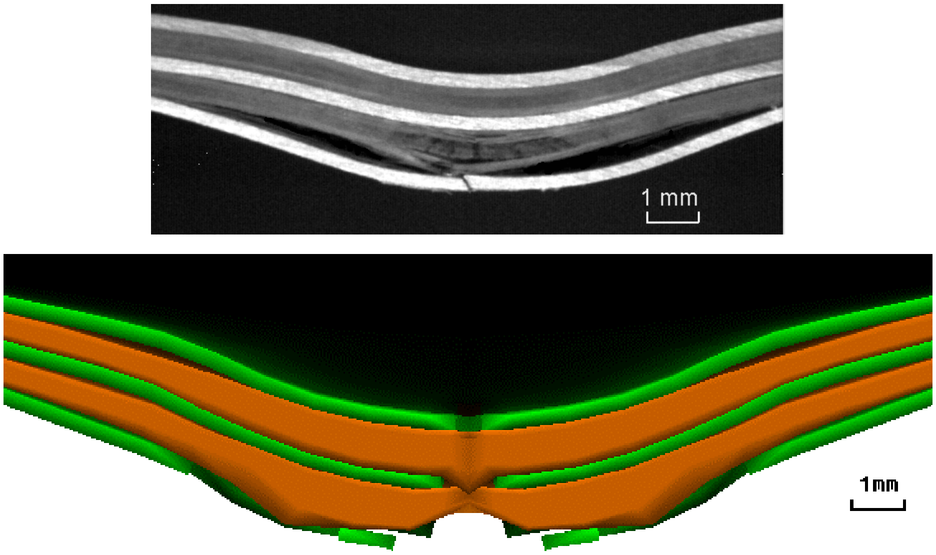

Figure 5.49 Cross-sections of GLARE 5 under 30-joule impact
(Top: experimental; Bottom: finite element simulation)

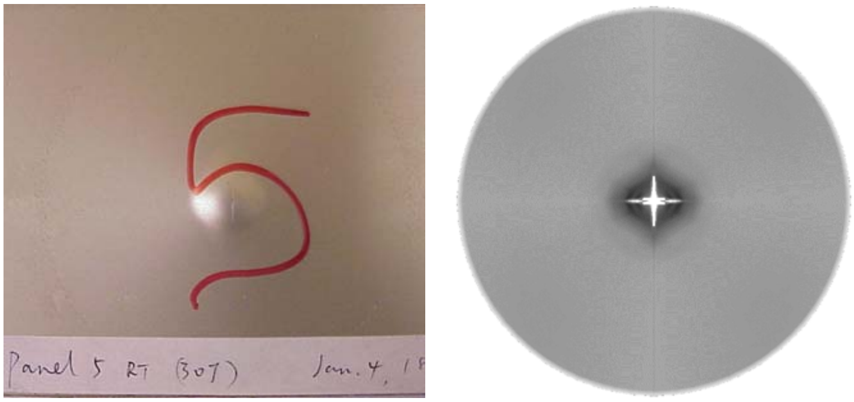

Figure 5.50 Non-impacted side of GLARE 5 under 30-joule impact
(Left: experimental; Right: finite element simulation)

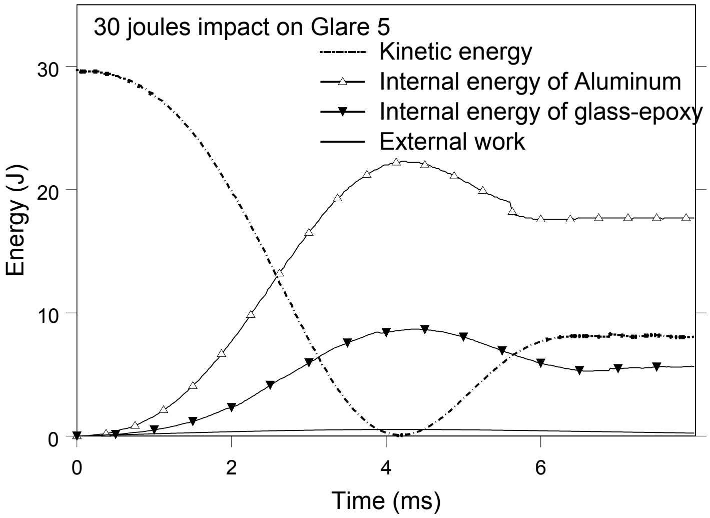

Figure 5.51 Energy partition of GLARE 5 under 30-joule impact

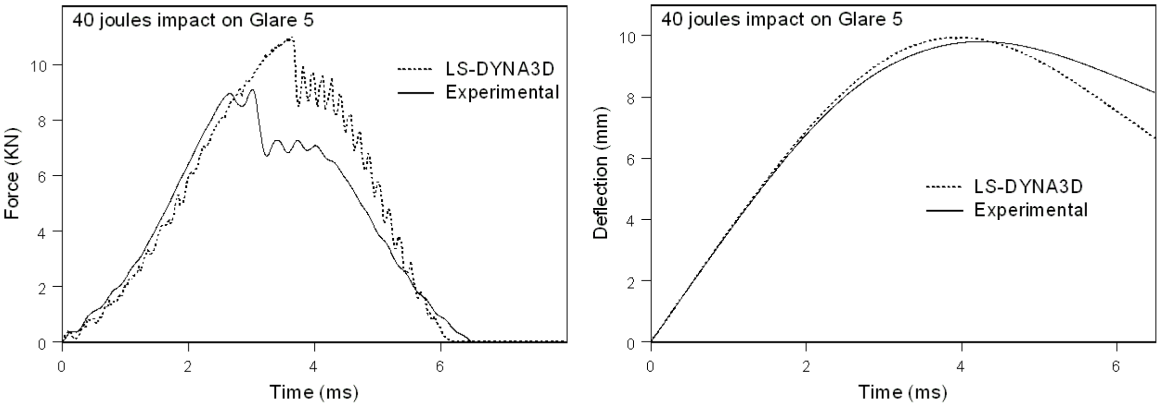

(a) Impact force histories

(b) Deflections of impactor

Figure 5.52 Impact responses of GLARE 5 under 40-joule impact

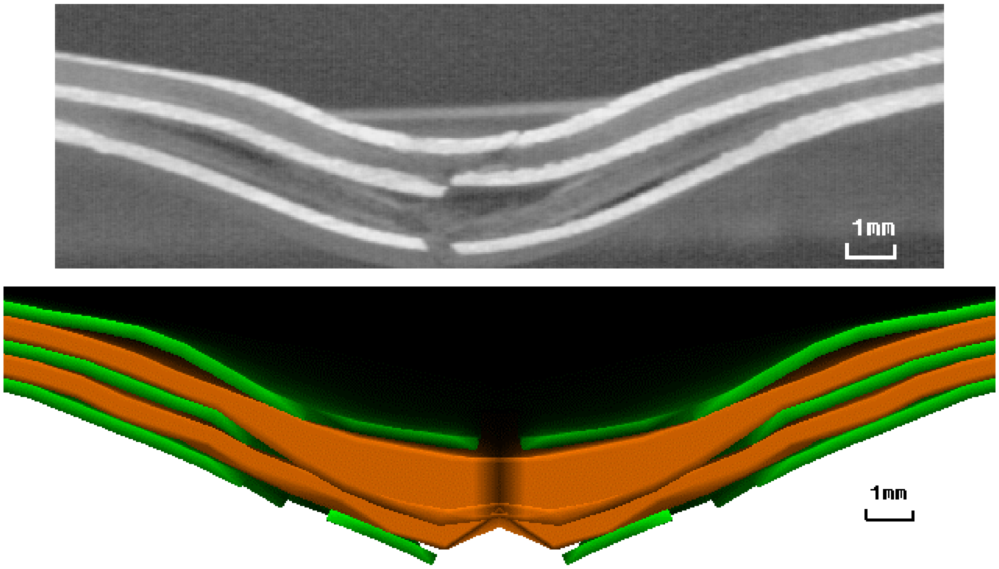

Figure 5.53 Cross-sections of GLARE 5 under 40-joule impact
(Top: experimental; Bottom: finite element simulation)

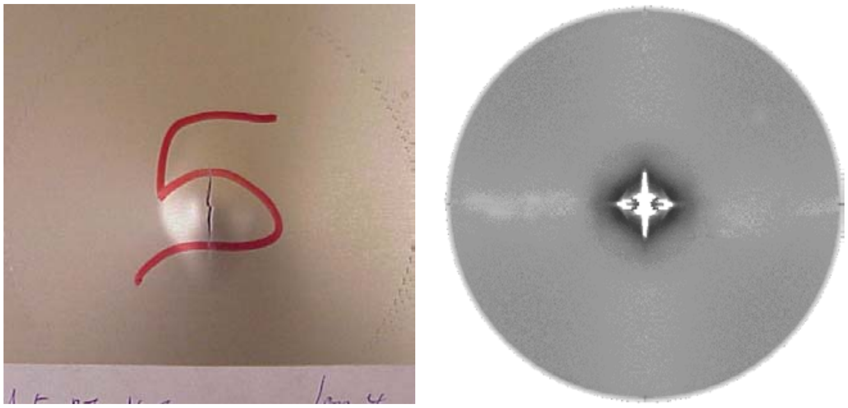

Figure 5.54 Non-impacted side of GLARE 5 under 40-joule impact
(Left: experimental; Right: finite element simulation)

Similarly, Simulation of GLARE 5 (3/2) subjected to 40-joule impact was performed. All results are presented in Figure 5.52 to Figure 5.55. Around 60% and 26% energy was absorbed by aluminum and glass-epoxy, respectively.

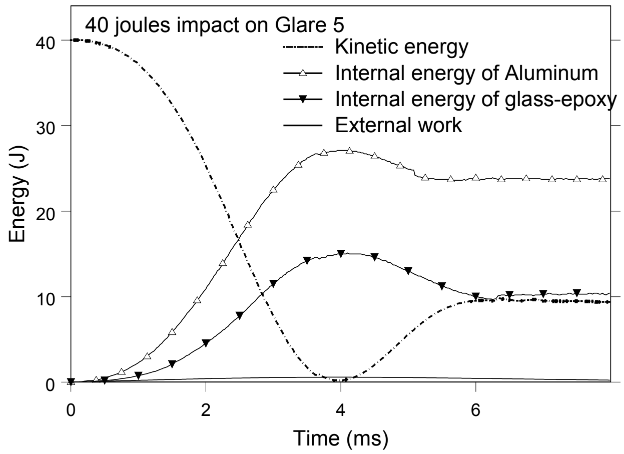

Figure 5.55 Energy partition of GLARE 5 under 40-joule impact

<u>5.4.2.2 Numerical simulations on CCNY A (unidirectional glass-epoxy)</u>. To further validate the finite element model, GLARE with unidirectional glass-epoxy was studied using the same model under the same impact conditions. Here CCNY A was simulated. Both 20-joule and 30-joule impact tests were calculated. The impact force histories, deflections of impactor and damage patterns are compared with the experimental results in Figure 5.56 to Figure 5.59. The force histories and deflections are close, but the cracks from simulations are shorter than cracks measured from real impacted specimens. A fracture based failure criterion may provide more accurate simulation results.

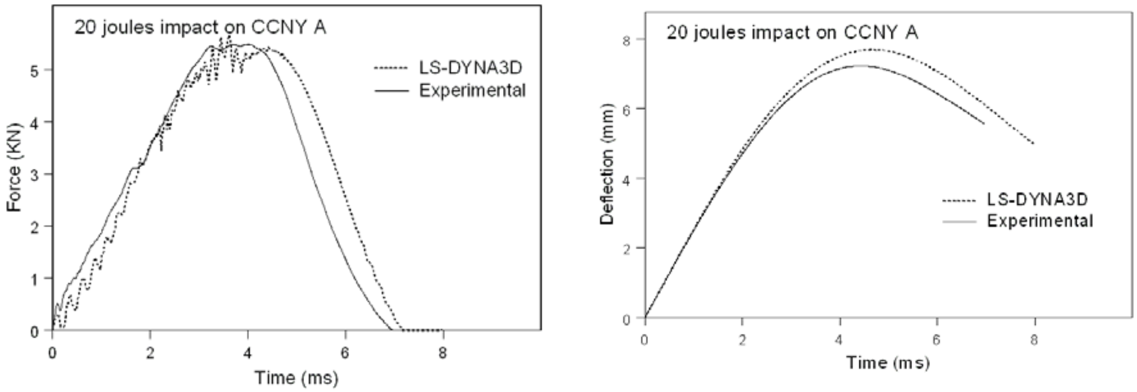

(a) Impact force histories (b) Deflections of impactor

Figure 5.56 Impact responses of CCNY A subjected to 20-joule impact

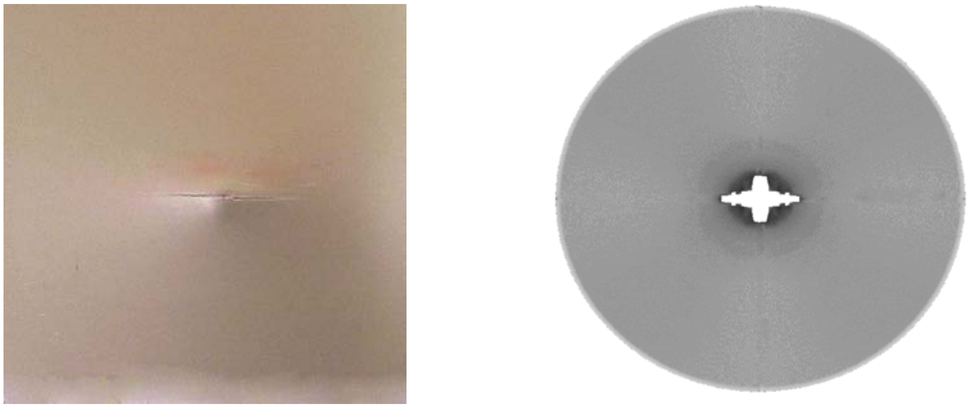

Figure 5.57 Damage in the non-impacted side of CCNY A subjected to 20-joule impact (Left: experimental; Right: finite element simulation)

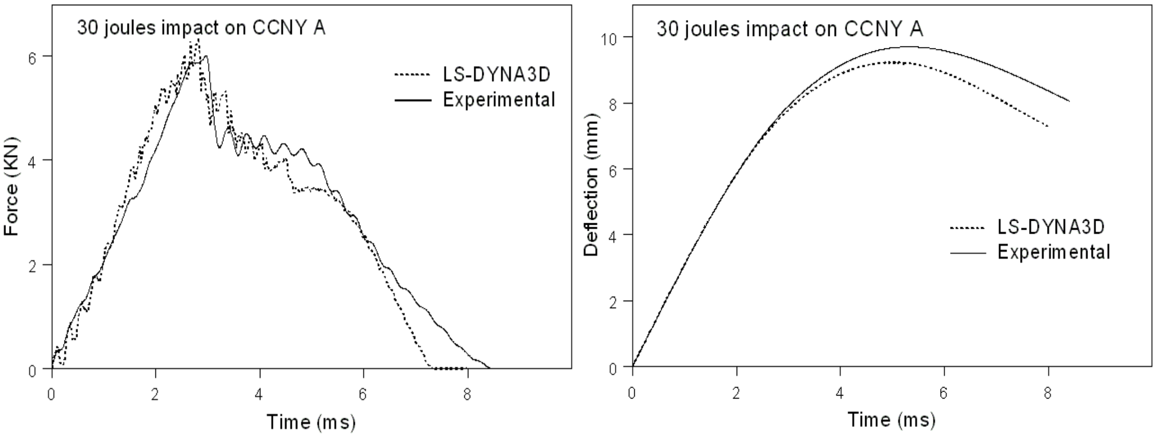

(a) Impact force histories (b) Deflections of impactor

Figure 5.58 Impact responses of CCNY A subjected to 30-joule impact

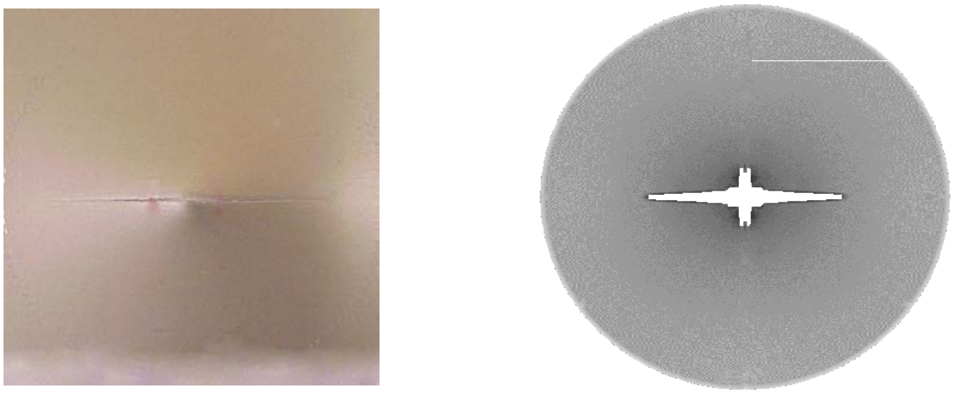

Figure 5.59 Damage in the non-impacted side of CCNY A subjected to 30-joule impact (Left: experimental; Right: finite element simulation)

5.4.2.3 Numerical simulations of impact with various impactors. GLARE 3 under impact was simulated first, where every aluminum sheet was modeled with single layer of elements and angle-plied glass-epoxy was modeled with two layers of elements so that each unidirectional sub-layer was modeled with one layer of element.

First, simulations were conducted when impacted by the 0.625" diameter indenter. Figure 5.60 and 5.61 shows the impact force histories and deflections of indenter under 20 and 30-joule impact, respectively. For lower energy impact case (20-joule), both force and deflection histories are fairly close between simulation and experiment. Whereas larger deviation occurs after GLARE 3 penal was severe damaged for 30-joule impact. Figure 5.62 and 5.63 provide the comparison of cross-sections between experiments and finite element simulation. The delamination size is larger in the finite element simulation than the actual size of delamination measured from center-cutted impacted specimens, which means the strength of interface could be even higher.

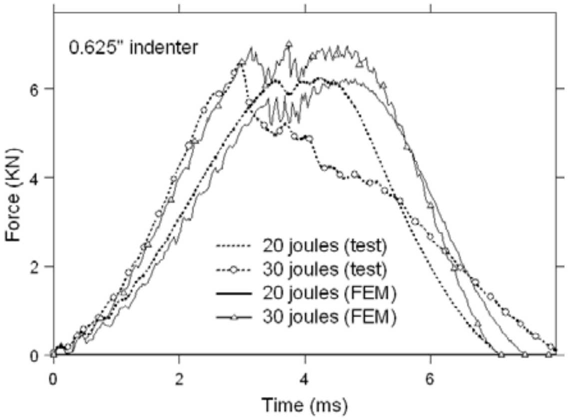

Figure 5.60 Impact force histories of GLARE 3 impacted by 0.625" indenter

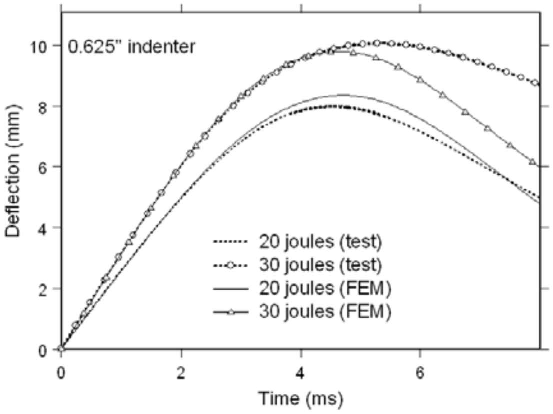

Figure 5.61 Deflection histories of indenter for GLARE 3 impacted by 0.625" indenter

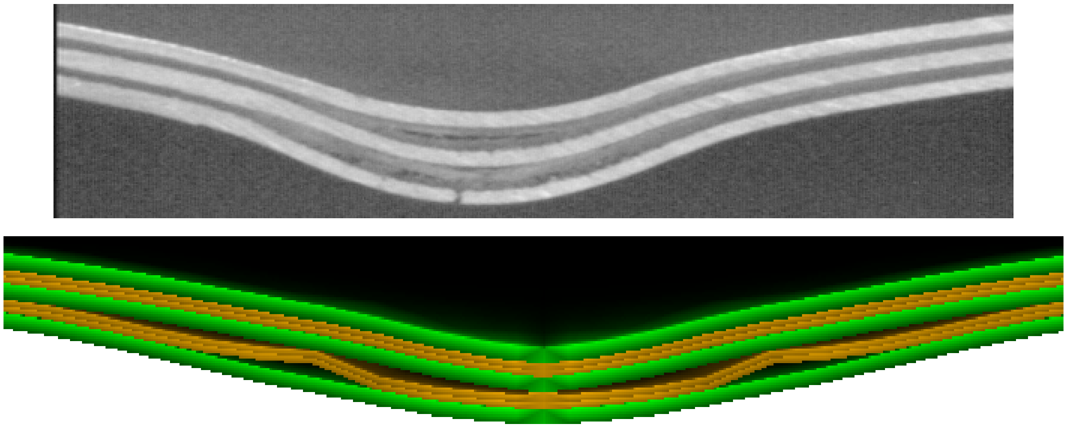

Figure 5.62 Cross-section of GLARE 3 subjected to 20-joule impact (0.625” indenter)
Top: Experimental, Bottom: Finite element simulation

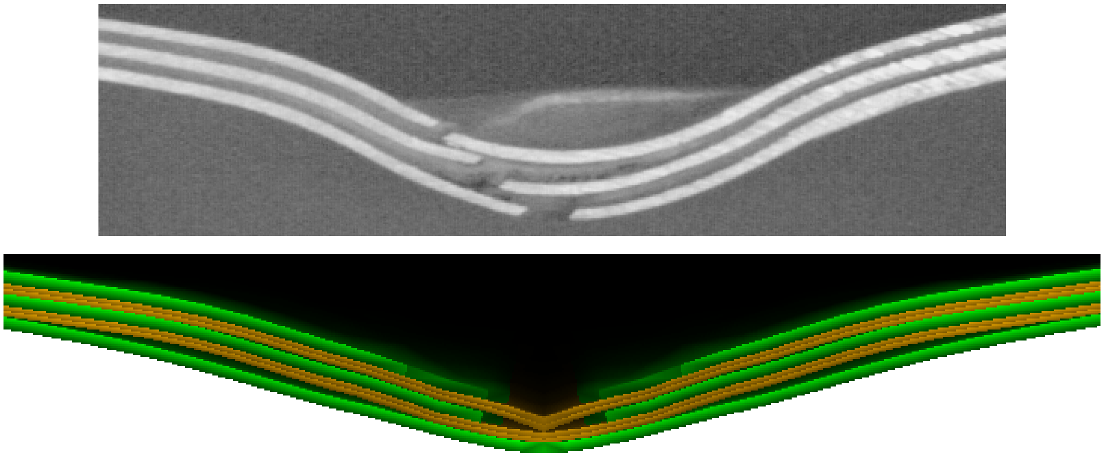

Figure 5.63 Cross-section of GLARE 3 subjected to 30-joule impact (0.625” indenter)
Top: Experimental, Bottom: Finite element simulation

For larger size indenter (1” diameter), results from simulation and experiments are showed as following. Figures 5.64 and 5.65 indicate that there are bigger errors of impact duration (around 8% to the duration of experiment) and deflection histories than the previous case (0.625” indenter). Under 30-joule impact, the cross-section of impact center is given in Figure 5.66. Again the delamination size is bigger in simulation than experiment and start from 3 mm away from the impact center. Simulation also shows the damage in the top layer of aluminum due to stress concentration.

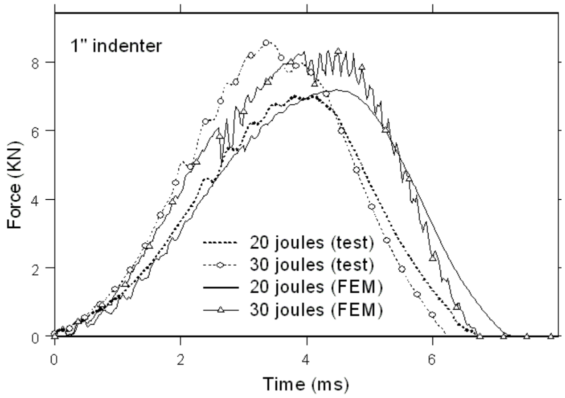

Figure 5.64 Impact force histories of GLARE 3 impacted by 1" indenter

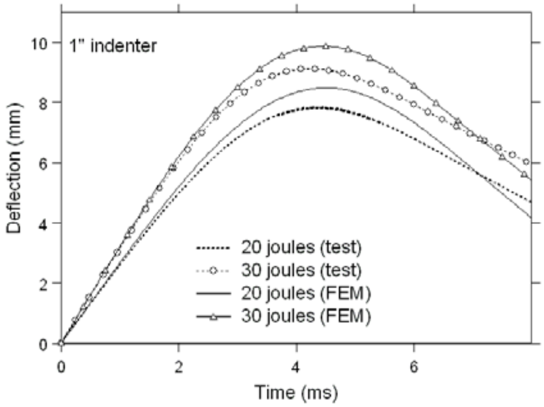

Figure 5.65 Deflection histories of GLARE 3 impacted by 1" indenter

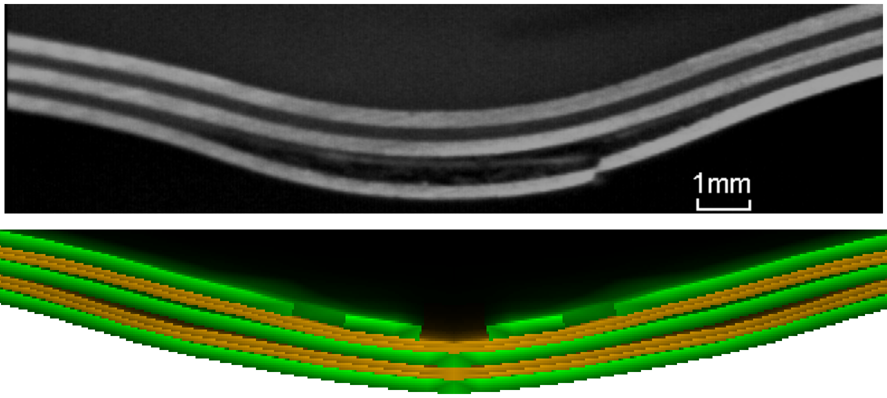

Figure 5.66 Cross-section of GLARE 3 subjected to 30-joule impact (1" indenter)
Top: Experimental, Bottom: Finite element simulation

When the diameter of indenter increases to 1.5", there are no severe damages (large delamination and cracks) in GLARE 3 for up to 30-joule impact. Figure 5.67 gives the impact force histories of GLARE 3 under impact of 1.5" diameter indenter. The error of impact duration from simulation was about 8%.

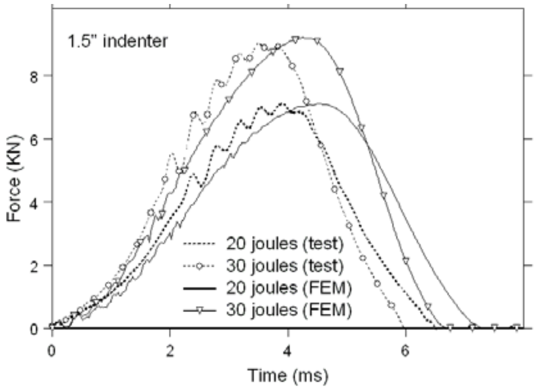

Figure 5.67 Impact force histories of GLARE 3 impacted by 1.5" indenter

For the line-like Charpy indenter, only one size of indenter (0.875” by 0.1875”) was chosen to conduct the finite element simulation. The relative angles between indenter and fibers were considered. The impact force histories were shown in Figures 5.68 and 5.69 for indenter parallel to the zero degree fibers and with a 45 degree to the fiber direction, respectively. Under 20-joule impact, results from simulation were close to the experimental data. But simulations under 30-joule impact can’t predict the severe damage that was detected in experiments. This may be improved by using finer finite element mesh around the impact center especially around the tips of indenter.

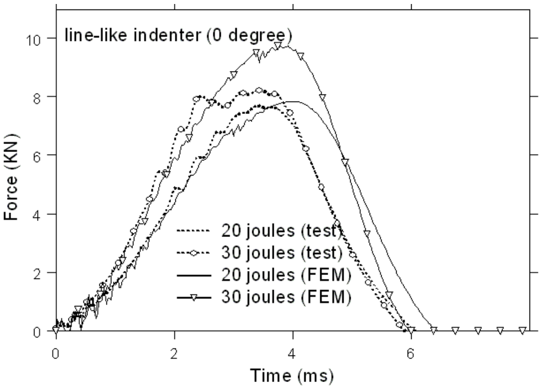

Figure 5.68 Impact force histories of GLARE 3 impacted by line-like indenter (0 degree)

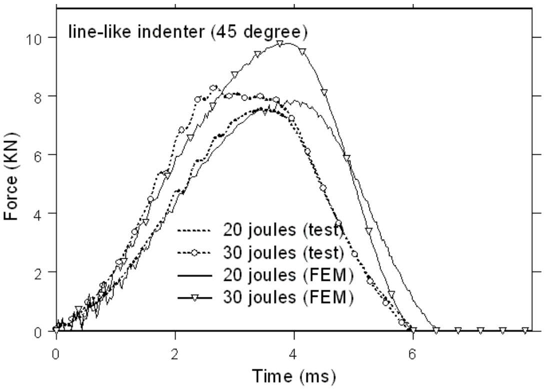

Figure 5.69 Impact force histories of GLARE 3 impacted by line-like indenter (45 degree)

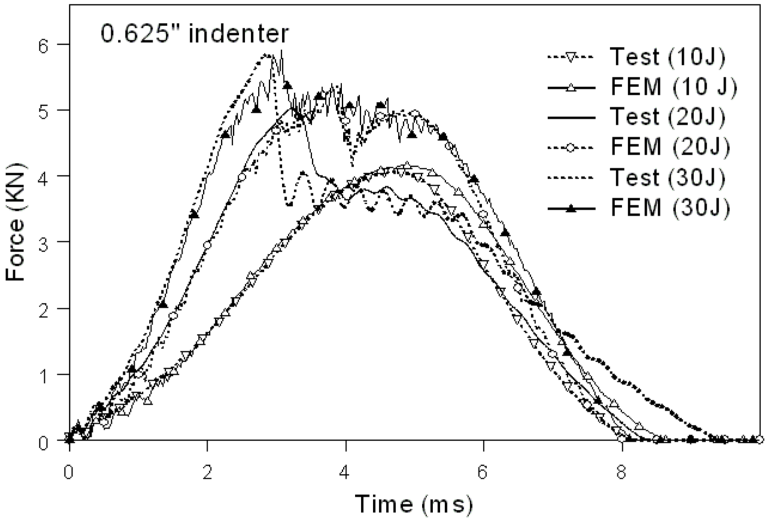

Figure 5.70 Impact force histories of GLARE 2 impacted by 0.625” indenter

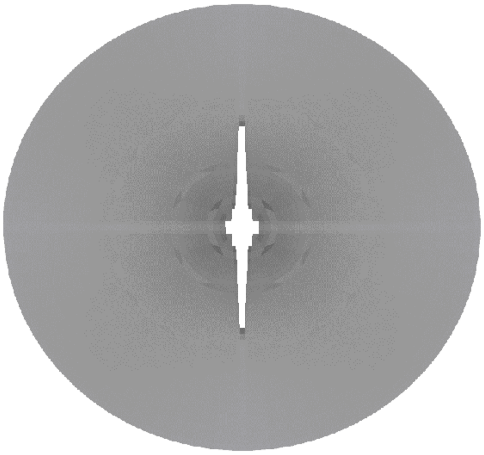

Figure 5.71 Crack in the non-impacted side of GLARE 2 subjected to 30-joule impact by a 0.625” indenter

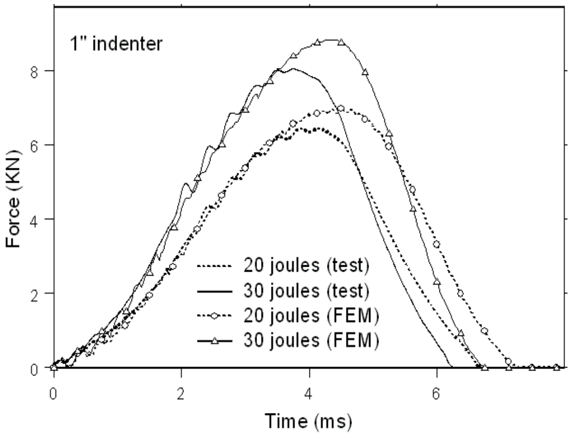

Figure 5.72 Impact force histories of GLARE 2 impacted by 1” indenter

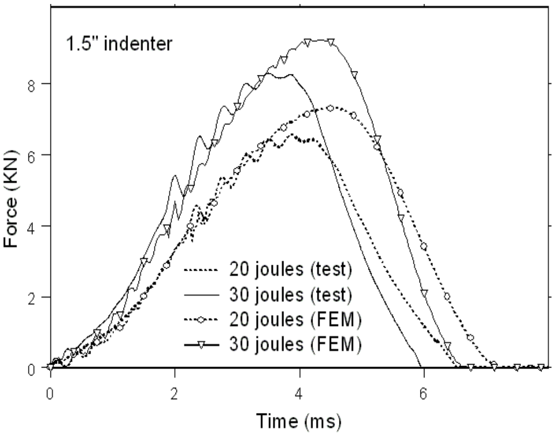

Figure 5.73 Impact force histories of GLARE 2 impacted by 1.5” indenter

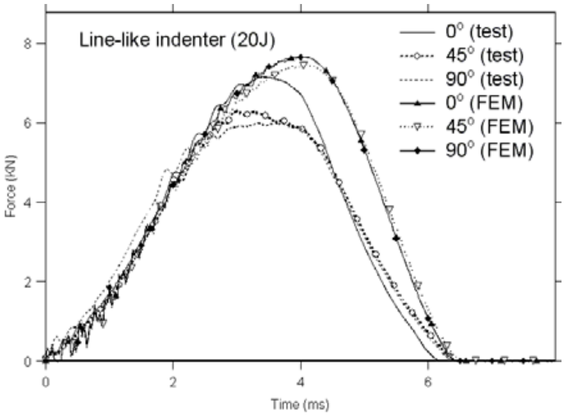

Figure 5.74 Impact force histories of GLARE 2 impacted by line-like indenter (20-joule)

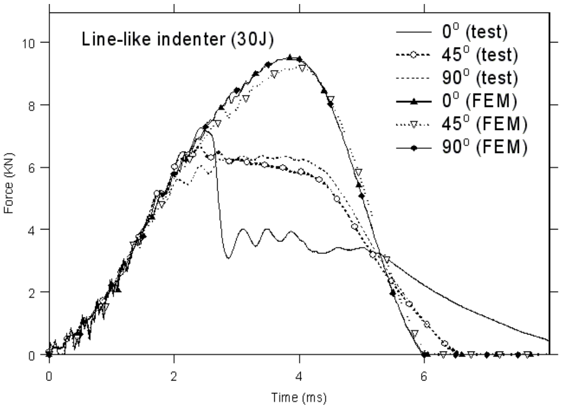

Figure 5.75 Impact force histories of GLARE 2 impacted by line-like indenter (30-joule)

Above finite element models were applied on the unidirectional GLARE 2 with the same assumption, same mesh and the same types of materials. All results are listed from Figure 5.70 to Figure 5.75 Similar to impact on GLARE 3, larger errors come with larger indenter for the impact duration. And for line-like Charpy indenter, simulation can't provide the damage patterns of GLARE 2 either. With 0.625" diameter indenter, through the thickness cracks were induced in GLARE 2 under 20 and 30-joule impact. LS-DYNA3D program can predict such kind of damage. Figure 5.71 shows the crack on the non-impacted side under 30-joule impact. The cracks in this simulation were shorter than the actual cracks measured from experiments. A fracture based failure criterion and finer mesh may need to provide more accurate results of simulation.

5.4.3 Summary

Finite element code LS-DYNA3D was used to simulate the impact on GLARE 5(3/2) with [0°/90°/90°/0°] cross-ply glass-epoxy, CCNY A with unidirectional glass-epoxy, as well as GLARE 2 and GLARE 3 subjected to various impactors. Results indicate that the impact force histories and deflection can be simulated fairly close to experimental results using the finite element model developed in this study. For more accurate damage patterns and impact responses, above finite element models need to be improved, especially when impact energy is higher and larger size impactors are adopted.

CHAPTER 6: CONCLUSIONS AND FUTURE STUDY

In this research, impact on fiber-metal laminates (ARALL and GLARE) was studied experimentally with a drop-weight tester and numerically using an explicit 3-D nonlinear dynamic finite element code, LS-DYNA3D.

The ultrasonic scanning and sectioning microscopy techniques were adopted to evaluate damage patterns. Damage includes indentation around impact center, delamination between aluminum and glass (*or* aramid)-epoxy composite layers, cracks in aluminum layers, and damage in composite layers. Relatively, more severe damage occurred on the nonimpact side of fiber-metal laminates. Usually, only the profile of damage zone can be detected by ultrasonic C-scan. Thus, in order to record the details of damage inside the fiber-metal laminates, the sectioning microscopy technique should be used.

GLARE (which consists of glass-fibers) possesses higher impact damage tolerance than ARALL (which uses aramid-fibers). The impact resistance of GLARE can be improved by using more ductile aluminum alloy (e.g., 2024-T3) as constituent materials. As far as the effect of lay-up sequence is concerned, GLARE made of unidirectional plies offers the worst impact damage resistance; it is followed by GLARE with 0°/90° cross-plies, while quasi-isotropic GLARE consisting of 0°/90°/±45° plies shows the best resistance to impact.

Increasing the thickness can increase the impact resistance of GLARE 5. The threshold impact energy causing the formation of visible cracks is parabolically proportional to the thickness. Thus, the impact energy can be used as a scale parameter of damage size.

The damage stages with increasing impact energies for thin fiber-metal laminates are as following: at lower energy impact, only delamination can be induced between the outer aluminum sheet and its adjacent fiber-epoxy layer on the nonimpact side; then, the nonimpact side aluminum sheet fractures in accompany with delamination inside; finally, through-thickness cracks occur under higher energy impact. For thicker FMLs, multiple delaminations occur near the impact side at relatively low impact energy. More severe damages, including cracks in the outer aluminum sheet and fiber breakage in composite layer, appear on the nonimpact side when higher impact energy is introduced.

For GLARE 5(3/2) in the temperature range of –50°C (–58°F) to 95°C (203°F), experimental results indicate that the environmental temperatures do not significantly affect its impact properties. However, testing results at 120°C (248°F) shows substantial reduction in the maximum impact force.

The smaller the indenter, the more severe local damages in GLARE laminates. Larger indenter can only induce global deflection with no significant cracks and delaminations around the impact site. There is no significant difference in impact response between GLARE 2 and GLARE 3 under the impact of larger indenter. Hence the unidirectional fiber-metal laminates should be avoided if impact damage is a major concern. This is true in particular for small-object impact. For line-like indenters, the relative angle between the indenter and fibers did not significantly affect the impact response of GLARE.

The finite element code LS-DYNA3D was used to distinguish the difference in impact behaviors of GLARE 5(3/2) (which contains [0°/90°/90°/0°] cross-ply glass-epoxy layers) and CCNY A (which is similar to GLARE 5(3/2) with exception for the unidirectional glass-epoxy layers). The code was also used to study GLARE 2 and GLARE 3 under impact with various shapes and sizes of impactors. The results indicate that the impact force and deflection histories can be simulated fairly close to experimental results using the finite element model developed in this study.

The main contributions of this study include:

- Through the investigation of the thickness effect, the different damage patterns between thinner and thicker FMLs were observed for the first time. Under low-velocity impact, damages in FMLs are dominated by bending for thinner specimens while damages become Hertzian damages for thicker specimens.
- For the first time, impact on FMLs with various indenters was conducted.
- Finite element models using commercially available package were successfully developed for fiber-metal laminates and can be used to help the optimal design of these novel materials.

Further investigation is needed in order to understand fully the behaviors of FMLs. Traditionally, fiber-metal laminates, such as the types used in this study, consist of thermoset epoxy. Newer FMLs, which are made of thermoplastic epoxy, have been developed recently and should be studied in more details for future engineering applications (see Cantwell, et al. [40]). Only low velocity impact studies were conducted in this study. Investigations under other conditions, which include fatigue, ballistic (high velocity) impact, and adverse environments, should be considered as well.

For more accurate damage patterns and impact responses, the above-mentioned finite element models need to be improved furthermore. In this study, the glass-fiber reinforced epoxy was assumed linearly elastic prior to damage. In the future, the material model of glass-fiber reinforced epoxy may be assumed as nonlinear elastic. All material properties used in finite element analyses of this study were assumed dynamic insensitive due to lack of experimental data of dynamic (strain rate) effect on mechanical behaviors. Further studies, especially those for ballistic impact problems, may need to take into account the sensitivities to strain-rate of mechanical properties. Finally, proper “erosion” criteria may also be added into finite element simulation for removing damaged elements numerically. This is especially important if one applies dynamic nonlinear finite element codes to high velocity impact problems.

APPENDIX: THEORETICAL BACKGROUND OF LS-DYNA

In this study, the commercial general-purpose finite element code LS-DYNA was used for analysis of large deformation impact response of structures. Some basic theoretical approaches adopted in this finite element code are presented here. For more information, please refer to the LS-DYNA theoretical manual [317].

A.1 Non-linear Finite Element Analysis

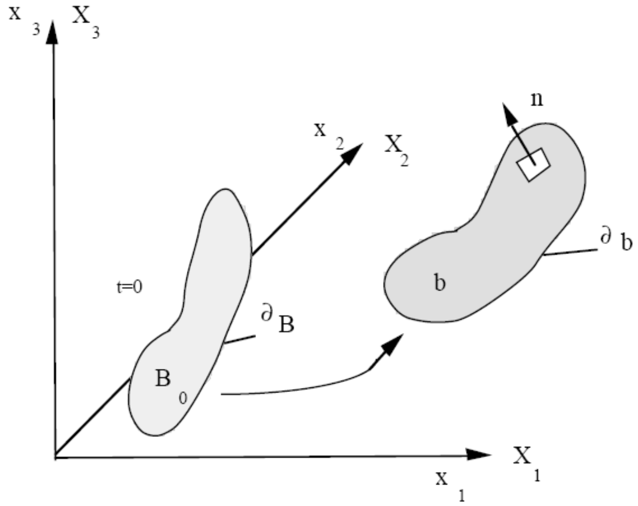

Figure A.1 Coordinate system

For the body shown in Figure A.1, a point in the solid body *b* initially at X_α ($\alpha = 1$, 2, 3) in the rectangular material coordinate system moves to point x_i ($i = 1$, 2 3) in the same coordinate system. By using the Lagrangian formulation, the time-dependant deformation can be expressed in terms of X_α and time *t*

$$x_i = x_i(X_\alpha, t) \tag{A-1}$$

with the initial condition at time $t = 0$

$$x_i(X_\alpha, 0) = X_\alpha \tag{A-2}$$

$$\dot{x}_i(X_\alpha, 0) = V_i(X_\alpha) \tag{A-3}$$

where V_i denotes the initial velocities. The momentum equation for above problem is

$$\sigma_{ij,j} + \rho f_i = \rho \ddot{x}_i \tag{A-4}$$

with the traction boundary conditions on ∂b_1

$$\sigma_{ij} n_i = t_i(t) \tag{A-5}$$

The displacement boundary conditions on boundary ∂b_2 is

$$x_i(X_\alpha, t) = D_i(t) \tag{A-6}$$

and the contact discontinuity along an interior boundary ∂b_3 when $x_i^+ = x_i^-$.

$$(\sigma_{ij}^+ - \sigma_{ij}^-) n_i = 0 \tag{A-7}$$

Here σ_{ij} is the Cauchy stress, ρ the current density, f the body force density, $\ddot{x}$ acceleration, and n_j an outward unit vector normal to the boundary of the solid, ∂b.

With V denotes the relative volume and ρ_0 the reference density, the mass conservation can be stated as

$$\rho V = \rho_0 \tag{A-8}$$

The determination of the deformation gradient matrix, F_{ij}, is defined as

$$F_{ij} = \frac{\partial x_i}{\partial X_j} \tag{A-9}$$

The energy equation

$$\dot{E} = V s_{ij} \dot{\varepsilon}_{ij} - (p + q)\dot{V} \tag{A-10}$$

is integrated in time and is used for equation of state evaluations and global energy balance. Here s_{ij} and p represent the deviatory stresses and pressure, respectively, and $\dot{\varepsilon}_{ij}$

is the strain rate tensor, which is defined as

$$s_{ij} = \sigma_{ij} + (p+q)\delta_{ij} \tag{A-11}$$

$$p = -\tfrac{1}{3}\sigma_{ij}\delta_{ij} - q = -\tfrac{1}{3}\sigma_{kk} - q \tag{A-12}$$

where q and δ_{ij} are the bulk viscosity and the Kronecker delta tensor, respectively.

Using Equations (A-4) to (A-7), we have

$$\int_v (\rho\ddot{x}_i - \sigma_{ij,j} - \rho f)\delta x_i dv + \int_{\partial b_1} (\sigma_{ij} n_j - t_i)\delta x_i ds + \int_{\partial b_3} (\sigma_{ij}^+ - \sigma_{ij}^-) n_j \delta x_i ds = 0 \tag{A-13}$$

with δx_i satisfies the boundary conditions on ∂b_2. Applying the divergence theorem in which

$$\int_v (\sigma_{ij}\delta x_i),_j \, dv = \int_{\partial b_1} \sigma_{ij} n_j \delta x_i ds + \int_{\partial b_3} (\sigma_{ij}^+ - \sigma_{ij}^-) n_j \delta x_i ds \tag{A-14}$$

and noting that

$$(\sigma_{ij}\delta x_i),_j = \sigma_{ij,j}\delta x_i + \sigma_{ij}\delta x_{i,j} \tag{A-15}$$

we have the weak form of the equilibrium equations:

$$\delta\pi = \int_v \rho\ddot{x}_i \delta x_i dv + \int_v \sigma_{ij}\delta x_{i,j} dv - \int_v \rho f_i \delta x_i dv - \int_{\partial b_1} t_i \delta x_i ds = 0 \tag{A-16}$$

Superimposing a mesh of finite elements interconnected at nodal points on a reference configuration and track particles through time, we have

$$x_i(X_\alpha, t) = x_i(X_\alpha(\xi,\eta,\varsigma),t) = \sum_{j=1}^{k} \phi_j(\xi,\eta,\varsigma) x_i^j(t) \tag{A-17}$$

where ϕ_j denotes the shape functions of the parametric coordinates (ξ,η,ς), k the number of nodes defining the element, and x_i^j the coordinate of j^{th} node in the i^{th} direction.

Taking the summation over the n elements

$$\delta\pi = \sum_{m=1}^{n} \delta\pi_m = 0 \tag{A-18}$$

and

$$\sum_{m=1}^{n} \{ \int_{v_m} \rho \ddot{x}_i \Phi_i^m dv + \int_{v_m} \sigma_{ij}^m \Phi_{i,j}^m dv - \int_{v_m} \rho f_i \Phi_i^m dv - \int_{\partial b_1} t_i \Phi_i^m ds \} = 0 \tag{A-19}$$

where $$\Phi_i^m = (\phi_1, \phi_2, \ldots, \phi_k)_i^m \tag{A-20}$$

In matrix notation, it becomes

$$\sum_{m=1}^{n} \{ \int_{v_m} \rho N^t N a dv + \int_{v_m} B^t \sigma dv - \int_{v_m} \rho N^t b dv - \int_{\partial b_1} N^t t ds \}^m = 0 \tag{A-21}$$

where *N* is an interpolation matrix, σ the stress vector defined as

$$\sigma^t = (\sigma_{xx}, \sigma_{yy}, \sigma_{zz}, \sigma_{xy}, \sigma_{yz}, \sigma_{zx}) \tag{A-22}$$

B the strain-displacement matrix and *a* the nodal acceleration vector

$$\begin{bmatrix} \ddot{x}_1 \\ \ddot{x}_2 \\ \ddot{x}_3 \end{bmatrix} = N \begin{bmatrix} a_{x_1} \\ a_{x_2} \\ \vdots \\ a_{y_k} \\ a_{z_k} \end{bmatrix} = Na \tag{A-23}$$

b the body force vector and *t* applied traction loads vector

$$b = \begin{bmatrix} f_x \\ f_y \\ f_z \end{bmatrix}, \; t = \begin{bmatrix} t_x \\ t_y \\ t_z \end{bmatrix} \tag{A-24}$$

A.2 Contact

The treatment of contact is an important issue for impact problems that involve contact between two or more components. In these problems, a contact force, which is normal to the contacting surfaces, is acting on the bodies when they touch each other. If there is friction between the surfaces, shear forces may be created that resist the tangential motion (sliding) of the bodies. The general aim of contact simulations is to identify the areas on the surfaces that are in contact and to calculate the contact pressures generated. In a finite element program, nodes lying in those contact surfaces are referred to as slave and master nodes, respectively.

In a finite element analysis, contact conditions are a special class of discontinuous constraint, allowing forces to be transmitted from one part of the model to another. The constraint is discontinuous because it is applied only when the surfaces are in contact. When the surfaces separate, no constraint is applied. The analysis has to be able to detect when surfaces are in contact and apply the contact constraints accordingly. Similarly, the analysis must be able to detect when surfaces separate and remove the contact constraints.

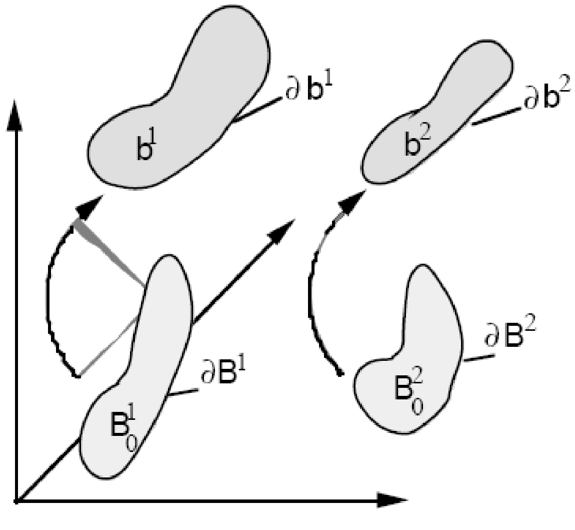

Figure A.2 Reference and deformed configuration

Consider the time-dependent motion of two bodies occupying regions B^1 and B^2 with ∂B^1 and ∂B^2 as the boundaries in their undeformed configuration at time zero (Figure A.2). Assume the intersection of them satisfies

$$B^1 \bigcap B^2 = 0 \tag{A-25}$$

The deformed configurations are shown in the same figure with occupying regions b^1 and b^2 bounded by ∂b^1 and ∂b^2. Under the condition of impenetrability,

$$b^1 \bigcap b^2 = 0 \tag{A-26}$$

as well as the contact interface of the intersection ∂b^c

$$\partial b^c = \partial b^1 \bigcap \partial b^2 = 0 \tag{A-27}$$

Once $\partial b^1 \bigcap \partial b^2 \neq 0$ occurs, constraints are needed to be applied in order to prevent penetration. There are four approaches usually adopted to treat the contact surface constraints [14], i.e.,

1. The Lagrange multiplier method
2. The penalty method
3. The augmented Lagrangian method
4. The perturbed Lagrangian method

To impose the contact constraints through the Lagrange multiplier approach, the Lagrange multiplier trial function $\lambda(X_\alpha, t)$ and the corresponding test function $\delta\lambda(X_\alpha, t)$ are defined as following

$$\lambda(X_\alpha, t) = \sum_{I \in \partial b^c} \Lambda_I(X_\alpha)\lambda_I(t) \tag{A-28}$$

with $\lambda(X_\alpha, t) \geq 0$ and $\delta\lambda(X_\alpha, t) \leq 0$ on ∂b^c

where $\Lambda_I(X_\alpha)$ are shape functions.

The weak form is

$$\delta\pi_L = \delta\pi + \delta G_L = \int_v \rho\ddot{x}_i \delta x_i dv + \int_v \sigma_{ij} \delta x_{i,j} dv - \int_v \rho f_i \delta x_i dv \\ - \int_{\partial b_1} t_i \delta x_i ds + \int_{\partial b^c} \delta(\lambda \gamma_N) ds \geq 0 \tag{A-29}$$

where γ_N is the rate of interpenetration of the two bodies on ∂b^c, i.e.,

$$\gamma_N(X_\alpha, t) = (\dot{x}_j^1 + \dot{x}_j^2) n_j^1 \tag{A-30}$$

Introducing the matrix notation, yield the equations of motion and the interpenetration condition

$$M\ddot{x} + f^{\text{int}} - f^{ext} + G^T \lambda = 0 \tag{A-31}$$

$$G\dot{x} \leq 0 \tag{A-32}$$

where $$G = \int_{\partial b^c} \Lambda^T \Phi ds \tag{A-33}$$

In the penalty method, the impenetrability constraint is imposed as a penalty normal traction along the contact surface. In contrast to the Lagrange multiplier method, the penalty method allows some interpenetration. Two forms of the penalty method are introduced here: a penalty proportional to the square of the interpenetration rate γ_N and a penalty, which is an arbitrary function of the interpenetration g_N and its rate γ_N. For the first penalty form, the equivalence of the weak form can be stated as follows:

$$\delta\pi_p = \delta\pi + \delta G_p = 0 \tag{A-34}$$

where $$\delta G_p = \int_{\partial b^c} \frac{\beta}{2} \delta(\gamma_N{}^2) \mathrm{H}(\gamma_N) ds \tag{A-35}$$

β is the penalty parameter and $\mathrm{H}(\gamma_N)$ is the Heaviside step function,

$$\mathrm{H}(\gamma_N) = \begin{cases} 1 & if\ \gamma_\mathrm{N} > 0 \\ 0 & if\ \gamma_\mathrm{N} < 0 \end{cases} \tag{A-36}$$

The above form of the penalty method often performs quite poorly since it may allow excessive interpenetration as the relative velocities of two surfaces become equal or negative, which causes the normal traction to vanish. Therefore, the second form of penalty method is adopted, in which an interface pressure $p = \overline{p}(g_N, \gamma_N)\mathrm{H}(\overline{p})$ is defined. The weak form becomes (A-34) as well as

$$\delta G_p = \int_{\partial b^c} \delta(\gamma_N p) ds \qquad \text{(A-37)}$$

An example of the penalty function is

$$p = \beta_1 g_N + \beta_2 \gamma_N \qquad \text{(A-38)}$$

The corresponding matrix form motion equation is

$$M\ddot{x} + f^{\text{int}} - f^{ext} + f^c = 0 \qquad \text{(A-39)}$$

where $$f^c = \int_{\partial b^c} \Phi^T p ds \qquad \text{(A-40)}$$

For the augmented Lagrangian method, the weak form is

$$\delta\pi_{AL} = \delta\pi + \delta G_{AL} \geq 0 \qquad \text{(A-41)}$$

$$\delta G_{AL} = \int_{\partial b^c} \delta(\lambda \gamma_N + \frac{\alpha}{2} {\gamma_N}^2) ds \qquad \text{(A-42)}$$

α is a positive parameter. The matrix form motion equations are

$$M\ddot{x} + f^{\text{int}} - f^{ext} + G^T \lambda + P_c \dot{x} = 0 \qquad \text{(A-43)}$$

$$G\dot{x} \leq 0 \qquad \text{(A-44)}$$

$$P_c = \int_{\partial b^c} \alpha \Phi^T \Phi ds \qquad \text{(A-45)}$$

The perturbed Lagrangian weak form is

$$\delta\pi_{PL} = \delta\pi + \delta G_{PL} = 0 \qquad \text{(A-46)}$$

with $$\delta G_{PL} = \int_{\partial b^c} \delta(\lambda \gamma_N^+ - \frac{1}{2\beta}\lambda^2) ds \qquad \text{(A-47)}$$

where β is a large constant and $\gamma_N^+ = \gamma_N \mathrm{H}(\gamma_N)$

So the matrix form equations become

$$M\ddot{x} + f^{\text{int}} - f^{ext} + G^T \lambda = 0 \qquad \text{(A-48)}$$

$$G\dot{x} - J\lambda = 0 \qquad \text{(A-49)}$$

$$J = \frac{1}{\beta}\int_{\partial b^c} \Lambda^T \Lambda ds \qquad \text{(A-50)}$$

A.3 Overview of Explicit Dynamics

The explicit dynamics procedure can be an effective tool for solving a wide variety of nonlinear solid and structural mechanics problems. The distinguishing characteristics of the explicit and implicit methods are:

- Explicit methods require a small time increment size that depends solely on the highest natural frequencies of the model and is independent of the type and duration of loading. Simulations generally take on the order of 10,000 to 1,000,000 increments, but the computational cost per increment is relatively small.
- Implicit methods do not place an inherent limitation on the time increment size; increment size is generally determined from accuracy and convergence considerations. Implicit simulations typically take orders of magnitude fewer increments than explicit simulations. However, since a global set of equations must be solved in each increment, the cost per increment of an implicit method is far greater than that of an explicit method.

The explicit method is especially well suited to solving high-speed dynamic events that require many small increments to obtain a high-resolution solution. If the duration of the event is short, the solution can be obtained efficiently. Contact conditions and other extremely discontinuous events are readily formulated in the explicit method and can be enforced on a node-by-node basis without iteration. The nodal accelerations can be adjusted to balance the external and internal forces during contact. The explicit method is often very efficient in solving certain classes of problems that are essentially static. Quasi-static process simulation problems involving complex contact such as forging, rolling, and sheet forming generally fall within these classes. Sheet forming problems usually include very large membrane deformations, wrinkling, and complex frictional contact conditions. Bulk forming problems are characterized by large distortions, flash formation, and contact interaction with the dies. Material degradation and failure often lead to severe convergence difficulties in implicit analysis programs, but explicit method can model such materials well.

The most striking feature of the explicit method is the lack of a global tangent stiffness matrix, which is required with implicit methods. Since the state of the model is advanced explicitly, iterations and tolerances are not required.

The procedures of explicit time integration are as following. At the beginning of the increment the program solves for dynamic equilibrium, which states that the nodal mass matrix, M, times the nodal accelerations, $\ddot{u}$, equals the total nodal forces (the difference between the external applied forces, f^{ext}, and internal element forces, f^{int}).

$$M\ddot{u} = f^{ext} - f^{\text{int}} \qquad \text{(A-51)}$$

The accelerations at the beginning of the current increment (time t) are calculated as

$$\ddot{u}\big|_t = (M)^{-1}(f^{ext} - f^{\text{int}})\big|_t \tag{A-52}$$

Since the explicit procedure always uses a diagonal, or lumped, mass matrix, solving for the accelerations is trivial, and there are no simultaneous equations to solve. The acceleration of any node is determined completely by its mass and the net force acting on it, making the nodal calculations very inexpensive.

The accelerations are integrated through time using the central difference rule, which calculates the change in velocity assuming that the acceleration is constant. This change in velocity is added to the velocity from the middle of the previous increment to determine the velocities at the middle of the current increment:

$$\dot{u}\Big|_{(t+\frac{\Delta t}{2})} = \dot{u}\Big|_{(t-\frac{\Delta t}{2})} + \frac{(\Delta t\big|_{(t+\Delta t)} + \Delta t\big|_{(t)})}{2}\ddot{u}\big|_{(t)} \tag{A-53}$$

The velocities are integrated through time and added to the displacements at the beginning of the increment to determine the displacements at the end of the increment:

$$u\big|_{(t+\Delta t)} = u\big|_{(t)} + \Delta t\big|_{(t+\Delta t)}\dot{u}\Big|_{(t+\frac{\Delta t}{2})} \tag{A-54}$$

Thus, satisfying dynamic equilibrium at the beginning of the increment provides the accelerations. Knowing the accelerations, the velocities and displacements are advanced “explicitly” through time. The term “explicit” refers to the fact that the state at the end of the increment is based solely on the displacements, velocities, and accelerations at the beginning of the increment. This method integrates constant accelerations exactly. For the method to produce accurate results, the time increments must be quite small so that the accelerations are nearly constant during an increment. Since the time increments must be small, analyses typically require many thousands of increments. Fortunately, each increment is inexpensive because there are no simultaneous equations to solve. Most of the computational expense lies in the element calculations to determine the internal forces of the elements acting on the nodes. The element calculations include determining element strains from he strain rate and applying material constitutive relationships (the element stiffness) to determine element stresses and, consequently, internal forces. Then set the next time step and start the same procedures all over again until the termination time is reached.

With the explicit method, the state of the model is advanced through a time increment, which is based on the state of the model at the start of the increment. The amount of time that the state can be advanced and still remain an accurate representation of the problem is typically quite short. If the time increment is larger than this maximum amount of time, the increment is said to have exceeded the *stability limit*. A possible effect of exceeding the stability limit is a numerical instability, which may lead to an unbounded solution. It generally is not possible to determine the stability limit exactly. So conservative estimates are used instead. The stability limit has a great effect on reliability and accuracy, so it must be determined consistently and conservatively. In LSDYNA, the time step increment is determined as following.

$$\Delta t = \alpha \cdot \min\{\Delta t_1, \Delta t_2, \Delta t_3, \cdots, \Delta t_N\} \tag{A-55}$$

where N is the number of elements. The scale factor α is typically set to 0.90 (default) or a smaller value. So the critical time increment is determined by the size and type of elements as well as the material properties.

For solid elements, the time increment is calculated as

$$\Delta t_e = \frac{L_e}{\{[Q + (Q^2 + c^2)^{1/2}]\}} \tag{A-56}$$

where Q is a function of the bulk viscosity coefficients C_0 and C_1:

$$Q = \begin{cases} C_1 c + C_0 L_e \left|\dot{\varepsilon}_{kk}\right| & for\ \ \dot{\varepsilon}_{kk} < 0 \\ 0 & for\ \ \dot{\varepsilon}_{kk} \geq 0 \end{cases} \tag{A-57}$$

L_e is a characteristic length:

$$\begin{cases} L_e = \dfrac{v_e}{A_{e\max}} & \text{8 node solids} \\ L_e = \text{minimum altitude} & 4\ node\ tetrahedras \end{cases} \tag{A-58}$$

with v_e as the element volume, A_{emax} as the area of the largest side, and *c* as the adiabatic sound speed. For elastic materials with a constant bulk modulus, density, ρ, Young's modulus, *E*, and Poisson's ratio, *v*, the sound speed is given by

$$c = \sqrt{\frac{E(1-\nu)}{(1+\nu)(1-2\nu)\rho}} \tag{A-59}$$

For beam or truss element with length, *L*, and wave speed $c = \sqrt{E/\rho}$, the time increment is

$$\Delta t_e = L/c \tag{A-60}$$

For shell with the characteristic length, L_s, the time step increment is given by

$$\Delta t_e = L_s/c \tag{A-61}$$

where

$$c = \sqrt{\frac{E}{(1-\nu^2)\rho}} \tag{A-62}$$

The stability limit is the transit time of a dilatational wave across the distance defined by the characteristic element length. If we know the size of the smallest element dimension and the wave speed of the material, we can estimate the stability limit. For example, if the smallest element dimension is 5 mm and the dilatational wave speed is 5000 m/s, the stable time increment is on the order of 1×10^{-6} s.

REFERENCES

1. Aboussaleh, M., and Boukhili, R. “The contact behavior between laminated composites and rigid impactors.” Composite Structures 43: 165-178 (1998).

2. Abrate, S. *Impact on Composite Structures*. Cambridge University Press, Cambridge, UK, 1998.

3. Abrate, S. “Localized impact on sandwich structures with laminated facings.” Applied Mechanics Review 50(2): 69-82 (1997).

4. Abrate, S. “Modeling of impacts on composite structures.” Composite Structures 51: 129-138 (2001).

5. Ambur, D.R., Prasad, C.B., and Waters, W.A., Jr. “A dropped-weight apparatus for low-speed impact testing of composite structures.” Experimental Mechanics: 77-82 (March 1995).

6. Ambur, D.R., and Starnes, J.H., Jr. “Low-speed impact damage-initiation characteristics of selected laminated composite plates.” AIAA J. 33(10): 1919-1925 (1995).

7. Anderson, T., and Madenci, E. “Experimental investigation of low-velocity impact characteristics of sandwich composites.” Composite Structures 50: 239-247 (2000).

8. Armanios, E.A., Rehfield, L.W., AND Weinstein, F. “Understanding and predicting sublaminate damage mechanisms in composite structures.” ASTM STP 1059: 231-250 (1990).

9. Aymerich, F., and Meili, S. “Ultrasonic evaluation of matrix damage in impacted composite laminates.” Composites: Part B 31: 1–6 (2000).

10. Behr, R.A., Kremer, P.A., Dharani, L.R., Ji, F.S., and Kaiser, N.D. “Dynamic strains in architectural laminated glass subjected to low velocity impacts from small projectiles.” J. Materials Science 34: 5749-5756 (1999).

11. Beissel, S.R., Johnson, G.R., and Popelar, C.H. “An element-failure algorithm for dynamic crack propagation in general directions.” Engineering Fracture Mechanics 61: 407-425 (1998).

12. Belingardi, G., Gugliotta, A., and Vadori, R. “Numerical simulation of fragmentation of composite material plates due to impact.” Int. J. Impact Engineering 21(5): 335-347 (1998).

13. Belingardi, G., and Vadori, R. “Low velocity impact tests of laminate glass-fiber-epoxy matrix composite material plates.” International Journal of Impact Engineering 27: 213–229 (2002).

14. Belytschko, T., Liu, W.K., and Moran, B. *Nonlinear finite elements for continua and structures.* John Wiley & Sons, LTD, 2000.

15. Benmedakhene, S., Kenane, M., and Benzeggagh, M.L. “Initiation and growth of delamination in glass/epoxy composites subjected to static and dynamic loading by acoustic emission monitoring.” Composites Science and Technology 59: 201-208 (1999).

16. Berthelot, J.M., and Le Corre, J.F. “A model for transverse cracking and delamination in cross-ply laminates.” Composites Science and Technology 60: 1055-1066 (2000).

17. Besant, T., Davies, G.A.O., and Hitchings, D. “Finite element modeling of low velocity impact of composite sandwich panels.” Composites: Part A 32: 1189-1196 (2001).

18. Bianchi, C. Thesis work: *Impact on Cargo Floors – a comparison between different sandwich materials*. TU Delft, October 1995.

19. Bishop, S.M. “The mechanical performance and impact behaviour of carbon-fibre reinforced PEEK.” Composite Structures 3: 295-318 (1985).

20. Bittencourt, E., and Creus, G.J. “Finite element analysis of three-dimensional contact and impact in large deformation problems.” Computers and Structures 69: 219-234 (1998).

21. Bogdanovich, A.E., and Iarve, E.V. “Numerical analysis of impact deformation and failure in composite plates.” J. Composite Materials 26(4): 520-545 (1992).

22. Bolduc, M., and Roy, C. “Evaluation of impact damage in composite materials using acoustic emission.” ASTM STP 1156: 127-138 (1993).

23. Boll, D.J., Bascom, W.D., Weidner, J.C., and Murri, W.J. “A microscopy study of impact damage of epoxy-matrix carbon-fibre composites.” J. Materials Science 21: 2667-2677 (1986).

24. Borg, R., Nilsson, L., and Simonsson, K. “Simulation of delamination in fiber composites with a discrete cohesive failure model.” Composites Science and Technology 61: 667–677 (2001).

25. Borg, R., Nilsson, L., and Simonsson, K. “Modeling of delamination using a discretized cohesive zone and damage formulation.” Composites Science and Technology 62: 1299–1314 (2002).

26. Bouzid, S., Nyoungue, A., Azari, Z., Bouaouadja, N., and Pluvinage, G. “Fracture criterion for glass under impact loading.” Int. Journal of Impact Engineering 25: 831–845 (2001).

27. Buynak, C.F., and Moran, T.J. “Characterization of impact damage in composites.” Review of Progress in Quantitative nondestructive Evaluation Vol. 6B: 1203-1211 (1987).

28. Buynak, C.F., Moran, T.J., and Donaldson, S. “Characterization of impact damage in composites.” SAMPE J. 24(2): 35-39 (1988).

29. Byun, C., and Kapania, R.K. “Nonlinear impact response of thin imperfect laminated plates using a reduction method.” Composites Engineering 2(5-7): 391-410 (1992).

30. Cairns, D.S. “A simple, elasto-plastic contact law for composites.” J. Reinforced Plastics and Composites 10(4): 423-433 (1991).

31. Cairns, D.S., and Lagace, P.A. “Transient response of graphite/epoxy and kevlar/epoxy laminates subjected to impact.” AIAA J. 27(11): 1590-1596 (1989).

32. Cairns, D.S., and Lagace, P.A. “A consistent engineering methodology for the treatment of impact in composite materials.” J. Reinforced Plastics and Composites 11(4): 395-412 (1992).

33. Cantwell, W.J., Davies, P., and Kausch, H.H. “Repair of impact-damaged carbon fiber PEEK composites.” SAMPE Journal 27(6): 30-35 (1991).

34. Cantwell, W.J., and Morton, J. “Detection of impact damage in CFRP laminates.” Compos0ite Structures 3: 241-257 (1985).

35. Cantwell, W.J., and Morton, J. “Geometrical effects in the low velocity impact response of CFRP.” Composite Structures 12(1): 39-59 (1989).

36. Cantwell, W.J., and Morton, J. “The impact resistance of composite materials-a review.” Composites 22(5): 347-362 (1991).

37. Cantwell, W.J., and Morton, J. “Comparison of the low and high velocity impact response of CFRP.” Composites 20(6): 545-551 (1989).

38. Cantwell, W.J. “The influence of fibre stacking sequence on the high velocity impact response of CFRP.” J. Materials Science Letters 7: 756-758 (1988).

39. Cantwell, W.J., Scudamore, R., Ratcliffe, J., and Davies, P. “Interfacial fracture in sandwich laminates.” Composites Science and Technology 59: 2079-2085 (1999).

40. Cantwell, W.J., Wade, G., et al. “The high velocity impact response of novel fiber metal laminates.” 2001 ASME IMECE2001/AMD-25423 (2001).

41. Caprino, G., Crivelli Visconti I., and Di Ilio, A. “Elastic behaviour of composite structures under low velocity impact.” Composites 15(3): 231-234 (1984).

42. Caprino, G., and Lopresto, V. “The significance of indentation in the inspection of carbon fibre-reinforced plastic panels damaged by low-velocity impact.” Composites Science and Technology 60: 1003-1012 (2000).

43. Caprino, G., and Lopresto, V. “On the penetration energy for fibre-reinforced plastics under low-velocity impact conditions.” Composites Science and Technology 61: 65-73 (2001).

44. Caprino, G., Lopresto, V., Scarponi, C., and Briott, G. “Influence of material thickness on the response of carbon-fabric/epoxy panels to low velocity impact.” Composites Science and Technology 59: 2279-2286 (1999).

45. Caprino, G., and Teti, R. “Impact and post-impact behavior of foam core sandwich structures.” Composite Structures 29(1): 47-55 (1994).

46. Carvalho, A., and Soares, C.G. “Dynamic response of rectangular plates of composite materials subjected to impact loads.” Composite Structures 34: 55-63 (1996).

47. Castrodeza, E.M., Bastian, F.L., Yawny, A., and Perez Ipina, J.E. “Fracture micromechanisms of fiber-metal laminates: In-Situ SEM observations.” Journal of Composite materials 36(4): 387-400 (2002).

48. Challenger, K.D. “The damage tolerance of carbon fiber reinforced composites-a workshop summary.” Composite Structures 6: 295-318 (1986).

49. Chamis, C.C., Hanson, M.P., and Serafini, T.T. “Impact resistance of unidirectional fiber composites.” ASTM STP 497: 324-349 (1972).

50. Chandrashekhara, K., Okafor, A.C., and Jiang, Y.P. “Estimation of contact force on composite plates using impact-induced strain and neural networks.” Composites Part B 29B: 363-370 (1998).

51. Chang, F.K., and Chang, K.Y. “A progressive damage model for laminated composites containing stress concentrations.” Journal of Composite materials 21(September): 834-855 (1987).

52. Chang, F.K., Choi, H.Y., and Jeng, S-T. “Characterization of impact damage in laminated composites.” SAMPE Journal 26(1): 18-25 (1990).

53. Chao, C.C., and Tu, C.Y. "Three-dimensional contact dynamics of laminated plates: Part 1. Normal impact." Composites: Part B 30: 9–22 (1999).

54. Chaudhuri, J., Choe, G.H., and Vinson, J.R. "Impact characterization of graphite fiber reinforced thermoplastic laminates." J. Reinforced Plastics and Composites 12: 677-685 (1993).

55. Chen, J.K., and Sun, C.T. "Analysis of impact response of buckled composite laminates." Composite Structures 3: 97-118 (1985).

56. Chen, J.K., and Sun, C.T. "Dynamic large deflection response of composite laminates subjected to impact." Composite Structures 4(1): 59-73 (1985).

57. Chen, J.L., and Sun, C.T. "Modeling of orthotropic elastic-plastic properties of ARALL laminates." Composites Science and Technology 36: 321-337 (1989).

58. Cheon, S.S., Lim, T.S., and Lee, D.G. "Impact energy absorption characteristics of glass fiber hybrid composites." Composite Structures 46: 267-278 (1999).

59. Choi, H.Y., Downs, R.J., and Chang, F.K. "A new approach toward understanding damage mechanisms and mechanics of laminated composites due to low-velocity impact: Part I-Experiments." J. Composite Materials 25: 992-1011 (Aug. 1991).

60. Choi, H.Y., Wang, H.S., and Chang, F.K. "Effect of laminate configuration and impactor's mass on the initial impact damage of graphite/epoxy/ composite plates due to line-loading impact." J. Composite Materials 26(6): 804-827 (1992).

61. Choi, H.Y., Wu, H.T., and Chang, F.K. "A new approach toward understanding damage mechanisms and mechanics of laminated composites due to low-velocity impact: Part II-analysis." J. Composite Materials 25: 1012-1038 (Aug. 1991).

62. Choi, H.Y., and Chang, F.K. "A model for predicting damage in Graphite/Epoxy laminated composites resulting from low-velocity point impact." J. Composite Materials 26(14): 2134-2169 (1992).

63. Christoforou, A.P., and Swanson, S.R. "Analysis of impact response in composite plates." Int. J. Solids Structures 27(2): 161-170 (1991).

64. Christoforou, A.P. "On the contact of a spherical indenter and a thin composite laminate." Composite Structures 26(1): 77-82 (1993).

65. Christoforou, A.P. "Impact dynamics and damage in composite structures." Composite Structures 52: 181-188 (2001).

66. Christoforou, A.P., and Yigit, A.S. "Characterization of impact in composite plates." Composite Structures 43: 15-24 (1998).

67. Chun, L., and Lam, K.Y. “Dynamic response of fully-clamped laminated composite plates subjected to low-velocity impact of a mass.” Int. J. Solids Structures 35(11): 963-979 (1998).

68. Clark, G. “Modeling of impact damage in composite laminates.” Composites 20(3): 209-214 (1989).

69. Clark, G., and Saunders, D.S. “Morphology of impact damage growth by fatigue in carbon fibre composite laminates.” Materials Forum 15(4): 333-342 (1991).

70. Collombet, F., Lalbin, X., Bonini, J., Martin, V., and Lataillade, J.L. “Damage criteria for the study of impacted composite laminates.” Composites Science and Technology 58: 679-686 (1998).

71. Collombet, F., Lalbin, X., and Lataillade, J.L. “Impact behavior of laminated composites: physical basis for finite element analysis.” Composites Science and Technology 58: 463-478 (1998).

72. Craig, D.M., and Chapman, C.E. “NDI of impact damaged composite panels.” British J. Non-destructive Testing 33(2): 64-68 (1991).

73. Curson, A.D., Leach, D.C., and Moore, D.R. “Impact failure mechanisms in carbon fiber/PEEK composites.” J. Thermoplastic Composite Materials 3: 24-31 (1990).

74. Curtis, P.T., and Bishop, S.M. “An assessment of the potential of woven carbon fibre-reinforced plastics for high performance applications.” Composites 15(4): 259-265 (1984).

75. Daniel, I.M. “Experimentation and modeling of composite materials.” Experimental Mechanics 39(1): 1-19 (1999).

76. Daniel, I.M., and Wooh, S.C. “Deformation and damage of composite laminates under impact loading.” In A.K. Mal, and Y.D.S. Rajapakse (eds.), Impact Response and Elastodynamics of Composites, ASME publication AMD-116: 11-26 (1990).

77. Daniel, I.M., Wooh, S.C., and Lee, J.W. “Defect and damage characterization in composite materials.” Review of Progress in Quantitative nondestructive Evaluation Vol. 6B: 1195-1202 (1987).

78. Davies, G.A.O., Hitchings, D., and Wang, J. “Prediction of threshold impact energy for onset of delamination in quasi-isotropic carbon/epoxy composite laminates under low-velocity impact.” Composites Science and Technology 60: 1-7 (2000).

79. Davis, G.A.O., and Zhang, X. “Impact damage prediction in carbon composite structures.” Int. J. Impact Engineering 16(1): 149-170 (1995).

80. Davis, G.A.O., Zhang, X., Zhou, G., and Watson, S. “Numerical Modeling of Impact Damage.” Composites 25(5): 342-350 (1994).

81. De Freitas, M., Silva, A., and Reis, L. “Numerical evaluation of failure mechanisms on composite specimens subjected to impact loading.” Composites: Part B 31: 199–207 (2000).

82. Delfosse, D., and Poursartip, A. “Energy-based approach to impact damage in CFRP laminates.” Composites Part A 28A: 647-655 (1997).

83. De Moura, M.F.S.F., Goncalves, J.P.M., Marques, A.T., and De Castro, P.M.S.T. “Modeling compression failure after low velocity impact on laminated composites using interface elements.” J. Composite Materials 31(15): 1462-1479 (1997).

84. De Moura, M.F.S.F., and Marques, A.T. “Prediction of low velocity impact damage in carbon-epoxy laminates.” Composites Part A 33: 361-368 (2002).

85. Demuts, E., Whitehead, R.S., and Deo, R.B. “Assessment of damage tolerance in composites.” Composite Structures 4: 45-58 (1985).

86. De Vries, T.J., Vlot, A., and Hashagen, F. “Delamination behavior of spliced Fiber Metal Laminates. Part 1. Experimental results.” Composite Structures 46: 131-145 (1999).

87. Dey, S.S., and Rao, V.T. “Transient response of circular plates and membranes: a numerical approach.” Int. J. Mechanical Science 39(12): 1405-1413 (1997).

88. Dobyns, A.L. “Analysis of simply supported plates subjected to static and dynamic loads.” AIAA J. 19(5): 642-650 (1981).

89. Dong, L., and Mistry, J. “Acoustic emission monitoring of composite cylinders.” Composite Structures 40(1): 43-53 (1998).

90. Dong, Y.J., Ye, N., and Bai, Y.L. “On-line observation of interlaminar damage by ultrasonic inspection.” Composites Science and Technology 59: 957-961 (1999).

91. Dorey, G., Sidey, G.R., and Hutchings, J. “Impact properties of carbon fibre/Kevlar 49 fibre hybrid composites.” Composites 9: 25-32 (1978).

92. El-Sayed, S.I., and Sridharan, S. “A study of crack growth in sandwich composite beams.” Proceedings of 2001 ASME IMECE/AD-25311 (November, 2001).

93. Espinosa, H.D., Lu, H-C, Zavattieri, P.D., and Dwivedi, S. “A 3-D finite deformation anisotropic visco-plasticity model for fiber composites.” J. Composite Materials 35(5): 369-410 (2001).

94. Evseev, E.G., and Morozov, E.V. "Explicit finite difference method in the dynamic analysis of composite structures." Composite Structures 39(3-4): 215-221 (1997).

95. Feng, Z.Q., Feng, Z.G., and Domaszewski, M. "Some computational aspects for analysis of low- and high-velocity impact of deformable bodies." International Journal of Non-Linear Mechanics 37: 1029-1036 (2002).

96. Flocker, F.W., and Dharani, L.R. "Stresses in laminated glass subject to low velocity impact." Engineering Structures 19 (10): 851-856 (1997).

97. *Foreign Object Impact Damage to Composites*. ASTM STP 568, American Society for Testing and Materials, 1975.

98. Found, M.S., and Howard, I.C. "Single and multiple impact behavior of a CFRP laminate." Composite Structures 32: 159-163 (1995).

99. Frock, B.G., Martin, R.M., Moran, T.J., and Shimmin, K.D. "Imaging of impact damage in composite materials." Review of progress in Quantitative Nondestructive Evaluation Vol. 7B: 1093-1099 (1988).

100. Fuoss, E., Straznicky, P.V., and Poon, C. "Effects of stacking sequence on the impact resistance in composite laminates – Part 1: parametric study." Composite Structures 41: 67-77 (1998).

101. Fuoss, E., Straznicky, P.V., and Poon, C. "Effects of stacking sequence on the impact resistance in composite laminates – Part 2: prediction method." Composite Structures 41: 177-186 (1998).

102. Ganapathy, S., Tripathy, B., and Rao, K.P. "damage and its growth in laminated composite circular/rectangular plates undergoing large deformations." Composite Structures 32: 367-373 (1995).

103. Gao, S.L., and Kim, J.K. "Scanning acoustic microscopy as a tool for quantitative characterization of damage in CFRPs." Composite Science and Technology 59: 345-354 (1999).

104. Gardiner, D.S., and Pearson, L.H. "Acoustic-emission monitoring of composite damage occurring under static and impact loading." Experimental Techniques: 22-28 (Nov. 1985).

105. Garg, A.C. "Delamination-a damage mode in composite structures." Engineering Fracture Mechanics 29(5): 557-584 (1988).

106. Gaudenzi, P., Barboni, R., and Mannini, A. "A finite element evaluation of single-layer and multi-layer theories for the analysis of laminated plates." Composite Structures 30: 427-440 (1995).

107. Gazonas, G.A. “Implementation of a finite strain plasticity model for Nylon 6/6 into DYNA3D.” Army Research Laboratory: ARL-RP-1 (September 2000).

108. Geubelle, P.H., and Baylor, J.S. “Impact-induced delamination of composites: a 2D simulation.” Composites Part B 29B**:** 589–602 (1998).

109. Ghasemi Nejhad, M.N., and Parvizi-Majidi, A. “Impact behaviour and damage tolerance of woven carbon fibre-reinforced thermoplastic composites.” Composites 21(2): 155-168 (1990).

110. Gong, J.C., and Sankar, B.V. “Impact properties of three-dimensional braided graphite/epoxy composites.” J. Composite Materials 25: 715-731 (1991).

111. Griffin, C.F. “Damage tolerance of toughened resin graphite composites.” ASTM STP 937: 23-33 (1985).

112. Gu, Z.L., and Sun, C.T. “Prediction of impact damage region in SMC composites.” Composite Structures 7: 179-190 (1987).

113. Guillaumat, L. “Reliability of composite structures - impact loading.” Computers and Structures 76: 163-172 (2000).

114. Guinard, S., Allix, O., Guedra-Degeorges, D., and Vinet, A. “A 3D damage analysis of low-velocity impacts on laminated composites.” Composites Science and Technology 62: 585–589 (2002).

115. Han, C., and Sun, C.T. “A study of pre-stress effect on static and dynamic contact failure of brittle materials.” International Journal of Impact Engineering 24: 597-611 (2000).

116. Hashagen, F., de Borst, R., and de Vries, T. “Delamination behavior of spliced Fiber Metal Laminates. Part 2. Numerical investigation.” Composite Structures 46: 147-162 (1999).

117. Hashagen, F., Schellekens, J.C.J., and De Borst, R. “Finite element procedure for modeling fibre metal laminates.” Composite Structures 32: 255-264 (1995).

118. Heitzer, J. “Dynamic interaction of a plate and an impactor.” Computers and Structures 60(5): 837-848 (1996).

119. Helms, J.E., Li, G.Q., and Pang, S.S. “Impact response of a composite laminate bonded to a metal substrate.” J. Composite Materials 35(3): 237-252 (2001).

120. Herup, E.J., and Palazotto, A.N. “Low-velocity impact damage initiation in graphite/epoxy/nomex honeycomb-sandwich plates.” Composites Science and Technology 57: 1581-1598 (1997).

121. Hirai, Y., Hamada, H., and Kim, J-K. "Impact response of woven glass-fabric composites-II. Effect of temperature." Composites Science and Technology 58: 119-128 (1998).

122. Hitchen, S.A., and Kemp, R.M.J. "The effect of stacking sequence on impact damage in a carbon fibre/epoxy composite." Composites 26(3): 207-214 (1995).

123. Hitchings, D., Robinson, P., and Javidrad, F. "A finite element model for delamination propagation in composites." Computers and Structures 60(6): 1093-1104 (1996).

124. Hong, S., and Liu, D. "On the relationship between impact energy and delamination area." Experimental Mechanics: 115-120 (June 1989).

125. Hoo Fatt, M.S., and Park, K.S. "Dynamic models for low-velocity impact damage of composite sandwich panels – Part A: Deformation." Composite Structures 52: 335-351 (2001).

126. Hoo Fatt, M.S., and Park, K.S. "Dynamic models for low-velocity impact damage of composite sandwich panels – Part B: Damage initiation." Composite Structures 52: 353-364 (2001).

127. Hou, J.P., Petrinic, N., Ruiz, C., and Hallett, S.R. "Prediction of impact damage in composite plates." Composites Science and Technology 60: 273-281 (2000).

128. Hou, J.P., Petrinic, N., and Ruiz, C. "A delamination criterion for laminated composites under low-velocity impact." Composites Science and Technology 61: 2069-2074 (2001)

129. Hu, N. "A solution method for dynamic contact problems." Computers and Structures 63(6): 1053-1063 (1997).

130. Hu, N., Sekine, H., Fukunaga, H., and Yao, Z.H. "Impact analysis of composite laminates with multiple delaminations." Int. Journal of Impact Engineering 22: 633-648 (1999).

131. Ireman, T., Thesken, J.C., et al. "Damage propagation in composite structural elements – coupon experiments and analyses." Composite Structures 36: 209-220 (1996).

132. Jackson, W.C., and Poe, C.C., Jr. "The use of impact force as a scale parameter for the impact response of composite laminates." J. Composites Technology and Research 15(4): 282-289 (1993).

133. Jansson, N.E., and Larsson, R. "A damage model for simulation of mixed-mode delamination growth." Composite Structures 53: 409-417 (2001).

134. Jayaraman, S., Sadeghipour, K., and Baran, G. “Finite element analysis of horizontal and branched subsurface cracks I brittle materials.” Wear 208: 237-242 (1997).

135. Ji, F.S., Dharani, L.R., and Behr, R.A. “Damage probability in laminated glass subjected to low velocity small missile impacts.” J. Materials Science 33(19): 4775-4782 (1998).

136. Jih, C.J., and Sun, C.T. “Prediction of delamination in composite laminates subjected to low velocity impact.” J. Composite Materials 27(7): 684-701 (1993).

137. Jones, R., Paul, J., Tay, T.E., and Williams, J.F. “Assessment of the effect of impact damage in composites: some problems and answers.” Composite Structures 10(1): 51-73 (1988).

138. Jones, R.H., Friesel, M.A., and Pathania, R. “Evaluation of stress corrosion crack initiation using acoustic emission.” Corrosion 47(2): 105-115 (1991).

139. Joshi, S.P., and Sun, C.T. “Impact induced fracture in a laminated composite.” J. Composite Materials 19: 51-66 (1985).

140. Kant, T., and Mallikarjuna “Non-linear dynamics of laminated plates with a higher-order theory and C^0 finite elements.” Int. J. Nonlinear Mechanics 26(3-4): 335-343 (1991).

141. Kant, T., Marur, S.R., and Rao, G.S. “Analytical solution to the dynamic analysis of laminated beams using higher order refined theory.” Composite Structures 40(1): 1-9 (1998).

142. Kawai, M., Hachinohe, A., Takumida, K., and Kawase, Y. “Off-axis fatigue behaviour and its damage mechanics modelling for unidirectional fibre–metal hybrid composite: GLARE 2.” Composites: Part A 32: 13–23 (2001).

143. Kawai, M., Morishita, M., Tomura, S., and Takumida, K. “Inelastic behavior and strength of fiber-metal hybrid composite: Glare.” Int. J. Mechanical Science 40(2-3): 183-198 (1998).

144. Keer, L.M., and Miller, G.R. “Contact between an elastically supported circular plate and a rigid indenter.” Int. J. Engineering Science 21(6): 681-690 (1983).

145. Kellas, S., Morton, J., and Jackson, K.E. “Damage and failure mechanisms in scaled angle-ply laminates.” ASTM STP 1156: 257-280 (1993).

146. Kim, C-G, and Jun, E-J. “Impact resistance of composite laminated sandwich plates.” J. Composite Materials 26(15): 2247-2261 (1992).

147. Kim, J-K, and Kang, K-W. “An analysis of impact force in plain-weave glass/epoxy composite plates subjected to transverse impact.” Composites Science and Technology 61: 135-143 (2001).

148. Kim, K., and Voyiadjis, G.Z. “Non-linear finite element analysis of composite panels.” Composites: Part B 30: 365–381 (1999).

149. Kim, S.J., and Goo, N.S. “Dynamic contact responses of laminated composite plates according to the impactor’s shapes.” Computers and Structures 65(1): 83-90 (1997).

150. Kim, S.J., Goo, N.S., and Kim, T.W. “The effect of curvature on the dynamic response and impact-induced damage in composite laminates.” Composites Science and Technology 57: 763-773 (1997).

151. Kistler, L.S., and Waas, A.M. “Experiment and analysis on the response of curved laminated composite panels subjected to low velocity impact.” Int. Journal of Impact Engineering 21(9): 711–736 (1998).

152. Kline, R.A., Madaras, E.I., and Boltz, E.S. “Nondestructive characterization of elastic anisotropy in carbon-composites.” NDE – Vol.5: 135-140 (1989).

153. Knight, N.F., Jr., and Qi, Y.Q. “On a consistent first-order shear-deformation theory for laminated plates.” Composites Part B 28B: 397-405 (1997).

154. Kumar, P., and Rai, B. “Impact damage on single interface GFRP laminates-An experimental study.” Composite Structures 18(1): 1-10 (1991).

155. Kutlu, Z., and Chang, F.K. “Modeling compression failure of laminated composites containing multiple through-the-width delaminations.” J. Composite Materials 26(3): 350-387 (1992).

156. Lagace, P.A., Ryan, K.F., and Graves, M.J. “Effect of damage on the impact response of composite laminates.” AIAA J. 32(6): 1328-1330 (1994).

157. Lal, K.M. “Low velocity transverse impact behavior of 8-ply, graphite-epoxy laminates.” J. Reinforced Plastics and Composites 2: 216-225 (1983).

158. Lam, K.Y., and Sathiyamoorthy, T.S. “Response of composite beam under low-velocity impact of multiple masses.” Composite Structures 44: 205-220 (1999).

159. Lambros, J., and Rosakis, A.J. “Dynamic crack initiation and growth in thick unidirectional graphite/epoxy plates.” Composites Science and Technology 57: 55-65 (1997).

160. Lammerant, L., and Verpoest, I. “Modeling of the interaction between matrix cracks and delaminations during impact of composite plates.” Composites Science and Technology 56: 1171-1178 (1996).

161. Lawcock, G., Ye, L., and Mai, Y.W. “Novel fiber reinforced metal laminates for aerospace applications - a review: Part I – Background and general mechanical properties.” SAMPE Journal 31(1): 23-31 (1995).

162. Lawcock, G., Ye, L., Mai, Y.W., and Sun, C.T. “The effect of adhesive bonding between aluminum and composite prepreg on the mechanical properties of carbon-fiber-reinforced metal laminates.” Composites Science and Technology 57: 35-45 (1997).

163. Lawcock, G.D., Ye, L., Mai, Y.W., and Sun, C.T. “Effect of fibre/matrix adhesion on carbon-fiber-reinforced metal laminates-I. Residual strength.” Composites Science and Technology 57: 1609-1619 (1997).

164. Lawcock, G.D., Ye, L., Mai, Y.W., and Sun, C.T. “Effect of fibre/matrix adhesion on carbon-fiber-reinforced metal laminates-II. Impact behaviour.” Composites Science and Technology 57: 1621-1628 (1997).

165. Leach, D.C., Curtis, D.C., and Tamblin, D.R. “Delamination behavior of carbon fiber/poly (etheretherketone) (PEEK) composites.” ASTM STP 937: 358-380 (1985).

166. Lee, L.J., Huang, K.Y., and Fann, Y.J. “Dynamic responses of composite sandwich plate impacted by a rigid ball.” J. Composite Materials 27(13): 1238-1256 (1993).

167. Lee, S-M, Cheon, J-S, and Im, Y-T. “Experimental and numerical study of the impact behavior of SMC plates.” Composite Structures 47: 551-561 (1999).

168. Lee, S.M., and Tsotsis, T.K. “Indentation failure behavior of honeycomb sandwich panels.” Composites Science and Technology 60: 1147-1159 (2000).

169. Lee, S-W. R., and Sun, C.T. “A quasi-static penetration model for composite laminates.” J. Composite Materials 27(3): 251-271 (1993).

170. Lee, Y-S, Kang, K-H, and Park, O. “Response of hybrid laminated composite plates under low-velocity impact.” Computers and Structures 65(6): 965-974 (1997).

171. Leylek, Z., Scott, M.L., Georgiadis, S., and Thomson, R.S. “Computer modeling of impact on curved fibre composite panels.” Composite Structures 47: 789-796 (1999).

172. Liao, C-L, and Tsai, J-S. “Dynamic analysis of laminated composite plates subjected to transverse impact using a partial mixed 3-D finite element.” Computers and Structures 53(1): 53-61 (1994).

173. Liaw, B.M., Liu, Y.X., and Villars, E.A. “Impact damage mechanisms in fiber-metal laminates.” SEM Annual Conference on Experimental and Applied Mechanics, Portland, OR: 536-539 (2001).

174. Lifshitz, J.M., and Gandelsman, M. “Effect of near-surface impact-induced damage on the residual strength of woven glass/epoxy composite beams.” Composites Science and Technology 57: 205-216 (1997).

175. Lin, H.J., and Lee, Y.J. “On the inelastic impact of composite laminated plate and shell structures.” Composite Structures 14: 89-111 (1990).

176. Liou, W.J. “Impact analysis of laminated composite plates with statical indentation laws.” Computers and Structures 62(5): 817-829 (1997).

177. Liptai, R.G. “Acoustic emission from composite materials.” ASTM STP 497: 285-298 (1972).

178. Liu, C., Rosakis, A.J., and Stout, M.G. “Dynamic fracture toughness of a unidirectional Graphite/Epoxy composite.” 2001 ASME IMECE/AMD-25400.

179. Liu, D. “Impact-induced delamination-a view of bending stiffness mismatching.” J. Composite Materials 22: 674-692 (1988).

180. Liu, D., Lee, C.Y., and Lu, X. “Reparability of impact-induced damage in SMC composites.” J. Composite materials 27(13): 1257-1271 (1993).

181. Liu, D., Lillycrop, L.S., Malvern, L.E., and Sun, C.T. “The evaluation of delamination-an edge replication study.” Experimental Techniques 11(5), 20-25 (1987).

182. Liu, D., and Malvern, L.E. “Matrix cracking in impacted glass/epoxy plates.” J. Composite Materials 21: 594-609 (1987).

183. Liu, S., and Chang, F.K. “Matrix cracking effect on delamination growth in composite laminates induced by a spherical indenter.” J. Composite Materials 28(10): 940-977 (1994).

184. Liu, S., Kutlu, Z., and Chang, F.K. “Matrix cracking-induced delamination propagation in graphite/epoxy laminated composites due to a transversely concentrated load.” ASTM STP 1156: 86-101 (1993).

185. Liu, S., Kutlu, Z., and Chang, F.K. “Matrix cracking and delamination in laminated composite beams subjected to a transverse concentrated line load.” J. Composite Materials 27(5): 436-470 (1993).

186. Luo, R.K. “The evaluation of impact damage in a composite plate with a hole.” Composites Science and Technology 60: 49-58 (2000).

187. Luo, R.K., Green, E.R., and Morrison, C.J. “Impact damage analysis of composite plates.” Int. Journal of Impact Engineering 22: 435–447 (1999).

188. Luo, R.K., Green, E.R., and Morrison, C.J. "An approach to evaluate the impact damage initiation and propagation in composite plates." Composites Part B 32: 513-520 (2001).

189. Mahajan, P. "Contact behavior of an orthotropic laminated beam indented by a rigid cylinder." Composites Science and Technology 58: 505-513 (1998).

190. Mahajan, P., and Dutta, A. "Adaptive computation of impact force under low velocity impact." Computers and Structures 70: 229-241 (1999).

191. Manet, V. "The use of ANSYS to calculate the behaviour of sandwich structures." Composites Science and Technology 58: 1899-1905 (1998).

192. Marissen, R., and Vogelesang, L.B. "Development of a new hybrid material: Aramid reinforced aluminum laminate (ARALL)." SAMPE Conference, Cannes, France. (1981).

193. Martin, R.H., and Jackson, W.C. "Damage prediction in cross-plied curved composite laminates." ASTM STP 1156: 105-126 (1993).

194. Matemilola, S.A., and Stronge, W.J. "Impact induced dynamic deformations and stresses in CFRP composite laminates." Composites Engineering 5(2): 211-222 (1995).

195. McCartney, L. N. "Predicting transverse crack formation in cross-ply laminates." Composites Science and Technology 58: 1069-1081 (1998).

196. Meimaris, C., and Day, J.D. "Dynamic response of laminated anisotropic plates." Computers and Structures 55(2): 269-278 (1995).

197. Mili, F., and Necib, B. "Impact behavior of cross-ply laminated composite plates under low velocities." Composite Structures 51: 237-244 (2001).

198. Mines, R.A.W., Worrall, C.M., and Gibson, A.G. "The static and impact behaviour of polymer composite sandwich beams." Composites 25(2): 95-110 (1994).

199. Mines, R. A. W., Worrall, C. M., and Gibson, A. G. "Low velocity perforation behaviour of polymer composite sandwich panels." Int. Journal of Impact Engineering 21(10): 855-879 (1998).

200. Morton, J., and Godwin, E.W. "Impact response of tough carbon fibre composites." Composite Structures 13(1): 1-19 (1989).

201. Mouritz, A.P., Townsend, C., and Shah Khan, M.Z. "Non-destructive detection of fatigue damage in thick composites by pulse-echo ultrasonics." Composites Science and Technology 60: 23-32 (2000).

202. Naganarayana, B.P., and Atluri, S.N. “Energy-release-rate evaluation for delamination growth prediction in a multi-plate model of a laminate composite.” Computational Mechanics 15(5): 443-459 (1995).

203. Naik, N.K., Sekher, Y.C., and Meduri, S. “Damage in woven-fabric composites subjected to low-velocity impact.” Composites Science and Technology 60: 731-744 (2000).

204. Nemes, J.A., and Simmonds, K.E. “Low-velocity impact response of foam-core sandwich composites.” J. Composite Materials 26(4): 500-519 (1992).

205. Nguyen, B.N. “Damage modeling of laminated composites by the use of multilayer volume elements.” Composites Science and Technology 58: 891-905 (1998).

206. Noor, A.K., Burton, W.S., and Bert, C.W. “Computational models for sandwich panels and shells.” Applied Mechanics Review 49(3): 155-199 (1996).

207. Oguibe, C.N., and Webb, D.C. “Finite-element modeling of the impact response of a laminated composite plate.” Composites Science and Technology 59: 1913-1922 (1999).

208. O’kane, B.A.A., and Benham, P.P. “Damage thresholds for low velocity impact on aircraft structural composites.” Aeronautical Journal 90(899): 368-372 (1986).

209. Olsson, R. “Impact response of orthotropic composite plates predicted from a one-parameter differential equation.” AIAA J. 30(6): 1587-1596 (1992).

210. Ousset, Y., and Roudolff, F. “Numerical analysis of delamination in multilayered composite plates.” Computational Mechanics 20: 122-126 (1997).

211. Pai, P.F., and Palazotto, A.N. “Nonlinear displacement-based finite-element analysis of composite shells-A new total Lagrangian formulation.” Int. J. Solids Structures 32(20): 3047-3073 (1995).

212. Palazotto, A.N., Herup, E.J., and Gummadi, L.N.B. “Finite element analysis of low-velocity impact on composite sandwich plates.” Composite Structures 49: 209-227 (2000).

213. Park, R., and Jang, J. “Impact behavior of Aramid fiber/Glass fiber hybrid composite: evaluation of impact behavior using delamination area.” J. Composite Materials 34(13): 1117-1135 (2000).

214. Pavier, M.J., and Clarke, M.P. “Experimental techniques for the investigation of the effects of impact damage on carbon-fibre composites.” Composites Science and Technology 55: 157-169 (1995).

215. Peck, S.O., and Springer, G.S. "The behavior of delaminations in composite plates-analytical and experimental results." J. Composite Materials 25: 907-929 (1991).

216. Peijs, A.A.J.M., Venderbosch, R.W., and Lemstra, P.J. "Hybrid composites based on polyethylene and carbon fibres part 3: impact resistant structural composites through damage management." Composites 21(6): 522-530 (1990).

217. Philippidis, T.P., and Lekou, D.J. "Probabilistic failure prediction for FRP composites." Composites Science and Technology 58: 1973-1982 (1998).

218. Pierides, A.M., Liu, Y.X., and Liaw, B.M. "Ultrasonic assessment of impact damages in fiber-metal laminated panels." ASME International Mechanical Engineering Congress & Exposition-IMECE'01, New York, 2001.

219. Pintado, P., Vogler, T.J., and Morton, J. "Impact damage development in thick composite laminates." Composites Engineering 1(4): 195-210 (1991).

220. Poe, C.C., Jr. "Simulated impact damage in a thick graphite/epoxy laminate using spherical indenters." J. Reinforced Plastics and Composites 10(5): 293-307 (1991).

221. Potel, C., Chotard, T., De Belleval, J-F, and Benzeggagh, M. "Characterization of composite materials by ultrasonic methods: modelization and application to impact damage." Composites Part B 29B: 159-169 (1998).

222. Preuss, T.E., and Clark, G. "Use of time-of-flight C-scanning for assessment of impact damage in composites." Composites 19(2): 145-148 (1988).

223. Prichard, J.C., and Hogg, P.J. "The role of impact damage in post-impact compression testing." Composites 21(6): 503-511 (1990).

224. Qian, Y., and Swanson, S.R. "Experimental measurement of impact response in carbon/epoxy plates." AIAA J. 28(6): 1069-1074 (1990).

225. Qian, Y., and Swanson, S.R. "A comparison of solution techniques for impact response of composite plates." Composite Structures 14: 177-192 (1990).

226. Razi, H., and Kobayashi, A.S. "Delamination in cross-ply laminated composite subjected to low-velocity impact." AIAA J. 31(8): 1498-1502 (1993).

227. Razi, P.S., and Raman, A. "Studies on impact fracture properties of wood-polymer composites." J. Composite Materials 34(12): 980-997 (2000).

228. Reddy, Y.S.N., Moorthy, C.M.D., and Reddy, J.N. "Non-linear progressive failure analysis of laminated composite plates." Int. J. Solids Structures 30(5): 629-649 (1995).

229. Reid, S.R., and Zhou, G. *Impact Behaviour of Fibre-reinforced Composite materials and Structures.* Woodhead Publishing Ltd and CRC Press LLC 2000.

230. Reis, L., and De Freitas, M. “Damage growth analysis of low velocity impacted composite panels.” Composite Structures 38(1-4): 509-515 (1997).

231. Reyes V., G., and Cantwell, W.J. “The mechanical properties of fibre-metal laminates based on glass fibre reinforced polypropylene.” Composites Science and Technology 60: 1085-1094 (2000).

232. Rhodes, M.D., Williams, J.G., and Starnes, J.H., Jr. “Low-velocity impact damage in graphite-fiber reinforced epoxy laminates.” Polymer Composites 2(1): 36-44 (1981).

233. Richardson, M.O.W, Zhang, Z.Y., Wisheart, M., Tyrer, J.R., and Petzing, J. “ESPI non-destructive testing of GRP composite materials containing impact damage.” Composites Part A 29A: 721-729 (1998).

234. Rief, C., Lindner, M., and Kromp, K. “Experimental investigations and a model proposal on damage mechanisms in a reinforced carbon-carbon composite.” ASTM STP 1059: 564-579 (1990).

235. Rippert, L., Wevers, M., and Huffel, S.V. “Optical and acoustic damage detection in laminated CFRP composite materials.” Composites Science and Technology 60: 2713-2724 (2000).

236. Rydin, R.W., and Karbhari, V.M. “Partitioning energy during low-velocity impact of RTM fiber-reinforced composites.” Int. Journal of Impact Engineering 21(9): 773–789 (1998).

237. Salpekar, S.A. “Analysis of delamination in cross-ply laminates initiating from impact induced matrix cracking.” J. Composites Technology and Research 15(2): 88-94 (1993).

238. Sankar, B.V., and Zhu, H.S. “The effect of stitching on the low-velocity impact response of delaminated composite beams.” Composites Science and Technology 60: 2681-2691 (2000).

239. Scarponi, C., and Briotti, G. “Ultrasonic technique for the evaluation of delaminations on CFRP, GFRP, KFRP composite materials.” Composites Part B 31: 237–243 (2000).

240. Schijve, J., Van lipzig, H.T.M., Van Gestel, G.F.J.A., and Hoeymakers, A.H.W. “Fatigue properties of adhesive-bonded laminated sheet material of aluminum alloys.” Engineering Fracture Mechanics 12: 561-579 (1979).

241. Schoeppner, G.A., and Abrate, S. “Delamination threshold loads for low velocity impact on composite laminates.” Composites: Part A 31: 903–915 (2000).

242. Sciuva, M.D., and Librescu, L. “Contribution to the nonlinear theory of multilayered composite shells featuring damaged interfaces.” Composites Part B 32: 219-227 (2001).

243. Sekine, H., Hu, N., Fukunaga, H., and Natsume, T. “Low-velocity impact response of composite laminates with a delamination.” Mechanics of Composite Materials and Structures 5: 257-278 (1998).

244. Shih, W.K., and Jang, B.Z. “Instrumented impact testing of composite sandwich panels.” J. Reinforced Plastics and Composites 8(5): 270-298 (1989).

245. Shih, J-H, and Mal, A.K. “Acoustic emission from impact damage in cross-ply composites.” Structural health Monitoring 2000 (Edited by Chang, F.K.): 209-217.

246. Shimamura, S., and Yamamoto, K. “Impact damage patterns studied by a model simulation.” J. Materials Science 31: 3299-3308 (1996).

247. Shivakumar, K.N., Elber, W., and Illg, W. “Prediction of low-velocity impact damage in thin circular laminates.” AIAA J. 23(3): 442-449 (1985).

248. Shivakumar, K.N., Elber, W., and Illg, W. “Prediction of impact force and duration due to low-velocity impact on circular composite laminates.” J. Applied Mechanics 52: 674-680 (1985).

249. Shupikov, A.N., Ugrimov, S.V., Kolodiazhny, A.V., and Yareschenko, V.G. “High-order theory of multilayer plates: the impact problem.” Int. J. Solids Structures 35(25): 3391-3403 (1998).

250. Sierakowski, R.L., and Chaturvedi, S.K. *Dynamic Loading and Characterization of Fiber-reinforced Composites.* John Wiley & Sons, Inc., New York, 1997.

251. Soden, P.D., Hinton, M.J., and Kaddour, A.S. “A comparison of the predictive capabilities of current failure theories for composite laminates.” Composites Science and Technology 58: 1225-1254 (1998).

252. Sridhar, C., and Rao, K.P. “Large deformation finite element analysis of laminated circular composite plates.” Computers and Structures 54(1): 59-64 (1995).

253. Srinivasan, K., Jackson, W.C., Smith, B.T., and Hinkley, J.A. “Characterization of damage modes in impacted thermoset and thermoplastic composites.” J. Reinforced Plastics and Composites 11(10): 1111-1126 (1992).

254. Strait, L.H., Karasek, M.L., and Amateau, M.F. "Effects of stacking sequence on the impact resistance of carbon fiber reinforced thermoplastic toughened epoxy laminates." J. Composite Materials 26(12): 1725-1740 (1992).

255. Suemasu, H., Kerth, S., and Maier, M. "Indentation of spherical head indenters on transversely isotropic composite plates." J. Composite Materials 28(17): 1723-1739 (1994).

256. Sun, C.T., and Chen, J.K. "On the impact of initially stressed composite laminates." J. Composite Materials 19: 490-504 (1985).

257. Sun, C.T., Dicken, A., and Wu, H.F. "Characterization of impact damage in ARALL laminates." Composites Science and Technology 49: 139-144 (1993).

258. Sun, C.T., and Jih, C.J. "Mechanics of delamination in composite laminates subjected to low velocity impact." In A.K. Mal, and Y.D.S. Rajapakse (eds.), Impact Response and Elastodynamics of Composites, ASME publication AMD-116: 1-10 (1990).

259. Sun, C.T., and Liou, W.J. "Investigation of laminated composite plates under impact dynamic loading using a three-dimensional hybrid stress finite element method." Computers and Structures 33(3): 879-884 (1989).

260. Sun, C.T., and Tao, J.X. "Prediction of failure envelopes and stress/strain behaviour of composite laminates." Composites Science and Technology 58: 1125-1136 (1998).

261. Swanson, S.R. "Impact response of fiber composite structures." Applied Mechanics Review 44(11): 256-263 (1991).

262. Swanson, S.R. "Mechanics of transverse impact in fiber composite plates and cylinders." J. Reinforced Plastics and Composites 12(3): 256-267 (1993).

263. Swider, P., Le Fichoux, B., and Jacquet-Richardet, G. "Dynamic modeling of a composite plate, a mixed numerical and experimental approach." Composite Structures 34: 301-308 (1996).

264. Tam, W.Y., Cheung, T.Y.H., and Li, R.K.Y. "Impact properties of glass fibre/impact modifier/polypropylene hybrid composites." J. Materials Science 35: 1525-1533 (2000).

265. Tan, T.M., and Sun, C.T. "Use of statical indentation laws in the impact analysis of laminated composite plates." J. Applied Mechanics 52: 6-12 (March 1985).

266. Toh, S.L., Gong, S.W., and Shim, V.P.W. "Transient stresses generated by low velocity impact on orthotropic laminated cylindrical shells." Composite Structures 31: 213-228 (1995).

267. Torre, L., and Kenny, J.M. "Impact testing and simulation of composite sandwich structures for civil transportation." Composite Structures 50: 257-267 (2000).

268. Tsai, X.G., and Tang, J.M. "The impact behavior of laminated glass fiber composites by weight dropping testing method." 36th International SAMPE Symposium and Exhibition Vol. 36A: 1118-1127 (1991).

269. Tu, C.Y., and Chao, C.C. "Three-dimensional contact dynamics of laminated plates: Part 2. Oblique impact with friction." Composites: Part B 30: 23–41 (1999).

270. Vaidya, U.K., Palazotto, A.N., and Gummadi, L.N.B. "Low velocity impact and compression-after-impact response of Z-pin reinforced core sandwich composites." J. Engineering Materials and Technology 122: 434-442 (2000).

271. Varadi, K., Neder, Z., Friedrich, K., and Flock, J. "Finite-element analysis of a polymer composite subjected to ball indentation." Composites Science and Technology 59: 271-281 (1999).

272. Vasek, A., Polak, J., and Kozak, V. "Fatigue crack initiation in fiber-metal laminate GLARE 2." Materials Science and Engineering A234-236: 621-624 (1997).

273. Vlot, A. "Impact properties of fibre metal laminates." Composites Engineering 3(10): 911-927 (1993).

274. Vlot, A. "Impact loading on fibre metal laminates." Int. J. Impact Eng. 18(3): 291-307 (1996).

275. Vlot, A. *High Strain Rate Tests on Fibre Metal Laminates*. Delft University Press 1998.

276. Vlot, A., Kroon, E., and La Rocca, G. "Impact response of fiber metal laminates." Key Engineering Materials 141-143: 235-276 (1998).

277. Vogelesang, L.B., and Vlot, A. "Development of fibre metal laminates for advanced aerospace structures." Journal of Materials Processing Technology 103: 1-5 (2000).

278. Voyiadjis, G.Z., and Kattan, P.L. *Advances in Damage Mechanics: Metals and Metal Matrix Composites.* Elsevier Science Ltd 1999.

279. Walter, M.E., and Ravichandran, G. "Experimental simulation of matrix cracking and debonding in a model brittle matrix composite." Exp. Mech. 37(2): 126–131 (1997).

280. Wang, C.J., Jang, B.Z., Panus, J., and Valaire, B.T. "Impact behavior of Hybrid-fiber and hybrid-matrix composites." J. Reinforced Plastics and Composites 10(7): 356-378 (1991).

281. Wang, C-Y, and Yew, C.H. “Impact damage in composite laminates.” Computers and Structures 37(6): 967-982 (1990).

282. Wang, Y.Y., Lam, K.Y., and Liu, G.R. “Detection of flaws in sandwich plates.” Composite Structures 34: 409-418 (1996).

283. Wiggenraad, J.F.M., Aoki, R., et al. “Damage propagation in composite structural elements – analysis and experiments on structures.” Composite Structures 36: 173-186 (1996).

284. Wiggenraad, J.F.M., Zhang, X., and Davies, G.A.O. “Impact damage prediction and failure analysis of heavily loaded, blade-stiffened composite wing panels.” Composite Structures 45: 81-103 (1999).

285. Williams, J.F., Stouffer, D.C., Ilic, S., and Jones, R. “An analysis of delamination behaviour.” Composite Structures 5: 203-216 (1986).

286. Williams, J.G., and Rhodes, M.D. “Effect of resin on impact damage tolerance of graphite/epoxy laminates.” ASTM STP 787: 450-480 (1981).

287. Williams, K.V., and Vaziri, R. “Application of a damage mechanics model for predicting the impact response of composite materials.” Computers and Structures 79: 997-1011 (2001).

288. Wilson Tsang, P.H., and Dugundji, J. “Damage resistance of graphite/epoxy sandwich panels under low speed impacts.” J. The American Helicopter Society 37(1): 75-81 (1992).

289. Wisheart, M., and Richardson, M.O.W. “The finite element analysis of impact induced delamination in composite materials using a novel interface element.” Composites Part A 29A: 301-313 (1998).

290. Wolfe, W.E., and Butalia, T.S. “A strain-energy based failure criterion for non-linear analysis of composite laminates subjected to biaxial loading.” Composites Science and Technology 58: 1107-1124 (1998).

291. Wooh, S-C, and Daniel, I.M. “Three-dimensional ultrasonic imaging of defects and damage in composite materials.” Materials Evaluation 52(10): 1199-1206 (1994).

292. Wu, E., Chao, J-C, and Yen, C-S. “Smooth contact of orthotropic laminates by rigid cylinders.” AIAA J. 31(10): 1916-1921 (1993).

293. Wu, E., and Shyu, K. “Response of composite laminates to contact loads and relationship to low-velocity impact.” J. Composite Materials 27(15): 1443-1464 (1993).

294. Wu, E., and Yen, C-S. “The contact behavior between laminated composite plates and rigid spheres.” J. Applied Mechanics 61: 60-66 (March 1994).

295. Wu, E., Yeh, J-C, and Yen, C-S. “Impact on composite laminated plates: an inverse method.” Int. J. Impact Engineering 15(4): 417-433 (1994).

296. Wu, H.F. “Statistical analysis of tensile strength of ARALL laminates.” J. Composite Materials 23: 1065-1080 (1989).

297. Wu, H.F. “Temperature dependence of the tensile properties of ARALL-4 laminates.” J. Materials Science 25: 1120-1127 (1990).

298. Wu, H-Y. T., and Chang, F.K. “Transient dynamic analysis of laminated composite plates subjected to transverse impact.” Computers and Structures 31(3): 453-466 (1989).

299. Wu, H-Y. T., and Springer, G.S. “Measurements of matrix cracking and delamination caused by impact on composite plates.” J. Composite Materials 22: 518-532 (1988).

300. Wu, H-Y. T., and Springer, G.S. “Impact induced stresses, strains, and delaminations in composite plates.” J. Composite Materials 22: 533-560 (1988).

301. Xia, Z.H., Chen, Y., and Ellyin, F. “A meso/micro-mechanical model for damage progression in glass-fiber/epoxy cross-ply laminates by finite-element analysis.” Composites Science and Technology 60: 1171-1179 (2000).

302. Xu, L.R., and Rosakis, A.J. “Impact failure characteristics in sandwich structures Part I: Basic failure mode selection.” International Journal of Solids and Structures 39: 4215–4235 (2002).

303. Yang, I-Y, and Im, K-H. “Impulsive stress analysis of plates at the concentrated impact loading point by the three-dimensional dynamic theory of elasticity.” Experimental Mechanics 36(4): 421-429 (1996).

304. Yang, S.H., and Sun, C.T. “Indentation law for composite laminates.” ASTM STP 787: 425-449 (1981).

305. Yeh, J.R. “Fatigue crack growth in fiber-metal laminates.” Int. J. Solids Structures 32(14): 2063-2075 (1995).

306. Yigit, A.S., and Christoforou, A.P. “On the impact between a rigid sphere and a thin composite laminate supported by a rigid substrate.” Composite Structures 30: 169-177 (1995).

307. Zhang, S.Y. “A new model for the energy release rate of fibre/matrix interfacial fracture.” Composites Science and Technology 58: 163-166 (1998).

308. Zhang, S.Y. “Debonding and cracking energy release rate of the fiber/matrix interface.” Composites Science and Technology 58: 331-335 (1998).

309. Zhao, Y., Pang, S.S., and Griffin, S.A. “Force-indentation study of transversely isotropic composite materials using a conical-tip indenter.” Composites Engineering 1(6): 393-402 (1991).

310. Zheng, S., and Sun, C.T. “A double-plate finite-element model for the impact-induced delamination problem.” Composites Science and Technology 53: 111-118 (1995).

311. Zhou, G. “Prediction of impact damage thresholds of glass fibre reinforced laminates.” Composite Structures 31: 185-193 (1995).

312. Zhou, G. “Damage mechanisms in composite laminates impacted by a flat-ended impactor.” Composites Science and Technology 54: 267-273 (1995).

313. Zhou, G., and Davies, G.A.O. “Impact response of thick glass fibre reinforced polyester laminates.” Int. J. Impact Engineering 16(3): 357-374 (1995).

314. Zhou, G. “Effect of impact damage on residual compressive strength of glass-fibre reinforced polyester (GFRP) laminates.” Composite Structures 35: 171-181 (1996).

315. Zhou, G. “The use of experimentally-determined impact force as a damage measure in impact damage resistance and tolerance of composite structures.” Composite Structures 42: 375-382 (1998).

316. Doyle, P.A., and Scala, C.M. “Crack depth measurement by ultrasonics: a review.” Ultrasonics: 164-170 (1978).

317. Hallquist, J.O. “LS-DYNA theoretical manual.” Livermore Software Technology Corporation, CA, 1998.

318. Structural Laminates Company – Customer Data Sheet. Delft, The Netherlands.

319. Rybicki, E.F., and Kanninen, M.F. “A finite element calculation of stress intensity factors by a modified crack closure integral.” Engineering Fracture Mechanics 9: 931-938 (1977).

320. Kam, T.Y., and Lai, F.M. “Experimental and theoretical predictions of first-ply failure strength of laminated composite plates.” International Journal of Solids and Structures 36: 2379-2395 (1999).

321. Castrodeza, E.M., Bastian, F.L., and Perez-Ipina, J.E. “Critical fracture toughness, J_C and δ_{5C}, of unidirectional fiber-metal laminates.” Thin-walled Structures 41(12): 1089-1111 (2003).

322. Reyes V., G., and Cantwell, W.J. “The high velocity impact response of composite and FML-reinforced sandwich structures” Composites Science and Technology 64: 35-54 (2004).

323. Meo, M., Morris, A.J., Vignjevic, R., and Marengo, G. “Numerical simulations of low-velocity impact on an aircraft sandwich panel.” Composite Structures 62: 353-360 (2003).

324. Liaw, B.M., Zeichner, G., and Liu, Y.X. “Impact delamination and fracture in aluminum/acrylic sandwich plates,” Proceedings of the SEM IX International Congress on Experimental Mechanics, Orlando, FL, June 5-8, 515-518 (2000).

325. Miravete, A., and Jimenez, M.A. “Application of the finite element method to prediction of onset of delamination growth.” Applied Mechanics Review 55(2): 89-106 (2002).

326. Tsai, Y.M., and Kolsky, H. “Study of fractures produced in glass block by impact.” J. Mech. Phys. Solids 15: 263-278 (1967).

327. Knight, C.G., Swain, M.V., and Chaudhri, M.M. “Impact of small steel spheres on glass surfaces.” J. Materials Science 12: 1573-1586 (1977).

328. Lawn, B.R., *Fracture of brittle solids*, 2nd Ed. Cambridge: Cambridge University Press, 1993.

329. Fineberg, J., and Marder, M. “Instability in dynamic fracture.” Physics Reports 313: 1-108 (1999).

330. Vaughan, H. “Crack propagation and the principal-tensile-stress criterion for mixed-mode loading.” Engineering Fracture Mechanics 59: 393-397 (1998).

331. Repetto, E.A., Radovitzky, R., and Ortiz, M. “Finite element simulation of dynamic fracture and fragmentation of glass rods.” Comput. Methods Appl. Mech. Engrg. 183: 3-14 (2000).

332. Andrews, E.W., and Kim, K.S. “Threshold conditions for dynamic fragmentation of glass particles.” Mechanics of Materials 31: 689-703 (1999).

333. Cao, Y.Q., and Zhang, G.M. “Multiple surface crack initiation and growth in glass-ceramics loaded by a sphere.” Engineering Fracture Mechanics 67: 277-292 (2000).

334. Koenke, C., Harte, R., Kratzig, W.B., and Rosenstein, O. “On adaptive remeshing techniques for crack simulation problems.” Engng Comput 15: 74-88 (1998).

335. Tradegard, A., Nillson, F., and Ostlund, S. “FEM-remeshing technique applied to crack growth problems.” Comput Meth Appl Mech Engng 160: 115-131 (1998).

336. Tang, C.A., and Kou, S.Q. "Crack propagation and coalescence in brittle materials under compression." Engineering Fracture Mechanics 61: 311-324 (1998).

337. Graff, K.F., *Wave motion in elastic solids. Dover Publications*, Inc., New York, 1991.

338. Callister, W.D., Jr., *Materials Science and Engineering: An Introduction*, 5th Ed. Wiley, New York, 2000.

339. Liaw, B.M., Pierides, A.M., and Liu, Y.X., "Ultrasonic assessment of impact damage in Aluminum/Acrylic sandwich plates." SEM Annual Conference on Experimental and Applied Mechanics, Portland, OR: 264-268 (2001).

340. Timoshenko, S.P., and Goodier, J.N. *Theory of elasticity*. McGraw-Hill Book Company, New York, 1970.

341. Segreti, M., Rusinek, A., and Klepaczko, J.R. "Experimental study on puncture of PMMA at low and high velocities, effect on the failure mode." Polymer Testing 23(6): 703-718 (2004).

342. Chaudhri, M.M. "Impact breakage of semi-brittle spheres." Powder Technology 143– 144: 31– 40 (2004).

343. Gorham, D.A., Salman, A.D., and Pitt, M.J. "Static and dynamic failure of PMMA spheres." Powder Technology 138: 229– 238 (2003).

344. LS-DYNA keyword user's manual, Livermore Software Technology Corporation, CA, 2001.

345. Mahfuz, H., Zhu, Y.H., Mamun, W.A., Haque, A., and Jeelani, S. "Failure analysis of hybrid armor under high velocity impact." AMD-Vol. 243, Dynamic Failure in Composite Materials and Structures, ASME 2000, pp. 115-127.

346. Mendelson, A. "Plasticity: Theory and Application." Robert E. Krieger Publishing Company, Florida, 1968.

347. Kwon, Y.W., and Wojcik, G.W. "Impact study of sandwich composite structures with delamination.' Journal of Composite Materials 32(5): 406-430 (1998).

348. Park, H.C., Park, J., Goo, N.S., Yoon, K.J., and Lee, J.H. "Analysis of low-velocity impact on composite sandwich panels using an assumed strain solid element**."** Key Engineering Materials 261-263: 283-288 (2004).

349. Meo, M., Morris, A.J., Vignjevic, R., and Marengo, G. "Numerical simulations of low-velocity impact on an aircraft sandwich panel." Composite Structures 62: 353-360 (2003).

350. Akil Hazizan, Md., and Cantwell, W.J. "The low velocity impact response of an aluminum honeycomb sandwich structure." Composites: Part B 34: 679-687 (2003).

351. Icardi, U., and Zardo, G. "C^0 plate element for delamination damage analysis, based on a zig-zag model and strain energy updating." International Journal of Impact Engineering (2004).

352. Kobayashi, A.S., Emery, A.F. and Liaw, B.M., "Dynamic Fracture Toughnesses of Reaction Bonded Silicon Nitride," Journal of the American Ceramic Society, 66 (2): 151-155 (1983).

353. Kobayashi, A.S., Emery, A.F. and Liaw, B.M., "Dynamic Fracture Toughness of Glass," *Fracture Mechanics of Ceramics*, Vol. 6, ed. by R.C. Bradt, A.G. Evans, D.P.H. Hasselman and F.F. Lange, Plenum Press, New York, 47-62 (1983).